THE
PHYSICAL REVIEW
A Journal of Experimental and Theoretical Physics Established by E. L. Nichols in 1893
VOL. 50, NO. 1 JULY 1, 1936 SECOND SERIES

$K\alpha$ Satellite Lines

LYMAN G. PARRATT,* *Cornell University*
(Received May 6, 1936)

With a two-crystal vacuum spectrometer, ionization curves of the $K\alpha_{3,4}$ group of x-ray satellite lines have been recorded for elements S(16) to Ge(32). In the $K\alpha_{3,4}$ satellite group are found five component lines for $16 \leq Z \leq 28$ and four components for $29 \leq Z \leq 32$. The wave-length position, relative intensity, and line width at half-maximum intensity of each satellite component has been measured. The widths and shapes of the $K\alpha_{1,2}$ lines were determined and a brief discussion of these data is given.

I. INTRODUCTION

SO-CALLED satellite lines are known to accompany many of the intense diagram lines in x-ray spectra. $K\alpha$ satellites[1–4] have been observed for elements Na(11) to Rh(45); $K\beta$ satellites[1–6] for elements Na(11) to Sn(50); satellites of certain L series lines[1, 7] for elements Ni(28) to U(92); and of M series lines[1, 8, 9] for elements Sm(62) to U(92). As many as twelve $K\alpha$ and seven $K\beta$ satellites have been reported. Although satellites comprise a large fraction of the total number of characteristic x-ray emission lines we do not yet have a generally acceptable explanation of the atomic phenomena involved in their production.

The term "nondiagram lines," in common use in referring to satellites, signifies that the atomic (or ionic) energy states involved in the emission of these lines are not included in the ordinary energy diagrams. A complete system of diagrams *must* include the levels involved in the satellite transitions: These transitions are apparently between energy states of multiply rather than singly-ionized atoms. As our understanding of these levels increases, the term "nondiagram lines" should become a misnomer as is the case for the term "forbidden lines" in x-ray spectra. Then, x-ray satellites may be known properly as second and higher order diagram lines. (The term "satellites" is purely descriptive and is noncommittal as to the origin of the lines.)

Several significant theoretical advances[10, 11]

* The author is indebted to the Carnegie Foundation for a grant-in-aid of this research.

[1] M. Siegbahn, *Spektroskopie der Röntgenstrahlen* (Julius Springer, 1931), and references.

[2] A. H. Compton and S. K. Allison, *X-Rays in Theory and Experiment* (D. Van Nostrand Co., Inc., 1935), and references.

[3] O. R. Ford, Phys. Rev. **41**, 577 (1932).

[4] M. H. Hulubei, Comptes rendus **201**, 544 (1935).

[5] H. Karlsson and M. Siegbahn, Zeits. f. Physik **88**, 76 (1934).

[6] E. C. Ingelstam, Zeits. f. Physik **87**, 283 (1934), and references.

[7] S. Kaufman, Phys. Rev. **45**, 385, 613 (1934).

[8] E. Lindberg, Nova Acta Reg. Soc. Sci. Upsaliensis Ser. (IV) **7**, No. 7, (1931).

[9] F. R. Hirsh, Jr., Phys. Rev. **38**, 914 (1931).

[10] M. J. Druyvesteyn, Zeits. f. Physik **43**, 707 (1927); B. B. Ray, Phil. Mag. **8**, 772 (1929); R. M. Langer, Phys. Rev. **37**, 457 (1931); M. Sawada, Kyota Coll. Sci. Mem. **15**, 43 (1932); H. C. Wolfe, Phys. Rev. **43**, 221 (1933) and others. See also R. D. Richtmyer, Phys. Rev. **49**, 1 (1936). For the double jump theory see F. K. Richtmyer, J. Frank. Inst. **208**, 325 (1929), and F. Bloch, Phys. Rev. **48**, 187 (1935).

[11] E. H. Kennard and E. G. Ramberg, Phys. Rev. **46**, 1040 (1934).

in the construction of higher order diagrams for x-rays have been made but the compromising assumptions and the difficulty of the calculations have hindered this development. However, the lack of unambiguous experimental descriptions of these lines has been perhaps the most important factor in allowing the enigmatic status of satellites to persist.[12]

Practically all of our information to date about satellites has been obtained from analyses of photographic plates. In supplying such information the photographic method is subject to two serious limitations: (1) The uncertain intensity calibrations, and (2) the low and indefinite effective resolving power. These limitations, especially serious in studying the faint satellite lines which appear on the side of an intense, overexposed diagram line, have restricted quantitative measurements, for the most part, to determinations of wave-length positions. Even in these measurements, because of the low resolving power and the uncertain satellite backgrounds, the accuracy leaves something to be desired.

Recently several important contributions[13–15] to our empirical knowledge of these lines have been made utilizing the high resolving power of the double spectrometer and the ionization method of recording intensities. In the present paper are reported experiments in which the two-crystal spectrometer was used in determinations of the relative intensities, wave-lengths, and widths and shapes of the various components of the $K\alpha_{3,4}$ group of satellites for elements S(16) to Ge(32). A measurement of the excitation potential of these lines has been reported in a previous paper.[14] Another $K\alpha$ satellite, α'', not of the $\alpha_{3,4}$ group, has also been studied and the results previously reported.[15]

Measurements of the widths and shapes of the $K\alpha_{1,2}$ lines for elements S(16) to Mo(42) and a brief discussion of these measurements in terms of the recent developments in the effects of radiationless transitions are also included in this study.

II. Experimental Part

Spectrometer

The two-crystal vacuum spectrometer and the accessory equipment employed in these experiments have been previously described.[16, 17] The experimental set-up was identical with that discussed in an earlier report[14] except in one regard: In studying radiations of wave-lengths less than 1.5A, methyl-bromide, at a pressure of one atmosphere, was placed in the ionization chamber instead of argon which was used with wave-lengths greater than 1.5A.

The accuracy with which the x-ray intensities, or the ionization currents, were measured has been previously discussed.[14]

In regard to the measurements of the line widths and shapes and of the relative intensities it is important that we have as much information as possible about the resolving power of the spectrometer. It is well known that the resolving power of the double spectrometer (with slits properly arranged) is limited by the diffraction patterns of the crystals. The calcite crystals used in the present work were specimens A_4B_4 which have been previously studied[17, 18] and found to be "spectrometrically perfect," that is, with diffraction pattern widths and shapes that yield a maximum effective resolving power.[19]

[12] The analogy between optical spectra and x-ray satellite spectra deserves further comment. From the point of view of theory there is a comparable degree of complexity between the two types of spectra. From the point of view of experiment the situations are somewhat different. This difference is due principally to the enormously greater relative widths of the x-ray lines. Because of the great line widths, wave-length positions cannot be determined with a comparable degree of precision and they do not have the practical physical meaning that obtains in the optical region. This circumstance has contributed materially to the relatively retarded progress in explaining x-ray satellites.

[13] For example, see F. K. Richtmyer and L. S. Taylor, Phys. Rev. **36**, 1044 (1930); J. W. M. DuMond and A. Hoyt, Phys. Rev. **36**, 799 (1930); and F. Wisshak, Physik. Zeits. **35**, 301 (1934).

[14] L. G. Parratt, Phys. Rev. **49**, 132 (1936).

[15] L. G. Parratt, Phys. Rev. **49**, 502 (1936).

[16] L. G. Parratt, Phys. Rev. **41**, 553 (1932) and Rev. Sci. Inst. **5**, 395 (1934).

[17] L. G. Parratt, Rev. Sci. Inst. **6**, 387 (1935).

[18] L. G. Parratt and F. Miller, Jr., Phys. Rev. **49**, 280 (1936).

[19] Greater resolving power than was used in the present experiments is possible, e.g., with the (11·0) planes of quartz crystals or, for wave-lengths less than 3A, with calcite crystals in second order reflection. However, in double-crystal as in single-crystal spectrometry, we are now obliged to accept a compromise between intensity and resolving power. The present calcite crystals, A_4B_4, in first order reflection, represent a satisfactory compromise in studying the faint satellite lines; higher resolving power would have been advantageous in studying the *complete shapes* of the intense diagram lines. In the latter study, as far as it is pursued in the present paper, it is hoped that our knowledge of the effects of the calcite crystals A_4B_4 is sufficient to permit adequate corrections for the crystals in the measurements of line *widths* at half-maximum intensity.

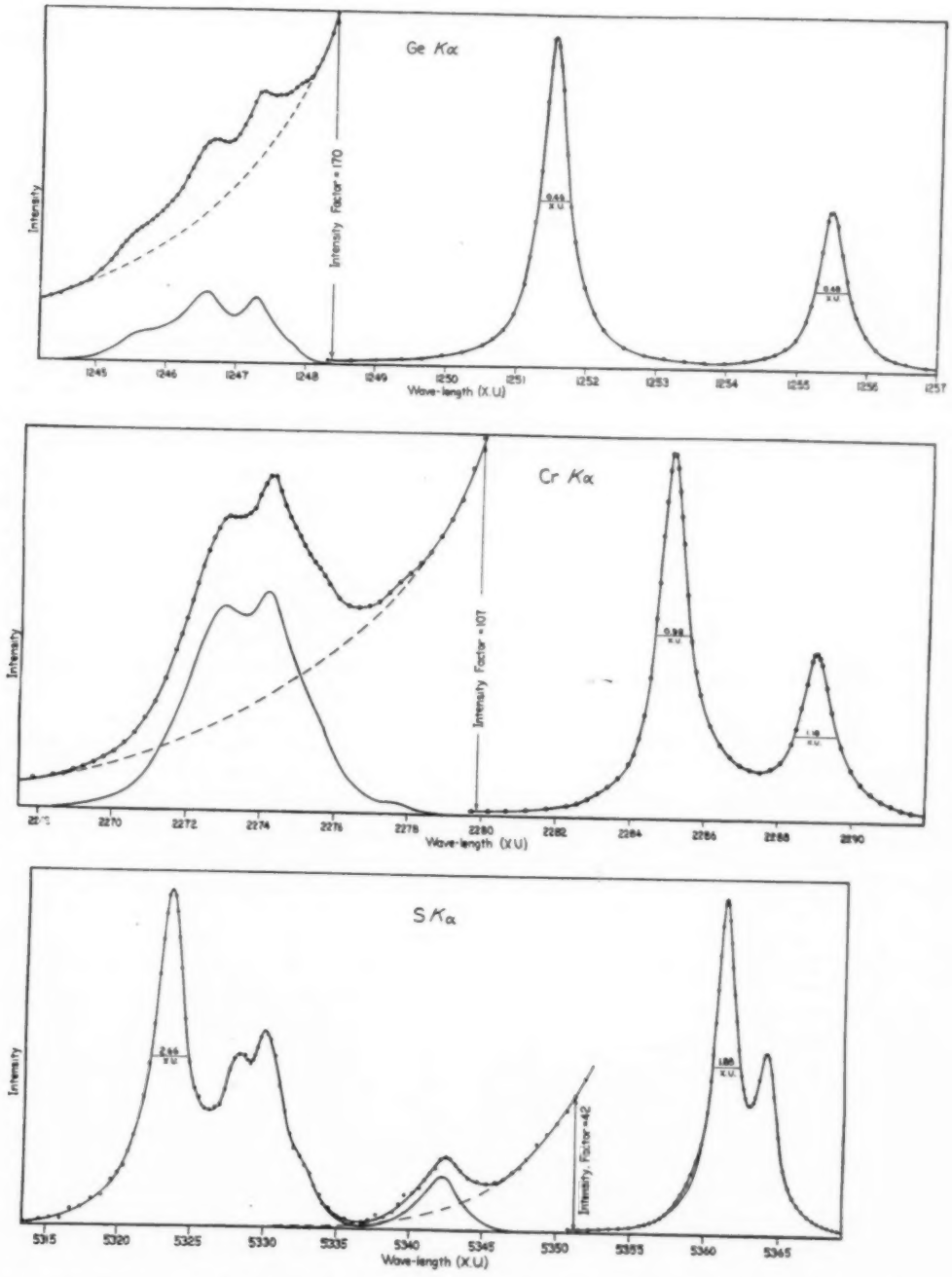

FIG. 1. Ionization curves of the $K\alpha$ region for Ge(32), Cr(24) and S(16). The $\alpha_{3,4}$ group of satellites is plotted in each case to an intensity scale magnified, relative to the scale of the $\alpha_{1,2}$ lines, by the intensity factor indicated. For each element the satellite background (the side of the α_1 line) is sketched in and the reduced satellite contour is drawn.

Targets

The preparation of a satisfactory target of a nonmetallic element is more difficult than of a metallic element. For the recording of an ionization curve of the relatively wide $K\alpha_{1,2,3,4}$ spectral region the emitted x-ray intensity must remain constant within the observational error for a period of several hours. And for recording curves of the weak satellite lines the power which must be dissipated by the target is relatively great: In the present experiments, with the focal spot approximately 2 mm in diameter, this power was of the order of 500 to 1200 watts. In photographic work these target problems are not so pertinent: Constant intensity is usually not necessary and long periods of exposure compensate for low power.

The targets of elements S(16) to V(23) used in the present experiments have been previously described.[15] Cr(24) and Mn(25) were electroplated onto copper. Elements Fe(26) to Ge(32) were used in the chemically pure metallic form and, except Ga(31), were soldered to the target carriage. Ga(31), a metallic liquid, rubbed and pressed with the finger onto a roughened copper surface, made a very satisfactory target: An ionization current of 3×10^{-12} amperes or an equivalent scale deflection, at maximum sensitivity, of more than 10,000 cm was observed for the peak of the Ga $K\alpha_1$ line. Targets of Br(35) and of Sr(38) were prepared by pressing powdered crystals of KBr and SrO into a roughened, pin-pricked copper surface. Zr(40) and Mo(42), in metallic form, were spotwelded to nickel.

Ionization curves

Representative of the observed $K\alpha_{3,4}$ regions, ionization curves for S(16), Cr(24) and Ge(32) are reproduced in Fig. 1. In these curves the $K\alpha_{3,4}$ group of satellite lines is plotted to an intensity scale 42, 107 and 170, respectively, times the scale used in plotting the $K\alpha_{1,2}$ lines. The accuracy with which the curves were recorded is indicated by the consistency of the observed points. In these figures the side of the α_1 line has been sketched in and the satellite contours have been reduced to a uniform background by a subtraction of the α_1 ordinates.

Curves similar to those of Fig. 1 are reproduced for Ti(22) in reference 14 and for Ca(20) in reference 15.

Resolution into components

The ionization curve of the $K\alpha_{3,4}$ group of satellites for each element from S(16) to Ge(32) has been reduced to a uniform background in the arbitrary manner indicated in Fig. 1. Special care was taken in recording the intensities on either side of the satellite group to minimize this background uncertainty, but, since no analytic function could be found to approximate satisfactorily the shape[20] of this region of the α_1 line for a series of elements, the consequent arbitrariness introduces an uncertainty in the reduced satellite contours which, for elements of atomic numbers above K(19), is greater than the random observational errors in the intensity readings.

The reduced satellite contour for each element is presented in Fig. 2. Each contour is plotted to arbitrary abscissae and ordinate scales. The two principal "humps" are the $\alpha_{3,4}$ lines, α_4 being on the left, the short wave-length side, of α_3. An inspection of the suggestive irregularities in the contours indicates five components for S(16). These components are, from right to left, with decreasing wave-length, α', α_3'' (a new component), α_3, α_3' and α_4. Each of the relatively intense $\alpha_{3,4}$ lines can be traced easily throughout the present range of elements. The α' line is likewise probably present for all the elements—"probably" because for many elements the contour irregularity indicating this component is close to, and in some cases within, the observational error. The intensity of the line α_3'' apparently decreases to zero near Ni(28). The external evidence for the reality of this line, α_3'', for elements Cr(24) to Ni(28) is meager.

The component α_3' appears conspicuously between α_3 and α_4 for S(16) and moves progressively as the atomic number increases. This progressive movement is inferred from the absence of the

[20] As mentioned later, the classical dispersion (Hoyt) shape, $I=p/1+(\Delta\lambda/w)^2$, matches fairly well the symmetrical part of the observed α_1 line when the constant w, half-width at half-maximum intensity, is adjusted. This fit, however, is not good enough (even when the constant p, as well as constant w, is adjusted to match more nearly the limited α_1 region adjacent to the satellites) to be of service in determining the satellite background.

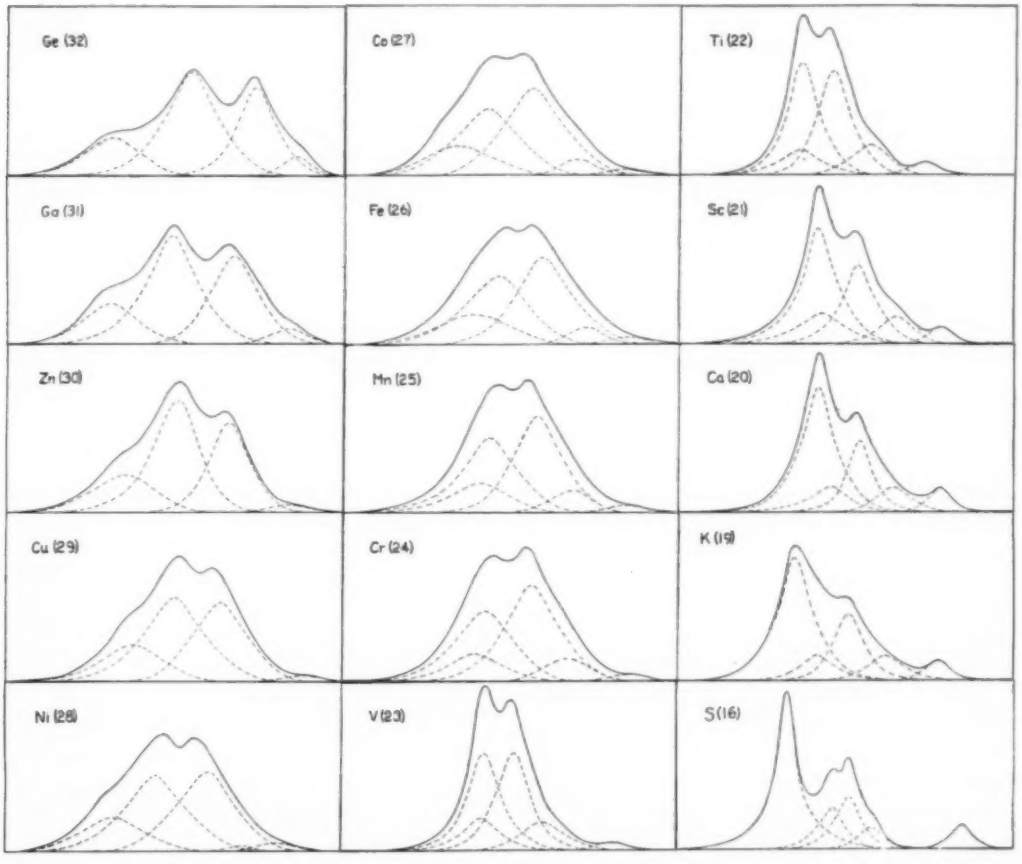

FIG. 2. Contours of the $K\alpha_{3,4}$ satellite group, reduced to a uniform background, for elements S(16) to Ge(32). Arbitrary abscissae and ordinate scales are used for each element. The reduced contours are resolved into the structural component lines as discussed in the text.

minimum between α_3 and α_4 for K(19), the slight trace of a component on the α_4 side of the minimum for Ca(20), the relatively sharp and narrow contours for Ti(22) and V(23), and the gradual appearance of a component on the short wave-length side of α_4 as the atomic number increases above V(23). For Ti(22) the α_3' and α_4 lines are approximately coincident in wave-length; for atomic numbers greater than 22, α_3' is on the short wave-length side of α_4.

From such an inspection of the ensemble the number of constituent components for each element was decided upon and the contours resolved as illustrated in Fig. 2. In this resolution the following criteria were used: The number of components was fixed, the component shapes were assumed to be roughly symmetrical, and the sum of the component intensities at any wave-length must add up to the intensity of the contour. For the region of elements Ca(20) to Cr(24), in which no specific irregularity in the contours was observed for the α_3' component, the intensity of α_3', relative to the intensity of the entire $\alpha_{3,4}$ group, was assumed to be about the same as for the adjacent elements. No other assumption as to relative intensities was made. A qualitative check on the resolution is afforded by the resultant consistency from element to element in the shapes of each component: No shape comes out to be what may be called "unreasonable."

The α'' component

For elements S(16) to V(23) inclusive another satellite component, the $K\alpha''$ line, not one of the $\alpha_{3,4}$ group, was observed close to and on the short wave-length side of the $K\alpha_1$ line. This component was first reported in 1922 by Dolejšek but, as far as the writer is aware, was not again detected until the present measurements were made. For S(16) the α'' line is indicated in Fig. 1. An earlier report[15] discusses this satellite line in more detail.

III. Measurements

Relative intensities

The relative intensity of two x-ray lines is defined as the ratio of areas under the line contours (the contours being plots of intensity *vs.* frequency) when the spectral analysis is complete, that is, when the contours are observed with an instrument of infinite resolving power. Although the two-crystal spectrometer has the greatest effective resolving power of all present x-ray instruments the $d\lambda$ interval cannot be neglected in case the two lines whose relative intensities are to be measured are of different widths and shapes. With calcite crystals A_4B_4 mounted on the instrument the $d\lambda$ interval[21] in first order reflection is about one-fourth the width of each of the $K\alpha_{1,2}$ lines at half-maximum intensity and is about one-twentieth the width of the $K\alpha_{3,4}$ region.

The perturbations due to the finite resolving power are present in the observed contours, and the appropriate corrections should be applied to the observed curves rather than to the resolved components. The observed curves for the present range of elements vary considerably in shape and, strictly speaking, different corrections should be applied to each contour. The corrections to be made in the wide satellite contours are within the experimental errors; the corrections for the $K\alpha_{1,2}$ lines are greater than the errors. For Ti(22) the correction to the ratio of the intensity of the entire $K\alpha_{3,4}$ group relative to the intensity of the $K\alpha_1$ line has been determined[14] as a factor of 1.05. This factor has been applied to the observed intensities relative to the $K\alpha_1$ intensities in the present work for each satellite component as well as for the $\alpha_{3,4}$ group for all the elements studied. The uncertainty of this correction is within the observational errors. In fact, for elements of atomic numbers greater than 29 the $\alpha_{3,4}$ group intensity relative to the α_1 intensity is uncertain by some 8 percent because of the indefiniteness of the satellite background.

It has been shown previously[14, 15, 22] that the intensity of $K\alpha$ satellite lines relative to the intensity of the $K\alpha_1$ line is constant for a given element when the x-ray tube voltage is greater than about twice the excitation potential. In the present work the voltage was maintained at two to five times the satellite excitation potential.

In Table I are listed the measured relative intensities, corrected for the resolving power of the crystals. In Fig. 3 the intensity of the $\alpha_{3,4}$ group relative to the intensity of the α_1 line is plotted for the range of elements Na(11) to Sr(38). A logarithmic ordinate scale in Fig. 3 provides a conveniently open scale for the low values.

Table I. *Intensities of $K\alpha$ satellite lines.* For each element the intensity of the $K\alpha_1$ line is taken as 100. Except in the cases of Na(11) and Si(14), recorded photographically, the correction for the finite resolving power has been applied to the $\alpha_{3,4}/\alpha_1$ ratio; the intensities of the component lines have been determined relative to the corrected intensity of the $\alpha_{3,4}$ group.

Target	Element	α_1	$\alpha_{3,4}$ Group (Corrected)	α'	α_2''	α_3	α_4	α_2'	α''
SrO	Sr(38)	100	0.08						
metal	Ge(32)	100	0.40	0.003		0.11	0.19	0.09	
liquid	Ga(31)	100	0.48	0.004		0.14	0.23	0.10	
metal	Zn(30)	100	0.50	0.005		0.16	0.23	0.10	
metal	Cu(29)	100	0.60	0.008		0.22	0.27	0.10	
metal	Ni(28)	100	0.65	0.01	0.01	0.25	0.27	0.11	
metal	Co(27)	100	0.77	0.014	0.03	0.32	0.28	0.12	
metal	Fe(26)	100	0.91	0.02	0.05	0.37	0.33	0.14	
electro-plated	Mn(25)	100	1.10	0.02	0.08	0.45	0.39	0.16	
electro-plated	Cr(24)	100	1.37	0.03	0.13	0.56	0.48	0.17	
metal	V(23)	100	1.80	0.04	0.20	0.68	0.66	0.22	0.30
metal	Ti(22)	100	2.20	0.07	0.23	0.80	0.84	0.24	0.90
Sc_2O_3	Sc(21)	100	2.78	0.11	0.24	0.78	1.25	0.41	1.40
CaO	Ca(20)	100	3.36	0.17	0.27	0.77	1.78	0.37	2.25
K_3PO_4	K(19)	100	3.90	0.23	0.31	0.84	2.07	0.45	2.10
$CaCl_2$	Cl(17)	100							1.40
FeS	S(16)	100	7.25	0.58	0.51	1.30	3.84	1.02	1.00
metal	Si(14)	100	17.						
NaCl	Na(11)	100	33.						

[21] The width of the $d\lambda$ interval is given roughly by the width of the curve observed with the crystals in positions of zero dispersion, the parallel positions. The reader is referred to previous papers, references 14 and 17, for discussions of the crystal-perturbations which distort the true x-ray line contours into the observed curves.

[22] D. Coster and W. J. Thijssen, Zeits. f. Physik **84**, 686 (1933). See also D. Coster, H. H. Kuipers and W. J. Huizinga, Physica **2**, 870 (1935).

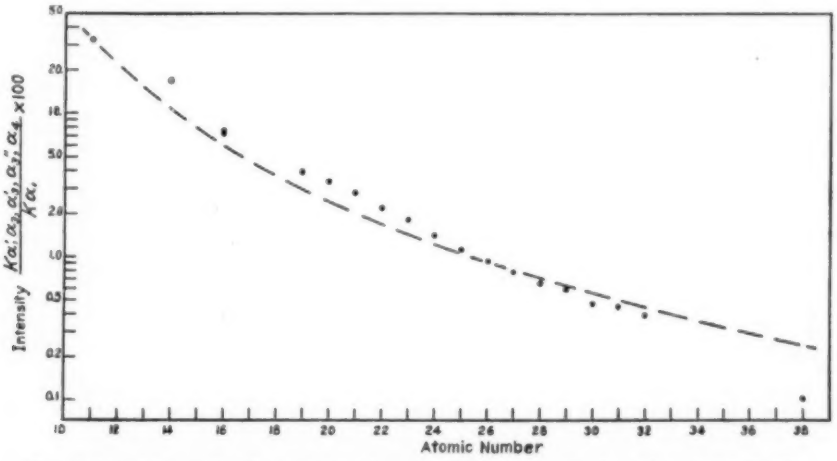

FIG. 3. Intensity of the $K\alpha_{3,4}$ group of satellites relative to the intensity of the $K\alpha_1$ line for elements Na(11) to Sr(38). The dashed curve represents Richtmyer's theoretical predictions. The open circles for Na(11), Si(14) and S(16) are values obtained photographically.

The photographic method, with a single gypsum crystal mounted on a Siegbahn type vacuum spectrograph, was used in measuring the satellite intensities for elements of atomic numbers lower than S(16), wave-lengths beyond the reach of the calcite crystals of the ionization double spectrometer. The experimental errors in the photographic data are much greater than in the ionization data although the average of several carefully exposed plates[23] for S(16) gave a relative intensity measurement in excellent agreement with that obtained with the double spectrometer. These measurements for the low atomic numbers were made so as to check the possible relative intensity maximum reported by Mrs. Pearsall.[24] No evidence for such a maximum was found.

Accurate satellite data for elements above Ge(32) were not obtained in the present study, but a preliminary measurement of the ratio of the intensity of the $K\alpha_{3,4}$ group to the intensity of $K\alpha_1$ for Sr(38) gave a value of less than 0.10 percent. More work on the satellites for elements $Z>32$ is now in progress.

In Fig. 4 is plotted, for the elements S(16) to Ge(32), the intensity of each component relative to the intensity of the entire $\alpha_{3,4}$ group. For the intensity plot of α'' see reference 15.

[23] The author is indebted to Dr. F. R. Hirsh for his generous assistance with the photographic plates.

[24] A. W. Pearsall, Phys. Rev. **48**, 133 (1935).

R. D. Richtmyer[10] has recently calculated the intensity of the $\alpha_{3,4}$ group as a whole relative to the intensity of the α_1 line, basing his calculations on the Wentzel-Druyvesteyn theory of satellite origin. Richtmyer's theoretical intensities are indicated by the dashed line in Fig. 3. The agreement between theory and experiment is remarkably good.[25]

Kennard and Ramberg[11] have calculated, on the basis of an extension of the Wentzel-Druyvesteyn theory, the relative intensities of α', α_3 and α_4 as being approximately[26] 1, 9 and 5,

[25] The relative intensity given by Richtmyer is, as a function of atomic number Z,

$$Is/I\alpha_1 = C(Z-\sigma)^{-3}$$

where σ, an internal screening constant, is taken for all elements as 4.5 and $C=91$ as determined from the computation for K(19).

[26] Kennard and Ramberg suggest the following coordinations:

$K\alpha'$	$\begin{cases} 1s2p^5\ {}^1P \rightarrow 2p^4\ {}^1S \\ 1s2s\ {}^1S \rightarrow 2s2p^5\ {}^1P \end{cases}$
$K\alpha_3$	$1s2p^5\ {}^3P \rightarrow 2p^4\ {}^3P$
$K\alpha_3'$	$1s2s\ {}^3S \rightarrow 2s2p^5\ {}^3P$
$K\alpha_4$	$1s2p^5\ {}^1P \rightarrow 2p^4\ {}^1D$

There is some difficulty in interpreting the relative intensity predictions from these coordinations. Two different types of transitions, $1s2p \rightarrow 2p^4$ and $1s2s \rightarrow 2s2p^5$, are considered by Kennard and Ramberg and the probability of one type of transition is *not* related in their work to the probability of the other type. Coordinated with the experimental α' line are transitions of both types, with $\alpha_{3,4}$ just one type, and with α_3' the other type alone. If we may relate the two transition probabilities by comparing the observed intensity of α_3' with the intensity of α_3 or of α_4 we obtain a probability of about 2 to 1 for the types of transitions $1s2p \rightarrow 2p^4$ and $1s2s \rightarrow 2s2p^5$, respectively. This

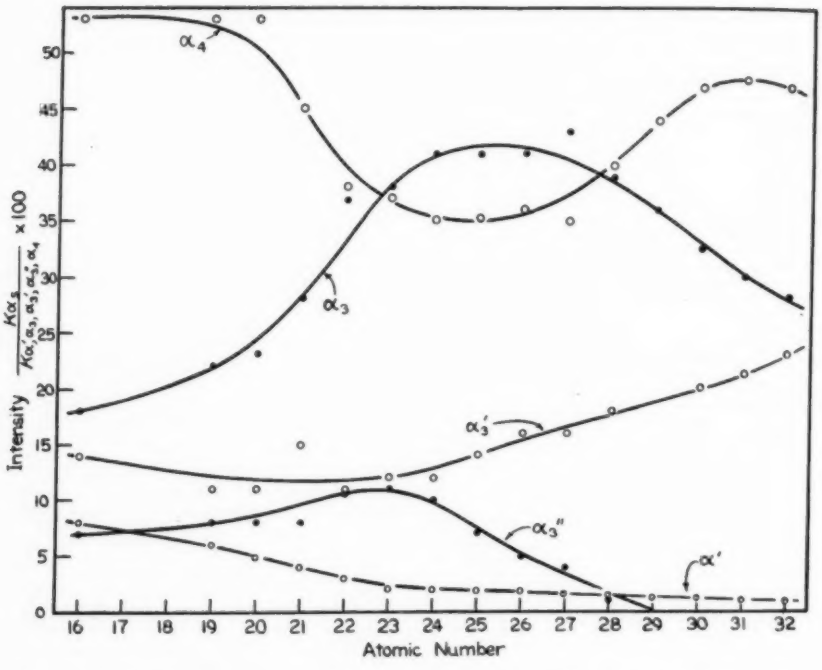

FIG. 4. Intensity of each component of the $K\alpha_{5,4}$ group of satellites relative to the intensity of the $K\alpha_{3,4}$ group as a whole for elements S(16) to Ge(32).

respectively, for Na(11) to 1, 3.75 and 5, respectively, for higher atomic numbers. The reversal in the relative intensities of α_3 to α_4 between P(15) and S(16) reported by Ford[3] may possibly be explained as suggested by Kennard and Ramberg[11] by the method of coordinating unresolved components with the α_3 line.[27] However, in view of the structures of the ensemble of Fig. 2, the two relative intensity reversals of α_3 and α_4 illustrated in Fig. 4 cannot be explained in this manner.

Hulubei[4] has recently detected and measured the wave-lengths of $K\alpha$ satellites for elements Cu(29) to Rh(45). For Rh(45) just the α_3' line was reported[28] indicating that, as the atomic number increases, the α_3' component becomes the most intense of the group. Conforming with this indication, an extrapolation of the curves of Fig. 4 gives at least two additional intensity reversals for higher atomic numbers.

Wave-lengths

The wave-length positions of the peaks of the resolved satellite components are listed in Table II. The writer's spectrometer does not have a precision circle so only relative wave-lengths can be determined; in the present work the peak of the $K\alpha_1$ line is taken as the reference wave-length. The estimated uncertainty of the satellite wave-lengths in Table II is of the order of 10^{-3} percent.

The excellent agreement between the present $\alpha_1 \rightarrow \alpha_2$ separations and those of Bearden and Shaw[29] checks the calibration of the spectrometer. Bearden and Shaw's measurements do

rough relation of 2 to 1 is in fair agreement with the ratio, 2.5 to 1, given (estimated) by Richtmyer, reference 10. However, the observed variations in the intensity ratios α_3' to α_3 and α_3' to α_4, Fig. 4, reduces this probability relation to a questionable status.

[27] In this intensity reversal observed by Ford, the α_3' and α_3 lines are experimentally coordinated unresolved components whose combined intensities are considered as the intensity of α_3. See footnote 12 of reference 15.

[28] The writer has previously called attention, reference 15, to the migratory nature of the α_3' component and that Hulubei's notation for α_3' and α_4 should be interchanged.

[29] J. A. Bearden and C. H. Shaw, Phys. Rev. **48**, 18 (1935).

TABLE II. *Wave-lengths in X. U. of $K\alpha$ satellite lines.* These measurements for each element are referred to the wave-length of the $K\alpha_1$ line.* The type of target used for each element is given in Table I.

ELEMENT	α_2	α_1	α''	α'	α_2''	α_3	α_4	α_3'
Ge(32)	1255.43	1251.48		1247.82		1247.31	1246.55	1245.60
Ga(31)	1341.24	1337.33		1333.40		1332.66	1331.83	1331.00
Zn(30)	1436.05	1432.22		1427.98		1426.98	1426.13	1425.28
Cu(29)	1541.22	1537.40		1533.01		1531.57	1530.70	1529.87
Ni(28)	1658.34	1654.51		1649.49	1648.80	1648.04	1647.04	1646.42
Co(27)	1789.17	1785.31		1780.10	1779.05	1778.10	1777.02	1776.40
Fe(26)	1936.00	1932.06		1926.05	1924.92	1923.94	1922.76	1922.16
Mn(25)	2101.44	2097.51		2090.92	2089.33	2088.32	2086.92	2086.55
Cr(24)	2288.89	2285.00		2277.70	2275.64	2274.43	2272.90	2272.58
V(23)	2502.24	2498.42	2496.5	2490.85	2487.74	2486.09	2484.45	2484.19
Ti(22)	2746.52	2742.87	2740.9	2734.40	2731.20	2726.91	2724.90	2724.90
Sc(21)	3028.35	3025.03	3022.8	3014.87	3011.65	3009.10	3006.31	3006.61
Ca(20)	3354.93	3351.69	3349.1	3340.10	3336.30	3333.44	3330.10	3330.97
K(19)	3736.82	3733.68	3730.9	3720.60	3716.20	3713.14	3709.01	3710.51
Cl(17)	4721.17	4718.2	4714.8					
S(16)	5364.12	5361.28	5359.4	5342.50	5333.10	5330.00	5323.45	5328.10

* The wave-lengths of the $K\alpha_1$ line for elements Ge(32) to Ti(22) are taken from Bearden and Shaw, Phys. Rev. **48**, 18 (1935); for elements Sc(21) to Cl(17) from Siegbahn, *Spektroskopie der Röntgenstrahlen*, 1931; and for S(16) from Valasek, Phys. Rev. **43**, 612 (1933).

not include elements of atomic numbers less than Ti(22) and the present $\alpha_1 \rightarrow \alpha_2$ separations for $15 < Z < 22$ are probably more reliable than the values given in Siegbahn's book.[1]

No simple relation is observed between the atomic number and the satellite separations from the $K\alpha_{1,2}$ lines. The evidence which has been presented in the literature in favor of the α_1 or of the α_2 line as being the "parent" line of a given satellite is to be understood in terms of empirical convenience only in classifying satellites. The present results do not yield the convenient linear relation.[30] The $\alpha_1 \rightarrow \alpha_2$ is a spin-doublet separation; the satellite$\rightarrow$"parent" line interval is a complex screening separation which also includes part of the $\alpha_1 \rightarrow \alpha_2$ separation. Without further evidence the center of intensity of the doublet seems as reasonable a reference wave-length as any other. In Fig. 5 are plotted the $\Delta\nu/R$ values for the satellite separations from this center of intensity reference; the values are listed in Table III.

It is interesting to compare the observed multiplet structure of the contours of Fig. 2 with the calculated structures of Fig. 1 of Kennard and Ramberg's paper.[11] The progressive shift of the α_3' component relative to the α_4 line is apparently qualitatively accounted for.

[30] The semi-Moseley graph $(\Delta\nu/R)^{\frac{1}{2}}$ *vs.* Z is closer to linearity when $\Delta\nu$ is referred to α_2 than when referred to α_1. Two factors are present: (1) The $\Delta\nu$ intervals are greater when referred to the α_2 lines and the *relative* deviations from linearity are less, and (2) a peculiar variation in the $\alpha_1 \rightarrow \alpha_2$ separation is present in the atomic number range Sc(21) to Cu(29), see Fig. 203 of Siegbahn, reference 1.

Widths and shapes of satellites

As mentioned above,[12] the fact that x-ray lines are so broad detracts from the definiteness of the wave-length positions, especially in cases of overlapping lines, and reduces the effectiveness of wave-lengths as a tool for comparing theory with experiment. However, compensation lies in the fact that the lines are so broad that their widths (and shapes if they do not seriously overlap with one another) can be measured with a fair degree of precision, and the property of widths (and shapes) may be of help in ascertaining the atomic processes involved in their production. In view of the recent rapid progress[31] in accounting for the widths of diagram lines by considering the Auger or radiationless transitions,

TABLE III. *Separation in $\Delta\nu/R$ units of the $K\alpha$ satellite lines referred to the center of intensity of the $K\alpha_{1,2}$ doublet lines.* The type of target used for each element is given in Table I.

ELEMENT	α_2	α_1	α''	α'	α_2''	α_3	α_4	α_3'
Ge(32)	1.532	0.76		2.90		3.21	3.65	4.19
Ga(31)	1.330	0.66		2.68		3.06	3.48	3.91
Zn(30)	1.135	0.57		2.46		2.90	3.28	3.66
Cu(29)	0.983	0.49		2.19		2.74	3.08	3.40
Ni(28)	0.853	0.43		2.10	2.33	2.59	2.92	3.13
Co(27)	0.732	0.37		1.87	2.17	2.44	2.75	2.92
Fe(26)	0.640	0.32		1.79	2.07	2.31	2.60	2.74
Mn(25)	0.542	0.27		1.64	1.97	2.18	2.47	2.55
Cr(24)	0.450	0.23		1.51	1.87	2.08	2.35	2.41
V(23)	0.373	0.19	0.47	1.30	1.75	1.99	2.23	2.27
Ti(22)	0.294	0.15	0.39	1.19	1.57	1.85	2.10	2.10
Sc(21)	0.222	0.111	0.33	1.13	1.46	1.71	1.99	1.96
Ca(20)	0.172	0.088	0.30	1.04	1.35	1.58	1.85	1.78
K(19)	0.138	0.069	0.25	0.93	1.22	1.42	1.69	1.59
Cl(17)	0.0813	0.041	0.18					
S(16)	0.0604	0.030	0.09	0.63	0.93	1.03	1.24	1.09

[31] See J. A. Prins, Physica **2**, 231 (1935), and references.

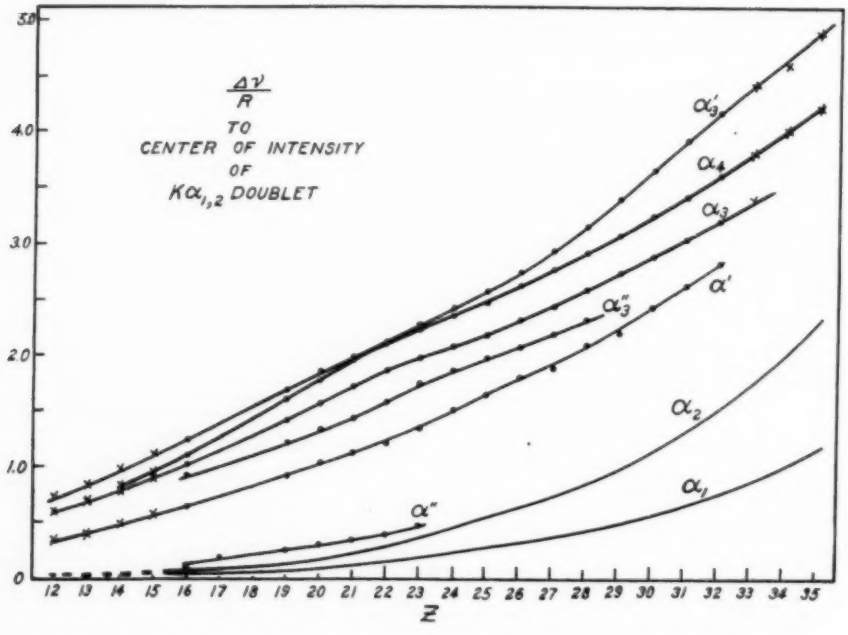

FIG. 5. Wave-length separations, $\Delta\nu/R$ units, of the satellite components from the center of intensity of the $K\alpha_{1,2}$ line doublet lines. The solid circles represent the present measurements, the crosses are values taken from Ford, reference 3, for the low atomic numbers, and from Hulubei, reference 4, for the high atomic numbers.

an experimental knowledge of the widths of satellite lines is very desirable.

The widths at half-maximum intensity of the component satellite lines, resolved in the manner discussed above, are listed in Table IV and shown graphically in Fig. 6. These widths can have no more quantitative value than the reader is willing to grant for the particular resolution in which the writer has indulged in Fig. 2. In some instances, as in the case of S $K\alpha_4$, the accuracy may be as high as 6 percent; in other instances, as in the cases of the weak α' and α_3'' components for $Z>22$, the uncertainty may be 50 percent. Another attempt in resolving the contours into components could give greater widths of the α' and α_3'' lines for $Z>22$ but the uncertainty is so large that such an attempt is not worth while. The consistent trends in the relative intensities, Fig. 4, and in the widths, Fig. 6. speak well of the somewhat blind resolution and, perhaps, add meaning to the measured values.

It may be significant that the variation in the widths of the satellite α_3, α_4 and α_2' follow more closely the variation in the widths of the α_2 line than of the α_1 line.

Very little can be said of the possible asymmetries of these satellite lines. One of the criteria used in the resolution is that the components be

TABLE IV. *Full widths, in X.U., at half-maximum intensity of Kα satellite lines.* These widths refer to the resolved component lines of the reduced contours of the observed ionization curves. No correction for the finite resolving power of the crystals has been made. The type of target used for each element is given in Table I.

ELEMENT	α''	α'	α_3''	α_3	α_4	α_2'
Ge(32)		0.48		0.65	0.73	0.79
Ga(31)		0.58		0.74	0.81	0.88
Zn(30)		0.62		0.84	0.96	1.07
Cu(29)		0.76		1.08	1.21	1.25
Ni(28)		0.87	0.97	1.26	1.39	1.43
Co(27)		0.90	1.18	1.35	1.63	1.69
Fe(26)		1.06	1.30	1.58	1.77	1.90
Mn(25)		1.24	1.58	1.71	1.89	1.95
Cr(24)		1.40	1.81	1.92	2.04	2.10
V(23)	1.02	1.63	2.16	2.16	2.21	2.30
Ti(22)	1.10	1.89	2.45	2.36	2.50	2.69
Sc(21)	1.16	1.98	2.68	2.60	2.74	3.06
Ca(20)	1.30	2.25	2.81	2.76	2.95	3.33
K(19)	1.38	2.41	3.01	2.92	3.09	3.25
Cl(17)	1.98					
S(16)	1.88	2.65	3.05	2.85	2.62	3.30

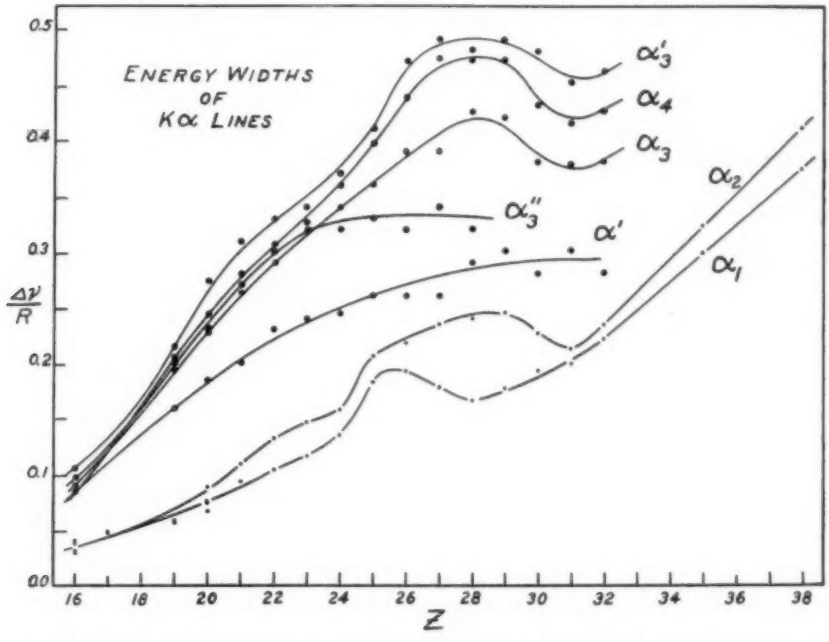

FIG. 6. Full widths, $\Delta\nu/R$ units, at half-maximum intensity of the $K\alpha$ lines. The widths of the α_1 and α_2 component lines are corrected for the crystals as discussed in the text. Effects of chemical binding in the $\alpha_{1,2}$ widths are indicated for Ca(20) and S(16). It is to be noted that the values of the satellite widths are very sensitive to the particular resolution affected; the values given in this figure are characteristic of the resolution illustrated in Fig. 2.

roughly symmetrical and, in every case, the components are so drawn. The greatest accuracy is present for S $K\alpha_4$ and the index of asymmetry at half-maximum intensity for this line is 1 ± 0.10.

IV. THE $K\alpha_{1,2}$ LINES

Ionization curves of the $K\alpha_{1,2}$ lines were of course recorded for each element in the present study. The observed contours for these overlapping doublet lines have been resolved into the α_1 and α_2 components. The arbitrariness of this resolution is zero at the high atomic numbers and increases as the atomic number decreases (see Fig. 1). The widths and asymmetries of the resolved doublet lines are given in Table V.

The author has previously reported[32] on the $K\alpha_{1,2}$ line widths for elements Ca(20) to Ni(28). The crystals employed in these early measurements were unfortunately poor specimens as judged from our present standards,[17] and, consequently, the previously reported widths are excessively large and now serve merely as con-

TABLE V. *Full widths, indices of asymmetry and overlapping factors of the $K\alpha_{1,2}$ doublet lines.* The type of target used for each element is given in Table I or discussed in the text. Obs. = observed contour of the overlapping doublet lines. Cor. = corrected for overlapping of the two lines. True = corrected for overlapping and also corrected for the finite resolving power of the spectrometer.

	Widths (X.U.)				Asymmetry Index				Overlapping Factor
	α_1		α_2		α_1		α_2		
Element	Obs.	True	Obs.	True	Obs.	Cor.	Obs.	Cor.	Obs.
Mo(42)	0.306	0.268	0.317	0.280	1.00	1.00	1.03	1.03	0.00
Zr(40)	0.340	0.300	0.360	0.320	1.02	1.02	1.04	1.04	0.010
Sr(38)	0.360	0.313	0.390	0.343	1.03	1.03	1.04	1.04	0.014
Br(35)	0.410	0.353	0.440	0.382	1.03	1.03	1.06	1.06	0.020
Ge(32)	0.457	0.379	0.482	0.404	1.04	1.04	1.11	1.11	0.030
Ga(31)	0.475	0.389	0.501	0.415	1.04	1.04	1.19	1.19	0.036
Zn(30)	0.530	0.434	0.606	0.510	1.11	1.11	1.33	1.33	0.037
Cu(29)	0.565	0.460	0.740	0.635	1.15	1.15	1.28	1.28	0.057
Ni(28)	0.622	0.504	0.85	0.72	1.22	1.22	1.23	1.25	0.093
Co(27)	0.760	0.63	0.97	0.82	1.44	1.44	1.27	1.30	0.116
Fe(26)	0.946	0.79	1.10	0.90	1.61	1.60	1.30	1.35	0.174
Mn(25)	1.06	0.89	1.24	1.00	1.45	1.43	1.19	1.27	0.23
Cr(24)	0.98	0.78	1.20	0.91	1.35	1.33	1.04	1.14	0.25
V(23)	1.02	0.81	1.34	1.02	1.26	1.23	0.96	1.09	0.29
Ti(22)	1.10	0.87	1.45	1.10	1.22	1.17	0.88	1.04	0.32
Sc(21)	1.16	0.95	1.46	1.12	1.01	0.97	0.89	1.01	0.31
Ca(20)	1.24	0.92	1.29	0.83	0.85	0.81	0.79	0.92	0.35
K(19)	1.38	0.90	1.62	0.88	0.99	0.96	0.78	1.05	0.45
Cl(17)	1.98	1.19		1.16	1.00	0.92		0.94	0.75
S(16)	1.88	0.99		0.94	1.15	1.00		1.00	0.77

[32] L. G. Parratt, Phys. Rev. **44**, 695 (1933).

vincing evidence of the importance of a knowledge of crystalline diffraction patterns and of their behavior in the antiparallel positions of the double spectrometer.

Bearden and Shaw[29] have recently made exacting measurements of the widths and shapes of the $K\alpha_{1,2}$ lines for elements Ti(22) to Ge(32). For these elements the present work adds nothing to the conclusions of Bearden and Shaw except that in comparing the measurements one finds differences which are slightly greater than the sum of the estimated errors. These differences are greatest in the case of Cr(24) where the present widths are about 4 percent less than those of Bearden and Shaw and in the case of Ti(22) where the present widths are about 4 percent greater. It is not likely that these differences can be explained in terms of different diffraction pattern shapes of the crystals employed. No explanation is offered except the suggestion of the possibility of the effects of an oxide film on the surfaces of the targets.

To obtain the true line widths from the observed widths one must apply a correction for the finite resolving power of the crystals. An empirical correction for crystals has recently been proposed:[17]

$$W_T = W_0 - 2.9 W_C^{1.7} \qquad (1)$$

where W_T is the true width in X.U., W_0 the width in X.U. of the curve observed in the $(n, +n)$ position of calcite crystals of Class I type of perfection whose $(n, -n)$ width is W_C X.U. The W_C values of the present crystals A_4B_4 are obtained by interpolating the data given in reference 18.

Eq. (1) has been applied to all the component $K\alpha_{1,2}$ lines of the present study and the true widths so obtained are included in Table V and in Fig. 6. Eq. (1) probably overcorrects the α_2 component widths for elements of low atomic numbers because of the difference in shape of the resolved component and the observed contour. In fact, Eq. (1) was derived explicitly for contours of the shape of the $K\alpha_{1,2}$ lines of Ti, Cu and Mo, and the application of the formula to contours of the shape of S $K\alpha_{1,2}$, for example, is not entirely justified. For this reason, together with the uncertainties in the reduced contours and in the resolution, the formula has not been applied to the satellite widths, although the true width of the S $K\alpha_1$ line is probably close to the value which would be obtained from Eq. (1).

The overlapping factors of the observed doublet contours and the indices of asymmetry of the observed curves and of the resolved components are also listed in Table V.

It is to be noticed that for elements $Z<21$ the true width of the α_2 lines are less than of the α_1 lines; also, in most cases, the indices of asymmetry are *less* than unity. The α_2 line has also been found[33] narrower than the α_1 line by Allison and by Wilhelmy for several elements in the atomic number range 36 to 45.

The effect of the $K\alpha''$ component on the observed asymmetries of the $K\alpha_1$ lines was suggested in the previous report.[15] At first glance one may suspect a multiplet structure in α'' sufficient to influence materially and be an uncorrected factor in the observed α_1 asymmetries. The α_1 asymmetry is a maximum at Fe(26) whereas the α'', with atomic numbers increasing above Ca(20), is losing in relative intensity and also is becoming farther removed from the α_1 peak. However, for the lower atomic numbers, S(16) and Cl(17), part of the shape of α_1 may, it must be recognized, be due to a possible multiplet structure of α''. That α'' is really a satellite line and not an unresolved component in the α_1 line is shown by the α''/α_1 intensity *vs.* voltage relation of Fig. 5 of reference 15.

The rather close correlation in the variations in line widths and in the indices of asymmetry, Table V, indicates that the two properties, widths and asymmetries, for the elements of the present atomic number range, may be considered together. The factors responsible for the width of an x-ray line may be listed as (1) radiation damping, of the order of 0.12 X.U. but varying with line and element,[31] (2) radiationless transitions or Auger effects, (3) linkage with neighboring atoms, i.e., the chemical and/or the alloy effect, (4) the presence of unresolved component lines, and (5) the external screening effects due to the various degrees of ionization (outer electrons) of the radiating atoms. Some of these factors may well be associated together but convenience indicates a need for the separate categories. In

[33] S. K. Allison, Phys. Rev. **44**, 63 (1933); E. Wilhelmy Zeits. f. Physik **97**, 312 (1935).

TABLE VI. *Effects of chemical binding on contour shapes of $K\alpha_{1,2}$ doublet lines for Ca(20), Cl(17) and S(16).**

TARGET	ELEMENT	WIDTHS (X.U.) α_1 Obs.	α_1 True	α_2 Obs.	α_2 True	ASYMMETRY INDEX α_1 Obs.	α_1 Cor.	α_2 Obs.	α_2 Cor.	OVERLAPPING FACTOR
metal	Ca(20)	1.40	1.07	1.44	0.92	1.00	0.97	0.82	0.95	0.41
CaO	Ca(20)	1.24	0.92	1.29	0.83	0.85	0.81	0.79	0.92	0.35
$CaCl_2$	Ca(20)	1.44	1.11	1.48	0.95	0.94	0.91	0.80	0.93	0.42
$CaCl_2$	Cl(17)	1.98	1.19		1.16	1.00	0.92		0.94	0.75
$CuCl_2$	Cl(17)	1.90	1.14		1.11	1.00	0.92		0.94	0.75
KCl	Cl(17)	1.95	1.18		1.16	1.00	0.92		0.94	0.75
$SrCl_2$	Cl(17)	1.98	1.19		1.16	1.00	0.92		0.94	0.75
FeS	S(16)	1.88	0.99		0.94	1.15	1.00		1.00	0.77
$BaSO_4$	S(16)	2.24	1.21		1.30	1.40	1.00		0.97	0.92

* The "true" widths of S $K\alpha_1$ are listed incorrectly in Phys. Rev. **49**, 14 (1936).

magnitude, in the case of $K\alpha$ lines for elements of atomic numbers less than 36, the Auger effect dominates,[34] and the radiation damping is theoretically of next importance. Of these several factors the first and second contribute to the line width symmetrically on either side of the maximum ordinate—the line shape due to these factors is the classical dispersion (or Hoyt) shape. The third factor is forced upon us experimentally and the asymmetry of the broadened or narrowed line, so far as the available data[35] indicate (Table VI), is usually not greatly altered. The data are insufficient to warrant generalizations as to the symmetry or asymmetry of the width contribution of factor three; however, irrespective of the shape of the contribution from each atom, one might expect some displacement of the maximum ordinate from some fraction of the emitting atoms relative to the maximum ordinate from other emitting atoms due to different types of atomic neighborhoods in the crystal lattice.[36] This sort of difference might produce in the observed line width an effective contribution of almost any shape and yet be, perhaps, of the classical dispersion shape so far as the individual atoms are concerned. In accounting for the observed asymmetries we have left, then, factor three and factors four and five. The width contributions of the last two factors may be expected to be asymmetrical and have maximum ordinates displaced relative to the maximum ordinate of the contributions of the first two factors alone.

In regard to the unresolved component lines, factor four, the possible momenta couplings between the inner $2p$ electrons with the outer $3d$ and $4s$ electrons in incompleted shells may cause splitting of the L_{II}, L_{III} doublet levels into single and triplet levels or into levels of greater multiplicity. The energy separations due to this splitting are small in any case and for closed outer shells, as for Zn(30), Ca(20) and A(18), there can be no such couplings. The disturbances in the outer shells for elements, especially metals, in the solid state probably invalidate the quantitative conclusions derived from the electronic configurations of the elements in the gaseous state. Nevertheless, it may be significant that the observed $K\alpha_{1,2}$ lines, corrected for overlapping, are practically symmetrical for S(16), Cl(17), K(19), Ca(20) (metal) and for Sc(21); are markedly asymmetrical for elements 22 to 30, the greatest asymmetry being observed for Fe(26); and are again practically symmetrical for elements of atomic numbers greater than Zn(30).

Another significant fact is in regard to the line shapes. Each of the asymmetrical α_1 and α_2 components may be analyzed into the constituent symmetrical and asymmetrical parts. The asym-

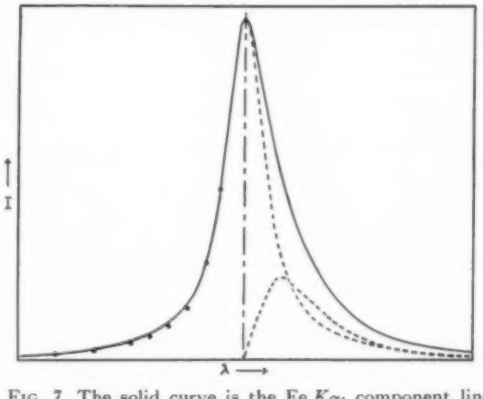

FIG. 7. The solid curve is the Fe $K\alpha_1$ component line from the (1, +1) contour of the $\alpha_{1,2}$ doublet. The dashed curves are the symmetrical and asymmetrical constituent parts of the solid curve. The circles represent the position of the classical dispersion curve matched with the symmetrical part of the α_1 component at the maximum and half-maximum ordinates.

[34] G. Wentzel, Zeits. f. Physik **43**, 524 (1927).

[35] For data in addition to those of Table VI see L. G. Parratt, Phys. Rev. **45**, 364 (1934), E. Wilhelmy, Zeits. f. Physik **97**, 312 (1935), L. G. Parratt, Phys. Rev. **49**, 14 (1936), and H. H. Roseberry and J. A. Bearden, Phys. Rev. **49**, 884A (1936).

[36] This argument is most apt in the case of alloy mixtures. As data accumulate we may distinguish between the width effect with metallic alloys and with chemical compounds of definite stoichometric proportions.

metrical part, itself very asymmetrical, as illustrated for Fe(26) in Fig. 7, lies on the long wave-length side of the maximum α_1 ordinate for all cases in which the index of asymmetry, Table V, is greater than unity. Then, the symmetrical part of the $K\alpha_{1,2}$ lines for a wide range of atomic numbers[37] approximates fairly closely[38] the classical dispersion shape as predicted by factors one and two of the above list, and, consequently, the anomalous width variations, Fig. 6, may be accounted for roughly in terms of the line asymmetries by the remaining asymmetrical width factors.[39]

If the line shape due to the chemical and/or alloy effect is symmetrical and agrees with the classical dispersion shape, whether or not the maximum ordinate coincides in wave-length with the maximum ordinate of the line due to the other factors, this shape may possibly be found in the Auger effect—as yet the predictions on the basis of Auger transitions have been made for gaseous atoms only. If this is true one might expect to find a chemical or alloy effect in experimental Auger coefficients (fluorescence yields) with compounds or alloys which give a pronounced effect in line widths. As an alternative, if the chemical width is asymmetrical, or not of the classical dispersion shape, it may possibly be contained in factors four and/or five.

Indeed, if each of the several factors contributing to line widths can be evaluated, it seems possible that, with more data, a more or less complete interchecking system of Auger coefficients and widths of x-ray lines and limits can be developed somewhat analogous to and somewhat more elaborate than the system of wave-lengths of lines and limits.

V. Effects of Chemical Binding

Since satisfactory targets of nonmetallic elements in the free state could not be prepared and, for these elements, resort to chemical compounds was necessary, a test of the effect of chemical binding on the satellite structure was attempted. For calcium targets of metallic calcium, calcium oxide and of calcium chloride no differences in the Ca $K\alpha_{3,4}$ satellite structure or in the wave-length separations were observed greater than the experimental errors. It is to be noticed also that no marked change in the satellite contour is observed for liquid gallium when compared with the solids adjacent in atomic number. This small effect of chemical binding or of the physical state of the target element is not surprising from the point of view of the Wentzel-Druyvesteyn theory of satellite origin, although in the satellite widths an effect of the same order of magnitude may be expected to be present as the effect observed in the $\alpha_{1,2}$ widths. The calcium oxide $\alpha_{1,2}$ lines are some 14 percent narrower than the lines for metallic calcium or for calcium chloride; an equivalent difference in the satellite widths may be present: The accuracy with which the widths of the Ca $K\alpha$ satellite components were measured is not better than ± 15 to 20 percent.

The greatest effects due to chemical binding are perhaps to be expected in cases of radical changes in valency, for example, sulphur in a sulphide as compared with a sulphate. Unfortunately no sulphate target could be made to serve satisfactorily in recording the satellite contours.

Bearden and Shaw[29] and Wilhelmy[35] have previously remarked on the small effect of the physical state of the target element in the contours of the $K\alpha_{1,2}$ lines for liquid gallium and for gaseous krypton as compared with the line contours for adjacent solids. This indicates that

[37] F. K. Richtmyer and S. W. Barnes, Phys. Rev. **46**, 352 (1934), have observed that the K series lines for W(74) are of the classical dispersion shape.

[38] An even better fit is obtained when the shape of the component line is corrected for the perturbations introduced by the finite resolving power of the crystals. This correction can be obviated effectively by observing the line contour with the crystals in second-order reflection. To a first approximation, contours observed in first-order reflection may be corrected roughly by Spencer's double inverse graphical method, see reference 14.

[39] It may be pointed out that the long wave-length side of the α_1 or α_2 component line, the side which, for the present lines, contains the asymmetrical part, also matches fairly well the classical dispersion shape. The symmetrical part, or the short wave-length side, of the line is discussed in the text because of the fact that the anomalies in the width plot of Fig. 6 involve excess widths and asymmetry indices greater than unity. Discussion of the other side, the long wave-length side, of the line may be pertinent for such cases as calcium oxide—the asymmetrical width contribution may be on the short wave-length side of the maximum ordinate. It is not inconceivable that in some cases the width "contribution" may be negative.

It should also be pointed out that an asymmetrical contribution which decreases abruptly to zero intensity at the position of the maximum ordinate, as drawn in Fig. 7, probably has little meaning. At the present time it is felt that the complexity of the superimposition of the line-shape factors, combined with the diffraction pattern uncertainties, make further analysis futile.

in some cases at least the line width contribution due to linkage with neighboring atoms is very small.[40]

The narrow $K\alpha_{1,2}$ lines for calcium oxide as compared with the widths for metallic calcium leads one to question the significance of the smoothness of the curves drawn in Fig. 6. The widths for scandium oxide may also be low compared with the widths one might measure for free scandium, but, on the other hand, the oxide of manganese gives wider lines than does pure manganese.[41]

[40] An analysis of the widths of the $K\alpha_{1,2}$ lines for Kr(36) measured by Wilhelmy is instructive. The observed widths are 0.37 and 0.33 X.U. for α_1 and α_2, respectively. Corrected for the crystals by Eq. (1) these widths become 0.31 and 0.27 X.U. Less the radiation damping width, 0.13 X.U. from Table I of Prins, reference 31, the respective widths are 0.18 and 0.14 X.U. Wentzel, Zeits. f. Physik **43**, 524 (1927), finds that the Auger width is about equal to the radiative width for Kr(36) so that there are left the small residual widths of 0.05 and 0.01 X.U. (about equal to the observational errors as estimated by Wilhelmy) to be accounted for by the width factors four and five as listed above. This is evidence that factors four and five (and also factor three in the cases of adjacent solid elements when the Kr $K\alpha_{1,2}$ widths are compared with the line widths for these adjacent elements) are of small importance in these lines for $Z=36$. The Kr $K\alpha_{1,2}$ lines are symmetrical and agree with the classical dispersion shape within the errors of observation.

VI. Acknowledgments

The author is pleased to express his indebtedness to Professor F. K. Richtmyer, Drs. E. G. Ramberg and C. H. Shaw for stimulating discussions, and especially to the University of Chicago for the loan of the double spectrometer with which the data were recorded.

[41] L. G. Parratt, Phys. Rev. **45**, 364 (1934); J. A. Bearden and C. H. Shaw, reference 29, footnote 16; and H. H. Roseberry and J. A. Bearden, Phys. Rev. **49**, 884A (1936).

JULY 1, 1936 PHYSICAL REVIEW VOLUME 50

A Precision World Survey of Sea-Level Cosmic-Ray Intensities[1]

Robert A. Millikan and H. Victor Neher, *Norman Bridge Laboratory of Physics, California Institute of Technology*

(Received April 23, 1936)

With sensitive, vibration-free, self-recording electroscopes sent to many parts of the globe on twelve different voyages a precision survey has now been completed of the variation of cosmic-ray intensities both with latitude and longitude, so that the earth as a whole can now be covered with sea-level, equal intensity, cosmic-ray lines. In going along the longitude line 75° W., which runs from the far north through Washington, D. C., and along the west coast of South America, there is no appreciable change until the magnetic latitude of about 41° is reached. The equatorial dip then begins to set in and shows a maximum decline of 8 percent off Peru and returns again to its normal value off Cape Horn. In going along longitude line 80° E. through southern India the maximum dip is 12 percent. In going south from Alaska in longitude 165° W. to New Zealand the maximum dip is 10 percent. In going south from Liverpool through the Atlantic Ocean—longitude 30° W.—and around Cape Horn the maximum dip is 8.5 percent. In the region most accurately studied—the west coast of the United States—the intensity remains exceedingly constant until the latitude of Pasadena—41° magnetic—is reached, and then drops remarkably suddenly. In the Atlantic Ocean the drop sets in at about the same magnetic latitude with equal suddenness. It appears also to take place quite suddenly at about magnetic latitude 41° in the southern hemisphere. Nevertheless, the existence of a longitude effect shows that in strictness there is no such thing as magnetic latitude. In other words, the earth's magnetic field, even at the remote distances of thousands of miles at which these deflections occur, is strikingly dissymmetrical with respect to any line passing through the earth's center. This method of study opens up the possibility of determining these dissymmetries at large distances from the earth. The observed magnetic effects are to be expected quite independently of whether cosmic rays are in their origin photonic or corpuscular.

THE first element in the high altitude survey of cosmic-ray intensities as a function of latitude organized in the fall of 1931[2] was the development of what the first of the authors has designated as "the Neher vibration free, cosmic-ray electroscope." It has been with its aid that this sea-level survey has been made.

[1] A condensed report of this work was published in Science **82**, 574 (1935).

[2] I. S. Bowen, R. A. Millikan and H. V. Neher, Phys. Rev. **44**, 246 (1933). See also International Conference on Nuclear Physics (Cambridge Univ. Press, 1934), p. 210.

§1. The Electroscope

This instrument was a modification of the cosmic-ray electroscope which Millikan and Cameron had developed in 1927 and had used in

all their cosmic-ray measurements made from 1927 to 1930. Like its predecessor it consisted of a spherical steel bulb of 3 mm wall thickness and 15 cm diameter filled with gas at pressures up to 30 atmospheres and holding at its center a gilded quartz fiber electroscope system, readable, by means of a short focus telescope, through a window in the wall. Such an electroscope with no outside connections of any kind, if properly dried with phosphorus pentoxide, eliminates the serious uncertainties and difficulties inherent in electroscopes having outside connections, especially when these are used in moist surroundings.

In the earlier years air was used as the filling gas but argon was also used beginning in the summer of 1931 and since 1932 it has been exclusively used. We have, however, one air electroscope that was filled at 30 atmospheres in September, 1928, the reading of which, within its 10 cm lead shield in the basement of one of our homes, now used as a standardizing laboratory, has not varied appreciably during these eight years. In a given cosmic radiation field its current is 13.8 times that found when its pressure is reduced to one atmosphere. Through comparison with it and with the aid of this multiplication factor, all our argon-electroscope readings are reduced to ionization in air at one atmosphere. Such reduction is made in most of the accompanying charts. The exactness of this reduction is not, however, important for the purposes of this paper, since the essential comparison is here merely between the reading of the given electroscope at Los Angeles, from which port it always starts out and to which it always returns, and its reading in the other localities to which it is taken.

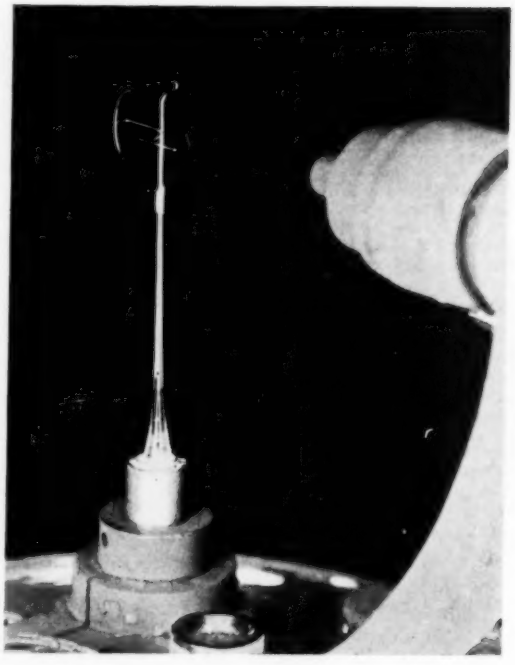

FIG. 2. Illustrating the quartz system when ready for installing into the ionization chamber. The lens mounting is supported by a rigid arm which is securely fastened to the same piece that holds the electroscope system.

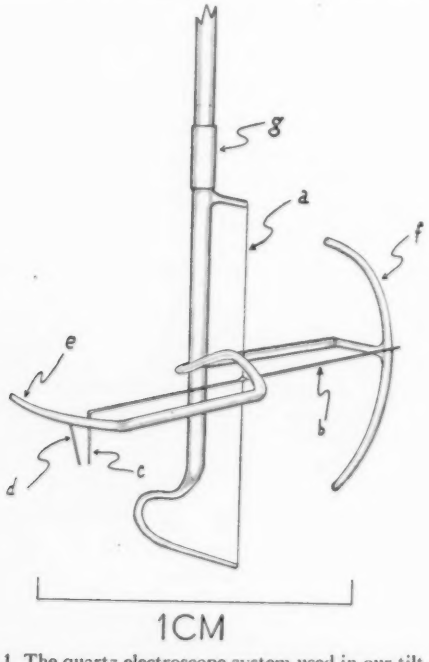

FIG. 1. The quartz electroscope system used in our tilt and vibration-free cosmic-ray instrument.

The design of the suspension of this electroscope is shown in Fig. 1. The system is of the torsion type and is made entirely of fused quartz. The 5μ fiber a is stretched until its length is increased about one percent. The 30μ movable cross arm b is bent at right angles at one end where it is drawn down to a thickness of about 10μ. The image of c cast on the recording film by a lens giving a magnification of 10 has then a convenient width on the film. The short bit of fiber d serves as a fiducial mark and it, together

with the part *e* (which is bent into the arc of a circle with the torsion fiber as a center) and the stop *f*, combines to give a linear scale over practically the whole range of discharge. *g* is a piece of platinum cemented to the quartz and is the point at which a new charge is automatically placed on the system at regular time intervals. With a very small oxygen flame all joints are fused together so that the whole system becomes essentially one piece of quartz. A twist of about 30° is placed permanently in the torsion fiber so that no motion of the movable arm takes place until about 250 volts are reached and then the full deflection of 2 mm results for the next 75 volts. The whole system from *g* down is covered with a conducting layer of gold by evaporation. The movable part *b* is balanced by cutting off one end until a tilt of 90° causes less than 0.005 mm actual motion of *c*. Besides being free from tilt the system because of the large ratio of strength to weight is quite insensitive to vibration.

The electrostatic capacity is approximately 0.43 cm. In a 100 div. scale placed in the eyepiece the voltage sensitivity is about 0.7 volt/div. This results in a charge sensitivity of approximately 10^6 ions/div.

Fig. 2 is a photograph of the suspension and its supports. The complete instrument is shown in Fig. 3 while Fig. 4 illustrates the recording mechanism as well as that available for visual observation. The film runs just behind a narrow horizontal slit in a disk at the right end of the brass tube connecting the electroscope chamber on the left with the recording chamber on the right. The image of *c* (Fig. 1) travels across this slit as the electroscope discharges so that where this image intersects the slit there is produced a unexposed point on the film which trav diagonally across the film as the electrosc discharges. In this survey the electroscope was automatically charged up once every hour. Fig. 5 shows a sample strip of the developed film. The rate of discharge during an hour's run is given by the slope of each diagonal line of this film. The mean of 24 of these slopes gives the mean intensity for the day in question. Fig. 6 shows the electroscope both completely and partly housed in its lead shield 11 cm thick,[3] the

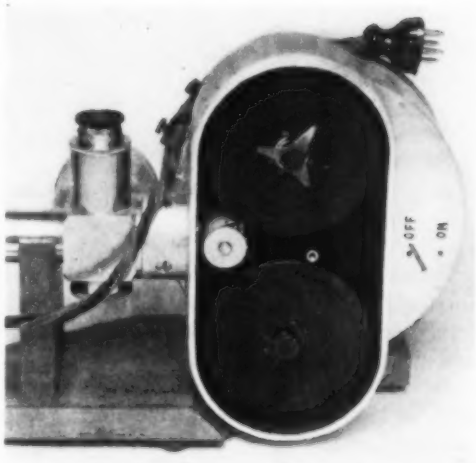

FIG. 4. The camera will take a one hundred foot reel of 35-mm motion picture film which is driven at a constant rate past the slit by a power clock. Changeable gears allow various rates of film speeds to be used, depending on the expected ionization.

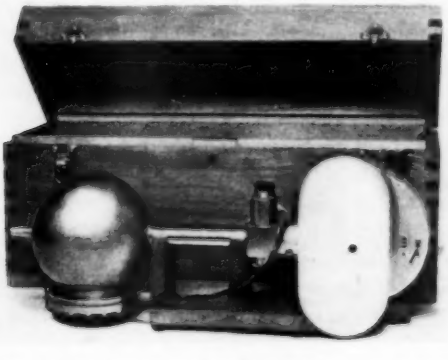

FIG. 3. The instrument used in this survey is usually shielded with lead and is placed in the box when used in most airplane flights.

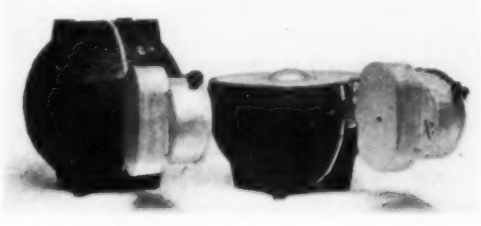

FIG. 6. An 11 cm lead shield protected by a one-half inch shell of cast iron has been used for most of the survey to insure freedom from local variations in radiation.

[3] The lead is actually 10 cm thick and we have often called it a 10-cm shield. Counting the iron rim, which prevents the distortion of the lead, it is the equivalent of a 11-cm Pb shield and is herein so designated.

all their cosmic-ray measurements made from 1927 to 1930. Like its predecessor it consisted of a spherical steel bulb of 3 mm wall thickness and 15 cm diameter filled with gas at pressures up to 30 atmospheres and holding at its center a gilded quartz fiber electroscope system, readable, by means of a short focus telescope, through a window in the wall. Such an electroscope with no outside connections of any kind, if properly dried with phosphorus pentoxide, eliminates the serious uncertainties and difficulties inherent in electroscopes having outside connections, especially when these are used in moist surroundings.

In the earlier years air was used as the filling gas but argon was also used beginning in the summer of 1931 and since 1932 it has been exclusively used. We have, however, one air electroscope that was filled at 30 atmospheres in September, 1928, the reading of which, within its 10 cm lead shield in the basement of one of our homes, now used as a standardizing laboratory, has not varied appreciably during these eight years. In a given cosmic radiation field its current is 13.8 times that found when its pressure is reduced to one atmosphere. Through comparison with it and with the aid of this multiplication factor, all our argon-electroscope readings are reduced to ionization in air at one atmosphere. Such reduction is made in most of the accompanying charts. The exactness of this reduction is not, however, important for the purposes of this paper, since the essential comparison is here merely between the reading of the given electroscope at Los Angeles, from which port it always starts out and to which it always returns, and its reading in the other localities to which it is taken.

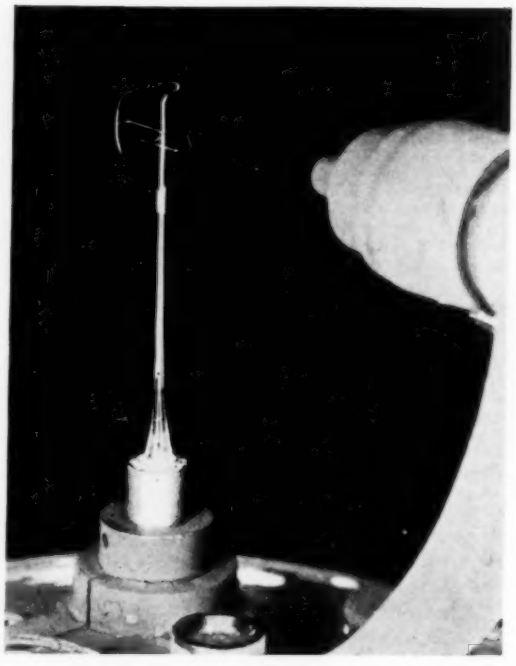

FIG. 2. Illustrating the quartz system when ready for installing into the ionization chamber. The lens mounting is supported by a rigid arm which is securely fastened to the same piece that holds the electroscope system.

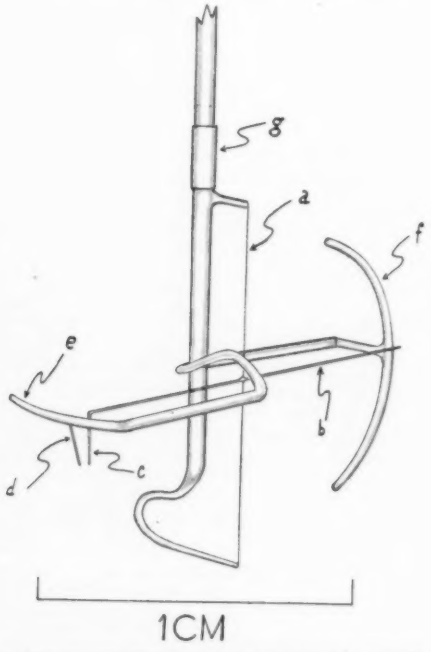

FIG. 1. The quartz electroscope system used in our tilt and vibration-free cosmic-ray instrument.

The design of the suspension of this electroscope is shown in Fig. 1. The system is of the torsion type and is made entirely of fused quartz. The 5μ fiber *a* is stretched until its length is increased about one percent. The 30μ movable cross arm *b* is bent at right angles at one end where it is drawn down to a thickness of about 10μ. The image of *c* cast on the recording film by a lens giving a magnification of 10 has then a convenient width on the film. The short bit of fiber *d* serves as a fiducial mark and it, together

with the part *e* (which is bent into the arc of a circle with the torsion fiber as a center) and the stop *f*, combines to give a linear scale over practically the whole range of discharge. *g* is a piece of platinum cemented to the quartz and is the point at which a new charge is automatically placed on the system at regular time intervals. With a very small oxygen flame all joints are fused together so that the whole system becomes essentially one piece of quartz. A twist of about 30° is placed permanently in the torsion fiber so that no motion of the movable arm takes place until about 250 volts are reached and then the full deflection of 2 mm results for the next 75 volts. The whole system from *g* down is covered with a conducting layer of gold by evaporation. The movable part *b* is balanced by cutting off one end until a tilt of 90° causes less than 0.005 mm actual motion of *c*. Besides being free from tilt the system because of the large ratio of strength to weight is quite insensitive to vibration.

The electrostatic capacity is approximately 0.43 cm. In a 100 div. scale placed in the eyepiece the voltage sensitivity is about 0.7 volt/div. This results in a charge sensitivity of approximately 10^6 ions/div.

Fig. 2 is a photograph of the suspension and its supports. The complete instrument is shown in Fig. 3 while Fig. 4 illustrates the recording mechanism as well as that available for visual observation. The film runs just behind a narrow horizontal slit in a disk at the right end of the brass tube connecting the electroscope chamber on the left with the recording chamber on the right. The image of *c* (Fig. 1) travels across this slit as the electroscope discharges so that where this image intersects the slit there is produced an unexposed point on the film which travels diagonally across the film as the electroscope discharges. In this survey the electroscope was automatically charged up once every hour. Fig. 5 shows a sample strip of the developed film. The rate of discharge during an hour's run is given by the slope of each diagonal line of this film. The mean of 24 of these slopes gives the mean intensity for the day in question. Fig. 6 shows the electroscope both completely and partly housed in its lead shield 11 cm thick,[3] the

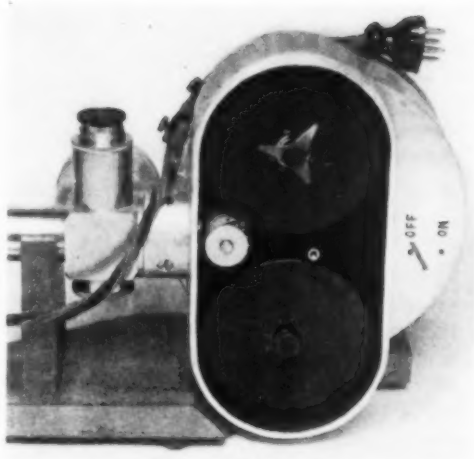

FIG. 4. The camera will take a one hundred foot reel of 35-mm motion picture film which is driven at a constant rate past the slit by a power clock. Changeable gears allow various rates of film speeds to be used, depending on the expected ionization.

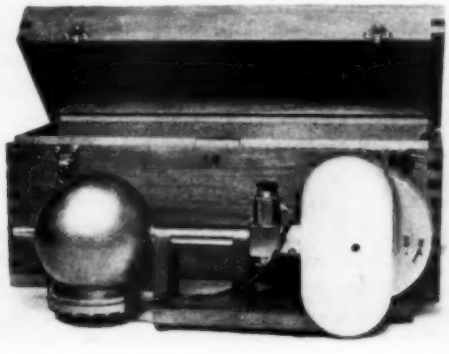

FIG. 3. The instrument used in this survey is usually shielded with lead and is placed in the box when used in most airplane flights.

FIG. 6. An 11 cm lead shield protected by a one-half inch shell of cast iron has been used for most of the survey to insure freedom from local variations in radiation.

[3] The lead is actually 10 cm thick and we have often called it a 10-cm shield. Counting the iron rim, which prevents the distortion of the lead, it is the equivalent of a 11-cm Pb shield and is herein so designated.

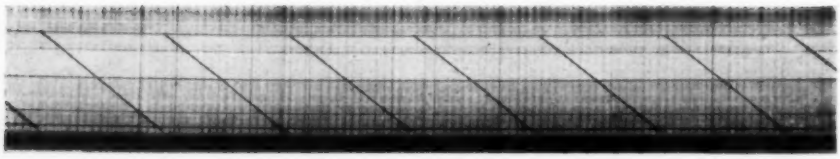

FIG. 5. Showing the type of record obtained at sea level in this world survey. Two of the horizontal lines give barometric and temperature records.

left hand assembly showing how it looks when placed aboard a ship. The accuracy and stability of this instrument as revealed by the high altitude airplane flights (up to 29,000 ft.) which we made with it in the summer of 1932 and the spring of 1933 in northern Canada, northern and southern United States, Panama and Peru, was such that in the winter of 1933 we introduced slow motion gears suitable to the slow rate of discharge found at the earth's surface and began the precision sea-level survey. This was completed in the fall of 1935 and is reported in full herewith.[4] The total weight is 625 lbs.

§2. The Equatorial Dip in the Longitude of the West Coast of South America

The aim of the survey was to attain as high an order of accuracy in comparing sea-level ionizations all over the world as had been attained in 1930 in comparing the mean cosmic-ray intensity at Pasadena with that at Churchill, Manitoba. In establishing the equality of the cosmic radiation existing between these two localities, the mean of not less than a week of continuous readings day and night with the same electroscope in each locality was taken and at the same temperature. Such precautions made it possible to assert with great certainty that the mean cosmic-ray intensity at Pasadena and at Churchill did not differ by as much as one percent.

Our first concern was to fix accurately the amount of the equatorial dip, or reduction of cosmic-ray intensity shown in the readings of an electroscope sent from Los Angeles to the western coast of South America. To get this with high precision it was necessary, as in 1930, to let the electroscope remain in the same place for a week or so at a time so as to render the mean as independent as possible of the erratic daily fluctuations which because of "Hoffmann bursts" rise sometimes to a two-percent value though ordinarily they are much less than this. The instrument was placed on board Capt. Allan Hancock's yacht, the *Valero III*, and in a voyage of three months' duration the results shown in Fig. 7 were obtained. The numbers attached to the most significant points give the number of days during which the ship remained stationary at these points. These fix with much precision the equatorial reduction in cosmic-ray intensity measured by an electroscope inside 11 cm of lead between the latitude of Los Angeles harbor at San Pedro (Geographical 33.7° N., magnetic 41° N.) and Mollendo (Geographical 17° S., magnetic 6° S.) as 7.1 percent. The crosses represent daily readings obtained on another voyage with the same electroscope from Panama to Mollendo (Peru) and return to Panama. These results have been checked by two other voyages with a shielded electroscope, one between Los Angeles and New York, via the Panama Canal, and one between Mollendo and New York, via the Panama Canal, with mean results which are in agreement with the findings of the *Valero III* to within about three-tenths of a percent.[5] These four separate voyages seem to us to fix the mean equatorial dip in this longitude with much certainty.

We then sent an unshielded electroscope between Mollendo and Los Angeles and found here too a seven percent lower reading at Mollendo than at San Pedro,[5] thus establishing the fact that *the equatorial dip is essentially the same as measured in percentages whether the readings are taken inside a 11 cm lead screen or outside.*

[4] A brief report has already appeared in the publications of the Carnegie Institution of Washington, No. 34, pp. 343–345. It was read in the Proceedings of the National Academy of Sciences for November, 1935.

[5] These curves have already been published, Phys. Rev. 47, 207 (1935).

§3. The Suddenness with Which the Equatorial Dip Sets In

The next point of much importance was to determine very accurately the change in sea-level intensity between, say, Los Angeles and Victoria, B.C. (Geological latitude 48.3°, magnetic 54.3° N). For this purpose we took two different electroscopes on a voyage from Seattle, via Victoria, to Los Angeles. In this case both of us accompanied the electroscopes, one of which was placed outside its lead shield and read visually every four hours, while the other was inside its shield and adjusted to move across the field once every hour. The instruments were in a state room next the bridge, the temperature of which was kept constant so that only barometric changes had to be allowed for and these were small. These results reveal so well the kind of consistency obtained in the readings as well as the extraordinary uniformity of the sea-level ionization over this range of latitudes that the summarized readings, taken continuously four hours apart by electroscope No. 1 over a period of five days, are given in Table I, as well as the corresponding readings of electroscope No. 2.

Both of these instruments had zero readings of the order of 1 ion per cc/sec., as determined by observation in a tunnel 250 ft. beneath the earth's surface, so that the ionization is practically all due to cosmic rays. It will be seen that the fluctuation from the 12 hour means never in these five days exceeds one percent. These readings show, then, with great conclusiveness that *within the limits of accuracy attained with these sensitive instruments there is no change in*

Table I. *Five-day study of sea-level variations of cosmic-ray intensities between Victoria, B. C. and Los Angeles.*

Electroscope No. 1—Unshielded (ions cc/sec.)				Electroscope No. 2—Shielded (11 cm Pb)			
	Lat.	4-hour Means	12-hour Means	Lat.	Long.	Mag. Lat.	12-hour Means
In Seattle Harbor	47.5	39.91	39.58*	47.5	122 W.	53.5 N.	24.60 Seattle
		39.25		48.3	123 W.	54.3 N.	24.71
In and near Victoria	48.4	39.41		46.5	124 W.	52.5 N.	24.65
		39.64	39.45	44.0	124 W.	50.0 N.	24.78
		39.29		41.0	124 W.	47.0 N.	24.49
At Sea	48.2	39.25		37.5	122 W.	43.5 N.	24.79 San Francisco
" "	47.2	39.52	39.53	36.0	122 W.	42.0 N.	24.57
" "	46.25	39.83		34.0	119 W.	40.6 N.	24.45†
						Mean	24.63
" "	45.3	39.31					
" "	44.3	40.12	39.67				
" "	43.5	39.58					
" "	42.5	39.44					
" "	41.6	39.94	39.69				
" "	40.8	39.69					
" "	40.0	39.28					
" "	39.0	39.12	39.33				
" "	38.0	39.62					
In San Francisco Harbor		39.72					
" " " "		40.38	39.82				
" " " "		39.36					
" " " "		40.04					
" " " "		39.54	39.61				
" " " "		39.25					
" " " "		39.65					
At Sea	37.3	39.55	39.65				
" "	36.4	39.76					
" "	35.5	39.71					
" "	34.7	39.76	39.65				
" "	34.2	39.43					
		Mean 39.60					

* 8-hour average.

† 9-hour average.

intensity whatever between Victoria, mag. Lat. 53, and Los Angeles, mag. Lat. 41. Taken in connection with Fig. 6 these figures show however that the equatorial dip sets in with quite surprising sharpness very close to Los Angeles.[6] Indeed, from the 10-day means taken in Los Angeles harbor at San Pedro and the means of more extended readings in Pasadena, which agree accurately with the mean readings both at Churchill, Manitoba, and at sea just north of Los Angeles, there seems to be a measurable fraction of a percent (about 0.7 percent) of drop in sea-level intensity between these two points Pasadena and San Pedro only 33 miles apart in a north-south line. Also, the suddenness of the change just south of Los Angeles harbor shows strikingly in Fig. 7. Further, the readings in this

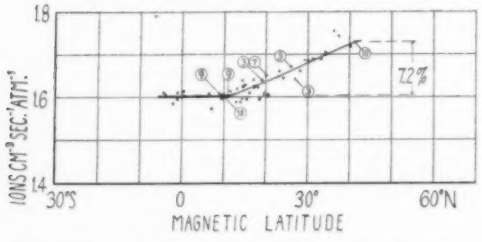

FIG. 7. Measurements taken aboard Captain Hancock's yacht, *Valero III*, have established accurately the amount of drop in ionization between Los Angeles harbor and the west coast of South America.

harbor are about this amount lower than the mean of the readings taken above magnetic latitude 41° in the neighborhood of New York in the two trips between Panama and New York. In consequence we are taking the equatorial dip in going from the polar and temperate latitude south through the equatorial belt along the longitude of the western coast of South America as eight percent and we feel confident that this cannot be as much as a percent in error.[7]

[6] It was because of the suddenness and the extent of the drop in the immediate neighborhood of Los Angeles harbor that Millikan and Cameron failed to notice the equatorial sea-level dip at all in the first voyage made in 1926 to check their theory that it ought to exist. They were unable to get their instruments installed and working on deck until they had been out about a day and a half. The constancy observed south of this point was quite consistent with the sensitivity of the electroscopes then in use.

[7] These curves have already been published, Phys. Rev. **47**, 207 (1935).

§4. The Equatorial Dip in the Longitude of Singapore

Our next objective was to determine the variations in sea-level intensity shown on the Dollar Line "round the world cruises," the route of which is Los Angeles, San Francisco, Honolulu, Kobe, Shanghai, Singapore, Red Sea, Genoa, Gibraltar, New York. The results of two such cruises on the *President Garfield*, *Captain Cullen*, and the *President Hayes*, *Captain Pierson*, are shown in graph form in Fig. 8. The *President*

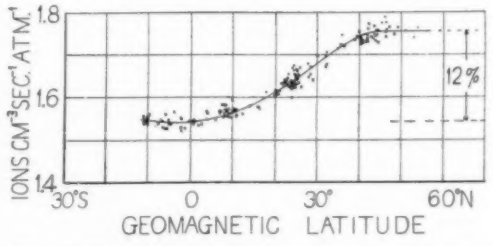

FIG. 8. These two trips around the world were taken by the same instrument and agree in showing the same relative as well as the same absolute values at times separated by one year.

Garfield cruise was made from August 1 to November 19, 1933. The *President Hayes* cruise was made from August 26 to December 16, 1934. Both the consistency of the readings on each cruise and the agreement between the observations in different years are noteworthy. It was the cruise of the *President Garfield* compared with the cruises from Los Angeles to the west coast of South America that brought to us our knowledge in January, 1934, of the longitude effect which was reported by us to the National Academy of Sciences and the Physical Society in April, 1934. This longitude effect was discovered independently and simultaneously by Clay and briefly mentioned in *Physica* in March, 1934. In our case the evidence inhered in the unambiguous finding that the equatorial dip in going across the magnetic equator in the longitude of Singapore was 12 percent instead of the eight percent value found on the South American side of the globe.

§5. Equatorial Dip in the Longitude of Samoa

In none of these voyages had we explored the rise in sea-level ionization in going from the

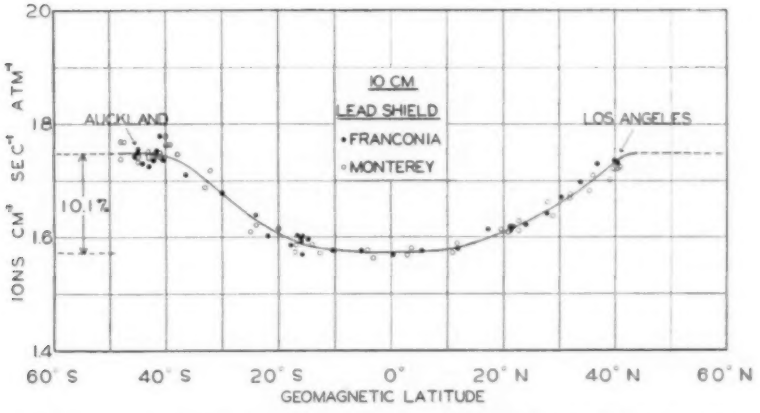

FIG. 9. The two trips here, made nine months apart, taken together with Fig. 8, show the consistency to be expected on going over the same route at different times.

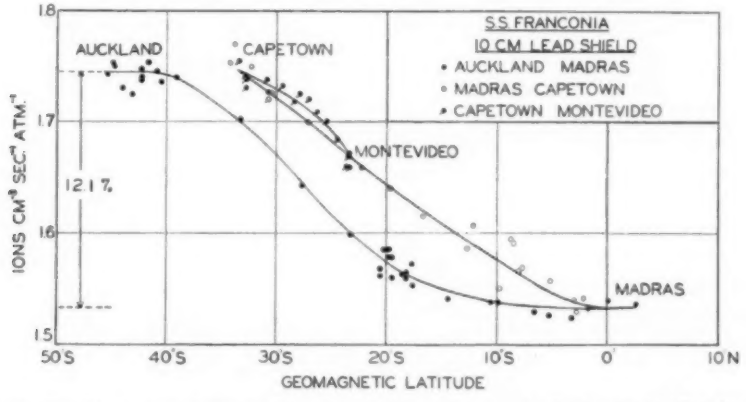

FIG. 10. On this section of the world cruise of the *S.S. Franconia* the longitude effect is very strikingly brought out.

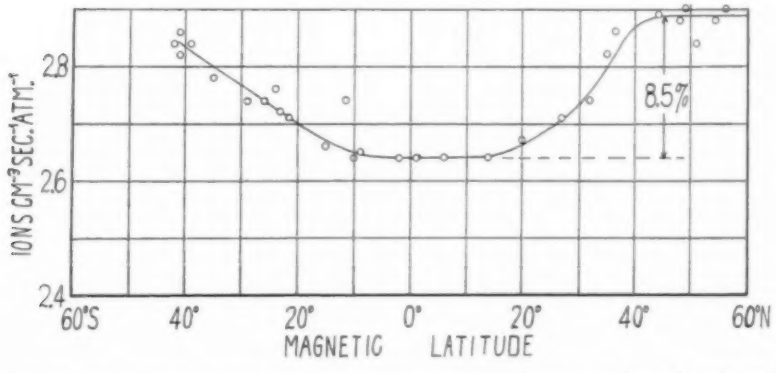

FIG. 11. The above data were obtained with an unshielded instrument from the trip of the *S.S. Reina del Pacifico* from Liverpool through the Straits of Magellan and up the west coast of South America. Both the shielded and unshielded instruments agree in showing that the drop at sea level sets in at about 41° geomagnetic latitude north.

equatorial zone to the southern temperate zone. Accordingly we sent two voyages across the equator and far into the southern hemisphere as follows: In June, 1934, we placed one shielded and one unshielded Neher electroscope in the room of First Officer Graham of the *S.S. Monterey* of the Matson Line and got an excellent record both going and coming between Los Angeles and Melbourne, Lat. 38 S., Mag. Lat. 48 S., in the case of the shielded electroscope, and a good record in the unshielded one on the way down. The percentage of dip was again quite the same with the shielded and with the unshielded electroscope and the dip itself, in crossing the equatorial belt in the longitude of the Samoan Islands, was ten percent, that is, a value intermediate between its values in South America and Asia.[8] To check these values and also get a more complete covering of the southern hemisphere, in January, 1935, we placed a shielded electroscope in a state room close to the bridge, in charge of Officer N. Kingscote of the Cunard liner *Franconia* bound for Honolulu, Samoa, Auckland, Sydney, Singapore, Madras, Colombo, Zanzibar, Capetown, Montevideo, New York. The notable consistency of the results obtained both in different years and different seasons between Los Angeles and Auckland is shown in Fig. 9, scarcely any day's run being off the line more than one percent. Fig. 10 shows the results obtained in going from Auckland to Madras, then to Capetown and from there to Montevideo.

It is quite clear that in going from Madras to Capetown the region of the earth which can produce a large equatorial dip is rapidly being left behind and the much smaller dip, like that first found on the west coast of South America, is being rapidly approached.

§6. Equatorial Dip in the Mid-Atlantic

This value of the equatorial dip, in going across the equatorial belt in the mid-Atlantic, was obtained by sending another Neher electroscope on the *S.S. Reina del Pacifico*, sailing from Mollendo up through the Panama Canal to Liverpool, then after a stay of a few weeks in that port south through the mid-Atlantic and around the end of South America. The results, without shield, from Liverpool to "Magallanes" are shown in Fig. 11 and from Magallanes to Valparaiso and then from Lima to Los Angeles, on another boat, in Fig. 12. The results obtained with this unshielded electroscope are much more erratic than any of the others which we have taken, presumably because the usual precautions were not taken to keep passengers away from an *unshielded* electroscope. The single point that is badly off the line in Fig. 11 is presumably due to this same cause or else to a large burst occurring on that day.

[8] These results are shown in the graphs found in Phys. Rev. **47**, 207 (1935).

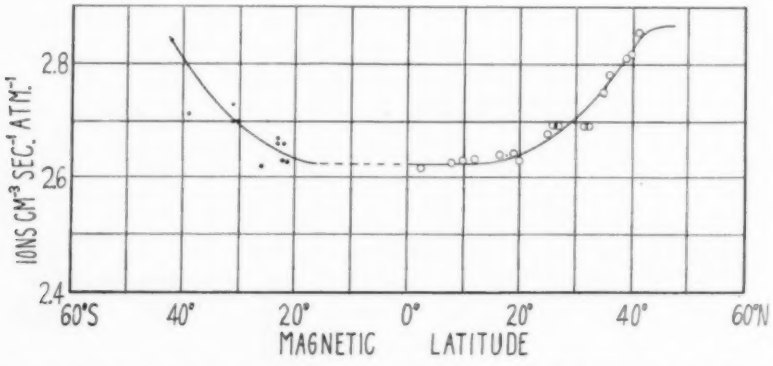

Fig. 12. The portion of the trip of the *Reina del Pacifico* up the west coast of South America to Valparaiso is compared with an unshielded instrument from Lima to Los Angeles harbor. Taken with Fig. 11 a longitude effect appears to be evident between the east and west sides of lower South America.

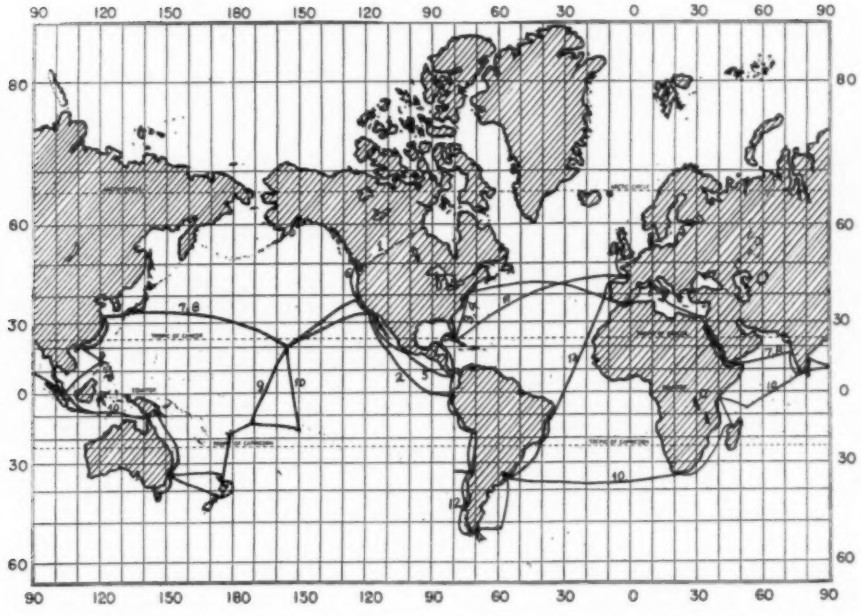

FIG. 13. This survey is the result of twelve different trips which have included most of the chief commercial routes on the oceans. No. 1 represents the Churchill trip in 1930.

§7. GENERAL SIGNIFICANCE OF THE SUDDENNESS OF THE SET-IN OF THE EQUATORIAL DIP

It is the extreme constancy of the sea-level readings down to the latitude of Pasadena, as shown in Table I, and the notable suddenness with which the equatorial drop in intensity begins to set in just south of Pasadena, as shown in Figs. 7, 8, and 9, that enables the resistance of the atmosphere to incoming electrons to be fixed, through the Epstein-Lemaitre-Vallarta analysis, at 6 billion electron-volts with an uncertainty of perhaps 20 percent.

This single sudden break in sea-level intensity also constitutes evidence against the existence of two kinds of incoming charged particles, such as protons and electrons, of notably different absorbabilities; since this would require two such breaks, one considerably farther north than magnetic latitude 41°, while no such second break actually appears.

Further, the constancy of the sea-level ionization down to magnetic latitude 41° shows that incoming particles of 6 billion electron-volts of energy have a sharply limited range. This constancy means that the effects of practically all incoming particles of higher energy than 6 billion electron-volts reach down to sea level. On the other hand, while incoming particles of lower energy definitely produce ionization effects in the *upper* atmosphere, as shown clearly by the difference between our altitude-ionization curve* taken at Pasadena (March Field), magnetic latitude 41°, and at Spokane, magnetic latitude 54°, yet they have no influence on sea-level ionization. Again, the identity of these altitude-ionization curves up to 22,000 feet between Spokane and The Pas (magnetic latitude 63°N), shows that the effects of 2.4 billion electron-volts (the energy required here to get through the blocking effect of the earth's magnetic field) cannot reach down to 22,000 feet, though they are abundantly found above this altitude.** *These definite indications of range phenomena in the incoming electrons are of much significance for the general understanding of the nature of the particle component of the incoming cosmic rays.*

* Bowen, Millikan and Neher, *International Conference on Physics*, Vol. I. "Nuclear Physics" (London, 1934), p. 210. Also Phys. Rev. **46**, 642 (1934).

** See Figs. 4 and 6 of above references.

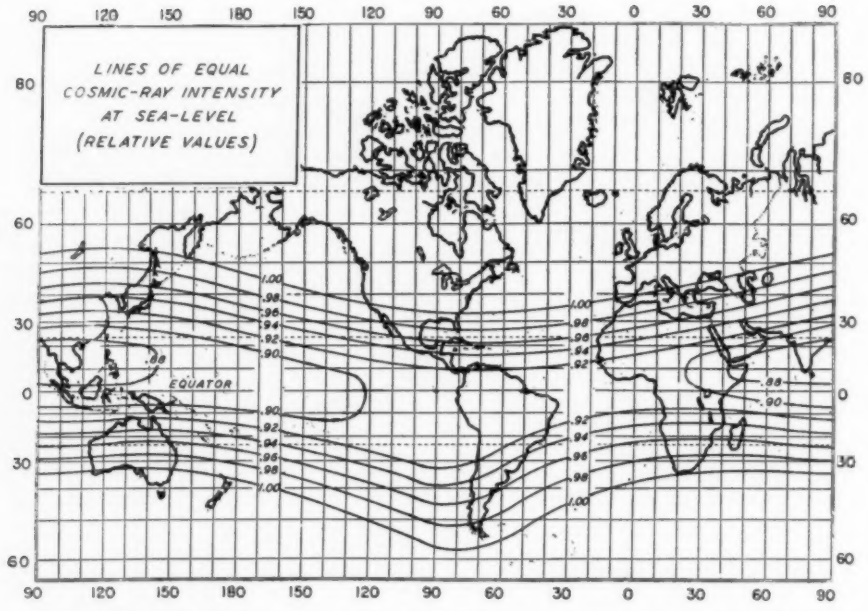

FIG. 14. The results of the survey at sea level are here represented in a consistent scheme of lines of equal cosmic-ray intensity. These lines in general are parallel to the geomagnetic equator, the notable exceptions being in the region of lower South America and along the magnetic equator where the longitude effect appears. From the upper line north, and from the lower line south, the intensity of cosmic radiation at sea level remains constant.

§8. SUMMARY

The whole of our work in this survey is condensed into the maps shown in Figs. 13 and 14. The former shows all the voyages, the latter shows how the lines of equal cosmic-ray, sea-level intensity are distributed over the earth's surface. Our films are all available at the Norman Bridge Laboratory of Physics at Pasadena so that others who may desire to make studies of geographical variations in sea-level, cosmic-ray intensities can do so exceedingly easily by simply remeasuring these sets of films. We have tried to keep the measurements free from the personal equation by having our films measured by two different observers whose points on the foregoing charts are actually completely indistinguishable.

We wish to make grateful acknowledgment to the Carnegie Corporation of New York and the Carnegie Institution of Washington which have supplied the funds with which this long continued survey has been made. Also, to the management and officers of the above mentioned vessels, who have allowed our installations to go into their ships and have kept our clocks wound up and running throughout the respective voyages, we herewith extend most hearty thanks.

The Absorption of Shower-Producing Cosmic Rays

J. H. SAWYER, *Rice Institute, Houston, Texas*

(Received March 20, 1936)

The coefficients of absorption of shower-producing cosmic rays have been measured in water, aluminum, iron and lead. The coefficients are nearly equal to 0.018 cm^{-1} times the densities. Showers from a lead scatterer were counted with three Geiger counters. A large block of aluminum was put above the scatterer to absorb the secondaries in the ordinary cosmic-ray beam and produce aluminum secondaries. An absorber which reduced the intensity of the primary rays was put above the aluminum block and its thickness was varied. The resulting variation of the number of showers gave the absorption of the primary rays producing the showers. Absorption coefficients have been obtained also for paraffin secondaries and for the tertiaries they produce in lead.

IT was shown in previous papers[1] that cosmic-ray showers are due to secondary rays in the ordinary cosmic-ray beam. The absorption coefficients of the secondary rays and the tertiary rays, or shower particles, were determined. The experiments described in the present paper were done with the object of measuring the absorption coefficients of the primary rays which produce the secondary and tertiary rays.

The apparatus used is shown in Fig. 1. The three circles represent Geiger counters and *S* is a lead plate. A large aluminum block was placed above the top counter as shown. The primary cosmic rays passing down through the aluminum block produce secondary rays. These secondaries produce showers of tertiary rays in the lead scatterer, *S*. The showers produce triple coincidences, in the three counters, which are recorded.

If a block of any material is placed above the aluminum block the number of showers recorded is reduced and so the absorption of the shower-producing primary rays in the material can be determined. It should be noted that the aluminum block must be thick enough to absorb the secondaries which accompany the primary rays and to replace them by aluminum secondaries. The aluminum block for this purpose was 13.0 cm thick, 30 cm long and 13 cm wide.

The Geiger counters consisted of a copper cylinder 4.8 cm in diameter and 20 cm long, with a fine tungsten wire for the central electrode. These were sealed in glass tubes containing argon at about 3 cm Hg pressure. The upper counter

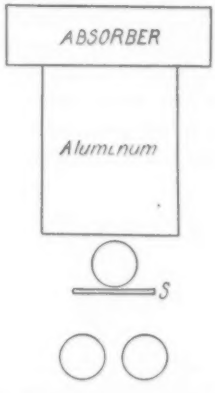

FIG. 1. Arrangement of apparatus.

was about 15 cm above the two lower ones which were 1.4 cm apart. The lead scatterer, *S*, was 0.85 cm thick, 10 cm wide and 30 cm long. The triple coincidences were recorded with the same amplifier used in the previous work.

The results obtained with an absorber of iron above the aluminum block are given in Table I.

TABLE I. *Observed and calculated number of coincidences with various thicknesses of iron absorber above the aluminum block.*

Thickness of Iron Absorber	Total No. of Coincidences	Time	Coincidences per Hour	
			Obs.	Calc.
0 cm	256	8.7 hrs.	29.5	29.5
1.20	204	7.4	27.6	27.3
2.54	370	14.7	25.2	25.2
5.08	297	12.6	23.5	22.2
7.65	381	18.3	20.8	20.1
10.28	545	28.2	19.3	19.6
12.82	253	14.2	17.8	17.5
15.34	495	29.0	17.0	16.8
17.88	417	24.7	16.9	16.3

[1] J. H. Sawyer, Phys. Rev. **44**, 241 (1933); **47**, 515 (1935); **47**, 635 (1935).

The iron absorber was 90 cm long, 25 cm wide and its thickness was varied.

The last column of Table I contains values of the expression $15+14.5e^{-0.137x}$ where x is the thickness of the iron absorber in cm. The constant, 15, is the triple coincidence counting rate when the lead scatterer, S, is removed. This corresponds to the usual "chance count." The calculated values agree with the observed numbers of coincidences per hour within the limits of error. The absorption coefficient of the primary rays is therefore approximately 0.137 cm^{-1} Fe.

Similar experiments have been done with water, lead and aluminum as absorbers. The water was in a tank 61 cm long and 42 cm wide. Its depth was varied from 0 to 115 cm. The lead absorber was 40 cm long, 18 cm wide and up to 11 cm thick. The aluminum absorber was 36 cm long, 13 cm wide and up to 9.5 cm thick. Table II

TABLE II. *Absorption coefficients in various absorbers.*

ABSORBER	ABSORPTION COEFFICIENT	100 COEFFICIENT/DENSITY
Water	0.0183 cm^{-1}	1.83
Aluminum	0.05*	1.9
Iron	0.137	1.74
Lead	0.197	1.74

* Owing to the small thickness of aluminum available for the absorber, this value is not as reliable as the others.

gives the absorption coefficients found. The large block of aluminum, 30 cm long, 13 cm wide and 15.5 cm thick, was used in each case to absorb the secondaries in the ordinary cosmic ray beam and to produce aluminum secondaries.

The last column of Table II gives the values of the absorption coefficients multiplied by 100 and divided by the densities. It appears that the coefficients are nearly proportional to the densities.

The absorption of the primary rays in lead was also measured using a large block of paraffin wax, $32\times12\times32.5$ cm, in place of the aluminum block. The lead absorber was the same size as before and was varied from 0 to 11 cm thick. The absorption coefficient was found to be 0.175 cm^{-1} which is a little smaller than the value found with the aluminum block.

The absorption coefficients in lead of the secondary rays from paraffin and the tertiary rays these secondaries produce in lead were determined. This was done by varying the thickness of the lead scatterer, as in the experiments described in previous papers. The absorption coefficient of the paraffin secondaries was found to be 0.85 cm^{-1} Pb and that of the tertiaries to be 1.9 cm^{-1} Pb.

Table III gives the values of all the absorption coefficients found in this paper and in the previous papers.

TABLE III. *Absorption coefficients found in this and in previous papers.*

PRIMARY RAYS PRODUCING SECONDARIES IN ALUMINUM					In paraffin
Absorber	H_2O	Al	Fe	Pb†	Pb
Coefficient (cm^{-1})	0.0183	0.05	0.137	0.197	0.175
Coefficient 100/Density	1.83	1.9	1.74	1.74	1.56
SECONDARY RAYS					
Substance giving the rays	Air*	Air and Roof	Aluminum	Paraffin	
Coefficient in lead (cm^{-1})	0.32	0.50	0.70	0.85	
TERTIARY RAYS FROM LEAD					
Substance giving the Secondary Rays	Air	Air and Roof	Aluminum	Paraffin	
Coefficient in lead (cm^{-1})	1.18	2.58	2.0	1.9	

* Values calculated from Rossi's (B. Rossi, Zeits. f. Physik **82**, 151 (1933)) and Funfer's (E. Funfer, Zeits. f. Physik *83*, 92 (1933)) results.
† The value, 0.5 cm^{-1} Pb, given previously (Phys. Rev. **47**, 635 (1935)) was wrong due to an arithmetical error.

The absorption coefficients of the primary shower-producing rays have been estimated previously by Johnson,[2] Montgomery[3] and Pickering.[4] They measured the number of showers at different altitudes or at different depths in water. The absorption coefficients they found are smaller than those found here, varying from 0.005 to 0.009 cm^{-1} H_2O. The difference may be due to the variation of the number of showers with the energy of the primaries. These and other writers have found that the number of showers increases with altitude much faster than the number of primary cosmic rays. This indicates a variation of the number of showers with the energy of the primaries, since the shape of the absorption curve for showers at any altitude is much the same.

I wish to thank Professor H. A. Wilson for many suggestions during the course of this work and for help in writing the paper.

[2] Johnson, Phys. Rev. **40**, 638 (1932); **45**, 569 (1934).
[3] Montgomery, Phys. Rev. **47**, 339 (1935).
[4] Pickering, Phys. Rev. **47**, 423 (1935).

The Photographic Infrared Absorption Spectrum of Gaseous Ammonia

SIU-HUNG CHAO,* *Ryerson Physical Laboratory, University of Chicago*

(Received March 2, 1936)

The photographic infrared absorption bands of ammonia at about 10,000A, 7920A, and 6470A have been measured with greater dispersion and resolving power than hitherto. Several series have been established in the first two bands by combination principle methods, but most of the band lines have not been classified. The complexity of structure occurs probably because each observed band is a composite of several parallel-type and perpendicular-type bands; the observed series, or most of them, probably constitute parallel bands. In the pure gas, the band lines are very sensitive to pressure, and do not become at all sharp until the latter is far below one atmosphere (cf. Fig. 1). In mixtures of ammonia and air, however, the air pressure produces very little broadening. The application of the combination principle to parallel, perpendicular, and Raman bands is discussed, taking into account the effects of unresolved but not negligible fine structure in the lines due to near-coincidence of lines of differing K values. Analysis of earlier data yields a rough value for a certain small rotational coupling coefficient and for the centrifugal deformation rotational coefficient, in the normal state of ammonia.

I. INTRODUCTION

THE absorption spectrum of the ammonia molecule, which belongs to the class of symmetrical top molecules, has been investigated in the infrared, visible and ultraviolet regions. The five bands in the photographic infrared and visible regions have been studied by the following investigators. Lueg and Hedfeld[1] reported having resolved 375 lines in the 10,230A band and 217 lines in the 8800A band, Badger and Mecke[2] reported 54 lines in the 7920A band and Badger[3] 57 lines in the 6470A band. The 5490A band has not been resolved. Because of the complexity of the structure, only partial analyses of these bands have been made. The present work[4] was undertaken in the hope of increasing the resolution in these bands, by using high dispersion and the special Eastman spectroscopic plates, so as to get accurately the rotational energy levels of the normal state of ammonia by a rigorous analysis according to the combination principle method, and to identify the upper vibrational levels of these bands.

In the present work, a higher resolution of these bands than previously has been attained. As an aid to the analysis, the constants of the rotational energy levels of the normal state of ammonia, found from the pure rotation band and from the Raman spectrum, were used. However, an analysis according to the combination principle method did not succeed very well. The difficulties and resulting conclusions will be stated in Section III.

II. REVIEW OF THEORETICAL CONSIDERATIONS[5]

The symmetry of ammonia is such that in equilibrium the molecule is a regular pyramid with three hydrogen atoms at the corners of an equilateral triangle. Dennison[6] showed that there should be four fundamental vibration frequencies, two belonging to nondegenerate symmetrical modes of vibration ("parallel-type" frequencies), and two degenerate frequencies, each corresponding to an unsymmetrical pair of modes of vibration ("perpendicular-type" frequencies).

The vibration bands may be divided into two types. In the "parallel" type, the electric moment oscillates parallel to the axis of symmetry. In the "perpendicular" type, it oscillates perpendicular to the axis. In ammonia, there should be two fundamental bands of the parallel type, say ν_1 and ν_3, and two fundamental bands of the perpendicular type, say ν_2 and ν_4, corresponding to the four fundamental frequencies.

The ammonia molecule in its equilibrium configuration belongs to the symmetry group C_{3v}. By group theory,[7] there exist three irreducible representations of this group, which have been called A_1, A_2 and E. Every vibrational wave

* Now at St. John's University, Shanghai, China.

[1] P. Lueg and K. Hedfeld, Zeits. f. Physik **75**, 599 (1932).

[2] R. M. Badger and R. Mecke, Zeits. f. physik. Chem. **B5**, 333 (1929).

[3] R. M. Badger, Phys. Rev. **35**, 1038 (1930).

[4] Preliminary account, S. H. Chao, Phys. Rev. **48**, 569*L* (1935).

[5] Cf. e.g., E. Teller, *Hand- und Jahrbuch der chemischen Physik*, Vol. 9-2 (1934).

[6] D. M. Dennison, Rev. Mod. Phys. **3**, 280 (1931).

[7] E. Wigner, *Göttinger Nachr. Math.-Phys. Klasse* (1930), p. 133; R. S. Mulliken, Phys. Rev. **43**, 279 (1933).

function of ammonia (neglecting the tunnel effect) must belong to one of these three representations. Of the three types, A_1 and A_2 are nondegenerate, while E is doubly degenerate. Of the four fundamental frequencies, the two nondegenerate can be shown to belong to representation A_1 and the two degenerate to representation E. Tisza[8] showed that the n-quantum overtones of frequencies of the types A_1 and E give vibrational states as follows:

$$[A_1^n]=A_1;$$
$$[E^n]=\begin{cases}E & \text{when } n \text{ is } 1,\\ A_1+E & \text{when } n \text{ is } 2,\\ A_1+A_2+E & \text{when } n \text{ is } 3; \text{ etc.}\end{cases} \quad (1)$$

Parallel bands can be shown to occur for transitions $A_1 \leftrightarrow A_1$, $A_2 \leftrightarrow A_2$, or $E \leftrightarrow E$, perpendicular bands for $A_1 \leftrightarrow E$, $A_2 \leftrightarrow E$, or $E \leftrightarrow E$. Since the normal state of ammonia is of type A_1, the four fundamental bands involving the normal state are $\nu_3(\|)=(A_1 \leftarrow A_1)$, $\nu_4(\perp)=(A_1 \leftarrow E)$, $\nu_1(\|)=(A_1 \leftarrow A_1)$ and $\nu_2(\perp)=(A_1 \leftarrow E)$.

As a result of the tunnel effect, in which the nitrogen atom can penetrate the potential barrier in the hydrogen triangle according to the quantum mechanics, each vibrational level as above classified is really split into two, denoted by α and β (symmetrical and antisymmetrical with respect to a central plane). There are selection rules as follows: (1) for the parallel type of band, $\alpha \leftrightarrow \beta$; (2) for the perpendicular type, $\alpha \leftrightarrow \alpha$ and $\beta \leftrightarrow \beta$; (3) for the Raman spectrum, $\alpha \leftrightarrow \alpha$ and $\beta \leftrightarrow \beta$.

It is now fairly certain[9] that the four fundamental bands of ammonia are as follows: 10.5μ, $\nu_3(\|)$; 6.13μ, $\nu_4(\perp)$; 3.0μ (ν_1, $\|$, overlapped by ν_2, $\perp$). Calculations by J. B. Howard[10] indicate that ν_2, $\perp$ should be at about 3450 cm^{-1}. Since such a band would overlap ν_1, $\|$ at 3.0μ, we have an explanation of the observed structure of the 3.0μ band which, although its strongest lines can be explained as ν_1, $\|$, with center at 3335 cm^{-1}, contains also many other lines. Further, M. Migeotte[11] has found in ND_3 a band analogous to the 3.0μ band of NH_3. This consists of two overlapping bands, one of parallel and one of perpendicular type, with the latter of somewhat lower frequency than the former.

The rotational energy of the symmetrical top rotator is given by

$$E_r=\frac{h^2}{8\pi^2}\left[\frac{J(J+1)}{I_A}+\left(\frac{1}{I_C}-\frac{1}{I_A}\right)K^2\right]+\cdots, \quad (2)$$

where $Jh/2\pi$ is the total angular momentum of the molecule and $Kh/2\pi$ is its component along the figure axis, I_C and I_A being the moments of inertia along and perpendicular to the symmetry axis. By substituting $B=h/8\pi^2cI_A$ and $\beta=(I_A/I_C)-1$, and assuming that the molecule is also deformed on account of rotation, the rotational energy in wave numbers is

$$F(J,K)\equiv E_r/hc=BJ(J+1)+\beta BK^2 +DJ^2(J+1)^2+\cdots, \quad (3)$$

where $K \leqq J$. When the vibrational state is of a degenerate type, there is an interaction between the angular momentum vector K and the angular momentum associated with the vibration, giving rise to a correction term $\pm 2\beta' BK$ which must be added to Eq. (3).[12]

The selection rules for transitions between rotational energy levels are (1) for the parallel type of band, $\Delta J=0, \pm 1$ and $\Delta K=0$; (2) for the perpendicular type, $\Delta J=0, \pm 1$ and $\Delta K=\pm 1$; and (3) for the Raman spectrum, $\Delta J=0, \pm 1, \pm 2$ and $\Delta K=0$.

Because of the nuclear spin of the hydrogen atoms, the quantum weights of those levels with quantum number K divisible by three (including 0) are doubled. Besides this, there is a weight factor $2J+1$ for $K=0$, $2(2J+1)$ for $K>0$.

III. Search for ΔF's and Difficulties in Analysis; Nature of Bands

In order to analyze the photographic vibration-rotation bands by the combination principle method, it is desirable to know the ΔF's of the normal state. Perhaps the most fundamental type of ΔF is the double difference between rotational energy levels of equal K, given by

[8] L. Tisza, Zeits. f. Physik **82**, 48 (1933).

[9] The writer is greatly indebted to Professor D. M. Dennison for correspondence (also to M. Migeotte for information on ND_3) relating to this point.

[10] J. B. Howard, J. Chem. Phys. **3**, 207 (1935); see this paper also for earlier literature.

[11] Private communication to Professor Mulliken.

[12] E. Teller and L. Tisza, Zeits. f. Physik **73**, 791 (1933); M. Johnson and D. M. Dennison, Phys. Rev. **48**, 868 (1935).

$$\Delta_2 F_K(J) \equiv F_K(J+1) - F_K(J-1). \quad (4)$$

For ammonia these quantities can be obtained approximately from the pure rotation band and the Raman spectrum. Another type of ΔF of some importance is the single difference for fixed K, given by

$$\Delta_1 F_K(J) \equiv F_K(J+1) - F_K(J). \quad (5)$$

Still other types of ΔF's can be given, e.g.,

$$\Delta_2 F_J(K) = F_J(K+1) - F_J(K-1), \quad (6)$$

with J fixed.

According to the combination principle,[13] in a given vibration-rotation band, if $\Delta K = 0$, the difference of the wave numbers of a P and an R line involving a common upper rotational (and vibrational) level is

$$\Delta_2 F_K''(J) = R_K(J-1) - P_K(J+1), \quad (7)$$

where $\Delta_2 F_K''(J)$ is a difference between two lower rotational energy levels. Assuming the lower rotational levels given by Eq. (3), Eq. (4) now yields

$$\Delta_2 F_K''(J) = 2(2J+1)[B'' + 2D''(J^2+J+1)]. \quad (8)$$

From a study of observed $\Delta_2 F_K''(J)$'s, B'' and D'' could be evaluated.

From two lines with a common lower level, one finds for the upper rotational levels

$$\Delta_2 F_K'(J) = R_K(J) - P_K(J). \quad (9)$$

In the type of band where $\Delta K = 0$ and $\Delta J = 0$, ± 1 (parallel type infrared bands), each line is composed of several, usually superposed, components due to lines with the same J' and J'' but different values of K. Since $K \leqq J$, the number of superposed lines depends upon the value of J. A similar superposition of components exists also for Raman bands ($\Delta K = 0$, $\Delta J = 0$, ± 1, ± 2).

In attempting to apply Eqs. (7)–(9) to parallel type infrared bands (which includes the "pure rotation" bands as a special case), the compositeness of the lines, just mentioned, causes difficulty. Thus the $\Delta_2 F$'s obtained by applying Eqs. (7)–(9) represent some sort of averages over several K values. These average ΔF's for parallel bands may be called ΔF_{Pa}'s, and are defined, e.g., by

$$\Delta_2 F_{Pa}''(J) = R_{Pa}(J-1) - P_{Pa}(J+1) = F_{Pa}(J+1) - F_{Pa}(J-1), \quad (10)$$

where the symbol R_{Pa} or P_{Pa} refers to the measured frequency of a composite line.

To be sure, the quantities $R_K(J)$, $P_K(J)$, $\Delta_2 F_K(J)$ would be independent of K, and all components of a P or R line would coincide exactly, if Eqs. (3) and (8) were exact, but in practice, as we shall find, this is not quite true. The frequency which is measured for a line, corresponding evidently to the maximum of intensity of the observed composite line, obviously depends somewhat on the distribution of intensity among the different unresolved components (different K values) which make up the observed line. It is clear that, in general, any observed $\Delta_2 F_{Pa}''(J)$ value obtained from Eq. (10) should lie somewhere between the $\Delta_2 F_K(J)$ values with $K = 0$ and with $K = J$. Wright and Randall[14] and Barnes[15] in measuring the pure rotation band of ammonia, have obtained data allowing the evaluation of $\Delta_2 F_{Pa}''(J)$'s.

A similar situation exists for Raman effect ΔF's. In the pure rotation Raman effect, the observed Raman shifts are precisely $\Delta_1 F(J)$'s for $\Delta J = \pm 1$, and $\Delta_2 F(J)$'s for $\Delta J = \pm 2$. We may define

$$(\Delta J = \pm 1): \ \Delta_1 F_{Rm}(J) = \nu_{Rm}(J)_{\Delta J=1} = F_{Rm}(J+1) - F(J), \quad (11)$$

$$(\Delta J = \pm 2): \ \Delta_2 F_{Rm}(J) = \nu_{Rm}(J-1)_{\Delta J=2} = F_{Rm}(J+1) - F_{Rm}(J-1). \quad (12)$$

Here again each ΔF is an average over several K values. The measured ν_{Rm} depends somewhat on the intensity distribution over the different K values. This can be shown to be different for the cases $\Delta J = \pm 1$ and ± 2 in the Raman effect, while $R(J-1) - P(J+1)$ in parallel type infrared bands is still different. Hence, unless the $\Delta_1 F_K(J)$'s and $\Delta_2 F_K(J)$'s are independent of K, one should find slight discrepancies between $\Delta_2 F_{Rm}(J)$ and $\Delta_2 F_{Pa}(J)$, and between $\Delta_2 F_{Rm}(J)$ and $\Delta_1 F_{Rm}(J-1) + \Delta_1 F_{Rm}(J)$.

In the Raman spectrum of ammonia, Lewis and Houston[16] found accurately not only $\Delta_2 F_{Rm}(J)$'s

[13] Cf. e.g., W. Jevons, *Band Spectra of Diatomic Molecules* (The Physical Society, London, 1932), p. 47.

[14] N. Wright and H. M. Randall, Phys. Rev. **44**, 391 (1933).

[15] R. B. Barnes, Phys. Rev. **47**, 658 (1935).

[16] C. M. Lewis and W. V. Houston, Phys. Rev. **44**, 903 (1933).

but also $\Delta_1 F_{Rm}(J)$'s. For the changes $\Delta J=\pm 2$, assuming $\Delta_2 F_{Rm}(J)$ to be given by the equation

$$\Delta_2 F_{Rm}(J)=2(2J+1)[B_0+2D_0(J^2+J+1)], \quad (13)$$

they found $B_0=9.92$ and $D_0=-0.00052$. If Eqs. (3) and (8) were exactly valid, the coefficients B_0, D_0 thus obtained should coincide with B'', D'' of Eqs. (3) and (8) as applied to the normal state of the molecule. However, the Raman shifts with $\Delta J=\pm 1$ calculated from these constants deviate systematically from the observed Raman shifts. The discrepancy may be accounted for in the following way.

As already noted, each line observed in the Raman spectrum is really composed of several components of differing K value, the number of which depends upon the value of J. From the formulas for calculating the theoretical intensities of the lines,[16] one finds that for a given observed line with $\Delta J=\pm 1$ the intensity of the components should be highest for the higher values of K. When $\Delta J=\pm 2$, however, the intensity of the components is highest for the smaller values of K.

Now suppose a small correction in the form $\alpha K^2 J(J+1)$ is added to Eq. (3). A correction of this form is to be expected theoretically. Eq. (3) then becomes

$$F(J, K)=(B+\alpha K^2)J(J+1) +\beta BK^2+DJ^2(J+1)^2. \quad (14)$$

When K varies from 0 to J, there is now a slight difference in frequency between the different K components of an observed line, although in practice these differences have been too small to resolve. Since the corrections are small, each observed line will correspond to the maximum intensity of the resultant of the different components. In order to determine the position of maximum intensity for this resultant, the intensity-frequency curve of each component was assumed to have a simple triangular form, whose base was made approximately twice the half-intensity breadth of the line, in such a way that the curves would overlap each other. The position of maximum intensity was then obtained by summing the individual intensities due to the different components, and should correspond to the frequency of the measured line in the Raman spectrum. Then the double difference for $\Delta J=2$ is

$$\Delta_2 F_{Rm}(J) =2(2J+1)[B''+2D''(J^2+J+1)+\alpha''\overline{K_2^2}], \quad (15)$$

and the difference between consecutive levels for $\Delta J=1$ is

$$\Delta_1 F_{Rm}(J) =2(J+1)[B''+2D''(J+1)^2+\alpha''\overline{K_1^2}], \quad (16)$$

where the bars denote averages. Values of $\overline{K_1^2}$ and of $\overline{K_2^2}$ obtained according to the procedure outlined above are given in Table I.

TABLE I. *Values of* $\overline{K_1^2}$ *and* $\overline{K_2^2}$.

J	$\overline{K_1^2}(\Delta J=1)$	$\overline{K_2^2}(\Delta J=2)$	J	$\overline{K_1^2}(\Delta J=1)$	$\overline{K_2^2}(\Delta J=2)$
0	0	0	5	16.9	3.4
1	1.4	0.2	6	24.0	7.0
2	3.2	0.4	7	33.0	8.0
3	6.2	0.6	8	44.0	10.0
4	10.9	1.3	9	57.5	11.0

If these values of $\overline{K_1^2}$ and $\overline{K_2^2}$ are plotted against J^2, it is found that the $\overline{K^2}$'s are approximately proportional to J^2, although there are some irregularities in the plot on account of doubling of the quantum weights of those levels for which K is a multiple of three (including 0). If we put $\overline{K_1^2}=cJ^2$ for $\Delta J=1$ and $\overline{K_2^2}=dJ^2$ for $\Delta J=2$, where c and d are constants of proportionality, the values of the constants are found to be approximately $c=0.69$ and $d=0.14$. Then the equations for the Raman shifts become

$$\Delta_2 F_{Rm}(J)=2(2J+1) \times[B''+2D''(J^2+J+1)+0.14\alpha''J^2] \quad (17)$$

and

$$\Delta_1 F_{Rm}(J)=2(J+1) \times[B''+2D''(J+1)^2+0.69\alpha''J^2]. \quad (18)$$

The values of c and d being known, α'' may be calculated from the difference between the *observed* $\Delta_1 F_{Rm}(J)$ Raman shifts, supposed to correspond to Eq. (18), and certain pseudo values of $\Delta_1 F_{Rm}(J)$ based on the observed $\Delta_2 F_{Rm}(J)$'s and calculated as if they were related to the latter as true $\Delta_1 F_K(J)$'s would be related to true $\Delta_2 F_K(J)$'s (cf. Eqs. (4), (5)). This difference is $2(c-d)\alpha''J^2(J+1)$. The best fit of the observed differences with this formula is obtained for $\alpha''=0.00154$. The probable error in this figure is, of course, relatively large. It should be men-

tioned especially that the observed differences do not fit the predicted form $CJ^2(J+1)$ very well.

By comparing Eq. (17) with the observed values of $\Delta_2F_{Rm}(J)$ from the Raman spectrum, taking $B''=9.92$, since B'' is evidently practically the same as B_0, D'' is found to be -0.00061. Thus in Eqs. (14)–(18) we have, for the normal state of ammonia, $B''=9.92$, $\alpha''=0.00154$, $D''=-0.00061$. Using Eqs. (4) and (14), we get

$$\Delta_2F_K''(J)=2(2J+1)\times[9.92-0.00123(J^2+J+1)+0.00154K^2]. \quad (19)$$

For parallel-type bands in the infrared spectrum (cf. Eq. (10)) the Eqs. (17) and (19) are replaced by

$$\Delta_2F_{Pa}''(J)=2(2J+1)\times[9.92-0.00123(J^2+J+1)+0.00154bJ^2], \quad (20)$$

where bJ^2 has been put in place of $\overline{K^2}$, b being similar to d of $\Delta_2F_{Rm}(J)$. On comparing the values calculated from Eq. (20) after omitting the last term in the bracket with those obtained from observed values of Barnes[15] in the pure rotation band of ammonia, the differences should be equal to $0.00308bJ^2(2J+1)$. Using Barnes' data, the value of b is found to be 0.45 and Eq. (20) becomes of the form

$$\Delta_2F_{Pa}''(J)=19.838+39.674J-0.00596J^2-0.00212J^3. \quad (21)$$

The value of b could also have been calculated from the intensity distribution of the K components in the lines of a parallel-type band, but this was not done here.

From Eqs. (19) and (21), double differences $\Delta_2F''(J)$ have been calculated for use in comparison with experimental data below. In the second and fourth columns, values of $\Delta_2F_K''(J)$ are given for $K=0$ and $K=J$; in the third column for a mean K^2 value corresponding to $\Delta_2F_{Pa}''(J)$.

For the perpendicular type band, the J double difference in wave numbers, with constant K, should be given by Eq. (19). If J is constant, the K double difference should be

$$\Delta_2F_J''(K)=\pm4\beta'B+4K[\beta B+0.00154J(J+1)]. \quad (22)$$

In analyzing the photographic bands of ammonia according to the combination principle

TABLE II.

J	$K=0$	$\overline{K^2}=bJ^2$	$K=J$
1	59.50 cm^{-1}	59.50 cm^{-1}	59.51 cm^{-1}
2	99.12	99.15	99.18
3	138.66	138.74	138.84
4	178.10	178.30	178.54
5	217.40	217.78	218.25
6	256.55	257.20	258.00
7	295.50	296.52	297.77
8	334.23	335.81	337.58
9	372.72	374.85	377.46
10	410.90	413.81	417.38
11	448.80	452.67	457.39

method, it was attempted to select pairs of lines with wave number differences about equal to the known double differences $\Delta_2F_K''(J)$ or $\Delta_2F_{Pa}''(J)$ of the normal state and to arrange these into series, but this procedure gave only a few good series.

Then simple types of parallel and perpendicular bands predicted by assuming the rotational constants of the upper state levels not much different from those of the normal state were compared with the observed bands. Only the 6470A band seems to follow at all the general structure of the simple perpendicular type, but detailed consideration[4] did not confirm this structure. Then a parallel-type band with different B and β in the upper and lower states was tried[17] but the general appearance of the observed bands is far different from this type.

It seems very likely[9] that the difficulties in analyzing the bands may be explained as follows. As several authors have pointed out, the frequencies of the main photographic bands are approximately multiples of the frequency of the band at 3.0μ. For example, Adel[17] gives the equation $\nu_n=3389n-50n^2-2n^3$. But if the 3.0μ band is composed of *two* overlapping fundamental bands (cf. Section II), then the bands here under consideration may involve not only harmonics of both these fundamentals, but also a variety of combination bands. Furthermore, it is to be noted that harmonics of a perpendicular-type fundamental include in general a set of several parallel and perpendicular-type bands. Thus each of the "bands" here considered may be composed really of a number of superimposed bands, some of parallel and some of perpendicular type.

[17] Cf. A. Adel, Phys. Rev. **48**, 103 (1935).

For example (cf. (1) and selection rules), the 10,230A band should according to this explanation consist of three perpendicular and three parallel bands, the λ7920 band of four parallel and five perpendicular bands, and the λ6470 band of five parallel and seven perpendicular bands. Besides, an additional doubling may appear in each band due to the tunnel effect (α, β doubling). Only some such degree of complexity as this seems to offer a reasonable explanation of the richness and apparent irregularity of the lines in each band, and the difficulty in carrying out an analysis with the help of the combination principle.

IV. Experimental Work

The five absorption bands in the long wavelength photographic region of gaseous ammonia were photographed with a 21-foot grating (Paschen mounting), the dispersion being about 2.6A per mm in the first order. A glass absorption tube, 32 mm in diameter and 4.3 m long, with plane glass windows fused on the two ends, and a 500-watt projection lamp as a source of light, were used. Eastman spectroscopic plates of the following types were used throughout the work: types *C* and *F* for 6470A and 5490A, type *R* for 7920A, types *P* and *Q* for 8800A and type *Q* for 10,230A. The spectrograms were made first with the absorption path equal to the length of the tube. Then by reflecting light through the tube with a right-angled prism, the path was increased to double the length of the tube. The time of exposure varied greatly with the type of plate and the region of the spectrum, from one-hour exposures for the second-order spectrum of the 6470A band to 85-hour exposures for the first-order spectrum of the 10,230A band. The plates were hypersensitized in an ice-cooled bath of 4 percent ammonia solution and dried before an electric fan after being washed in alcohol. The tube was filled with ammonia gas from a small tank containing pure liquid ammonia, very kindly supplied by Professor W. C. Johnson of the Department of Chemistry. Experiments were also made at the temperature of solid CO_2 (−77°C), with which the absorption tube was packed during exposure, the ammonia pressure indicated being 14 mm. Only the strong lines of the 10,230A band then appeared on the plates, while those of the other bands were too weak to be photographed.

The ammonia absorption lines were compared with standard lines of the second and third order spectra from a 220-volt iron arc. The wave numbers in vacuum were calculated in the usual way, except that those of the lines beyond 10,000A were computed in the way indicated by Babcock[18] by extending the use of Kayser's *Tabelle der Schwingungszahlen*, in the neighborhood of 10,000A. From the best spectrograms the following numbers of lines were measured: 714 lines in 10,230A, 304 lines in 7920A and 162 lines in 6470A. Absorption lines (only a few in number) due to the water vapor band, 9420A, were identified and eliminated from the 10,230A band.

Complete tables of lines in wave numbers are given in the Appendix.

V. Pressure Broadening of the Ammonia Band Lines

When Badger[3] employed pressures of one to five atmospheres in photographing the ammonia 6470A band, he noticed that increasing the pressure of the gas broadened the absorption lines. All the ammonia lines in the photographic region show the same effect of broadening when the pressure is varied, and all appear to show the same degree of broadening at atmospheric pressure. In order to get the best resolution of the lines, it is important to know their width under various pressures.

The accompanying spectrograms of the 7920A band (cf. Fig. 1), of which only the central portions are reproduced, show the variation of the width of the absorption lines with pressure. The lines at 750 mm pressure are about 0.55A broad and at 95 mm they become fairly sharp. They become still sharper at still lower pressures. This is shown in the 10,230A band, where at a pressure of 14 mm when the temperature of the gas is −77°C, the line widths become extremely small. The widths of the lines depend much more upon pressure of the gas than upon path length. The different absorbing lengths under the same pressure show apparently the same degree of broadening.

[18] H. D. Babcock, Phys. Rev. **46**, 382 (1934).

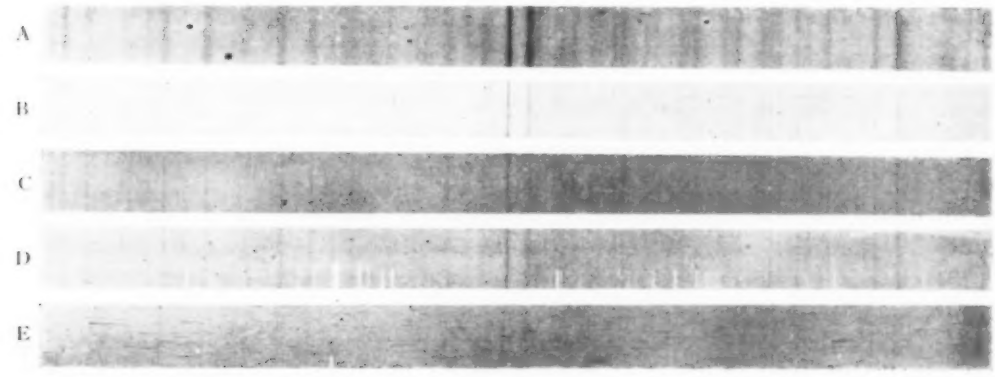

FIG. 1. 7920A band.

	A	*B*	*C*	*D*	*E*
Pressure (mm)	750	190	140	140+610 (air)	95
Absorption length (m)	4.3	8.6	8.6	8.6	4.3

The influence of a foreign gas (air) on the widths of the lines is shown in spectrogram (*D*), Fig. 1, for which air was admitted into the absorption tube containing ammonia at a pressure of 140 mm, making a total pressure of one atmosphere. The spectrogram of ammonia gas alone at 140 mm is also shown in (*C*), Fig. 1. In these two cases, the numbers of absorbing ammonia molecules are the same. Though there is a slight broadening effect of air on the absorption lines, this effect is very much smaller than that of the absorbing ammonia molecules on one another. The widths of the lines at 140 mm pressure plus 610 mm of air are shown nearly equal to those of the lines of ammonia alone at 190 mm.

In comparing the spectrogram of the ammonia lines at 750 mm pressure with that of the HCN absorption band 1.04μ at 630 mm and that of the HCl 1.20μ band, both obtained by Herzberg and Spinks,[19] the widths of the ammonia lines are smaller than those of the HCN lines but are about the same as those of the HCl lines. The widths of the HCN lines are about 1.4 times those of the ammonia lines at atmospheric pressure.

In the infrared spectrum of HCl, Lasareff[20] and Grasse[21] report that broadening of the absorption lines of the 3.46μ band caused by the presence of different gases is nearly the same as that caused by the absorbing gas (HCl) itself. They explained the phenomenon on the classical theory of Lorentz collision broadening. In ammonia, as well as in HCN, the pressure broadening of the lines cannot be attributed to this cause, but instead to intermolecular forces. It seems that the effect observed in ammonia may be explained in part by the intermolecular Stark effect due to the dipole moments of the molecules. Such an effect would be proportional to the dipole moment and to the number of molecules per cc.[22] The dipole moment of HCN is greater than those of NH_3 and HCl, the moments being 2.5–2.6, 1.44, and 1.03×10^{-18} e.s.u., respectively.[23]

An attempt has also been made to look for a dependence of the widths of the lines upon the quantum number J, but it appears that the effect, if any, must be comparatively small.

VI. Frequency Data and Analysis

10,230A and 8800A Bands

These two bands have been investigated by Lueg and Hedfeld,[1] but only a number of equal intervals in these bands were indicated by them. The 10,230A band appears in the present work to consist, as has not been noted previously, of

[19] G. Herzberg and J. W. T. Spinks, Proc. Roy. Soc. **A147**, 434 (1934); Zeits. f. Physik **89**, 477 (1934).
[20] W. Lasareff, Zeits. f. Physik **64**, 598 (1930).
[21] W. Grasse, Zeits. f. Physik **89**, 261 (1934).
[22] V. Weisskopf, Physik. Zeits. **34**, 1 (1933). See also H. Margenau, Phys. Rev. **48**, 755 (1935).
[23] Trans. Faraday Soc. **30**, following p. 904 (1934).

TABLE III. *Band:* $\nu_0 = 9760.38sb$.

POSSIBLE J	POSSIBLE P BRANCH	POSSIBLE R BRANCH	POSSIBLE $\Delta_2F''(J)$	POSSIBLE $\Delta_2F'(J)$
0		9779.85*s*		
		9780.39*s*		
1	9740.31*s*	9799.54*s*	59.58	59.23
	9741.22*sb*	9800.86*m*	59.13	59.64
2	9720.27*m*	9820.09*s*	99.16	99.82
	9721.26*s*	9820.92*s*	99.08	99.66
3	9700.38*m*	9840.13*s*	138.69	139.75
	9701.78*m*	9840.89*w*	138.59	139.11
4	9681.40*s*	9860.43*w*	178.80*	179.03
	9682.33*m*	9861.30*m*	178.67*	178.97
5	9661.33*sb*	9880.57*m*	217.67	219.24*
	9662.22*sb*	9881.95*w*	217.59	219.73*
6	9642.76*s*	9900.70*wb*	256.73	257.94
	9643.71*m*	9901.64*sb*	256.97	257.93*
7	9623.84*m*		295.90	
	9624.98*s*		295.70*	
8	9604.80*m*			
	9605.89*s*			

TABLE IV. *Band:* $\nu_0 = 10{,}099.74mb$.

POSSIBLE J	POSSIBLE P BRANCH	POSSIBLE R BRANCH	POSSIBLE $\Delta_2F''(J)$	POSSIBLE $\Delta_2F'(J)$
0		10,119.47*sb*		
1	10,079.84*mb*	10,139.31*sb*	59.71	59.47
2	10,059.76*mb*	10,159.17*w*	99.62*	99.41
3	10,039.69*s*	10,179.01*s*	139.17*	139.32*
4	10,020.00*s*	10,198.67*s*	178.92	178.67
5	10,000.09*s*	10,218.45*mb*	218.43*	218.36
6	9,980.24*w*			

TABLE V. *Band:* $\nu_0 = 10{,}104.86s$.

POSSIBLE J	POSSIBLE P BRANCH	POSSIBLE R BRANCH	POSSIBLE $\Delta_2F''(J)$	POSSIBLE $\Delta_2F'(J)$
0		10,125.31*s*		
1	10,084.77*m*	10,145.86*s*	60.49*	61.09
2	64.82*mb*	65.71*s*	102.17	100.89*
3	43.69*s*	85.98*sb*	142.49	142.29
4	23.22*m*	10,205.89*sb*	183.37	182.67*
5	02.61*sb*	26.37*m*	224.70	223.76*
6	9,981.19*s*	47.42*s*	266.52	266.23
7	59.85*s*		307.80	
8	39.62*s*			

two separate bands which can be distinguished by their intensity in absorption and which slightly overlap at 10,150A. The one of the longer wave-length is the stronger and its center is approximately at 10,230A. This stronger band has also been observed by Unger[24] using infrared technique. The center of the weaker band appears to be at 9900A.

On the high frequency side in the stronger band (10,230A), there are several groups of strong lines with intervals of about 10cm^{-1}, half the spacing characteristic of parallel-type infrared bands, suggesting a similarity to perpendicular type bands such as the 1.97μ band, studied by Stinchcomb and Barker, which also show 10 cm^{-1} spacings.

The strongest 200 lines, approximately, were taken from the 10,230A band and all pairs of lines with wave-number differences about equal to the double differences $\Delta_2F_{Pa}''(J)$ for $J=1$, 2, 3 and 4 were sorted out. For instance, taking the double difference for $J=3$ as about 138.7 cm^{-1} (cf. Table II), about ten pairs of lines giving $\Delta\nu$'s agreeing with this value to within ± 0.05 cm^{-1} were found. The most probable number[25] of accidental interval coincidences caused by random distribution of spectrum lines over 420 cm^{-1} (the approximate width of the band) is about 6, thus indicating that some but not nearly all of the $\Delta\nu$'s may represent real $\Delta_2F_{Pa}''(J)$'s. One series of close pairs of lines given in Table III gives $\Delta\nu$'s which agree very well with $\Delta_2F''(J)$'s given in Table II. The lines belonging to the series form arrangements like P and R branches of a parallel band (cf. Fig. 2, where the most likely J'' values are shown, preceded by a minus sign in the case of the P branch lines). The strong line in the center of the series corresponds to the Q branch (ν_0). No other series of lines giving $\Delta\nu$'s corresponding to Δ_2F'''s were found in the 10,230A band.

The structure of the 9900A band (cf. Fig. 3) is simpler than that of the 10,230A band. Two series of lines, given in Tables IV and V, were found in this band, one agreeing quite well with predicted $\Delta_2F''(J)$ values given in Table II, the other not agreeing with the predicted values though it forms a good series by itself.

The doublet series with $\nu_0=9760.38$ in the 10,230A band and the series with $\nu_0=10{,}099.74$ in the 9900A band presumably correspond to two of the three predicted parallel bands expected near 10,000A (cf. end of Section III). The doubling in the series with $\nu_0=9760.38$ is most likely the α, β (tunnel effect) doubling. The explanation of the band with $\nu_0=10{,}104.86$ is not obvious; it might involve an excited lower state, but seems too strong for this; besides, no temperature-sensitiveness was observed. Perhaps the arrangement in a series is spurious.

[24] H. J. Unger, Phys. Rev. **43**, 123 (1933).
[25] G. R. Harrison, Rev. Sci. Inst. **4**, 581 (1933).

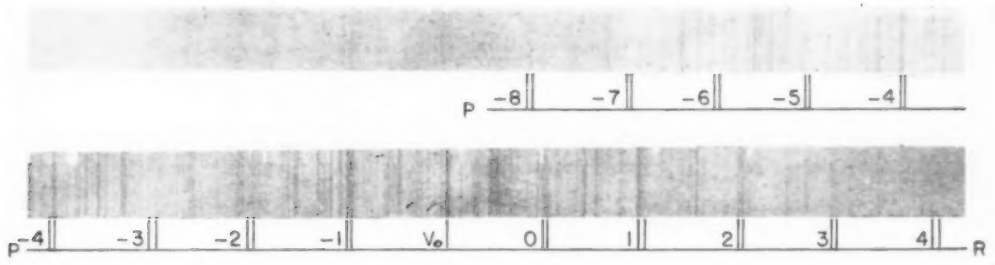

FIG. 2. 10,230A band. (ν_0 should be ν_0.)

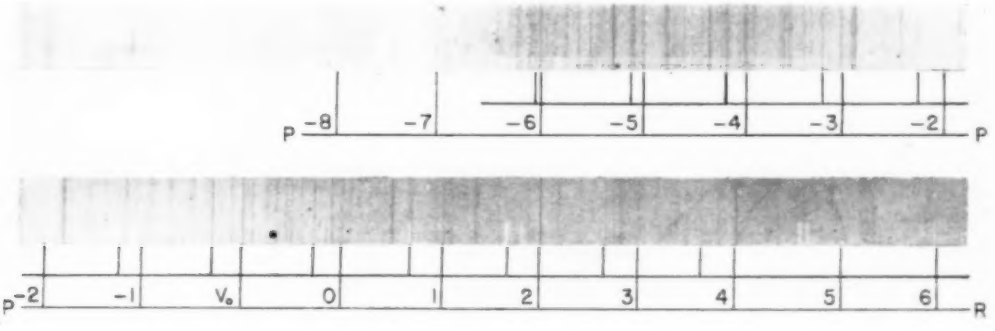

FIG. 3. 9900A band. (ν_0 should be ν_0.)

The 8800A band was also photographed but because of the rapid falling off of sensitiveness of the plate in this region, it was not used for measurement.

In the preceding tables, the small letters following the wave number of each line denote its intensity, *viz.*, *ss*=very strong, *s*=strong, *m*=medium, *w*=weak and *b*=broad. The lines in series are arranged, and J values assigned, so as to give double differences as close as possible to the $\Delta_2F_{Pa}''(J)$ values from Eq. (21), but the J numbering might still be shifted in some cases. The broad lines are usually due to blending of two or more lines and therefore their measurements are less reliable. When differences of observed Δ_2F"s from calculated values can be explained as due to blending with other lines, or to inaccuracy of measurement due to weakness of a line, they are marked with an asterisk.

7920A BAND

Badger and Mecke[2] found 54 lines in this band and arranged them into several series with a mean interval between adjacent lines equal to 19.88 cm^{-1}. They assumed the selection rule $\Delta K=\pm1$, corresponding to the case of a perpendicular type band. Thus they took the spacing between the two strong lines in the center of the band with several lines in their neighborhood as the mean value of the coefficient of K^2 in Eq. (2), so that the moment of inertia, I_C, could apparently (but cf. Ref. 12) be evaluated.

In the present work an attempt was made to analyze the band rigorously by the combination principle method, but the structure does not fit the form either of a perpendicular type band or of a parallel type band. Two series, given in

TABLE VI. *Band:* $\nu_0=12{,}609.24s$.

POSSIBLE J	POSSIBLE P BRANCH	POSSIBLE R BRANCH	POSSIBLE $\Delta_2F''(J)$	POSSIBLE $\Delta_2F'(J)$
0		12,629.64*s*		
1	12,589.71*w*	49.33*sb*	59.73	59.62
2	69.91*s*	69.96*s*	99.07	100.05
3	50.26*m*	89.42*s*	138.73*	139.16
4	31.23*w*	12,708.95*s*	178.23	177.72
5	11.19*m*	29.12*m*	217.31*	217.93
6	12,491.64*w*	48.68*s*	257.32	257.04
7	71.80*w*	68.18*m*		296.38

TABLE VII. *Band:* $\nu_0 = 12{,}619.75s$.

POSSIBLE J	POSSIBLE P BRANCH	POSSIBLE R BRANCH	POSSIBLE $\Delta_2F''(J)$	POSSIBLE $\Delta_2F'(J)$
0		12,639.50*s*		
1	12,599.32*m*	58.65*s*	59.60	59.33
2	79.90*m*	79.19*sb*	99.20	99.29
3	59.45*sb*	98.37*m*	138.76	138.92
4	40.43*m*	12,718.86*s*	178.39	178.43
5	19.98*w*	37.62*s*	217.83	217.64
6	01.03*w*	56.29*s*	256.37	255.26
7	12,481.25*w*	75.71*m*		294.46

Tables VI and VII, were found, however. The $\Delta\nu$'s found in the two series agree with the double differences of the normal state as calculated from Eq. (21) (see Table II). The interval between the zero-lines of these two series is about 10 cm^{-1}.

It seems likely that the two series found in the 7920A band represent two of the four parallel bands expected in this region (cf. end of Section III).

6470A AND 5490A BANDS

Badger[3] has investigated these two bands and found 57 lines in the 6470A band, but he indicated only that the mean value of the spacing of the lines in series was 19.74 cm^{-1}. The structure of this band looks more like a perpendicular than a parallel type band. A group of strong lines which are nearly equally spaced in the center of the band suggests the Q branch of a perpendicular band, while there are also other groups of lines resembling P and R branches. However, on detailed consideration[4] it was not found possible to reconcile the structure with that expected for either a perpendicular or a parallel band. This is not surprising in view of the considerations given at the end of Section III.

The writer wishes to express his appreciation to Professor R. S. Mulliken for the proposal of the problem and for constant inspiration and valuable advice throughout the investigation, also to Professors D. M. Dennison and E. F. Barker for helpful correspondence. He also wishes to thank Professor G. S. Monk for valuable suggestions during the work and Professor W. C. Johnson for the pure liquid ammonia.

APPENDIX

10,230.1 and 9900.1 bands

Characteristics of the line are denoted as follows: *ss* = very strong, *s* = strong, *m* = medium, *w* = weak, and *b* = broad.

9503.74*w*	14.98*s*	84.58*w*	60.76*sb*	11.52*sb*	9868.58*w*	42.20*m*	12.56*sb*	82.90*mb*	56.10*w*
06.67*w*	16.09*w*	9685.63*s*	61.71*m*	13.03*s*	69.36*w*	42.66*m*	10013.75*s*	83.55*s*	57.02*m*
08.29*w*	17.49*w*	86.22*s*	62.87*w*	9814.03*mb*	70.18*s*	43.46*mb*	14.66*sb*	84.77*m*	10158.32*w*
10.57*w*	9618.88*w*	87.57*s*	63.39*s*	15.30*sb*	71.24*w*	9943.99*w*	16.29*s*	85.67*w*	59.17*w*
14.17*m*	20.56*w*	88.89*s*	9763.94*w*	16.97*s*	72.36*s*	44.66*m*	17.20*w*	10086.10*mb*	60.31*m*
9518.02*m*	21.34*m*	90.04*s*	64.51*s*	17.70*s*	9873.28*s*	46.06*s*	17.83*w*	86.76*m*	61.64*w*
22.94*m*	22.66*m*	9690.24*s*	65.46*m*	18.03*s*	73.95*s*	46.49*w*	10018.71*m*	87.86*w*	62.32*w*
28.60*m*	23.84*m*	90.84*w*	65.83*m*	9818.37*w*	76.01*s*	46.95*w*	19.45*m*	89.62*s*	10163.09*s*
33.80*s*	9624.98*s*	91.33*m*	66.37*s*	19.24*sb*	76.91*wb*	9947.47*w*	20.00*s*	90.18*s*	64.11*w*
34.26*w*	25.93*w*	91.80*sb*	9767.04*s*	20.09*s*	77.25*w*	48.94*w*	20.84*m*	10090.83*w*	64.57*w*
9534.66*m*	27.69*s*	93.20*m*	67.73*w*	20.42*w*	9877.83*w*	49.33*w*	21.72*w*	91.46*m*	65.71*s*
35.09*w*	28.94*m*	9694.11*m*	69.18*s*	20.92*s*	78.27*m*	49.95*w*	10022.55*m*	92.74*mb*	67.16*sb*
35.52*w*	29.38*m*	94.84*s*	69.91*m*	9821.53*s*	79.09*w*	50.50*m*	23.22*m*	94.46*mb*	10168.09*mb*
36.29*w*	9630.12*w*	95.43*s*	70.70*s*	22.41*sb*	79.76*m*	9950.92*s*	23.75*s*	95.07*s*	69.30*m*
37.06*m*	30.92*w*	96.40*m*	9771.35*s*	23.15*w*	80.57*m*	51.66*s*	24.23*m*	10096.57*mb*	69.84*w*
9538.40*m*	31.97*s*	97.35*m*	72.12*s*	23.83*s*	9881.95*w*	52.15*s*	25.48*mb*	97.32*mb*	70.40*w*
39.20*w*	32.54*s*	9698.32*m*	72.67*m*	27.54*m*	82.60*w*	53.12*m*	10025.91*w*	98.14*m*	71.34*w*
40.65*s*	33.10*w*	700.38*m*	73.38*s*	9828.19*w*	83.44*w*	53.94*w*	27.11*w*	98.74*s*	10172.17*w*
42.84*w*	9635.12*m*	01.78*m*	73.93*m*	28.86*m*	85.04*w*	9954.49*w*	27.58*w*	99.74*mb*	73.04*w*
44.93*w*	35.77*m*	02.48*m*	9774.70*m*	29.31*m*	85.76*w*	55.01*w*	28.61*w*	10100.74*s*	73.61*m*
9546.80*s*	36.40*mb*	03.22*m*	75.22*m*	29.91*sb*	9886.46*w*	55.83*m*	29.65*w*	02.56*s*	74.59*w*
47.45*m*	37.92*w*	9703.63*s*	75.87*w*	30.68*s*	87.77*w*	56.76*w*	10030.88*w*	03.27*s*	75.49*w*
52.28*s*	38.53*m*	04.59*s*	76.79*m*	9831.32*w*	88.64*w*	58.04*s*	31.73*m*	03.91*w*	10176.42*m*
52.71*w*	9639.57*s*	05.97*s*	77.56*mb*	31.91*m*	89.23*m*	9959.13*s*	32.65*s*	04.86*s*	79.01*s*
54.23*w*	40.14*s*	07.19*s*	9778.85*s*	32.39*m*	89.89*w*	59.85*s*	33.23*s*	10105.61*wb*	80.72*s*
9554.80*w*	41.17*m*	08.39*s*	79.08*s*	33.40*w*	9890.71*w*	61.08*s*	34.27*m*	06.90*s*	82.11*sb*
55.74*m*	41.92*s*	9709.15*s*	79.85*s*	33.82*m*	92.44*m*	61.81*s*	10035.14*m*	09.50*m*	82.79*w*
56.66*w*	42.76*s*	10.68*s*	80.39*s*	9834.40*w*	93.08*w*	63.74*s*	36.06*s*	10.18*m*	10184.46*w*
57.56*s*	0643.71*m*	12.31*m*	81.16*s*	34.63*w*	93.56*s*	9965.67*w*	36.87*m*	11.76*sb*	85.98*sb*
58.41*w*	44.60*mb*	13.92*s*	9781.89*w*	35.20*w*	94.42*w*	66.71*w*	37.44*sb*	10112.33*w*	89.02*w*
9562.48*s*	45.09*mb*	16.78*m*	82.61*m*	35.77*m*	9895.48*w*	68.72*w*	38.63*wb*	13.11*w*	89.84*w*
63.65*s*	45.94*mb*	9718.26*s*	83.09*s*	36.32*m*	96.84*mb*	69.94*w*	10039.69*s*	13.74*s*	90.77*w*
64.68*w*	46.61*mb*	19.23*s*	83.56*m*	9837.22*w*	97.73*s*	71.01*w*	40.55*m*	14.76*m*	10192.03*w*
65.33*m*	9649.87*s*	20.27*m*	84.19*w*	37.74*s*	98.57*w*	9972.33*sb*	41.21*wb*	16.93*s*	93.51*mb*
67.86*s*	50.98*s*	21.26*s*	9784.79*w*	39.13*s*	99.86*wb*	73.08*s*	42.56*wb*	10117.79*s*	93.95*w*
9569.54*s*	52.33*sb*	23.89*m*	85.29*w*	40.13*s*	9900.70*wb*	73.66*w*	43.69*s*	18.57*m*	95.92*sb*
70.96*s*	54.11*w*	9724.79*s*	85.44*w*	40.89*w*	01.64*sb*	74.10*w*	10044.85*w*	19.47*sb*	97.63*s*
73.23*m*	54.03*sb*	27.36*s*	86.38*w*	9841.58*w*	02.99*mb*	75.13*s*	45.88*s*	20.35*w*	10198.67*s*
74.74*s*	9654.34*sb*	28.40*s*	87.01*m*	42.18*w*	03.76*w*	9975.86*w*	46.58*s*	20.86*m*	202.35*s*
75.23*s*	55.80*w*	29.66*s*	9787.92*s*	42.86*s*	04.44*w*	76.51*m*	47.63*wb*	10121.87*m*	05.89*sb*
9576.05*w*	56.60*w*	30.22*s*	88.60*s*	43.45*s*	9905.36*w*	77.14*m*	48.59*wb*	22.98*s*	07.20*w*
76.39*m*	57.43*s*	9734.45*s*	89.96*s*	44.11*w*	06.46*s*	79.05*s*	10049.52*wb*	23.53*w*	09.14*m*
77.67*w*	59.07*m*	35.59*m*	90.75*s*	9844.78*m*	08.70*w*	79.60*w*	50.61*mb*	24.00*w*	10212.64*s*
78.54*m*	9660.00*w*	36.00*m*	91.17*m*	45.64*w*	09.44*w*	9980.24*w*	52.24*s*	24.55*m*	13.42*w*
79.50*w*	61.33*sb*	37.07*s*	9791.69*w*	46.41*m*	09.94*w*	81.19*s*	54.04*w*	10125.31*s*	14.63*s*

10,230A and 9900A bands—Continued

9580.60*s*	62.22*sb*	38.78*mb*	92.11*w*	47.43*s*	9910.38*m*	82.76*wb*	54.71*w*	26.18*s*	15.43*w*
82.43*s*	64.43*w*	9740.31*s*	93.24*s*	49.12*s*	11.23*mb*	83.73*w*	10055.29*w*	26.82*s*	17.19*wb*
83.34*s*	65.12*w*	40.72*sb*	93.64*m*	9849.40*w*	12.60*m*	84.26*w*	56.10*s*	27.70*w*	10218.45*mb*
86.29*s*	9665.92*s*	41.22*sb*	94.86*s*	50.11*s*	13.47*m*	9984.73*w*	57.05*w*	28.38*m*	19.84*sb*
87.66*s*	66.29*s*	42.15*w*	9795.38*w*	51.03*w*	14.50*s*	85.94*w*	57.29*w*	10129.27*m*	20.35*w*
9587.99*m*	67.15*m*	42.52*w*	95.86*m*	52.13*w*	9915.53*w*	86.63*s*	58.38*w*	30.70*mb*	21.39*w*
89.42*s*	68.52*w*	9743.32*m*	96.55*s*	52.47*w*	17.05*s*	87.96*w*	10058.83*w*	32.43*m*	22.63*mb*
91.12*w*	69.28*m*	43.83*m*	97.00*w*	9853.63*mb*	18.97*s*	89.26*s*	59.76*mb*	35.39*sb*	10225.46*wb*
91.64*s*	9670.11*s*	44.81*w*	97.30*w*	54.16*w*	20.48*w*	9990.32*w*	60.35*w*	38.72*sb*	26.37*m*
93.77*s*	71.58*w*	45.39*m*	9797.61*w*	55.28*m*	22.03*m*	91.64*s*	61.66*w*	10139.31*sb*	27.63*m*
9594.84*w*	72.14*w*	46.30*w*	98.11*w*	56.36*m*	9923.61*m*	92.72*m*	63.21*w*	41.24*w*	28.58*w*
95.40*w*	72.98*s*	9747.80*s*	98.92*w*	57.44*w*	25.41*s*	93.53*m*	10064.82*mb*	41.95*w*	29.98*w*
96.10*m*	73.58*s*	48.57*s*	99.54*s*	9857.93*s*	26.17*w*	94.67*m*	65.95*w*	42.65*w*	10230.53*s*
97.64*m*	9674.16*s*	49.50*m*	9800.12*m*	58.38*s*	26.83*w*	9995.51*m*	67.13*s*	43.17*w*	31.91*w*
601.27*w*	74.98*w*	50.10*w*	9800.86*m*	59.22*w*	29.62*s*	96.34*s*	67.98*m*	10143.96*s*	32.50*s*
9603.70*s*	75.76*s*	50.70*s*	01.39*w*	59.53*w*	9930.93*s*	98.19*w*	68.60*s*	44.52*s*	33.57*s*
04.80*m*	76.36*s*	9750.95*w*	01.99*w*	60.43*w*	32.15*w*	98.99*m*	10069.36*m*	45.86*s*	34.11*w*
05.33*w*	76.65*s*	52.04*m*	02.96*w*	9861.30*m*	33.06*w*	99.63*m*	70.01*m*	46.64*m*	10234.60*w*
05.89*s*	9678.39*s*	52.66*m*	03.45*w*	61.43*w*	34.77*m*	10000.09*s*	71.59*m*	47.35*m*	47.42*s*
06.98*m*	78.75*s*	53.46*s*	9804.19*m*	62.19*w*	36.61*sb*	00.61*s*	73.45*sb*	10147.71*s*	48.11*w*
9608.38*m*	79.64*s*	54.39*s*	05.19*m*	62.84*w*	9937.97*sb*	02.61*sb*	74.75*s*	48.48*w*	53.14*w*
08.95*s*	80.13*w*	9755.53*s*	06.59*s*	63.33*w*	38.47*w*	07.06*s*	10077.02*mb*	49.02*m*	
09.80*w*	80.78*s*	56.61*s*	07.72*s*	9863.74*s*	39.09*w*	07.62*s*	78.47*mb*	50.23*w*	
11.57*s*	9681.40*s*	58.19*mb*	08.50*w*	64.19*w*	39.62*s*	10008.89*s*	79.84*mb*	51.70*w*	
12.32*w*	82.33*m*	59.24*s*	9808.66*s*	65.04*w*	40.47*s*	09.52*sb*	80.95*s*	10152.59*sb*	
9613.13*w*	82.95*m*	59.80*s*	09.83*sb*	66.10*s*	9941.05*s*	10.35*s*	81.44*s*	54.12*w*	
13.52*m*	83.91*m*	9760.38*sb*	10.56*s*	67.06*mb*	41.51*w*	11.13*s*	10082.30*w*	55.23*m*	

7920A band

12454.35*w*	11.19*m*	49.61*w*	83.42*sb*	12.27*m*	12637.33*w*	65.07*w*	99.52*m*	25.91*w*	64.30*s*
64.55*w*	11.82*m*	50.26*m*	85.58*w*	12612.81*m*	37.98*w*	66.32*sb*	700.86*m*	26.43*s*	12765.55*m*
65.93*w*	12.99*m*	51.89*mb*	12587.24*w*	13.19*w*	38.99*s*	67.85*m*	01.66*m*	12727.76*s*	66.22*m*
67.20*w*	14.64*m*	12552.92*w*	88.42*w*	13.73*s*	39.50*s*	68.74*w*	12702.39*m*	29.12*m*	68.18*m*
68.24*w*	12815.88*m*	54.49*s*	88.81*sb*	14.54*m*	40.76*m*	12669.96*s*	03.22*w*	30.48*m*	68.90*m*
12469.77*mb*	17.11*s*	54.84*s*	89.71*w*	14.94*m*	12641.48*m*	70.84*m*	04.04*w*	31.13*s*	71.30*m*
71.80*w*	18.48*m*	56.28*sb*	91.25*w*	12616.06*m*	42.15*m*	71.14*m*	04.61*w*	31.48*s*	12772.78*m*
76.71*w*	19.98*w*	58.12*w*	12592.01*w*	17.23*sb*	43.61*s*	72.22*sb*	05.61*s*	12732.78*m*	75.71*m*
77.59*w*	21.71*sb*	12558.60*w*	92.80*m*	18.48*w*	44.03*m*	73.72*sb*	12706.98*w*	33.70*m*	77.80*m*
77.98*w*	12522.72*w*	59.45*sb*	94.23*m*	19.49*w*	45.21*s*	12675.46*w*	07.92*m*	35.68*m*	80.06*w*
12479.94*w*	24.16*m*	60.75*m*	94.64*m*	19.75*s*	12646.32*w*	76.29*w*	08.57*s*	36.09*s*	81.15*w*
81.25*w*	25.46*mb*	62.18*sb*	95.98*s*	12620.72*m*	47.23*w*	77.15*sb*	08.95*s*	37.62*s*	12782.25*m*
84.41*w*	26.87*mb*	62.96*w*	12596.44*s*	21.53*m*	48.36*w*	79.19*sb*	10.22*m*	12739.15*s*	84.45*m*
84.94*w*	28.12*w*	12564.44*w*	97.61*m*	22.50*w*	49.33*sb*	81.24*m*	12710.78*m*	39.84*s*	88.06*w*
85.66*w*	12529.46*w*	66.00*m*	98.81*m*	12624.36*ss*	50.08*m*	12682.07*m*	11.57*s*	40.88*s*	89.84*w*
12490.31*w*	30.29*m*	66.81*w*	99.32*m*	25.35*w*	12651.74*mb*	82.85*s*	12.18*m*	41.82*m*	94.43*w*
91.64*w*	31.23*w*	68.11*w*	600.08*w*	12626.38*w*	53.52*w*	83.76*w*	12.67*m*	44.16*m*	12797.47*w*
92.47*w*	33.53*w*	69.60*s*	12600.58*w*	12627.73*ss*	54.29*w*	84.87*m*	13.97*s*	12744.92*m*	800.62*w*
93.72*w*	36.17*mb*	12569.91*s*	01.24*w*	12628.30*ss*	55.30*s*	85.80*m*	12714.82*s*	45.49*m*	02.20*w*
94.88*w*	12537.49*w*	73.68*w*	01.54*m*	28.66*w*	55.86*s*	12686.89*w*	15.45*m*	46.02*s*	05.30*w*
12496.12*w*	38.62*mb*	74.78*m*	02.56*s*	29.07*m*	12656.52*s*	88.32*m*	16.66*m*	46.94*s*	06.19*w*
97.87*m*	39.83*w*	75.82*w*	03.08*s*	12629.64*s*	57.23*w*	89.42*s*	17.61*s*	47.87*s*	12807.64*w*
99.21*w*	40.43*m*	76.23*w*	12604.15*m*	30.16*s*	57.54*w*	91.50*s*	18.86*s*	12748.68*s*	09.46*w*
501.03*w*	41.39*w*	12576.89*w*	05.54*m*	31.33*s*	58.20*w*	93.20*m*	12719.31*s*	50.61*s*	09.63*w*
02.25*w*	12542.20*sb*	77.48*w*	06.04*m*	32.96*s*	58.65*s*	12694.01*m*	20.33*m*	52.46*s*	21.77*w*
12503.20*w*	43.96*s*	79.42*w*	07.38*w*	33.19*s*	12659.78*m*	95.57*s*	21.10*m*	54.46*s*	
04.94*w*	44.35*s*	79.90*m*	07.96*m*	12633.89*m*	61.28*w*	95.87*s*	22.83*s*	55.36*s*	
05.65*w*	44.68*s*	80.31*m*	12609.05*w*	34.48*m*	61.96*w*	96.43*w*	23.20*s*	12756.29*s*	
06.53*m*	46.31*m*	12581.56*w*	09.24*s*	35.31*w*	62.77*s*	97.06*s*	12723.93*w*	59.87*m*	
08.01*m*	12547.36*w*	82.12*w*	10.59*m*	36.10*s*	63.65*s*	12698.37*m*	24.32*w*	60.64*m*	
12509.82*mb*	48.36*sb*	82.74*m*	11.44*w*	36.58*m*	12663.83*w*	99.02*m*	25.29*m*	63.59*m*	

6470A band

15263.8*w*	29.7*m*	65.9*m*	97.2*m*	21.6*w*	15442.8*m*	72.3*m*	03.5*w*	29.7*s*	65.5*w*
68.6*w*	31.8*m*	15367.2*w*	98.2*w*	23.4*m*	44.5*s*	73.5*w*	15506.3*s*	30.8*w*	69.3*w*
72.3*m*	36.2*m*	68.2*m*	401.5*w*	15425.1*m*	46.8*s*	74.4*m*	08.2*s*	31.7*w*	15570.4*w*
89.4*w*	15339.3*m*	69.4*w*	02.8*m*	26.2*w*	47.8*w*	15477.8*m*	10.2*s*	32.6*w*	75.4*w*
94.6*w*	41.1*w*	70.4*w*	15404.4*s*	27.6*m*	48.8*w*	78.9*m*	12.5*s*	15533.4*w*	76.1*w*
15295.9*w*	42.4*w*	72.4*w*	05.5*w*	28.6*m*	15449.9*s*	82.4*s*	14.4*m*	34.8*s*	96.0*w*
300.2*m*	47.6*w*	15376.4*s*	08.2*s*	29.4*s*	50.8*m*	85.4*m*	15515.4*w*	35.9*m*	99.3*w*
02.2*w*	49.3*w*	78.7*w*	09.1*w*	15431.5*m*	52.5*s*	88.9*s*	16.5*s*	39.0*s*	15605.5*w*
04.2*w*	15351.3*w*	80.3*s*	10.0*w*	32.4*w*	53.7*w*	15489.9*s*	17.6*m*	41.1*m*	06.2*w*
07.5*w*	53.1*s*	83.3*s*	15411.1*w*	33.8*w*	55.5*m*	91.0*w*	18.9*s*	15543.9*w*	
15310.4*w*	54.3*s*	85.6*m*	12.2*w*	34.7*w*	15457.8*m*	92.0*w*	20.0*w*	45.7*w*	
16.4*w*	55.7*w*	15386.6*w*	13.9*m*	35.9*w*	58.7*w*	93.3*s*	15522.0*w*	48.4*m*	
17.2*w*	56.5*w*	87.6*s*	15.1*m*	15437.6*w*	59.9*m*	94.5*w*	22.7*w*	49.6*w*	
20.2*w*	15358.5*s*	90.6*s*	16.5*w*	38.1*m*	62.7*s*	15497.1*s*	23.9*w*	52.2*m*	
20.7*w*	61.9*m*	94.2*m*	15417.6*m*	39.4*w*	64.8*w*	99.6*s*	25.2*w*	15555.3*w*	
15324.3*w*	63.0*m*	95.0*w*	18.4*w*	40.2*m*	15466.0*m*	15501.5*m*	26.4*s*	57.8*w*	
26.4*w*	64.8*m*	15395.9*w*	20.0*s*	41.2*s*	66.9*m*	02.3*w*	15528.3*s*	59.3*w*	

Concerning the Shape of the Compton Lines

(From a Letter to A. H. Compton)

A. SOMMERFELD, *Munich, Germany*

(Received May 1, 1936)

The structure of the spectrum of the modified x-radiation scattered by bound electrons is discussed. It is shown that the well-known continuous Compton band must have a definite limit on the short wave side (i.e., toward the unmodified line). Between this limit and the unmodified Rayleigh line, theory predicts the existence of a spectrum of discrete lines, which are appropriately classed as Raman lines. They are composed of those scattered photons which have excited, but not ionized the scattering atom. The conditions under which it might be possible to observe these Raman lines are discussed. There is no abrupt change in the specific intensity (per unit wave-length interval) as the limit of the discrete spectrum is crossed. It is suggested that the lines reported by B. B. Ray in 1930 may be interpreted as residue of Compton bands cut off by the foresaid limit.

WHILE the Compton radiation from free electrons is monochromatically sharp, that from bound electrons consists of a continuous band. The shape of this band in the case of hydrogen can be calculated explicitly on the basis of certain simplifying assumptions.[1] If $\Delta\lambda$ is the distance in wave-length from the center of the band, Δl the value of $\Delta\lambda$ at half-maximum, and $x=\Delta\lambda/\Delta l$, then the specific intensity is

$$J=J_{\max}/[1+(2^{\frac{1}{3}}-1)x^2]^3. \tag{1}$$

For elements other than hydrogen, one must use methods of numerical calculation.[2]

The point to which I would direct attention is that the Compton band should have a definite limit, g, on the short wave side, i.e., toward the unmodified Rayleigh line. The existence of this limit follows directly from the energy equation

$$h(\nu-\nu')=W+W_0 \tag{2}$$

if one sets $W=0$. (W=kinetic energy of the recoil electron, W_0 its binding energy, ν=frequency of the unmodified Rayleigh line, ν' =frequency of an individual point in the modified Compton band.) The distance of this limit from the Rayleigh line, $\Delta\lambda_g$, is thus found to be

$$\Delta\lambda_g=\lambda^2W_0/hc. \tag{3}$$

We compare this with the distance $\Delta\lambda_c$ of the center of the Compton band from the Rayleigh line:

$$\Delta\lambda_c=2(h/mc)\sin^2(\theta/2) \tag{4}$$

and obtain from (3) and (4) with $W_0=e^2/2a$, $a=h^2/me^2$ for hydrogen:

$$\Delta\lambda_c/\Delta\lambda_g=((4\pi a/\lambda)\sin(\theta/2))^2. \tag{5}$$

If we disregard extremely soft radiation, then $\lambda<4\pi a$ ($4\pi a\sim 6$A for hydrogen). If one chooses $\theta\sim 180°$, then

$$\Delta\lambda_g<\Delta\lambda_c,$$

i.e., our limit g cuts *a small piece from the short wave side* of the Compton band (Fig. 1). But if one makes

$$\sin(\theta/2)=\lambda/4\pi a, \tag{6}$$

e.g., $\theta=13\frac{1}{2}°$ for $\lambda=1.5$A (Cu $K\alpha$) and $a=\frac{1}{2}$A, then the limit cuts the Compton band *precisely in its center* (Fig. 2). If we proceed further in this direction, for $\theta\sim 0$, the Compton band will be cut on the other side of its center and the *remaining part may*, in extreme cases, *be very small* (Fig. 3).

What becomes of the intensity of the Compton band that is thus suppressed? We know that the combined Rayleigh and modified scattering is equal in intensity to the classical Thomson scattering. We know further, that in calculating the total incoherent scattering we must sum over all energy values of the *complete* system of characteristic functions. The *discrete* energy levels belong to this system as well as do the *continuous* ones. While the transition to a continuous level signified the production of a recoil electron, a transition to a discrete level represents the case in which the electron remains *bound in an excited state*. Since, in the case of hydrogen the nth excited state has the energy $W_n=-W_0/n^2$, the energy Eq. (2) must be replaced by

[1] Fritz Schnaidt, Dissertation, Munich, Ann. d. Physik **21**, 89 (1934).

[2] G. Burkhardt, Dissertation, Munich, to appear in Ann. d. Physik (1935).

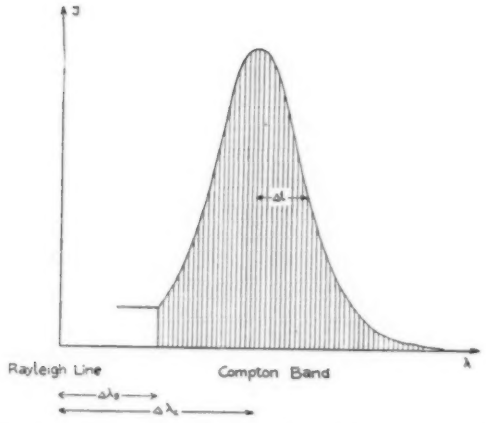

FIG. 1. Showing limit of Compton line on short wave-length side for $\theta = 180°$.

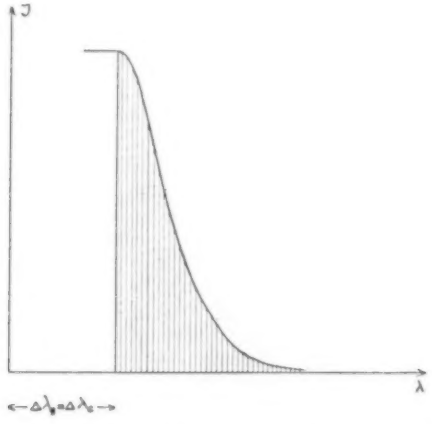

FIG. 2. Showing limit of Compton line on short wave-length side for $\theta = 13.5°$.

$$h\nu_n' = h\nu - W_0(1 - 1/n^2). \qquad (7)$$

This ν_n' is greater than the ν' at our limit g, which corresponds to $W = 0$. The corresponding wave-lengths of the radiation are thus less than the wave-length λ_g of this limit, and approach it for $n \to \infty$. The continuous Compton band is thus extended beyond g as a series of discrete lines. In Figs. 1, 2, and 3, the unshaded extensions of the Compton band toward the left indicate that the intensity of this series of lines also joins continuously on to the intensity of the band, insofar as one distributes the finite intensity of each line over the interval between it and its neighbor. This is quite analogous to the well-known continuity of intensity in passing from the Balmer series to the Balmer continuum.

The discrete lines which have just been described will be called the *Raman spectrum* of hydrogen. We can therefore say: *The continuous Compton band is extended on the short wave side by a discrete Raman spectrum.*[3]

The question arises whether this Raman radiation can be detected experimentally, and what conditions will be favorable for this purpose. From Fig. 2 one will suspect: If the Compton band is cut through the center, then the Raman spectrum must—because of the continuity of intensity—be particularly strong. The corresponding angle of scattering, we have seen in a special case to be $\theta \pm 13.5°$. But it is clear that with such small angles of scattering, the resolution of the Rayleigh line and Compton band, and *a fortiori* the resolution of the Rayleigh and Raman lines, will be difficult. One must recall that by Eq. (4) the center of the Compton band moves toward the Rayleigh line as θ diminishes. In Fig. 4 the position and *line* intensity of the Rayleigh and Raman lines are drawn approximately to scale (i.e., heights of the Raman lines are to the

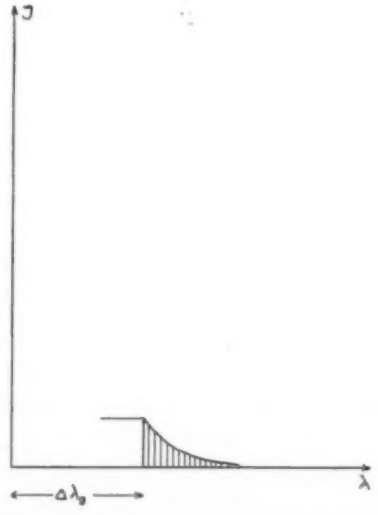

FIG. 3. Showing limit of Compton line on short wave-length side for $\theta = 0°$.

[3] Compare, Compton and Allison, *X-Rays in Theory and Experiment* (Van Nostrand, 1935), p. 239.

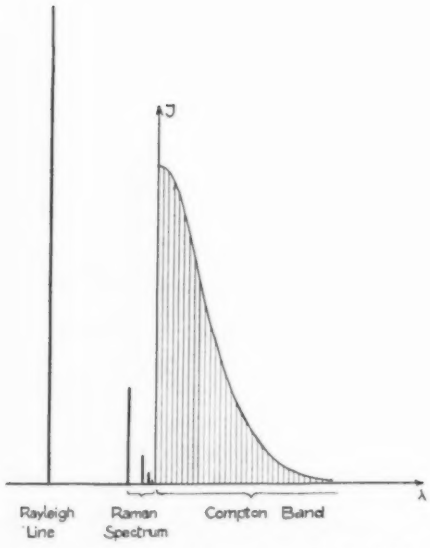

FIG. 4. Showing relative intensities of Rayleigh and Raman lines.

height of the Rayleigh line in the ratio of their intensities; the *specific* intensity of the Compton band is plotted on the scale of the previous figures, and is not directly comparable to the lines). The first Raman line (transition $n=1\rightarrow 2$) is more intense than all others; in the most favorable case, it has $\frac{1}{3}$ the intensity of the Rayleigh line.[1] This first Raman line is shown by Eq. (7), to be separated from the Rayleigh line by $\frac{3}{4}$ of the distance between the latter and the limit g. The succeeding Raman lines diminish rapidly in intensity (proportionally with $1/n^3$). With sufficient resolving power, the first line might perhaps be resolved.

This conclusion concerning the most favorable angle θ, which has been reached from a consideration of Fig. 2, is confirmed by the more exact calculations of Schnaidt.[1] Our present considerations and those of Schnaidt are, strictly speaking, valid only for hydrogen. They may be extended qualitatively to other atoms if the altered structure of the Raman spectrum is appropriately taken into consideration.

In conclusion, I would call attention to observations of B. B. Ray,[4] which have not, however, been confirmed by others.[5] They concern the passage of Röntgen rays through very thin layers, e,g., of carbon, which resulted in the formation of a "very weak, broad, diffuse" line on the long wave-length side of the primary line, which "appeared to have a more or less definite edge on its short wave side." This description reminds one of our Fig. 3, which was drawn to represent very small angles of scattering. The Compton band is reduced to a very small residue by the limit g. In the case of carbon this residue would correspond to the K electrons, and the limit g to the K limit (the L electrons, being much less firmly bound, would contribute only to the central part of the Compton band, which, in turn is cut off by our limit g). This coincides with Ray's observation that his line was separated from the primary one by the wave number of carbon $K\alpha$, which differs very little from that of the carbon K limit. The corresponding separation was also observed when nitrogen and oxygen were used as scattering substance. We would therefore like to interpret these lines as the residues of the K electron contribution to the Compton band (in distinction to Mr. Ray, who speaks of a "partial absorption of the Röntgen rays"). No mention of the Raman lines is to be found in Ray's paper. These should lie between the Compton band and the Rayleigh line and it is probable that the conditions were not favorable for their observation.

We do not consider it to be impossible that future repetitions of these experiments may lead to a positive result, if they are performed with reference to the theoretical views given here. In general terms, the object of such investigations should be to exhibit the anomalous forms of the Compton band (Figs. 2 and 3) and its extension as a Raman spectrum.

---

[4] B. B. Ray, Zeits. f. Physik **66**, 261 (1930) and subsequent notes of R. C. Majumdar, S. Bargava and J. B. Muckerjee, Nature **127**, 92, 273 (1931).

[5] Compare, e.g., J. M. Cork, Phys. Rev. **37**, 1555 (1931), O'Leary, ibid. p. 873.

The Nuclear Separation of the S_2 Molecule by Electron Diffraction

LOUIS R. MAXWELL, V. M. MOSLEY AND STERLING B. HENDRICKS, *Bureau of Chemistry and Soils, U. S. Department of Agriculture, Washington, D. C.*

(Received May 8, 1936)

Rotational analyses of S_2 bands as carried out by various workers have led to the following values for the nuclear separation; 1.60A, 1.84A, 1.73A, and 1.93A. In the present work this distance was determined by electron diffraction from S_2 vapor at 800°C and was found to be 1.92 ± 0.03A. This value is based upon the measured relative intensities of scattering in the region of the third maximum, $(1/\lambda) \sin \frac{1}{2}\theta$ from 0.70 to 1.0, and upon visual measurements on the fourth, fifth and sixth diffraction maxima. When the temperature of sulphur vapor is decreased appreciably below 800°C its electron diffraction pattern shows the presence of higher molecular types. The results obtained can be explained on the basis of S_{2+n} molecules where $n = 1, 2, 3 \cdots$ with a S−S−S valence angle of about 100° and a S−S distance, between closest neighbors, of *ca.* 2.1A. These values are in agreement with those found for the symmetrical puckered ring-shaped S_8 molecule present in crystalline sulphur.

INTRODUCTION

CONSIDERABLE uncertainty has existed concerning the correct rotational analysis of the diatomic sulphur bands. This is caused by the complexity of the spectrum for there is found considerable overlapping of the lines which has made the analysis difficult. As a result, the internuclear separation obtained from the band spectra measurements has been in dispute. Electron diffraction from gases gives directly the internuclear separation free from the difficulties inherent in band spectra analysis. It has been tested for its accuracy by comparison with band spectra data for the diatomic molecules Cl_2,[1] Br_2[2] and I_2.[3] In these cases complete agreement has been obtained, therefore we expect that equally good agreement must be found in the case of S_2.

The situation concerning the nuclear separation of the S_2 molecule is summarized below. (1) Naudé and Christy[4] studied five ultraviolet emission bands of S_2 taken in the third order of a 21-ft./grating (0.87A/mm). A study of the rotational structure of these bands showed that they were due to the same type of electronic transitions as found for the Schumann Runge bands of O_2, i.e., $^3\Sigma_u^- \rightarrow {}^3\Sigma_g^-$. The nuclear separation of the lower state r_e'' was found to be 1.60×10^{-8} **cm.** Also since alternate levels were missing it was concluded that the angular momentum of the S^{32} nucleus is zero. Independently P. Swings[5] reported to have confirmed the results of Naudé and Christy from an investigation of the fluorescence spectra of S_2. (2) Badger[6] pointed out that the value of 1.60A for the internuclear distance of S_2 seemed very abnormal according to expected covalent bond radii and to certain empirical rules by which the internuclear distances can be calculated from vibrational frequencies. He found that the measured lines obtained by Naudé and Christy could be reassigned to the various branches so that a different set of combinations could be obtained. This revised treatment led to $r_e'' = 1.84$**A.** Badger however concluded that the sulphur molecule is antisymmetrical in the nuclei. (3) Van Dijk and Lameris[7] took new photographs in the 4th order of a 21-ft. grating (0.6A/mm) and reported that they failed to find on their plates a great many lines given by Naudé and Christy. On making a new analysis of the S_2 bands they obtained a value of **1.73A** for the internuclear distance. The wave functions of the S_2 molecule were found by them to be symmetrical in the nuclei. (4) In an abstract[8] of the present work it was shown that the nuclear separation of the S_2 molecule as found by electron diffraction was 1.94 ± 0.03**A**, a value definitely greater than any of the previous band spectra measurements. (5) Recently Olsson[9] carried out

[1] L. O. Brockway and L. Pauling, Proc. Nat. Acad. Sci. **19**, 68 (1933). See also, J. Am. Chem. Soc. **57**, 2684 (1935).
[2] R. Wierl, Ann. d. Physik **8**, 521 (1931).
[3] S. B. Hendricks, L. R. Maxwell, V. M. Mosley and M. E. Jefferson, J. Chem. Phys. **1**, 549 (1933).
[4] S. M. Naudé and A. Christy, Phys. Rev. **37**, 490 (1931).
[5] Reference 4, note added in proof.
[6] R. M. Badger, Phys. Rev. **46**, 1025 (1934).
[7] E. W. Van Dijk and A. J. Lameris, Physica **2**, 785 (1935).
[8] Baltimore Meeting November 30, 1935, Phys. Rev. **49**, 199 (1936).
[9] E. Olsson, Zeits. f. Physik **99**, 114 (1936).

a rotational analysis of S_2 using Naudé and Christy's data for seven bands in the ultraviolet. He finds zero nuclear spin and a nuclear separation in the ground state of **1.93A.**

Procedure

The intensity of electron scattering $I(x)$ from diatomic sulphur can be expressed as follows:

$$I(x)=k\left\{2\psi_s^2(1+\sin x/x)+\frac{32\cdot S(\nu_s)}{(\sin \tfrac{1}{2}\theta/\lambda)^4}\right\}, \quad (1)$$

where $$x=4\pi l_{s-s}(1/\lambda)\sin \tfrac{1}{2}\theta. \quad (2)$$

l_{s-s} is the separation of the sulphur atoms while the remaining terms are expressed in the usual notation.[10] Intensity distribution calculated from this equation is shown in Fig. 1. It is noticed that the interference properties appear only as slight humps on a smooth curve; however for sake of convenience they will be referred to as maxima. After first drawing a continuation of the smooth portion of the curve through the region of variation then the position of these maxima are determined by a vertical line which approximately divides the enclosed area into equal parts. An arbitrary method of this kind is entirely justifiable provided exactly the same procedure is used for locating the maxima on the corresponding experimental scattering curve. After having determined the position of the theoretical maxima in terms of x and the experimental maxima in terms of $(1/\lambda)\sin \frac{1}{2}\theta$, l_{s-s} is immediately obtained from Eq. (2).

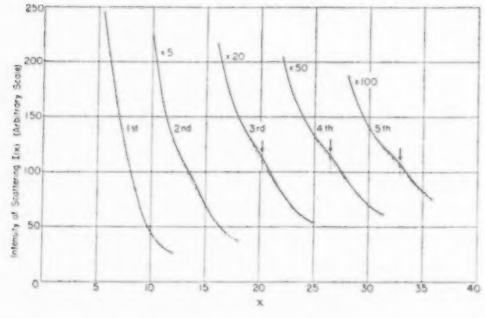

FIG. 1. Theoretical electron scattering curve for S_2.

Experimental Arrangement

In order to obtain a source of S_2 molecules free from association it was necessary at the pressures used (*ca.* 60 mm Hg) to raise the temperature of the gas to about 800°C. Under these conditions dissociation of sulphur vapor into S_2 is almost complete.[11]

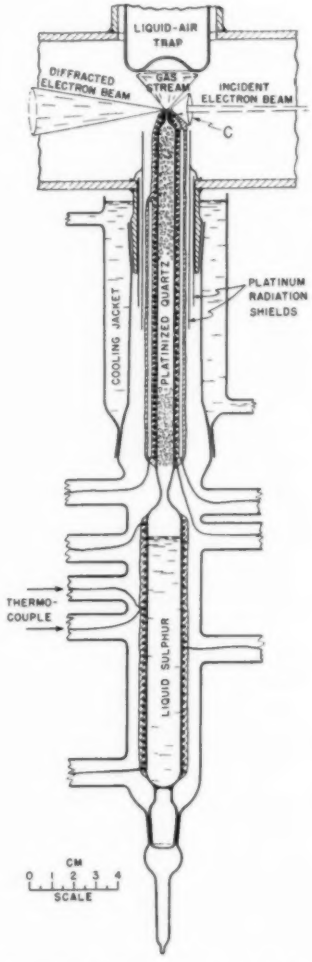

FIG. 2. Diagram showing sulphur boiler and heating tube for producing S_2 vapor. Gas jet and electron diaphragm are mounted together.

[10] R. Wierl, Ann. d. Physik **8**, 521 (1931). For a formulation of the incoherent scattering, see for instance L. Bewilogua, Physik. Zeits. **33**, 688 (1932). The F values used were obtained from the calculated values of R. W. James and G. W. Brindley, Phil. Mag. **12**, 81 (1931), and also from L. Pauling and J. Sherman, Zeits. f. Krist. **81**, 1 (1932).

[11] G. Preuner and W. Schupp, Zeits. f. physik. Chemie **68**, 129 (1909).

Electron diffraction photographs were taken from S_2 vapor produced from two different sources: first, from iron pyrite (FeS_2) at 850°C which readily decomposes into FeS and S_2 giving an ample source of S_2;[12] second, by passing sulphur vapor through a bed of hot platinized fused quartz pieces at 800°C as illustrated in Fig. 2. The inner tube containing the sulphur and the platinized quartz was made of fused quartz and was wound with platinum wire for heating. The platinum cone C containing a hole 0.11 mm in diameter defined the size and location of the electron beam while the gas jet in proper position had a diameter of 0.25 mm and length of 3 mm. The important features of this type of assembly have been previously discussed.[13] Temperature measurements of the heater tube and gas jet were made by the use of an optical pyrometer. The electron diffraction pattern was recorded on a photographic plate (insensitive in the red) at a distance of 10.0 cm using generally a de Broglie wave-length of 0.060A. Final relative intensity scattering curves were obtained by transforming the densitometer records obtained into intensity curves by the use of calibration plates made from electron exposures.

Results and Discussion

Electron diffraction photographs obtained showed no diffraction rings at the smaller values of $(1/\lambda)\sin\frac{1}{2}\theta$. This is to be expected from the theoretical scattering curves, for it is seen in Fig. 1 that the first maximum is entirely absent while the second is barely detectable thus giving no ring suitable for measurement until the third maximum is reached. A typical experimental intensity of scattering curve obtained in the region of the third maximum is shown in Fig. 3a. This prominence appears very similar in shape to the corresponding theoretical maximum and from its position a S−S distance of 1.91±0.02A is obtained. Direct comparison between observed and calculated intensities is shown in Fig. 3b. In general good agreement between the two curves is obtained; however the experimental intensity curve is found to decrease slightly less rapidly than does the theoretical curve.

[12] For data on the dissociation pressure of pyrite, see E. I. Allen and R. H. Lombard, Am. J. Sci. **43**, 175 (1917).
[13] L. R. Maxwell, S. B. Hendricks and V. M. Mosley, J. Chem. Phys. **3**, 699 (1935).

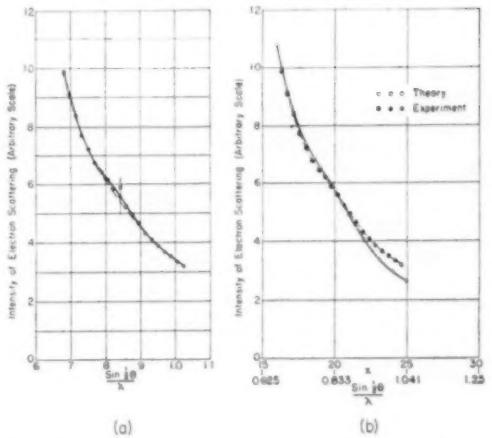

FIG. 3a. Experimental electron scattering curve for S_2. 3b. Comparison between theoretical and experimental electron scattering curves of S_2 for a S−S distance of 1.91A. The two curves were made to fit in intensity at $x=20.2$.

Position of the fourth, fifth and sixth maxima were measured visually. The positions of these maxima are not only useful in determining l_{s-s} but also confirm the fact that the vapor used was diatomic, i.e., l_{s-s} was found to be independent of the maximum used. *Visual measurements were also made on electron diffraction photographs obtained from Cl_2 vapor* for purposes of comparison, since Cl_2 and S_2 give almost the same type of diffraction pattern. Visual measurements on the 4th, 5th and 6th maxima of Cl_2 gave $l_{Cl-Cl}=2.00+0.02$A in agreement with the band spectra value of 1.98A. For the case of the visual measurements on the 5th and 6th maxima the values of x used in Eq. (2) were simply the maxima of the $\sin x/x$ function. These values of x_{max} do not differ appreciably from those found by using the exact formula in the manner described above. One should expect therefore that the visual measurements on S_2 should agree with the band spectra value to within about one percent.

Final results of the visual measurements, together with a summary of all the data obtained, are given in Table I. Good agreement between the visual and intensity determination is found. The position of the third maximum for S_2 from FeS_2 was located from the densitometer records in a manner similar to that used on the intensity curves. By considering all the data

TABLE I. *Summary of electron diffraction photographs of S_2.*

	1st MAX.	2nd MAX.	3rd MAX.	4th MAX.	5th MAX.	6th MAX.
S_2 vapor from FeS_2:						
Exp. values for $(1/\lambda)\sin\frac{1}{2}\theta$	—	diffuse halo	0.827 ± 0.008	1.09 ± 0.02		
Method of measurement	—	—	from dens. rec.	visual		
x_{max} theoretical curve	none	very slight	20.2	26.5		
l_{s-s}	—	—	1.94 ± 0.02A	1.93 ± 0.03A		
S_2 vapor from sulphur passed through platinized quartz pieces at 850°C						
Exp. values for $(1/\lambda)\sin\frac{1}{2}\theta$	—	diffuse halo	0.840 ± 0.004	1.10 ± 0.005	1.37	1.63
Method of measurement			from exp. int. curve	visual	visual	visual
x_{max} theoretical curve	none	very slight	20.20	26.5	32.95	39.24
l_{s-s}	—	—	1.91 ± 0.02	1.92 ± 0.01	1.91 ± 0.01	1.92 ± 0.02

Most probable separation of S_2 molecule in normal state is 1.92 ± 0.03A.

obtained we arrive at **1.92 ± 0.03A as the average value for the S−S nuclear separation of S_2.** The distance 1.93A given by Olsson from band spectra analysis is in close agreement with the final electron diffraction value which indicates that only his rotational analysis of S_2 can possibly be correct.

TEMPERATURE EFFECT AND THE HIGHER MOLECULAR FORMS OF SULPHUR

Intensity corrections for S_2

Since high gas temperatures were necessary for electron diffraction from S_2 some consideration must be given concerning the mutual molecular vibrations present and how they will affect the intensity of scattering. James[14] has shown for x-ray scattering from gaseous diatomic molecules that the temperature correction appears in the form of e^{-A} which is a variable coefficient of the term $\sin x/x$ in Eq. (1). A is defined by the relation

$$A=\frac{h}{\mu\nu}\coth\frac{h\nu}{2kT}\cdot\left(\frac{\sin(\theta/2)}{\lambda}\right)^2,$$

where μ is the reduced mass, T the absolute temperature, k the Boltzmann constant and ν the frequency of the oscillator. This correction can be used directly for the case of electron scattering and it was found for S_2 to make only a very slight change in the intensity of scattering. Also one can see directly that the temperature could not produce any appreciable errors in the determination of the nuclear separation because at these temperatures (1073°K) about 60 percent of the molecules are still in the ground state with less than 25 percent in the first vibrational level and about 9 percent in the second vibrational level. The mean time position of the molecule estimated from this population of the different vibrational levels is to within less than $\frac{1}{2}$ percent of the equilibrium position in the ground state.

ELECTRON DIFFRACTION FROM THE HIGHER MOLECULAR FORMS OF SULPHUR

When the temperature of the sulphur gas is appreciably decreased below 800°C the electron diffraction pattern changes completely. A prominent ring comes at $(1/\lambda)\sin\frac{1}{2}\theta=0.516\pm0.005$ (measured from densitiometer records) and an outer ring at 0.790 ± 0.008 which was measured both visually and from the densitometer traces. These results clearly indicated the formation of S_{2+n} molecules in the gas where $n=1, 2, \cdots$. The structure was determined approximately and it was found that the molecule must have a S−S−S valence angle of about 100° and approximately 2.1A as the S−S distance between neighboring atoms. Below 96°C sulphur crystallizes into a stable orthorhombic form. Warren and Burwell[15] have shown from x-ray diffraction data that this structure contains S_8 molecules in the shape of symmetrical puckered rings. They arrived at a S−S distance of 2.12A between

[14] R. W. James, Physik. Zeits. **33**, 737 (1932).

[15] B. E. Warren and J. T. Burwell, J. Chem. Phys. **3**, 6 (1935).

closest neighbors and a bond angle of 105°, values with which the electron diffraction results are in close agreement. Apparently the valence angle and the nuclear separations are maintained even when molecules are formed in a gas at high temperature where the S_8 ring is probably broken, leaving molecular chains of irregular lengths.

The writers wish to thank Dr. O. R. Wulf and Dr. E. J. Jones for the interest they have shown in this work.

Note added in proof: June 3rd, 1936. From a more recent rotational analysis of S_2, Olsson[16] has found $r_e''=1.88$A which is somewhat lower than his previous value of 1.93A; both values are only slightly different from the final electron diffraction value 1.92 ± 0.03A. He further suggests that the electron diffraction results should be slightly higher than the band spectra value because of the presence of molecular vibrations. The importance of considering the molecular vibrations in electron diffraction measurements has been discussed above. It can be seen that no appreciable differences in the internuclear distances in S_2 can be attributed to a temperature effect.

[16] Olsson, Nature **137**, 745 (1936).

JULY 1, 1936 PHYSICAL REVIEW VOLUME 50

Radio and the Sunspot Cycle

L. C. Young and E. O. Hulburt, *Naval Research Laboratory, Washington, D. C.*

(Received May 6, 1936)

The observed optimum frequency f for long distance daylight communication averaged over the year during the period from 1923 to 1936 was found to vary with the yearly average relative sunspot number s according to the relation $f=7.8(s+12)^{\frac{1}{2}}$. The march of the sunspot curve from 1749 to 1935 suggests the possibility of greater sunspot numbers in coming solar cycles than the value $s=78$ which occurred at the 1928 maximum. By means of the f,s relation, radio conditions for sunspot numbers from 100 to 160 are calculated.

IT is well known that radio communication phenomena vary with the cycle of solar activity. In the following paragraphs, radio and solar data are assembled to bring out the relations which exist. The radiofrequencies useful for long distance daylight communication during the years 1923 to 1936 are found to fall in more closely with the yearly average sunspot numbers than with the magnetic character and solar constant during this period.

In Fig. 1 are plotted the values of the optimum frequencies for daylight communication for 1000, 3000 and 5000 nautical miles averaged over the year for the years from 1923 to 1936. The period covers the cycle of solar activity with minima in 1923 and 1933 and the maximum in 1928. In the first two columns of Table I are given further radio observations for the years 1928 and 1933. The data were assembled from published radio literature[1] and refer to world-wide conditions. Experience has shown that the optimum frequency is that frequency which places the receiver in the zone of reception beyond the fewest number of areas of skip.

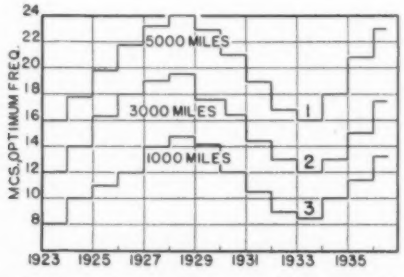

FIG. 1. Optimum frequencies for daylight communication.

TABLE I. *Observed and calculated relationship between sunspot number and optimum radiofrequency for long distance day communication.*

YEAR	OBSERVED 1928	OBSERVED 1933	CALCULATED FROM (2)			
Sunspot number	78	5.7	100	120	140	160
Long distance day communication						
Optimum	24 megacycles	16	25.3	26.4	27.4	28.4
Many cases	30–33	20–22	32–35	33–36	34–38	35–39
Occasional	33–36	22–24	35–38	36–40	38–41	39–43
Few	above 38	25	40	41	43	45

[1] Particular mention may be made of the Technical Publications, Bell Telephone System; of papers by Prescott, Proc. Inst. Rad. Eng. **18**, 1797 (1930); and by Mögel, Telefunken Zeitung, Nr. 67, 23 (1934).

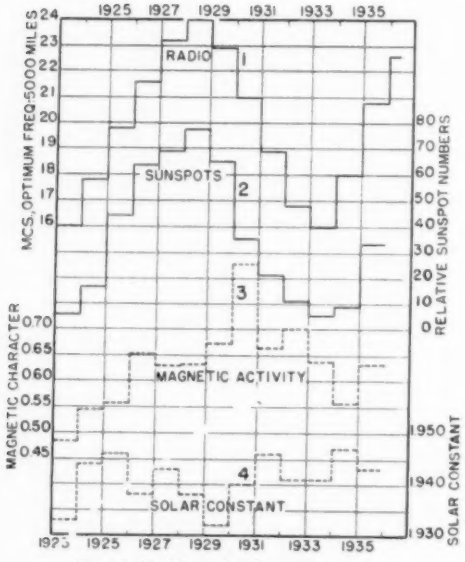

FIG. 2. Radio and solar phenomena.

Curve 1 of Fig. 1 is plotted again as curve 1 of Fig. 2 and with it are plotted the curves of relative sunspot numbers,[2] of world-wide magnetic activity,[3] and of the solar constant;[4] all data are yearly averages. It is seen from Fig. 2 that the radio curve shows closer detailed correspondence with the sunspot curve than it does with the curve of terrestrial magnetic activity. This is to be expected, since the magnetic activity curve is essentially a record of storms in the high atmosphere and the radio curve refers to radio communication during good weather in the high atmosphere. The absence of correspondence between the radio curve and the solar constant curve indicates merely that solar radiations in the visible and infrared portions of the spectrum on which the solar constant is based do not vary in close accord with the ultraviolet radiations from the sun which in the main account for the ionospheric ionization and thereby influence radio wave propagation.

Sunspot numbers greater than the 78 maximum of 1928 may occur in future solar cycles and it is of interest to estimate radio conditions in such event. In order to extrapolate the radio curve to higher values of sunspot numbers, a relation between the optimum radio frequency f for long distance communication and the relative sunspot number s must be found. This may be done either empirically or better, if possible, by theory. A theoretical connection may be derived in the following way: Since the optimum radio-frequency is that for which the receiver is just beyond the skip zone or zones, $f^2 \sim y$ approximately,[5] where y is the density of ionization of the region of the ionosphere which refracts the radio ray. This is approximately true provided that the height of the ionization above sea level and the distribution of the ionization with height remain unchanged from sunspot minimum to maximum, which may not be true. Assuming that y is an equilibrium value[6] for equality between the rate of production q of ionization by the ionizing radiations of sunlight and a rate of loss due to recombination proportional to y^2, then $y^2 \sim q$. Hence, $f^4 \sim q$. Assume that $q \sim (s+b)$, where b, a constant, is introduced in recognition of the fact that y and q have values other than zero when s is zero, i.e., when there are no sunspots. Then

$$f = a(s+b)^{\frac{1}{4}}. \tag{1}$$

Curve 1 of Fig. 1 is plotted as curve 2 in Fig. 3. Curve 2, Fig. 3, is plotted from (1) with $a = 7.8$ and $b = 12$, or

$$f = 7.8(s+12)^{\frac{1}{4}}, \tag{2}$$

and is seen to agree with curve 1 within experimental certainty. Empirically, a simple relation between f and s may be derived by inspection of the f and s curves of Fig. 2, curves 1 and 2, respectively. The relation is

$$f = 0.1s + 16. \tag{3}$$

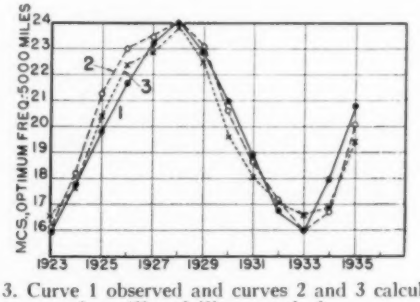

FIG. 3. Curve 1 observed and curves 2 and 3 calculated from (2) and (3), respectively.

[2] Terr. Mag. and Atmos. Elec. **39**, 231 (1934).
[3] DeBilt, *Charactère Magnétique*.
[4] Abbott, Smithsonian Misc. Coll., Vol. 94.
[5] Taylor and Hulburt, Phys. Rev. **27**, 189 (1926).
[6] Hulburt, Phys. Rev. **31**, 1018 (1928).

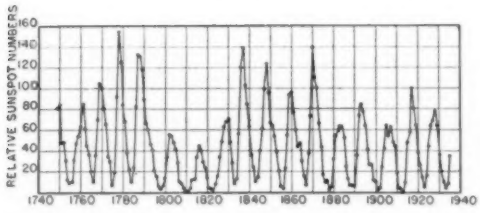

FIG. 4. Relative sunspot numbers.

The f,s curve from (3) is plotted as curve 3, Fig. 3, and is seen to agree with curve 1 about as well as curve 2 does.

From 1923 to 1935 short wave radio technique improved and the use of short waves expanded greatly. The query arises whether the march of the curves of Fig. 1 might have been influenced by such factors as these as well as by conditions of wave propagation. However, it has turned out that curves 2 or 3, Fig. 3, which were based on the relation with sunspots, agreed with the observed curve 1, Fig. 3, throughout the entire period from 1923 to 1935 with no indication of a systematic departure. This is strong presumption for the conclusion that the data of Fig. 1 were functions of the conditions of wave propagation only, as the ionosphere, and not of technique or number of stations.

The extrapolation of the radiofrequencies to higher sunspot numbers than 78 was carried out by means of (2) and is given in the last four columns of Table I for relative sunspot numbers 100, 120, 140 and 160. If (3) had been used instead of (2), the values of the frequencies would be from 4 to 8 percent greater.

The relative sunspot numbers for the years since 1749 are plotted in Fig. 4. If the high peaks of the latter part of the eighteenth century and of the middle part of the nineteenth century are evidence of a cyclical or recurrent phenomenon, sunspot maxima in the not too far distant future will be greater than those since 1880. On this basis, one may suggest that radio conditions during coming sunspot maxima may be those of one of the last four columns of Table I.

The agreement between observation and the theoretical relation (1) is sufficiently close to permit certain other estimates. From (1) it follows that approximately

$$y \sim (s+12)^{\frac{1}{2}}, \tag{4}$$

TABLE II. *Values of the density of ionization in the ionosphere, y, skip distance, d, highest frequency useful for long distance communication, f_1, and the "critical frequency" of the radio echo measurements, f_c as a function of sunspot number, s.*

s	y	d	f_1 and f_c
5.7	1	1	1
20	1.35	0.86	1.15
40	1.72	0.77	1.30
60	2.02	0.71	1.41
80	2.29	0.67	1.50
100	2.52	0.63	1.58
120	2.73	0.61	1.64
140	2.92	0.59	1.70
160	3.14	0.57	1.77

$$d \sim 1/(s+12)^{\frac{1}{2}}, \tag{5}$$

$$f_1 \text{ and } f_c \sim (s+12)^{\frac{1}{2}}, \tag{6}$$

where y is density of ionization in the ionosphere, d is the skip distance of radio waves,[6, 7] f_1 is the highest frequency useful for long distance communication,[6, 7] and f_c the "critical frequency" of the radio echo measurements of the ionosphere,[8] i.e., the lowest frequency which will just pierce a region of the ionosphere at normal incidence. (4), (5) and (6) involve mathematic approximations and the simplifying physical assumptions, (1) that the heights of the ionospheric regions do not change with sunspots; (2) that the distribution of ionization with height does not change with sunspots; and (3) that the ionization densities of the various regions of the ionosphere vary in approximately the same manner with sunspots. Ionosphere measurements since 1930 indicate that these assumptions are approximately true, although it would be surprising if they were exactly true.

From (4), (5) and (6) Table II was prepared which gives as a function of s the values of y, d, f_1 and f_c relative to their respective values for 1933 when s was 5.7. The table is admittedly inexact but offers a rough idea of the changes with sunspot number to be expected in the overhead ionization and radio phenomena. For example, from the table for $s=80$ the skip distances should be about 2/3 of their 1933–1934 values,[7] which is in good agreement with the values observed[9] in 1928.

[7] Hulburt, Proc. Inst. Rad. Eng. **23**, 1492 (1935).
[8] Kirby, Berkner and Stuart, Proc. Inst. Rad. Eng. **22**, 481 (1934).
[9] Taylor and Young, *Radio Engineering Handbook* (edited by Henny, McGraw-Hill, 1933), p. 442.

Thin Film Field Emission

LOUIS MALTER, *Cornell University**

(Received April 23, 1936)

Aluminum, oxidized electrolytically, and subsequently treated with caesium and oxygen possesses new and interesting properties when subjected to electron bombardment in the presence of an adjacent collector electrode whose potential is held positive with respect to the aluminum. True secondary electron emission from the treated surface results in the establishment of a positive charge on the surface and a polarization of the oxide film. This positive charge acting through the thin oxide film produces a high gradient, resulting in the emission of electrons through the surface. The emission increases with collector voltage and beam currents, obeying power laws, but exhibits saturation tendencies. The removal of the primary beam does not result in the immediate cessation of the field emission, but rather in a slow decay which is due to the fact that the surface charge takes an appreciable time to leak away. Similar time lags are noticed when the beam is first applied, particularly if the collector voltage has been reversed while the beam impinges on the surface. The surfaces are also light sensitive, in that light causes a decrease in the field emission and a speeding up of decay. Attempts were made to demonstrate this effect for other surfaces, but, with a few exceptions, the results were negative.

INTRODUCTION

THIS paper constitutes a more extended report of a letter published recently[1] under the title "Anomalous Secondary Electron Emission." Considerable criticism of this name for the phenomenon involved has arisen as not being descriptive of its apparent nature and, consequently, the above title suggested by Dr. J. A. Becker has been adopted.

In a search for a surface possessing a high secondary emission ratio, a considerable number of composite surfaces of various types were investigated. In the case of aluminum oxide treated with caesium and oxygen in a manner to be described below, it was found that a primary electron beam impinging upon the surface caused a current flow to a positive collector which, in certain cases, was several thousand times as great as the primary current. The phenomenon differed from that in the case of normal secondary emission in that the collector current was dependent upon the collector potential and primary current density. It exhibited very marked time lag characteristics and was also affected by light.

EXPERIMENTAL PROCEDURE

A. Tube and circuit

A diagram of the tube employed, together with the accompanying circuit is shown in Fig. 1.

The cathode was of the barium oxide-strontium oxide type. The electron gun parts were made of tantalum. The electrodes on the walls of the tube were platinum formed by the reduction of Hanovia platinizing solution. The regions around the "side contacts" were coated with silver formed by the reduction of Hanovia silver paste.

The platinum film consisted of two portions, the first serving as the so-called "second anode" of the electron gun. The second portion served to collect the electrons emitted from the target. If a single film is used as both second anode and collector, a change in collector voltage (V_c) causes a much greater change in beam spot size than if two separate films are employed as shown. This precaution was necessary in view of the dependence of the collector current upon beam spot size.

The caesium was produced by exploding compressed pellets of powdered caesium chromate and zirconium in a side tube.

Two pairs of deflecting coils (not shown in Fig. 1), mounted just beyond the first anode (at right angles to each other), served to position the beam on the target.

B. Formation of the oxide film

The aluminum oxide was formed by making the aluminum the anode in a bath wherein the cathode was a platinum foil. Various composition baths were tried. Satisfactory results were obtained with a saturated solution of borax and boric acid.

* Now at RCA Manufacturing Company, Camden, New Jersey.

[1] Malter, Phys. Rev. **49**, 478 (1936).

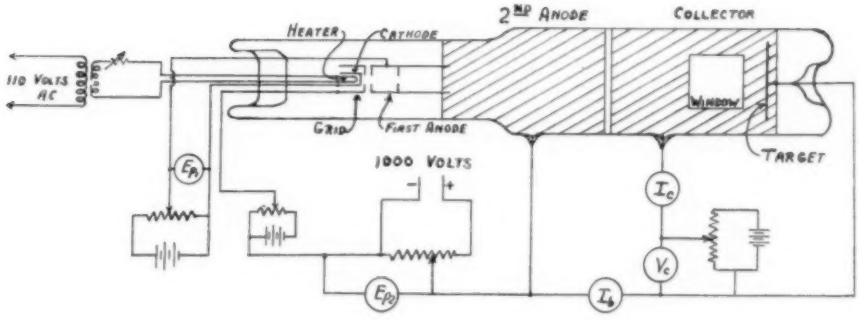

FIG. 1. Schematic diagram of apparatus.

It has been shown[2] that for times of formation in excess of a few minutes the thickness of the oxide film formed is practically independent of the time and the bath employed. The thickness is given by the relation

$$D = 17.0V,$$

where D is the oxide thickness in A and V is the applied potential in volts. However, the resistance of the film does depend upon these factors. No real study of the effect of the nature of the bath upon the film properties appears to have been made.

If at any time during the oxidation process, the applied voltage is gradually reduced, it is found that plots of the logarithm of the applied voltage against the logarithm of the current through the film yield curves of the form shown in Fig. 2. It is seen that below a certain voltage the curve is linear. Güntherschulze and Betz[3] have shown that over this linear region the current is purely electronic, whereas above this point ions move through the oxide lattice and contribute to an increase in its thickness. The portion of the current lying below the extended linear portion of the curve is electronic, whereas that above is ionic.

The prepared aluminum foil was mounted on a nickel plate for support and its edges were painted with willemite in order to permit the position of the beam to be seen by the fluorescence excited. Equally spaced circles were scratched lightly on the willemite in order that it be possible to determine the size of the spot. For intense beams (in excess of 3 to 4 microamperes) a faint blue fluorescence appeared on the oxide surface, permitting of a direct determination of the position and diameter of the electron beam.

The tube was pumped and baked at 475°C until the pressure dropped below 10^{-5} mm of Hg. After cooling, the parts of the electron gun were outgassed by means of high frequency and the oxide cathode activated so as to be thermionically emissive.[4]

Caesium was now introduced into the tube and

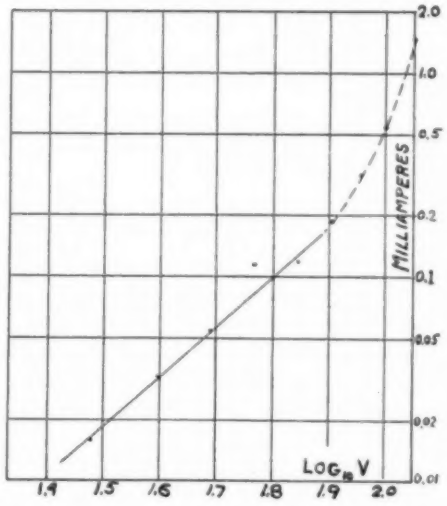

FIG. 2. Current voltage characteristic of aluminum oxide film after formation in saturated borax and boric acid bath for one hour.

[2] Güntherschulze and Betz, Zeits. f. Elektrochemie **37**, 8–9 (1931).

[3] Güntherschulze and Betz, Zeits. f. Physik **92**, 367 (1934).

[4] Dushman, Rev. Mod. Phys. **2**, 381 (1930).

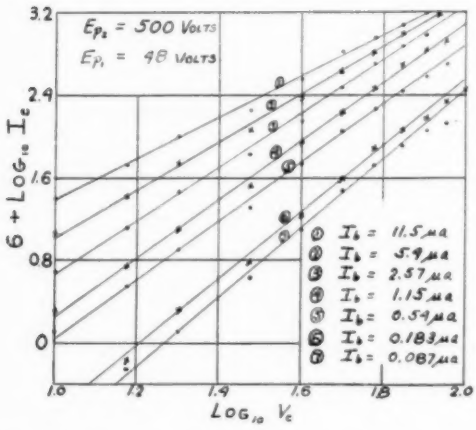

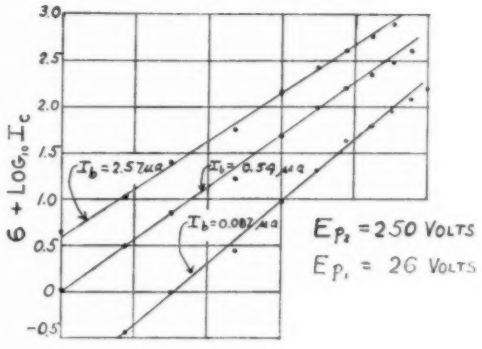

FIG. 3 (left) and FIG. 4 (right). Variation of collector current with collector potential for different values of beam current. Spot size held constant.

the tube then baked at 200°C for ten minutes. After cooling, oxygen was admitted into the tube to a pressure of 1 mm of Hg and pumped out after a few seconds. This treatment was sufficient to bring about the appearance of the thin film field emission, or enhance it in cases where it was present prior to any treatment.

It was found impossible to secure completely reproducible results. In an effort to determine the possible reason for this, all chemicals used were recrystallized and the water redistilled, and, in addition, the purest obtainable aluminum was secured from the Rheinische Blattmetall A.G.[5] However, their material was no better in this respect than the available commercial "electrolytic condenser" aluminum.

EXPERIMENTAL RESULTS

Except where noted the measurements given were obtained from a tube having aluminum with an oxide thickness of 2000A. While the exact results obtained differ from those in other foils with the same oxide thickness, the essential conclusions and laws are the same, the actual magnitudes only being affected.

A. Variation of collector voltage (V_c)

If the beam current (I_b), second anode voltage (Ep_2) and spot size are held constant, the variation of the collector voltage (V_c) causes a rapid variation in the collector current (I_c).

The results for different values of I_b for the cases wherein ($Ep_2=500$ volts, $Ep_1=48$ volts) and ($Ep_2=250$ volts, $Ep_1=26$ volts) have been plotted in logarithmic coordinates in Figs. 3 and 4. These combinations of Ep_1 and Ep_2 yield the same spot size.

In general, it is seen that:

$$I_c=B(V_c)^m. \tag{1}$$

At this point, it should be made clear that the results apply to only one region of the target. The values of I_c obtained from different regions of this surface vary considerably. However, if one restricts oneself to a particular region and is careful not to alter the surface in the manner to be described below, the results are reproducible. In these measurements as well as in those that follow (except where noted) all the data were obtained at the spot on the surface which yielded largest collector currents.

B. Variation of beam current

A series of readings were taken, everything being held constant except I_b. The results for $Ep_2=500$ volts, $Ep_1=48$ volts, and different values of V_c are plotted in Fig. 5. All of these curves are "repeats." It is found that if I_b is increased in steps, and corresponding values of I_c obtained, a curve is obtained which does not

[5] Rheinische Blattmetall A. G. Grevenbroich (Niederrhein).

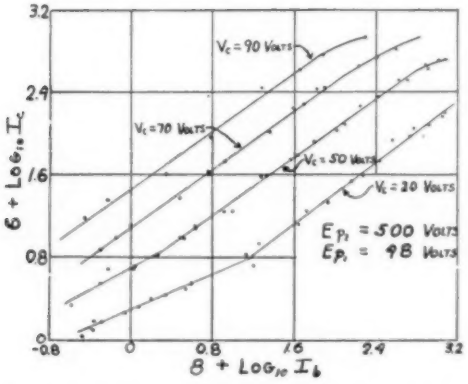

FIG. 5. Variation of collector current with beam current for different values of collector voltage. Spot size held constant.

repeat itself at low values of I_b. However, after the first run, all succeeding curves do repeat themselves. These stabilized I_b, I_c points, which are plotted in Fig. 5, and the curves obtained, are the "repeats" referred to above.

To illustrate the nature of this deviation for the initial run at low values of I_b, three successive runs are plotted in Fig. 6. The circles are the first run, the crosses and triangles the second and third, respectively. It is seen that after the first run, the succeeding runs lie along the same line. The nature of the polarization and time lag effects which give rise to the deviations in the first run will receive more detailed consideration below.

Returning to a consideration of Fig. 5, it is seen that except for low values of V_c and I_b, the

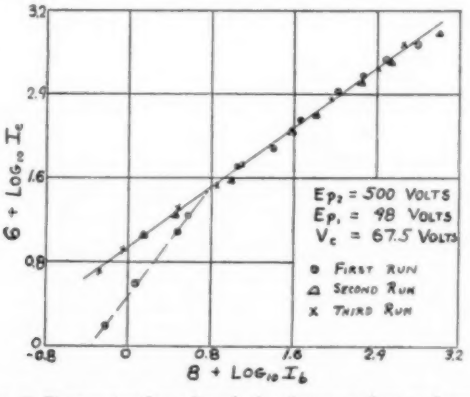

FIG. 6. Demonstration of variation between first and succeeding runs wherein beam current is varied.

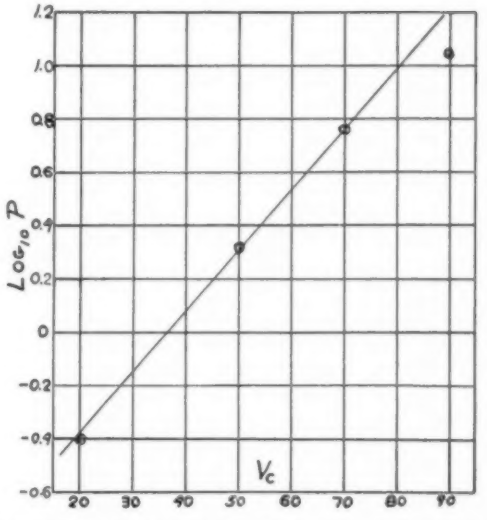

FIG. 7. Plot of intercepts of collector current—beam current characteristics as a function of collector voltage.

curves are all straight lines of the same slope. These results can be represented by:

$$I_c = PI_b^{0.71} \tag{2}$$

$\log_{10} P$ as a function of V_c is plotted in Fig. 7. If $V_c < 70$ volts,

$$P = 0.145 \times 10^{0.023 V_c}. \tag{3}$$

By substituting (3) in (2), there results:

$$I_c = 0.145 \times 10^{0.23 V_c} (I_b)^{0.71}. \tag{4}$$

This relation holds for all values of I_b and I_c except for those beyond the linear regions of the curves of Figs. 5 and 6.

C. Variation of spot size

In order to see whether Eqs. (1) and (4) could be expressed in terms of current density, a series of runs were taken at different spot sizes, the spot sizes being determined by deflecting the spot onto the willemite. Because of a slight misalignment of the first anode, the spot was oval instead of circular. This made the determination of the spot size quite inaccurate, but it was felt that an approximation of the current density law could certainly be obtained.

In Fig. 8, the values of I_c/A and I_b/A for various values of I_b are plotted on logarithmic scale, where A is the spot size. When consider-

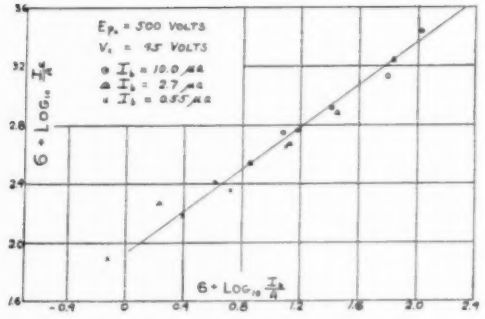

FIG. 8. Variation of collector current divided by spot size with beam current density.

ation is taken of the large error in the determination of A, it seems that the best representation of the results is a straight line drawn among the widely scattered points. We have thus:

$$\log 10^6 I_c/A = 1.92 + 0.73 \log 10^6 I_b/A. \quad (5)$$

The fact that the slope is practically the same as that for Eq. (4) indicates that the linear relationship expressed in Eq. (5) is a reasonable representation.

The agreement between Eqs. (4) and (5) is very good and consequently Eq. (4) may be generalized into the form:

$$A(I_c/A) = 0.145(10)^{0.023V_c} A^{0.71} (I_b/A)^{0.71} \quad (6)$$

and since Eq. (4) was derived at $Ep_2 = 500$ volts, $Ep_1 = 48$ volts, for which values $A = 0.72$ cm^2; we can insert this value of A in Eq. (6) and obtain:

$$J_c = 0.160(10)^{0.023V_c} J_B^{0.71}, \quad (7)$$

where $J_B = I_B/A$ and $J_c = I_c/A$.

Eq. (7) is the law representing the collector current as a function of beam current, spot size, and collector voltage for the oxide thickness employed and over the surface region investigated. In general, the law is of the form:

$$J_c = \alpha e^{\beta V_c} J_B^{\gamma}, \quad (8)$$

where α, β, and γ are functions of the oxide thickness and formation conditions. This law does not apply if V_c and I_c are above or below certain values. Possible reasons for this will be discussed below.

D. Decay characteristics

If I_b is suddenly reduced to zero by increasing the negative voltage on the grid of the electron gun, it is found that I_c does not immediately vanish but decreases rapidly at first, and then more slowly, and finally approaches a zero value asymptotically.

Samples of the decay characteristics for the same surface for which the preceding gain studies were made are shown in Fig. 9. Decay characteristics are extremely erratic in that small motions of the spot position cause large

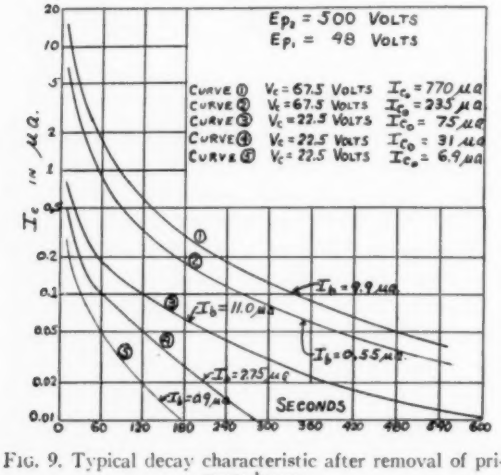
Ep_2 = 500 VOLTS
Ep_1 = 48 VOLTS
CURVE ① V_c = 67.5 VOLTS I_{c_0} = 770 μa
CURVE ② V_c = 67.5 VOLTS I_{c_0} = 235 μa
CURVE ③ V_c = 22.5 VOLTS I_{c_0} = 75 μa
CURVE ④ V_c = 22.5 VOLTS I_{c_0} = 31 μa
CURVE ⑤ V_c = 22.5 VOLTS I_{c_0} = 6.9 μa
I_b = 9.9 μa
I_b = 11.0 μa
I_b = 0.55 μa
I_b = 2.75 μa
I_b = 0.9 μa
SECONDS
I_c IN μa.

FIG. 9. Typical decay characteristic after removal of primary beam.

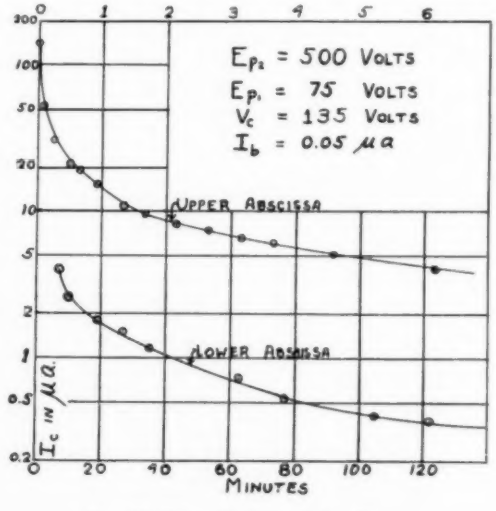

FIG. 10. Example of very slow decay.

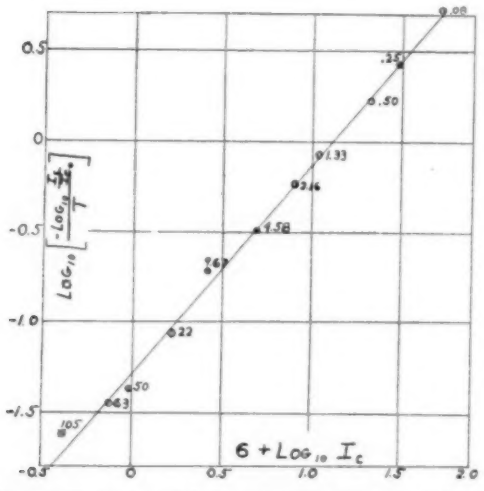

FIG. 11. Illustration of linear relation obeyed by persistent emission.

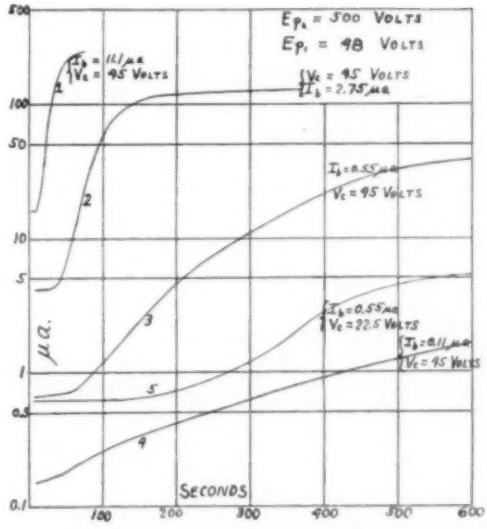

FIG. 12. Building-up curves obtained after reversal of collector potential with beam impinging on target.

changes in the rate of decay. However, in general it is true that the greater the gain, the slower the absolute decay but the more rapid the relative decay. To show the extreme variability of the decay characteristics another curve is shown in Fig. 10. This is the decay characteristic for an entirely different surface, formed at the same voltage as the one previously described. The gains from this surface were slightly higher than from the one studied. Unfortunately, before further measurements could be made, this surface was destroyed by overheating with high frequency. The decay time for this surface was of an entirely different order of magnitude, being measured in minutes rather than seconds. Current to the collector could be detected after 24 hours.

It has been found that if $\log[-\log(I_c/I_{c_0})/T]$ is plotted against $\log I_c$, a straight line is obtained. (T is the decay time). The case corresponding to Fig. 10 is shown in Fig. 11. The small numbers adjacent to the points represent the corresponding decay time in minutes. This linearity indicates that the neutralization of the surface charge is due primarily to the field emission itself.

If at any time during the decay the lead to the collector is opened momentarily, it is found on closing the circuit that I_c has dropped to practically zero. If V_c is reduced at any time during the decay, the rate of decrease of I_c is not affected unless V_c is reduced below some definite value, this value being lower the longer the decay period that has elapsed.

A more detailed consideration of the significance of decay characteristics will be given after the theory of the effect.

E. "Building-up" characteristics

If, at any time, I_b is first cut off by an increase in the grid bias, and then after I_c has dropped to a negligible value, I_b is suddenly restored to its original value, I_c returns to its final value very rapidly. If, instead of biasing off I_b, V_c is reduced to zero and then restored to its original value, I_c also returns to its original value very rapidly.

If, however, instead of reducing V_c to zero with I_b unchanged, V_c is actually reversed in direction so that the collector is negative with respect to the target, upon restoring V_c to its original positive value, the building-up takes on new and interesting forms. Some of these results are shown in Fig. 12 for cases wherein $V_c = 22.5$ volts and 45 volts. It is seen that the lower the values of I_b and V_c, the slower the building up. A curious feature is the fact that I_c remains constant for a considerable time before beginning its rise, particularly for low values of I_b and V_c.

If, instead of reversing V_c, a negative voltage

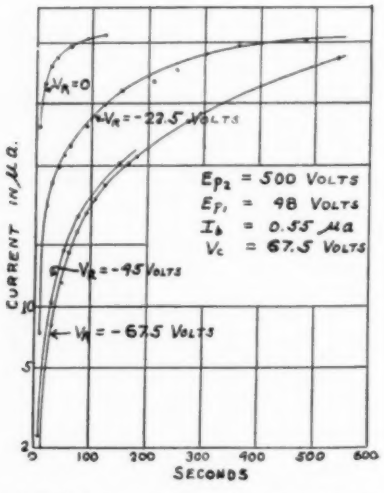

FIG. 13. Building-up curves when collector potentials are reversed to different negative values and subsequently restored to same positive value.

(V_R) different from V_c is applied to the collector and then the collector voltage is restored to its original V_c value, the building-up curves are altered. In Fig. 13 are plotted the building-up characteristics for $V_R=0$, -22.5, -45 and -67.5 volts, for the case where $V_c=67.5$ volts. As V_R is made smaller in absolute value, the building-up becomes more rapid. An interpretation of the various building-up curves will be given below.

F. Scintillations and alteration of characteristics

If V_c and I_b are increased beyond certain points, scintillations are observed on the aluminum oxide surface, their number and frequency increasing as V_c and I_b are raised. These scintillations alter the surface characteristics and, consequently, in the preceding experimental work, care was taken to keep them at a minimum. Their complete elimination is impossible except for very low values of V_c. Scintillations are undoubtedly due to momentary ruptures of the oxide film.

Continued scintillation causes a slow decrease in the gain characteristics, but a very rapid alteration in the decay characteristics. Continuous and rapid scintillations finally cause the complete disappearance of the thin film emission. A surface formed at 12 volts was run with $V_c=90$ volts. Under these conditions, the surface was covered with a uniformly dense distribution of pin-points of scintillation. After one-half hour these scintillations had completely disappeared, but so had the thin film emission.

G. Light effects

It was noted that the shining of light upon the surface always causes a marked decrease in I_c. In addition, light causes a marked increase in the rate of decay after I_b is cut off. The effects upon gain and decay were most marked for tubes with the longest decay. In certain cases a decrease in I_c of 200 microamperes was observed when a flashlight was shone upon the surface. The same light impinging upon a caesiated silver oxide surface resulted in a current yield of only 10 microamperes. Thus when used in this way the device is many times more "photosensitive" than the best surface heretofore known.

DISCUSSION OF EXPERIMENTAL RESULTS AND PROPOSED DESCRIPTION OF THE PHENOMENON

In the case of normal secondary electron emission, the primary electron reacts with the conduction electrons of the substance being bombarded in the presence of the force fields of the atoms or ions constituting the latter, resulting, in certain cases, in the transfer of sufficient backward momentum to conduction electrons to permit of their escape through the surface. The theory for the case of the uniform metallic lattice has been treated by Fröhlich.[6]

Thin film field emission appears to be due to an entirely different mechanism. The phenomenon appears to be closely related to one described by Güntherschulze[7] wherein extremely fine particles of aluminum oxide (among other substances) sprinkled on a semiconductor which serves as the cathode in a gas discharge, emit a copious stream of electrons with velocities corresponding to the cathode-anode difference of potential. In this case, according to Güntherschulze, positive ions lodge on the sides of the oxide particles away from the semiconductor and build up a positive charge thereon. If the gradient across any of the

[6] Fröhlich, Ann. d. Physik **13**, 229 (1932).
[7] Güntherschulze, Zeits. f. Physik **86**, 778 (1933).

particles becomes sufficiently great, electrons will be extracted from the underlying semiconductor. The effect disappears after several hours, apparently due to the mechanical rupture of the oxide particles by the high fields and high current densities present, with a consequent destruction of their insulating structure.

In the case of the thin film field emission the primary electrons impinging upon the treated aluminum oxide surface cause the release of true (i.e., normal) secondary electrons therefrom, these being attracted to the collector electrode. If the secondary emission ratio is greater than unity, more electrons will leave the surface than impinge upon it. Because of the high resistance of the oxide film, a positive charge is built up on the surface, this charge ultimately causing the extraction of electrons from the aluminum and aluminum oxide because of the intense gradients established. Thus in this case the emitted true secondary electrons take the place of the arriving positive ions in Güntherschulze's experiment.

Concomitant with the building up of the surface charge, the oxide becomes polarized, the polarization as well as the surface charge persisting after the removal of the primary beam. Evidence for the persistent polarization of aluminum oxide has been found by Güntherschulze and Betz.[8] In addition, space charges are established within the oxide, the sign of the charge depending upon the sign of the collector.

This picture enables the various manifestations of the phenomenon to be explained in a very convincing manner. These will be considered in turn.

1.

The reason for the special treatment required with caesium and oxygen is made clear. This treatment serves to form a thin, nonconducting film on the surface of the aluminum oxide whose true secondary emission ratio is considerably greater than unity, resulting in the rapid building up of the positive charge on the surface when bombarded with primary electrons. It is believed that the layer of caesium oxide is monomolecular. This belief is founded upon the following evidence:

(1) The amount of caesium beyond a certain minimum amount does not appear to affect the magnitude of the phenomenon.

(2) No change can be detected in the appearance of the oxide surface. In the case of silver oxide, on the other hand, the reduction of the oxide to appreciable depths by means of caesium is shown by the decided change in appearance.

(3) The heat of formation of aluminum oxide is so high that it cannot be reduced by metallic caesium. It is quite likely, however, that the heat of adsorption of caesium on aluminum oxide exceeds the heat of formation of the oxide.

The mere formation of the caesium layer on the surface, while it enhances the true secondary emission, does not by itself result in the appearance of the anomalous effect. This is due to the fact that the pure caesium film on the surfaces is conducting and thus prevents the positive charge from being established.

2.

The relation between collector current, beam current and collector voltage is expressed by Eqs. (1) and (4). It is of interest to note that Eq. (1) is of the same form as the relation between voltage and current for the composition material "Thyrite."[9] For this material the current is given by:

$$I = B V^m, \tag{9}$$

where B and m are constants which depend upon the proportions and nature of the constituents. Thyrite is composed of particles of carborundum coated with silica imbedded in a highly resistive matrix. Güntherschulze has ascribed the non-ohmic characteristic to the establishment of high gradients across the particles with a resultant "cold emission" through the particles. This view is borne out by the fact that the "cold emission" through the oxide films in this experiment, i.e., the thin film field emission, obeys a law of the same type.

The identity in form of the Thyrite law, Eq. (9), and the thin film field emission law, Eq. (1), indicates that in the case of this effect, the potential of the front surface of the aluminum oxide surface with respect to the underlying aluminum (denoted by (V_s)) is proportional to V_c, i.e.,

$$V_s \propto V_c.$$

[8] Güntherschulze and Betz, Zeits. f. Physik **73**, 580 (1932).

[9] McEachron, U. S. Patent #1,822,742.

3.

The time lags which are a feature of this effect are immediately explained by this picture. If the beam is turned on or increased, it takes an appreciable length of time for the region being bombarded to come to equilibrium under the opposing actions of the charging due to the true secondary emission and discharging due to leakage through the film, as well as for the polarization of the oxide and internal space charge to assume equilibrium values.

The time lag of the space charge is apparently very much greater than that of the surface charge. This belief is borne out by the experiments in which V_c was reversed with the beam on. On restoring V_c to its original direction, the surface charge undoubtedly reassumes its original positive value in a time no greater than the building up required when V_c is not reversed, but merely reduced to zero. Yet, the reversal of V_c greatly increases the building-up time. This increase can be due only to the fact that the field effective in extracting the electrons is weakened by the presence of negative space charge produced while the collector potential was reversed.

The persistence of the surface charge when the beam is cut off is demonstrated by the slow decay of I_c. Only a small portion of the field emission serves to neutralize the surface charge. This is also borne out by the virtual disappearance of collector current after a momentary opening of the collector circuit.

4.

The scintillations which appear for intense beams and high collector voltages are due to a violent breakdown of the oxide film. It was thought at first that this rupture would occur only if the surface target potential exceeded the formation voltage of the film. However, it was soon found that scintillations occurred when the collector voltage was less than the formation voltage. It was then believed that scintillations should not occur if the target surface potential were less than the critical potential V_b in the formation curve. (See Fig. 3.) It would appear that if the surface potential exceeded V_b there would be a tendency for ions to move through the film. However, since there is no electrolytic bath to supply the loss of ions at the outer surface, a rupture would occur. However, it was found that scintillations occurred when the collector voltage was considerably less than V_b. Apparently the breakdown is due to there being weak spots in the oxide film. When the sample is in the bath, any tendency to breakdown is overcome by the oxidizing action of the bath. This cannot, of course, occur in the vacuum tube. It is probable that invisible breakdowns occur down to very small values of V_c. Recently, Zauscher[10] has established a relation between film thickness and breakdown voltage for a film in air. For small thicknesses ($<$4000A), the relationship is given by:

$$\text{Breakdown Voltage} = 8\times 10^5 d,$$

where d, the film thickness, is measured in cm.

Thus for the 2000A film studied above, the breakdown voltage is 16 volts, whereas V_b is 78 volts and the formation voltage 116 volts.

The deviations from the laws as expressed in Eqs. (1) and (4) at high values of V_c may be due to V_S exceeding some definite value which may be the critical value of Zauscher's relation.

The fact that the deviation from linearity at the upper ends of Fig. 8 occur for approximately the same value of I_c and appear to be independent of V_c indicates that V_S is a function of I_c/A only.

5.

The sensitiveness of the treated surface to light appears to be explainable only by the ad hoc hypothesis that the aluminum oxide is photoconductive. Light falling upon the oxide causes a decrease in its effective resistance. When the electron beam and light are simultaneously impinging upon the surface, the surface equilibrium potential will take on a smaller value than with the light absent. The light also causes an increase in decay rates by permitting the surface charge to leak away more rapidly through the lessened effective resistance of the oxide film.

Thin Film Field Emission from Other Surfaces

Güntherschulze and Fricke[11] obtained field emission from a number of substances in a gas

[10] Zauscher, Ann. d. Physik **23**, 597 (1935).
[11] Güntherschulze and Fricke, Zeits. f. Physik **86**, 821 (1933).

discharge where the positive surface charge was produced by positive ions. A set-up similar to theirs was employed in which finely powdered material was rubbed onto an aquadag surface. The tube was treated with caesium and oxygen in the same manner as for aluminum oxide surfaces. The materials were then bombarded by an electron beam with an adjacent collector highly positive with respect to the aquadag. Field emission would be demonstrated by the presence of scintillations. The following materials were tried in this way: Ta_2O_5, MgO, $CaCO_3$, Al_2O_3, Zn_2SiO_4, willemite, $BeCO_3$, SiO_2, ZrO_2, and ThO_2, all of these materials having yielded positive results in the experiments of Güntherschulze and Fricke. Scintillations were observed in the cases of Al_2O_3, SiO_2, MgO, and willemite. The nonoccurrence of scintillations for the other materials does not indicate that field emission did not occur, but simply that the gradients established were not sufficient to cause breakdown. The coverage of the materials used was too small to enable the demonstration of any field effects as regards the collector current.

In addition, a number of other oxides were tried in tubes, but the results were generally negative. However, E. R. Piore, of the Electronic Research Laboratory of the RCA Manufacturing Company, obtained a pronounced field effect from Be oxidized in a glow discharge, then caesiated, and finally heated to dull redness inside the tube by means of high frequency induction. He has also observed the phenomenon with hot activated barium and strontium oxide cathodes.

The reason for the appearance of the phenomenon only in the case of a few out of a host of oxides tried can be accounted for on the basis of the possible chemical interactions between caesium and oxides. If an oxide is capable of reduction by the caesium, then the introduction of caesium into the tube will cause the destruction of the resistive properties of the oxide film. This will, of course, prevent the appearance of the field effect. In Table I, column one shows the oxide studied, column two its method of preparation, column three the heat of formation of the oxide *per unit atom* of oxygen, and column four the results achieved in an attempt to obtain field emission.

TABLE I. *Field emission from various oxides.*

1 Oxide	2 Mode of Preparation	3 Heat of Formation Per Unit Oxygen Atom (Cal.)	4 Results for Anomalous Effect
Al_2O_3	Electrolytically in borax plus boric acid bath	126,700	Positive
BeO	Glow discharge in oxygen	?	"
CaO	" " " "	151,900	Negative
CbO	Electrolytically in .1N H_2SO_4	?	"
Ag_2O	Glow discharge in oxygen	7,000	"
CuO	" " " " and heating in air	37,000	"
NiO	Glow discharge in oxygen and heating in air	57,900	"
Ta_2O_5	Electrolytically in .1N H_2SO_4	60,300	"
WO_2	" " "	65,700	"
ZrO	" " "	86,800	"

Since the heat of formation of Cs_2O is 82,700 calories, only the oxides of Al, Ca, Mg, Si, and Zr in the above list should show the field effect. The result is believed to be negative in the case of Ca because of the low resistance of the oxide.

An attempt to evaporate SiO_2 from a carbon cup subjected to intense electron bombardment, as described by O'Brien,[12] failed because of the reduction of the SiO_2 by the carbon, with the consequent profuse evolution of CO resulting in a gas discharge. No further attempt was made to evaporate quartz. However, the previously described experiment with the quartz powder indicates that it should yield field emission.

The Zr yielded a negative result, although from the figures cited a positive result should have appeared. However, in heating the tube to 200°C to promote the distribution of the caesium, apparently the heat of formation of the zirconium oxide dropped below that of the caesium oxide. This is evidenced by the decided change in color of the zirconium oxide during caesiation.

This change in the appearance of the oxide upon caesiation occurred whenever field emission failed to occur. The aluminum oxide, on the other hand, shows no change in appearance under the same conditions. This is evidence in favor of the belief that the caesium on the aluminum oxide is in the form of a monatomic layer.

[12] O'Brien, Rev. Sci. Inst. **5**, 125 (1934).

ACKNOWLEDGMENTS

I wish to express my appreciation to Professor Lloyd P. Smith, under whose direction this work was carried out, for his constant advice and encouragement.

I also wish to express my gratitude to Dr. V. K. Zworykin, of the Electronic Research Laboratory of the RCA Manufacturing Company, for extending to me the facilities of the laboratories for this work, as well as to express my appreciation for his constant advice and encouragement.

I am particularly indebted to Dr. E. G. Ramberg for many valuable discussions and for his contributions to the explanation of the phenomenon.

I wish to express my thanks to Messrs. H. W. Leverenz and H. W. Rhoades for the care in preparing the various oxidizing baths employed.

JULY 1, 1936 PHYSICAL REVIEW VOLUME 50

Theory of Brillouin Zones and Symmetry Properties of Wave Functions in Crystals

L. P. BOUCKAERT,* R. SMOLUCHOWSKI AND E. WIGNER, *The Institute for Advanced Study Princeton University, Princeton, New Jersey and the University of Wisconsin*

(Received April 13, 1936)

It is well known that if the interaction between electrons in a metal is neglected, the energy spectrum has a zonal structure. The problem of these "Brillouin zones" is treated here from the point of view of group theory. In this theory, a representation of the symmetry group of the underlying problem is associated with every energy value. The symmetry, in the present case, is the space group, and the main difference as compared with ordinary problems is that while in the latter the representations form a discrete manifold and can be characterized by integers (as e.g., the azimuthal quantum number), the representations of a space group form a continuous manifold, and must be characterized by continuously varying parameters. It can be shown that in the neighborhood of an energy value with a certain representation, there will be energy values with all the representations the parameters of which are close to the parameters of the original representation. This leads to the well-known result that the energy is a continuous function of the reduced wave vector (the components of which are parameters of the above-mentioned kind), but allows in addition to this a systematic treatment of the "sticking" together of Brillouin zones. The treatment is carried out for the simple cubic and the body-centered and face-centered cubic lattices, showing the different possible types of zones.

I.

INVESTIGATIONS of the electronic structure of crystal lattices in particular in metals, made on the basis of Bloch's theory, led to the conception of the so-called Brillouin zones.[1] In spite of these investigations, which cover a large part of the field, it seems desirable to develop the theory from a unique point of view. It appears that taking into account special symmetry properties of different lattices brings out interesting features of the constitution of the B-Z which are not evident from the existing general theory. These features can be dealt with

* C. R. B. Fellow.

[1] The existence of these zones was first noticed by M. J. O. Strutt, Ann. d. Physik **85**, 129 (1928); **86**, 319 (1929); and then, independently, by F. Bloch, Zeits. f. Physik **52**, 555 (1928); cf. also P. M. Morse, Phys. Rev. **35**, 1310 (1930). From another point of view, they were discussed by R. Peierls, Ann. d. Physik **4**, 121 (1930). Their connection with x-ray reflection was first pointed out by L. Brillouin (cf. e.g., *Die Quantenstatistik* (Berlin, 1931)). Important physical applications were given by H. Jones, Proc. Roy. Soc. **A144**, 225 (1934); **147**, 396 (1934); H. Jones, N. F. Mott and H. W. B. Skinner, Phys. Rev. **45**, 379 (1934); J. C. Slater, Phys. Rev. **45**, 794 (1934); Rev. Mod. Phys. **6**, 209 (1934); F. Hund and B. Mrowka, Ber. Sachs. Akad. D. Wiss. **87**, 185, 325 (1935). Compare also F. Hund, Zeits. f. tech. Physik **16**, 331, 494 (1935); Zeits. f. Physik **99**, 119 (1936). Hund's work deals with those properties of the Brillouin zones which are common to all zones of the same lattice (as matter of fact he does not discriminate between different types of zones at all). We consider here the different types of zone separately. The differences between the different types are of the same kind as e.g. the difference between even and odd terms in atomic spectra. It is surprising that there are at all common properties of all zones but Hund has shown that this is the case for the more complicated crystal structures.

uniformly by the methods of group theory,[2] and we propose to take up the subject here from this point of view. The first start in this direction has been made by F. Seitz,[3] and we shall use his results extensively, though a knowledge of his work should not be necessary for the understanding of this paper.

In the theory of Bloch, every electron has a separate wave function. This assumption is identical with the Hartree-Fock approximation method and amounts to neglecting the statistical correlations between electrons. If we neglect these correlations, every electron obeys a separate Schrödinger equation of the type

$$-\frac{\hbar^2}{2m}\left(\frac{\partial^2}{\partial x^2}+\frac{\partial^2}{\partial y^2}+\frac{\partial^2}{\partial z^2}\right)\psi+V\psi=E\psi \qquad (1)$$

in which V contains the ordinary and exchange potentials of the ions and electrons.[4] The potential V has the whole symmetry of the lattice, that is, the group of our Schrödinger equation (1) is the space group of the lattice.

It is clear from the ordinary group theory[2] that every characteristic value of (1) belongs to a certain representation of the space group and the dimension of the representation is equal to the number of characteristic functions belonging to this characteristic value.[5] Thus far the group theory of the B-Z is not different from the group theory of any other system. But while in atoms, molecules, etc., the characteristic values of (1) are well separated, the characteristic values of (1) for a crystal form a continuous manifold. There will be several characteristic values in the neighborhood of any one E and the representations of these characteristic values will be said to form the neighborhood of the representation of E for this B-Z. Thus a certain topology for the representations must exist and it will be shown that part of this topology is independent of the special B-Z. Even if E, E', $\cdots$ be in different B-Z but have the same representation, there will be energy values neighboring E (with a few exceptions) with the same representations as those of energy values neighboring E', etc. The investigation of the "topology" of representations will be essentially the subject of this paper, from the mathematical point of view.

II.

We must review next, the theory of representations of space groups. F. Seitz[3] has shown that all space groups are soluble groups and their representations can be obtained according to the general theory for these.[3, 6] Seitz first considers the invariant subgroup formed by the translations. Since these commute, the corresponding matrices in the representation can be assumed to have the diagonal form. This means that we shall consider such linear combinations ψ_μ ($\mu=1, 2, \cdots n$, where n is the dimension of the representation) of the wave functions, which are merely multiplied by constant factors ("multipliers") $\omega_{\mu 1}$, $\omega_{\mu 2}$, $\omega_{\mu 3}$ if a displacement by the three elementary identity periods is made. In other words, the matrix corresponding to the displacement by the first elementary identity period is a diagonal matrix with the diagonal elements ω_{11}, ω_{21}, $\cdots$, ω_{n1}, with similar matrices for the representatives of the other displacements. Since all matrices must be unitary, $|\omega_{\mu 1}|=|\omega_{\mu 2}|=|\omega_{\mu 3}|=1$; and if one writes

$$\begin{aligned}\omega_{\mu 1}&=e^{i(k_x x_1+k_y y_1+k_z z_1)}\\ \omega_{\mu 2}&=e^{i(k_x x_2+k_y y_2+k_z z_2)}\\ \omega_{\mu 3}&=e^{i(k_x x_3+k_y y_3+k_z z_3)}\end{aligned} \qquad (2)$$

with x_1, y_1, z_1, x_2, y_2, z_2, x_3, y_3, z_3, the x, y, z components of the first, second and third identity periods, the vector $\mathbf{k}$ is called[7] "the reduced wave number vector." Of course, $\mathbf{k}$ will be, in general, different for the different wave functions ψ_1, ψ_2, $\cdots$, ψ_n. It must be remembered, how-

[2] Cf. e.g., E. Wigner, *Die Gruppentheorie und ihre Anwendungen* (Braunschweig, 1931). The first application of group theory to crystal lattices has been given by H. Bethe, Ann. d. Physik **3**, 133 (1929).

[3] F. Seitz, Ann. of Math. **37**, 17 (1936).

[4] L. Brillouin, *Actualités Scientifiques et Industrielles* (Paris, 1933).

[5] To the symmetry operations of the space group, the "reversal of time" (cf. E. Wigner, Gott. Nachr. 546 (1932)) should be added. It has been remarked by F. Hund (reference 1) that this will often be of great importance. It can be omitted, however, in the case of the cubic lattices investigated here.

[6] G. Frobenius, Berl. Ber. 337 (1893); I. Schur, Berl. Ber. 164 (1906).

[7] Cf. A. Sommerfeld and H. Bethe's article in *Handbuch der Physik*, Vol. 24 (Berlin, 1933), chapter 3. Also J. C. Slater, Rev. Mod. Phys. **6**, 209 (1934). For a simple cubic lattice $x_1=y_2=z_3=d$; $y_1=z_1=x_2=z_2=x_3=y_3=0$. For a face centered lattice $y_1=z_1=x_2=z_2=x_3=y_3=d/2$; $x_1=y_2=z_3=0$, etc.

ever, that the reduced wave vector **k** is defined by (2) only up to an integer multiple of a vector **r** of the reciprocal lattice, i.e., a vector **r**, for which

$$\begin{aligned} r_x x_1 + r_y y_1 + r_z z_1 &= 2\pi n_1 \\ r_x x_2 + r_y y_2 + r_z z_2 &= 2\pi n_2 \\ r_x x_3 + r_y y_3 + r_z z_3 &= 2\pi n_3 \end{aligned} \tag{2a}$$

always can be added to **k**, without changing its meaning. The space of **k** is periodic with all the periods **r**, satisfying (2a); two reduced wave vectors differing by such an **r** are considered identical. If there are no essential gliding planes and screw axes in the space group,[8] one needs to consider, in addition to the above translations, rotations and reflections only. If such a transformation is applied to ψ_μ, it will be transformed into a wave function, say ψ_λ, the reduced wave vector of which arises from that of ψ_μ by just the rotation or reflection considered. Thus the reduced wave vectors of the wave functions of one representation all arise from one another by the pure rotations and reflections of the group, i.e., the elements of the crystal class. If the reduced wave vector of one ψ_μ is transformed by every element of the crystal class into a different vector, this will be true for all of them, and we shall have as many wave functions $\psi_1, \cdots, \psi_n$ as the crystal class has elements. The matrices of the representation corresponding to rotations and reflections will merely interchange the different ψ_μ. If there are symmetry elements which leave a wave vector invariant, they form a group which we shall call *the group of the wave vector*. So, for example, if the wave vector lies in the x direction, its group will contain all rotations around x and all reflections in planes through x.

A wave function ψ_μ with a wave vector **k** either is left invariant under the transformations of the group of **k**, or else transformed into a new ψ_λ with the same wave vector, **k**, however. In the first case there will be only one wave function with the wave vector **k**. In the second case there will be several of them and they will transform under the transformations of the group of **k** by an irreducible representation of this group, which we shall call the *small representation*. These are the results of Seitz.

Hence the representations of the space group must be characterized by two symbols. The first gives the reduced wave vectors (or set of ω) which occur in the representation; the figure of all these wave vectors forms a "star" with all the rotational and reflection symmetries of the lattice. Three such stars are given in Fig. 1 for

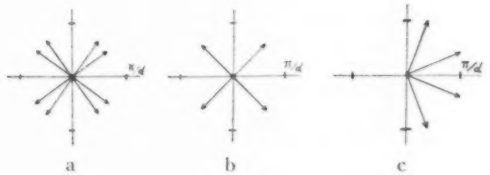

a b c

FIG. 1.

a two-dimensional quadratic lattice. The second symbol characterizes the small representation, which is an irreducible representation of the group of one wave vector (the groups of all wave vectors of a star are holomorphic). If the wave vectors lie in general positions (Fig. 1a) their group will contain the unit element only. In this case the second symbol may be omitted. It may be emphasized again that two wave vectors must be considered identical, if the corresponding set of ω's is the same. Thus for example, if the three $k_x x_i + k_y y_i + k_z z_i$ are all integer multiples of π (not necessarily of 2π) the wave vector k_x, k_y, k_z is identical with the wave vector $-k_x$, $-k_y$, $-k_z$ and the inversion ($x \to -x$, $y \to -y$, $z \to -z$) always belongs to the group of the wave vector.[9]

III.

We now consider an energy value E with a certain representation D and the wave functions $\psi_1, \cdots, \psi_n$. If we multiply one of these by $e^{i(\kappa_x x + \kappa_y y + \kappa_z z)}$ where κ_x, κ_y, κ_z, are the components

[8] We mean by this that all symmetry elements can be considered as products of two symmetry elements, the one of which is a pure translation, the other a pure rotation or reflection. This is the case in the most important space groups.

[9] It is in this connection that the time reversal is important (cf. F. Hund, reference 1). If the crystal class does not contain the inversion, k_x, k_y, k_z will still be carried over into $-k_x$, $-k_y$, $-k_z$ by the "time reversal." Since, as we shall see, the above consideration determines the surface of the *B-Z*, this will be fundamentally affected by the operation of time reversal.

of a very small vector, it will have the wave vector $\mathbf{k}+\boldsymbol{\kappa}$ and belong to a new representation D'. The set of new representations obtained in such a way will be called the neighborhood of D. It is clear that there will be near E, an E' with a representation D'. For if ψ_1 satisfies (1), $\psi_1 e^{i(\kappa_x x+\kappa_y y+\kappa_z z)}=\psi_1'$ satisfies

$$\left(-\frac{\hbar^2}{2m}\Delta+V\right)\psi_1'+\frac{\hbar^2 i}{m}\left(\kappa_x\frac{\partial}{\partial x}+\kappa_y\frac{\partial}{\partial y}+\kappa_z\frac{\partial}{\partial z}\right)\psi_1'$$
$$=\left(E+\frac{\hbar^2}{2m}(\kappa_x^2+\kappa_y^2+\kappa_z^2)\right)\psi_1'. \quad (3)$$

In this equation the second term is small, and its negative value may be treated as a perturbation. Performing the perturbation calculation, we shall obtain a characteristic value E' of (1) which is near E and the wave function of which will have the same translational symmetry as ψ_1', since both the original operator in (3), and the perturbation

$$-\frac{\hbar^2 i}{m}\left(\kappa_x\frac{\partial}{\partial x}+\kappa_y\frac{\partial}{\partial y}+\kappa_z\frac{\partial}{\partial z}\right) \quad (3a)$$

have the whole translational symmetry of the lattice.

This is all the general theory we need. If E had a star of the general type, the star of E' also will be of the general type and our result merely states the well-known fact, that the energy is a continuous (and even differentiable) function of the components of the wave vector. The set of all energies and wave functions which may be obtained from one single energy level continuously by this operation, never touching a point in which the star degenerates, is properly defined as one Brillouin zone. The restriction to such representations, the stars of which are of the general type, is necessary for the definition of a Brillouin zone, since, as we shall see, two or more Brillouin zones may stick together for degenerated stars (as those in Figs. 1b and 1c).

If we consider an energy value, the wave vectors of which are left invariant by some of the rotation or reflection operations, the situation still will be left essentially unchanged, if no two wave functions have the same reduced wave vector (the same multipliers). If, however, two or more (say s) wave functions have the same wave vector, and we choose κ_x, κ_y, κ_z in such a way that the new wave vector $(\mathbf{k}+\boldsymbol{\kappa})$ has the general position, there will be s orthogonal wave functions, with the wave vector $\mathbf{k}+\boldsymbol{\kappa}$ and with energies near E. Since for general wave vectors it never happens that two wave functions with the same wave vector belong to the same energy value, we must conclude that they all belong to different B-Z which are very close for small $\boldsymbol{\kappa}$ and that for the original energy value E these s B-Z "stick together." The sticking together will, therefore, always occur for such wave vectors which are left invariant by some symmetry operations.[10]

We must investigate two more cases. First let $\boldsymbol{\kappa}$ be such a vector that $\mathbf{k}+\boldsymbol{\kappa}$ still has the group of $\mathbf{k}$. In this case, the small representation of E is equivalent to the small representation of E'. Otherwise the wave functions would have to change abruptly even for a small change of $\mathbf{k}$. The sticking together will be the same along symmetry elements.

In the second case, the group of $\mathbf{k}+\boldsymbol{\kappa}$ is only a subgroup of $\mathbf{k}$, but still contains more than the identity. This case occurs, for instance, if we pass from a symmetry axis to a symmetry plane through this axis, or from the vector $\mathbf{k}=0$ to a symmetry axis. The small representations of E' will be irreducible representations of the subgroup, and if the small representation of E is not irreducible as representation of the group of $\mathbf{k}+\boldsymbol{\kappa}$, the B-Z which stuck together for $\mathbf{k}$ will be partly separated for $\mathbf{k}+\boldsymbol{\kappa}$. The small representations in these B-Z will be, for $\mathbf{k}+\boldsymbol{\kappa}$, the irreducible parts of the small representation of the group of $\mathbf{k}$.

The proposed characterization of a B-Z is given, hence, by the small representations of the groups of all wave vectors, which have a group greater than unity. For wave vectors lying in equivalent symmetry elements, the small representations are equivalent, and for a symmetry element which is a subgroup of another, the small representation must be contained in the small representation of the latter. Wherever the small representation is s dimensional, we have a sticking together of s B-Z, all of them having this same small representation for the

[10] Including the time reversal.

symmetry element under consideration. Again, it is important to remember that the group of the wave vector for which

$$k_x x_i + k_y y_i + k_z z_i = n_i \pi \quad (\text{for } i = i_1) \qquad (4)$$

holds for one i, say $i = i_1$, contains all elements which transform $\mathbf{k}$ in such a way, that $(k_x x_i + k_y y_i + k_z z_i)/\pi$ remains an integer for $i = i_1$ and is unchanged for the two other i, since the corresponding wave vectors are all the same.

The argument which shows that the small representation will be the same all along a symmetry element, breaks down for such points in which two B-Z touch each other, if no such touching is required by symmetry considerations. In the case that the energy for a certain value of $\mathbf{k}$ is the same in two B-Z, without this being the result of the symmetry, we speak of an accidental degeneracy.[10a] In points of accidental degeneracy, the small representations of the two B-Z may be interchanged, but the case of such an accidental degeneracy is explicitly excluded from the following considerations. One can see that it does not occur for very large lattice constants, though it may occur for the actual ones.

In the following sections, these results will be applied to the three most important cubic lattices, the simple, the face-centered, and the body-centered cubic lattices. Since, for instance all small representations of wave vectors in the fourfold axes are the same, this small representation will be called "the representation along the fourfold axis" and a similar notation will be used for the other symmetry elements.

It has been pointed out by J. C. Slater[1] that the energy as function of $\mathbf{k}$ should be considered as a periodic, multivalued function, the periods being the vectors of the reciprocal lattice. The "discontinuities" then arise from considering for some $\mathbf{k}$ one, for other $\mathbf{k}$ other branches of this multivalued function. In our way of talking, the periodicity is expressed by the fact that two wave vectors differing by a vector $\mathbf{r}$ of the reciprocal lattice, are considered identical. It is convenient to single out from all sets of "identical" vectors one (generally the shortest), and not to consider the rest at all. The manifold of these "reduced wave vectors" forms the inner of the B-Z, their boundary in the $k_x k_y k_z$ space (where the discontinuities are assumed ordinarily) forms the surface of the B.-Z.

The energy as function of $\mathbf{k}$ has, furthermore, all the symmetry of the (reciprocal) lattice. This is clear, since wave functions with all the $\mathbf{k}$ of a star belong to the same representation, and have the same energy, hence.

IV.

We want to consider the effect of the time reversal, first. This transforms $\mathbf{k}$ into $-\mathbf{k}$. Thus $-\mathbf{k}$ is always in the star of $\mathbf{k}$, even if there is no inversion center present: the energy as function of $\mathbf{k}$ is always equal for $\mathbf{k}$ and $-\mathbf{k}$. Just as for x-ray reflection, the inversion is always added to the symmetry of the problem.[11]

For a triclinic lattice, for instance, this means that the derivative of energy with respect to $\mathbf{k}$ is zero in the middle of the faces, edges and at the corner points of the B-Z, i.e., for

$$k_x x_i + k_y y_i + k_z z_i = n_i \pi \quad (i = 1, 2, 3). \qquad (5)$$

One can see directly also, that the group of these $\mathbf{k}$ contains the time reversal and the wave functions are real, hence. Thus the average value of the perturbation operator (3a) vanishes for these wave functions and the energy change goes with κ^2.

This cannot be claimed, however, for all the surface of the B-Z, i.e., for points for which only one of Eq. (5) is satisfied. The derivative of energy with respect to $\mathbf{k}$ will not vanish in these points and they will not really form the surface of the Brillouin zone.[12]

According to the program of section III, we shall determine now the small representations and their connections in the different types of B-Z for the simple cubic, body-centered, and face-centered cubic lattice. We shall begin with the simple cubic lattice, although no metal with this structure is known.

[10a] The case of an accidental degeneracy will be treated in a paper by C. Herring, to appear shortly. We wish to thank Mr. Herring for interesting discussions on this subject.

[11] Cf. G. Friedel, Comptes rendus **157**, 1533 (1913). For a more critical discussion of Friedel's rule, cf., however, e.g., P. P. Ewald's article in *Handbuch der Physik*, Vol. 23/2 (Berlin, 1933).

[12] It is not always true, thus, that the k for which $\partial E/\partial k = 0$, are those for which the Bragg conditions are satisfied.

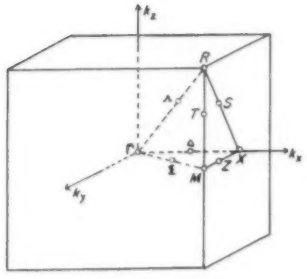

FIG. 2.

V.

Simple cubic lattice. Here the surface of the B-Z is a cube as represented in Fig. 2, with the cube edge $2\pi/d$. The inner symmetry elements are: the center Γ, the threefold axis Λ, the fourfold axis Δ, the twofold axis Σ, the symmetry planes $\Delta\Sigma$, $\Sigma\Lambda$ and $\Lambda\Delta$. The simplest way to obtain the group of a wave vector ending on the surface is to draw in all equally long wave vectors which are "identical" with it. The group of the figure constructed in this way is the group of the wave vector. For the arbitrary vector of the surface π/d, k_y, k_z, for instance, the figure contains the vector $-\pi/d$, k_y, k_z, and the group of the wave vector is, hence, the symmetry plane k_yk_z. Similarly, for the point T, there are four vectors $\pm\pi/d$, $\pm\pi/d$, k_z, and the group contains the fourfold axis k_z and all the symmetry planes through it. It is holomorphic with the group of the wave vector ending at Δ which contains the fourfold axis k_z and the symmetry planes through this. The group of S is holomorphic with that of Σ; that of Z contains the symmetry planes k_xk_y and k_yk_z and the rotation by π about k_y. R has the full cubic group like Γ; M has the group of T and, in addition, the symmetry plane k_xk_y. X has the same symmetry.

The tables[13] give the characters of the irreducible representations for the groups of the wave vectors designated in the upper left corner. The corresponding representations will be the "small representations" characterizing the B-Z. The upper right corner contains the group elements. E is the identity, its character will be the dimension of the representation. C_3 is the threefold axis; C_4, the rotation by $\pm\pi/2$ about the fourfold axis; C_4^2, the rotation by π about the same axis; and C_2 is the rotation about the twofold axis; J is the inversion. JC_4 is the product of J and C_4, etc. JC_2 and JC_4^2 are the reflections in the symmetry planes perpendicular to the twofold and fourfold axes, respectively. The figures before the symbols of group elements denote how many group elements of that kind are present in the group. The lower left corner gives the notation to be used to designate the small representation in question; it is always given for one of the wave vectors only, as, for instance, for Γ in Table I. The small representation of the wave vector R which has the same character as Γ_{12}' will be designated by R_{12}', etc. The lower right corner contains the character of the group element above it, for the representation to the left.

In order to save space we have included in the

[13] The representations of most crystallographic groups were given already by H. Bethe, loc. cit., reference 2. All of them are given in E. Wigner, Gött. Nachr. (1930), p. 133.

TABLE I. *Characters of small representations of* Γ, R, H.

Γ, R, H	E	$3C_4^2$	$6C_4$	$6C_2$	$8C_3$	J	$3JC_4^2$	$6JC_4$	$6JC_2$	$8JC_3$
Γ_1	1	1	1	1	1	1	1	1	1	1
Γ_2	1	1	−1	−1	1	1	1	−1	−1	1
Γ_{12}	2	2	0	0	−1	2	2	0	0	−1
Γ_{15}'	3	−1	1	−1	0	3	−1	1	−1	0
Γ_{25}'	3	−1	−1	1	0	3	−1	−1	1	0
Γ_1'	1	1	1	1	1	−1	−1	−1	−1	−1
Γ_2'	1	1	−1	−1	1	−1	−1	1	1	−1
Γ_{12}'	2	2	0	0	−1	−2	−2	0	0	1
Γ_{15}	3	−1	1	−1	0	−3	1	−1	1	0
Γ_{25}	3	−1	−1	1	0	−3	1	1	−1	0

TABLE II. *Characters for the small representations of* Δ, T.

Δ, T	E	C_3^2	$2C_4$	$2JC_3^2$	$2JC_2$
Δ_1	1	1	1	1	1
Δ_2	1	1	−1	1	−1
Δ_2'	1	1	−1	−1	1
Δ_1'	1	1	1	−1	−1
Δ_3	2	−2	0	0	0

TABLE III. *Characters for the small representations of* Λ, F.

Λ, F	E	$2C_3$	$3JC_2$
Λ_1	1	1	1
Λ_2	1	1	−1
Λ_3	2	−1	0

TABLE IV. *Characters for the small representations of* Σ, S.

Σ, S	E	C_2	JC_4^2	JC_2
Σ_1	1	1	1	1
Σ_2	1	1	−1	−1
Σ_3	1	−1	−1	1
Σ_4	1	−1	1	−1

tables some wave vectors (H and F) important for the body-centered lattice only.

For the points dealt with so far, it was sufficient to denote the group elements by the symbols C_2, C_3, etc., all the rotations about twofold axes being in the same class and having the same character in all representations. But for the point M, the rotation by π about the fourfold axes k_x, k_y is not equivalent to the rotation about the fourfold axis, k_z, which is perpendicular to the wave vector. The latter will be denoted by $C_4^2\perp$. Although the groups of the wave vectors ending at M and at X are holomorphic, the element in the second group which corresponds to $C_4^2\perp$ of the first is the rotation by π about k_x, which is the axis parallel to the wave vector ΓX. It will be denoted by $C_4^2\parallel$.

TABLE V. *Characters of small representations of* M, X.

M / X	E / E	$2C_4^2$ / $2C_4^2\perp$	$C_2\perp$ / $C_2\parallel$	$2C_4\perp$ / $2C_4\parallel$	$2C_2$ / $2C_2'$	J / J	$2JC_4^2$ / $2JC_4^2\perp$	$JC_2\perp$ / $JC_4^2\parallel$	$2JC_4\perp$ / $2JC_4\parallel$	$2JC_2'$ / $2JC_2''$
M_1	1	1	1	1	1	1	1	1	1	1
M_2	1	1	1	−1	−1	1	1	1	−1	−1
M_3	1	−1	1	−1	1	1	−1	1	−1	1
M_4	1	−1	1	1	−1	1	−1	1	1	−1
M_1'	1	1	1	1	1	−1	−1	−1	−1	−1
M_2'	1	1	1	−1	−1	−1	−1	−1	1	1
M_3'	1	−1	1	−1	1	−1	1	−1	1	−1
M_4'	1	−1	1	1	−1	−1	1	−1	−1	1
M_5	2	0	−2	0	0	2	0	−2	0	0
M_5'	2	0	−2	0	0	−2	0	2	0	0

TABLE VI. *Characters of small representations of* Z, G, K, U, D.

Z / G, K, U / D	E / E / E	C_4^2 / C_2 / C_2'	JC_4^2 / JC_4^2 / JC_2'	$JC_4^2\perp$ / JC_2 / $JC_2\perp$
Z_1	1	1	1	1
Z_2	1	1	−1	−1
Z_3	1	−1	−1	1
Z_4	1	−1	1	−1

This finishes the investigation of the symmetry axes in Fig. 2, and there remain only the symmetry planes. A somewhat closer inspection will show, however, that the small representations

TABLE VII. *Compatibility relations between* Γ *and* Δ, Λ, Σ.

Γ_1	Γ_2	Γ_{12}	Γ_{15}'	Γ_{25}'
Δ_1	Δ_2	$\Delta_1\Delta_2$	$\Delta_1'\Delta_5$	$\Delta_2'\Delta_5$
Λ_1	Λ_3	Λ_3	$\Lambda_3\Lambda_3$	$\Lambda_1\Lambda_3$
Σ_1	Σ_4	$\Sigma_1\Sigma_4$	$\Sigma_2\Sigma_3\Sigma_4$	$\Sigma_1\Sigma_3\Sigma_3$
Γ_1'	Γ_2'	Γ_{12}'	Γ_{15}	Γ_{25}
Δ_1'	Δ_2'	$\Delta_1'\Delta_2'$	$\Delta_1\Delta_5$	$\Delta_2\Delta_5$
Λ_2	Λ_1	Λ_3	$\Lambda_1\Lambda_3$	$\Lambda_2\Lambda_3$
Σ_2	Σ_3	$\Sigma_2\Sigma_3$	$\Sigma_1\Sigma_3\Sigma_4$	$\Sigma_1\Sigma_2\Sigma_4$

TABLE VIII. *Compatibility relations between* M *and* Σ, Z, T.

M_1	M_2	M_3	M_4	M_1'	M_2'	M_3'	M_4'	M_5	M_5'
Σ_1	Σ_4	Σ_1	Σ_4	Σ_2	Σ_3	Σ_2	Σ_3	$\Sigma_2\Sigma_3$	$\Sigma_1\Sigma_4$
Z_1	Z_1	Z_3	Z_3	Z_2	Z_2	Z_4	Z_4	Z_2Z_4	Z_1Z_3
T_1	T_2	T_2'	T_1'	T_1'	T_2'	T_2	T_1	T_5	T_5

TABLE IX. *Compatibility relations between* X *and* Δ, Z, S.

X_1	X_2	X_3	X_4	X_1'	X_2'	X_3'	X_4'	X_5	X_5'
Δ_1	Δ_2	Δ_2'	Δ_1'	Δ_1'	Δ_2'	Δ_2	Δ_1	Δ_5	Δ_5
Z_1	Z_1	Z_4	Z_4	Z_2	Z_2	Z_3	Z_3	Z_3Z_2	Z_1Z_4
S_1	S_4	S_1	S_4	S_2	S_3	S_2	S_3	S_2S_3	S_1S_4

prevailing on the symmetry axes already determine the representations for the symmetry planes, i.e., they determine whether the wave function will remain unchanged or assume the negative value, if reflected in one of the symmetry planes.

A B-Z must be characterized by one each of the following 10 symbols: Γ, Δ, Λ, Σ, R, T, M, S, X and Z. If there is an accidental degeneracy, however, the representation may change on an axis, etc. Not all the combinations of symbols correspond to possible B-Z. The small representation Δ on the fourfold axis must be contained in the representation Γ of the center, if this is considered as a representation of the group of Δ, and similar conditions exist between all pairs of adjoining symmetry elements. Table VII shows with which Δ, Λ, Σ, a certain Γ can be combined in the symbol of a possible B-Z. The compatibility relations between R and T, Λ, S, are the same as those between Γ and Δ, Λ, Σ. (Table VII.) These compatibility relations reduce considerably the number of possible types of B-Z. In addition to these compatibility relations, there are others originating from the four sets of wave vectors characterized by $k_z=0$; $k_x=k_y$; $k_y=k_z$; $k_x=\pi/d$. Every wave

vector satisfying one of these equations, has a group consisting of a symmetry plane, and the corresponding wave function will belong either to the symmetric, or to the antisymmetric representation of this group. This representation must be contained in the small representations of the axes lying in this plane. Table X gives, under +,

TABLE X. *Compatibility relations on symmetry planes.*

SYMMETRY PLANE	+	−
$k_z=0$	$\Sigma_1\Sigma_4$ $\Delta_1\Delta_2\Delta_5$ Z_1Z_3	$\Sigma_2\Sigma_3$ $\Delta_1'\Delta_2'\Delta_5$ Z_2Z_4
$k_x=k_y>k_z$	$\Sigma_1\Sigma_3$ $\Lambda_1\Lambda_3$ $T_1T_2'T_5$	$\Sigma_2\Sigma_4$ $\Lambda_2\Lambda_3$ $T_2T_1'T_5$
$k_y=k_z<k_x$	$\Lambda_1\Lambda_3$ S_1S_3 $\Delta_1\Delta_2'\Delta_5$	$\Lambda_2\Lambda_3$ S_2S_4 $\Delta_2\Delta_1'\Delta_5$
$k_x=\pi/d$	S_1S_4 $T_1T_2T_5$ Z_1Z_4	S_2S_3 $T_1'T_2'T_5$ Z_2Z_3

those representations along the axes, which are compatible with the symmetric representation in the plane, and under − those which are compatible with the antisymmetric representation. It shows that, for instance, Σ_1 is incompatible with Δ_1', Δ_2', Z_2, Z_4, Λ_2, T_2, T_1'.

As an example, we may consider the three B-Z which stick together at $k_x=k_y=k_z=0$ having for this wave vector the representation Γ_{25}. These three B-Z will be separated along the twofold axis, having there the small representations Σ_1, Σ_2, Σ_4, respectively (Table VII). We may consider the one with Σ_2. This necessarily goes with Δ_5 along the fourfold axis (Tables VII and X), and sticks together with one of the other zones there. Along the threefold axis it may have one of the two representations Λ_2 or Λ_3. We shall assume that it has Λ_2. For R, we still have the choice of R_2, R_{15}', R_1' or R_{25}. We shall choose R_2. This requires, then, S_4 and T_2, and hence Z_4. According to Table VIII, it will have M_3' and according to Table IX, X_5'. Its whole symbol will be $\Gamma_{25}\Sigma_2\Delta_5\Lambda_2R_{15}T_2S_4Z_4M_3'X_5'$ and we see that most small representations were uniquely given by the compatibility tables and the previous choices.

We believe that the above description of B-Z for the simple cubic lattice is complete from the point of view of symmetry. We are well aware, of course, that many of the types which are possible geometrically will not be important physically, since they have, for example, too high energies. It appeared to us, however, that for the sake of clarity a complete geometric discussion should be given once for a simple case.

The construction of the compatibility tables is very easy. If one is interested, e.g., in the compatibilities between Σ and M, one considers for M the characters corresponding to elements which are contained in Σ. These elements are E, C_2, $JC_4^2\perp$, JC_2 (one must take $JC_4^2\perp$, not JC_4^2, since the latter are the symmetry planes k_xk_z, k_yk_z which do not occur in the group of Σ). The corresponding characters in M_5, for instance, are 2, 0, −2, 0. One sees that this is the sum of the characters of Σ_2 and Σ_3 and these are, consequently, compatible with M_5. Thus it will not be necessary to give the compatibility relations for the other lattices explicitly.

VI. BODY-CENTERED CUBIC LATTICE

The shape of the surface of the B-Z is self-evident in the simple cubic lattice but not in the body-centered lattice. The identity periods can be taken as three space diagonals, with coordinates $1/2d$, $\pm1/2d$, $\pm1/2d$. The shortest vectors of the reciprocal lattice are the face diagonals, with coordinates 0, $\pm2\pi/d$, $\pm2\pi/d$; $\pm2\pi/d$, 0, $\pm2\pi/d$; $\pm2\pi/d$, $\pm2\pi/d$, 0. Since the inner of the B-Z should contain only different vectors $\mathbf{k}$, the addition of a vector of the reciprocal lattice to a $\mathbf{k}$ lying inside the B-Z must lead to a vector in the outside. This is most simply accomplished by choosing the rhombododecahedron of Fig. 3 as the surface, in which

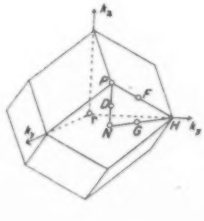

FIG. 3.

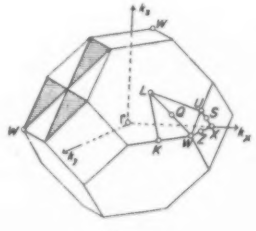

FIG. 4.

opposite faces just differ by a vector of the reciprocal lattice. The distance ΓH is $2\pi/d$.[14]

The symmetry elements in the inside of the B-Z are the same as in the simple cubic lattice, Γ, Δ, Λ, Σ, and the compatibility relations between these are also maintained. The point H has, however, the full cubic symmetry, since the vectors of the reciprocal lattice transfer it to all the end points of the coordinate axes. The point P is identical with three similar vertices, forming a tetrahedron.

TABLE XI. *Characters for the small representations of P.*

P	E	$3C_4^2$	$8C_3$	$6JC_4$	$6JC_2$
P_1	1	1	1	1	1
P_2	1	1	1	−1	−1
P_3	2	2	−1	0	0
P_4	3	−1	0	−1	1
P_5	3	−1	0	1	−1

TABLE XII. *Characters for the small representations of N.*

N	E	C_4^2	C_2H	$C_{2\perp}$	J	JC_4^2	$JC_{2\perp}$	JC_2H
N_1	1	1	1	1	1	1	1	1
N_2	1	−1	1	−1	1	−1	−1	1
N_3	1	−1	−1	1	1	−1	1	−1
N_4	1	1	−1	−1	1	1	−1	−1
N_1'	1	−1	1	−1	−1	1	1	−1
N_2'	1	1	1	1	−1	−1	−1	−1
N_3'	1	1	−1	−1	−1	−1	1	1
N_4'	1	−1	−1	1	−1	1	−1	1

The small representations for the other points were already given in the previous tables. We shall not give the compatibility relations between axes and points, since they are easily obtained by the method outlined in the previous section. It may be mentioned that the group of the vectors ending in a general point of the surface is the symmetry plane JC_2. The following relations are analogous to those of Table X.

TABLE XIII. *Compatibility relations for symmetry planes.*

SYMMETRY PLANE	+	−
$k_z=0$	$\Sigma_1\Sigma_4$, $\Delta_1\Delta_2\Delta_5$, G_1G_4	$\Sigma_1\Sigma_2$, $\Delta_1'\Delta_2'\Delta_5$, G_2G_3
$k_x=k_y>k_z$	$\Sigma_1\Sigma_3$, $\Lambda_1\Lambda_3$, D_1D_3	$\Sigma_2\Sigma_4$, $\Lambda_2\Lambda_3$, D_2D_4
$k_y=k_z<k_x$	$\Lambda_1\Lambda_3$, $\Delta_1\Delta_2'\Delta_5$, F_1F_3	$\Lambda_2\Lambda_3$, $\Delta_2\Delta_1'\Delta_5$, F_2F_3
$k_x+k_y=2\pi$	D_1D_4, F_1F_3, G_1G_3	D_2D_3, F_2F_3, G_2G_4

[14] The vectors $\mathbf{k}$ in the inside of the *B-Z* are transformed under this choice again into vectors in the inside by every symmetry element.

Since the surface of the B-Z is a symmetry plane, the derivative of the energy perpendicular to this plane is zero on the surface.

VII. FACE-CENTERED CUBIC LATTICE

The B-Z of the face-centered cubic lattice have a rather complicated structure. The reciprocal lattice is the body-centered lattice, the shortest vectors of which are the space diagonals with components $\pm 2\pi/d$, $\pm 2\pi/d$, $\pm 2\pi/d$. If we assume the inner of the B-Z to be bounded by the octahedron with the 8 planes $\pm x \pm y \pm z = 3\pi/d$, then no wave vectors of the inside will differ by one such vector. Nevertheless, some of them will be equivalent, differing by the sum of two shortest vectors of the reciprocal lattice, $\pm 4\pi/d, 0, 0; 0, \pm 4\pi/d, 0; 0, 0, \pm 4\pi/d$. In order to exclude these, one must cut off the corners of the octahedron by planes parallel to the coordinate planes at the distance $\pm 2\pi/d$ from these. The resulting figure is the well-known truncated octahedron of Fig. 4. With this choice of the surface of the B-Z, every wave vector of the inside will go over into a wave vector of the inside by all the symmetry operations. This requirement, however, which determines the whole shape of the surface for the simple cubic and body centered cases, fixes the surface here only at the truncating planes, but not at the octahedral planes. One could, for instance, bulge out in all octahedral planes the part which is shaded on one of the planes in Fig. 4 and bulge in by an equal amount the unshaded regions. The resulting surface would still satisfy all requirements. The truncating planes, on the other hand, cannot be deformed. If we pushed out a point on the $k_x=2\pi/d$ plane, we would have to push in the corresponding point on the $k_x=-2\pi/d$ plane. After this, however, the reflection on the k_yk_z plane would carry over wave vectors of the inside to the outside of the surface of the B-Z.

The B-Z is always uniquely determined if there is a symmetry plane perpendicular to the vector $\mathbf{r}$ of the reciprocal lattice,[15] which generates that part of the surface. In this case the surface lies at the distance $r/2$ on both sides of the symmetry plane. This was true for the vectors parallel to the coordinate axes which generated the surface

[15] Cf. Eq. (2a).

for the simple cubic lattice, it was true for the vectors parallel to the face diagonals in the body-centered structure and it is true for the vectors generating the truncating planes in Fig. 4. The situation for the octahedral plane of Fig. 4, however, is similar to that for the triclinic lattice and will be shown to have similar consequences.

Although the surface of the B-Z is thus left undetermined by general requirements, it is certainly allowable to assume it to have the shape of Fig. 4.

In the inside of the B-Z we have again the same situation as for the simple cubic lattice with the same compatibility relations holding between the small representations of Γ and the two-, three- and fourfold axes. This also applies to the points X, S and Z on the cubic plane. The point W is identical with three other points of the surface, two of which are shown on the figure, while one at the bottom is hidden. The small

TABLE XIV. *Characters of small representations of W.*

W	E	C_4^2	$2C_2$	$2JC_4$	$2JC_4^2$
W_1	1	1	1	1	1
W_1'	1	1	1	−1	−1
W_2	1	1	−1	1	−1
W_2'	1	1	−1	−1	1
W_3	2	−2	0	0	0

TABLE XV. *Characters of small representations of L.*

L	E	$2C_3$	$3C_2$	J	$2JC_3$	$3JC_2$
L_1	1	1	1	1	1	1
L_2	1	1	−1	1	1	−1
L_3	2	−1	0	2	−1	0
L_1'	1	1	1	−1	−1	−1
L_2'	1	1	−1	−1	−1	1
L_3'	2	−1	0	−2	1	0

representations for the points K and U were given in Table VI. L is identical with its antipode. The points Q on the line LW cannot be moved in or out. They belong to the surface, since they are carried over into themselves (i.e., into the "identical" point on the opposite face) by the twofold axis bisecting the Z and $-X$ axes. The wave function of the wave vector ending at Q will be either symmetric or antisymmetric with respect to this rotation. In the former case it is compatible with L_1, L_1', L_3, L_3' on one side and with $W_1W_1'W_3$ on the other. If it is antisymmetric, it is compatible with L_2, L_2', L_3, L_3' and W_2, W_2' and W_3.

The group of the points on the lines LK, KW, LU, UW contains only the symmetry plane on which they lie, they have no additional symmetry owing to their position on the surface. This is natural, since the surface can be shifted away from them. The Compatibility Table X holds for $k_x=k_y>k_z$ between Σ and Λ, but there is nothing to replace T, and T must be omitted also from the last section of $(k_z=\pi/d)$ of this table. The rest of the table remains valid, however, and should be supplemented by the compatibilities just given, owing to the symmetry of the point Q.

The surface of the B-Z at the octahedral planes cannot be chosen in such a way that the "identical" point $k_x-2\pi/d$, $k_y-2\pi/d$, $k_z-2\pi/d$ to every point of the surface could be reached by a symmetry operation also. This has the consequence that the derivative of the energy perpendicular to the somewhat arbitrarily chosen plane octahedral face will only vanish on the diagonals (LW) corresponding to the separating lines between shaded and unshaded regions. On the other hand, it will have the consequence also that the energy for $k_x=\pi/d+\mu$, $k_y=\pi/d-\mu-v$, $k_z=\pi/d+v$ will be equal to the energy for $-\pi/d+\mu$, $-\pi/d-\mu-v$, $-\pi/d+v$ and, because of the twofold axis, also equal to the energy for $\pi/d-v$, $\pi/d+\mu+v$, $\pi/d-\mu$. The energy as function of $\mathbf{k}$ will be symmetric with respect to the line LW on the surface and, hence, will have on the octahedral *surface*, a sixfold rotational symmetry.

The Heat Conductivity of Tungsten and the Cooling Effects of Leads upon Filaments at Low Temperatures

IRVING LANGMUIR AND JOHN BRADSHAW TAYLOR, *General Electric Company*

(Received May 4, 1936)

The theory and the equations governing the temperature distribution, resistance, and heat flow in a tungsten filament as affected by its leads are given for the low temperature range (<600°K), both for the general case and for several special cases. *A low temperature vs. current scale for tungsten* is calculated from these equations using measurements of heat conductivity given in this paper and previously obtained data on the radiating properties and resistance of tungsten. It is given in the form of tables and formulas from which, knowing the current, filament dimensions, and lead and bulb temperatures one can find the maximum temperature, T_1, of the filament. Methods are described for calculating the effect on T_1 of a spring attached to one end of the filament. *The heat conductivity of tungsten*, λ, was determined experimentally for this low temperature range. λ at 273°K is 1.66 watts cm^{-1} deg.$^{-1}$ and decreases with rising temperature according to the equation $\log \lambda \pm 0.9518 = 0.30 \log T$ to 1.31 at 600°K.

I. INTRODUCTION

IN a recent paper[1] we have described experiments with an evacuated tube containing a tungsten filament attached to leads which could be maintained at any desired temperature (220° to 600°K). In the experiments already considered, the lead temperature, T_0 (°K), was higher than the bulb temperature T_B; and the current A through the filament was adjusted so that the filament was also at the temperature T_0, as indicated by its resistance, the resistance-temperature curve having been previously determined. In this way the cooling effect of the leads was eliminated and thus the power input gave directly the difference between the power radiated and that absorbed from the back-radiation from the bulb.

The results were accurately expressible by the equation

$$W = K(T^{\omega} - T_B{}^{\omega-\epsilon}T^{\epsilon}), \qquad (1)$$

where $\omega = 5.332$; $\epsilon = 0.87$; $\log_{10} K = 83.7105 - 100$; and W is the net radiation in watts cm^{-2} at a temperature T in a bulb at T_B.

It is the object of the present paper to describe experiments with the same tube in which the current A is no longer held at the value which makes the filament temperature equal to T_0. Measurements of the resistance and voltage input enable us to calculate the heat conductivity of the filament and the temperature distribution along the filament.

Forsythe and Worthing[2] have measured the temperature distribution along incandescent filaments near the leads and have calculated the heat conductivity λ. Their results are reproduced (within 0.2 percent) by the equation

$$\lambda = 0.840(T/1000)^{0.4} \text{ watts cm}^{-1} \text{ deg.}^{-1}. \qquad (2)$$

Langmuir, MacLane, and Blodgett[3] used this relation in developing equations for calculating the change in any of the characteristics of a filament which results from the cooling effect of the leads. The temperature distribution, determined by an optical pyrometer, over the central part of short filaments agreed well with that calculated and thus confirmed the accuracy of the Forsythe-Worthing values of the heat conductivity at temperatures above 1500°K. The analysis of the data, however, led to the conclusion that at lower temperatures the heat conductivity must be greater than is given by Eq. (2).

The heat conductivity of tungsten at 0°C is given by Barratt[4] as 1.60 watts cm^{-1} deg.$^{-1}$ and by Kannuluik[5] as 1.66. The experimental method of Kannuluik appears to be very accurate, but it should be noted that he "annealed" the tungsten only at 1300°C, a temperature which is quite insufficient to bring drawn tungsten wires into a steady state. He gives the specific electric re-

[1] I. Langmuir and J. Bradshaw Taylor, J. Opt. Soc. Am. **25**, 321 (1935). (Referred to as Paper I.)

[2] W. E. Forsythe and A. G. Worthing, Astrophys. J. **61**, 146 (1925).

[3] I. Langmuir, S. MacLane and K. B. Blodgett, Phys. Rev. **35**, 478 (1930). References to previous literature on the cooling effects of leads are given.

[4] T. Barratt, Proc. Phys. Soc., London **26**, 347 (1914).

[5] W. G. Kannuluik, Proc. Roy. Soc. **A131**, 320 (1931); **A141**, 159 (1933).

sistance of the wires as 6.0×10^{-6} after annealing at 200°C and 5.65×10^{-6} after annealing at 1300°C. These resistances are 20 and 13 percent, respectively, higher than normal values for well aged tungsten. Langmuir has shown[6] that a drawn tungsten wire undergoes a 15 to 20 percent decrease in cold resistance when first heated to 1500° for one minute and a further decrease of 2 to 4 percent upon aging for 24 hours at 2400°K.

There is therefore evidently a need to know λ more accurately in the range of temperatures below 1500°K. In some studies of the adsorption of caesium on thoriated tungsten filaments by methods already described[7] we have needed to know accurately the relation between the temperature at the midpoint of the filament and the heating current even when the filament temperature only slightly exceeds the bulb temperature.

II. Theory[8] of the Effect of Leads on the Temperature Distribution and Resistance

The general equation for the temperature distribution along a filament of nonuniform temperature is given by

$$\pi r^2\frac{d}{dx}\left(\lambda\frac{dT}{dx}\right)=2\pi rW-A^2R/\pi r^2. \tag{3}$$

Here r is the radius of the filament, λ is the heat conductivity, T is the absolute temperature at a point x along the filament, W is the net radiation from the filament at the point x in watts cm^{-2}, A is the current through the filament in amperes, and R is the specific resistance of the filament in ohm cm.

It is desirable to express Eq. (3) in terms of dimensionless quantities. For this purpose we will replace T by θ defined as follows:

$$\theta=(T-T_0)/T_0; \quad \text{or} \quad T=(1+\theta)T_0, \tag{4}$$

where T_0 is the temperature of the leads.

Let A_0 be the current in amperes, which must be passed through the filament in order to maintain the filament at the uniform temperature T_0 when the bulb is at 0°K, or at any temperature so low that there is no appreciable back-radiation from the bulb. The value of A_0 is evidently given by Eq. (3) if we place $dT/dx=0$, so that

$$A_0^2=2\pi^2r^3W_0/R_0, \tag{5}$$

where W_0 and R_0 are the values of W and R which correspond to the case that the bulb is at 0°K and the whole filament is at T_0.

The current A is conveniently expressed in terms of a dimensionless quantity β defined by

$$\beta=(A/A_0)^2. \tag{6}$$

When the current A is small so that θ is small compared with unity, the values of θ should increase approximately in proportion to A^2, or in other words θ should vary approximately linearly with β.

If we insert these values from Eqs. (4), (5), and (6) into Eq. (3), we obtain

$$H\frac{d}{dx}\left(\frac{\lambda}{\lambda_0}\frac{d\theta}{dx}\right)=\frac{W}{W_0}-\beta\frac{R}{R_0}, \tag{7}$$

where H, a quantity having the dimensions of the square of a length, is given by

$$H=r\lambda_0T_0/2W_0. \tag{8}$$

Here λ_0 is the value of λ which corresponds to T_0.

By Eq. (1) we see that

$$W_0=KT_0^{\omega} \tag{9}$$

and

$$W/W_0=(1+\theta)^{\omega}-(1+\theta_B)^{\omega-\epsilon}(1+\theta)^{\epsilon}, \tag{10}$$

where θ_B is the value of θ corresponding to the bulb temperature T_B. We have seen that to maintain the filament at T_0 when $T_B=0$ requires that $\beta=1$. Let β_0 be the value of β which corresponds to the current required to maintain the filament at T_0 when the bulb is at any temperature T_B. In this case we may put in Eq. (7) $d\theta/dx=0$ and $R=R_0$ and so obtain

$$\beta_0=W/W_0 \quad \text{when} \quad \theta=0$$

and then by Eq. (10) we find

$$\beta_0=1-(1+\theta_B)^{\omega-\epsilon}. \tag{11}$$

---

[6] I. Langmuir, Phys. Rev. **7**, 302 (1916), see p. 313.

[7] J. Bradshaw Taylor and I. Langmuir, Phys. Rev. **44**, 423 (1933).

[8] The theory and equations in this part and in Part III enabled us to develop a temperature current scale for tungsten (Part V) in a convenient form but need not be referred to when calculating temperatures since Part V has been made complete in itself.

By using this relation, Eq. (10) may be written

$$W/W_0=(1+\theta)^\omega-(1-\beta_0)(1+\theta)^\epsilon. \quad (12)$$

Over very wide ranges of temperature the specific resistance R of tungsten increases in proportion to T^ρ where ρ is a constant. Therefore, we have

$$R/R_0=(1+\theta)^\rho. \quad (13)$$

We shall see that λ does not have a large temperature coefficient. Within a reasonably large range of temperatures we may assume that λ varies in proportion to a power of the temperature, so that

$$\lambda=\lambda_0(1+\theta)^k, \quad (14)$$

where k is a constant.

Instead of expressing our equations in terms of x, the absolute length along the filament, let us now use a new variable φ defined by

$$\varphi=(W_0/r\lambda_0T_0)^{\frac{1}{2}}x=x(2H)^{-\frac{1}{2}}. \quad (15)$$

With these substitutions into Eq. (7) we have

$$\frac{1}{2}\frac{d^2\theta}{d\varphi^2}+\frac{k}{2(1+\theta)}\left(\frac{d\theta}{d\varphi}\right)^2=(1+\theta)^{\omega-k}-(1-\beta_0)(1+\theta)^{\epsilon-k}-\beta(1+\theta)^{\rho-k}. \quad (16)$$

By replacing $(d\theta/d\varphi)^2$ and $\log(1+\theta)$ by new variables, this equation can be brought to the linear form and one integration can be performed. In this way we obtain

$$(1+\theta)^k(d\theta/d\varphi)=2(F-F_1)^{\frac{1}{2}}, \quad (17)$$

where

$$F=[(1+\theta)^{\omega+k+1}-1]/(\omega+k+1)-(1-\beta_0)[(1+\theta)^{\epsilon+k+1}-1]/(\epsilon+k+1)-\beta[(1+\theta)^{\rho+k+1}-1]/(\rho+k+1). \quad (18)$$

The quantity F_1 may be regarded as an integration constant.

In general we shall measure x and φ from the point where the filament temperature is a maximum, but if the two leads which cool the filament are at the same temperature T_0, then the maximum is also the midpoint. For this condition then, at the center of the filament the temperature gradient is zero and therefore $d\theta/d\varphi=0$. Let the value of θ at the maximum (center in this case) be θ_1. Then the value of F_1 is given by Eq. (18) if we replace θ by θ_1.

Let x_0 and φ_0 be the values which correspond to the ends of the filament where $T=T_0$. These quantities then represent the half-length of the filament. By integration of Eq. (17) we obtain

$$\varphi=(1/2)\int_0^{\theta_1}(1+\theta)^k(F-F_1)^{-\frac{1}{2}}d\theta. \quad (19)$$

We can thus express θ as a function of φ and so obtain the temperature distribution along the filament.

We are also interested in knowing the resistance of the filament. Let Ω be the resistance of the half-length x_0 of the filament when the current A is passing and let Ω_0 be the value of Ω when the filament is at the temperature T_0. Then by Eq. (13) we have

$$\Omega/\Omega_0=\int_0^{x_0}(1+\theta)^\rho(dx/x_0). \quad (20)$$

By Eq. (15) φ is proportional to x, and therefore

$$dx/x_0=d\varphi/\varphi_0=(d\theta/\varphi_0)(d\varphi/d\theta). \quad (21)$$

Substituting this into Eq. (20) and combining with Eqs. (17) and (19) gives

$$(\Delta\Omega)/\Omega_0=(1/2\varphi_0)\int_0^{\theta_1}[(1+\theta)^\rho-1]\times(1+\theta)^k(F-F_1)^{-\frac{1}{2}}d\theta. \quad (22)$$

In this equation $\Delta\Omega$ has been used to denote the increase in resistance $(\Omega-\Omega_0)$ caused by increasing the current from A_0 to A.

Relation between φ_0 and the voltage V_0

Let us consider again the filament maintained at the lead temperature T_0 by the current A_0 while the bulb is at 0°K. Then according to the definitions already given, the radiation in watts per cm² is W_0 and the specific resistance is R_0. Let V_0 be the voltage drop along the half-length, x_0, of the filament. Then we have

$$W_0=A_0V_0/2\pi rx_0 \quad (23)$$

and

$$R_0=\pi r^2V_0/A_0x_0. \quad (24)$$

Multiply these equations and solve for V_0 and obtain

$$V_0=(2W_0R_0/r)^{\frac{1}{2}}x_0. \quad (25)$$

Eq. (15) furnishes us with another relation involving W_0/r. If we eliminate this factor between Eqs. (15) and (25) we get

$$V_0 = h_0 \varphi_0, \tag{26}$$

where $$h_0 = (2R_0 T_0 \lambda_0)^{\frac{1}{2}} \tag{27}$$

and h_0 is the value, at $T = T_0$, of a quantity h defined by

$$h = (2RT\lambda)^{\frac{1}{2}}. \tag{27a}$$

This parameter h is a specific property of tungsten as it depends on the temperature but not on the dimensions of the filament. We see from Eq. (26) that it has the dimensions of a voltage.

According to the Wiedemann-Franz law, λR, at a given temperature, is nearly the same for all metals and according to Lorenz λR increases in proportion to T. If these laws are applicable, h should increase in proportion to T but should be the same for all metals.

Flow of heat along the filament

Let Q be the heat flux along a filament in watts; then

$$Q = \pi r^2 \lambda dT/dx. \tag{28}$$

By Eqs. (4), (14), and (27) this becomes

$$Q = (\pi r^2 h_0^2 / 2R_0)(1+\theta)^k d\theta/dx. \tag{29}$$

In Eq. (15) we can eliminate $\lambda_0 T_0$ by using Eq. (27) and by Eq. (5) we obtain

$$x = (\pi r^2 h_0 / A_0 R_0)\varphi. \tag{30}$$

By combining Eqs. (17), (30), and (29) we find

$$Q = A_0 h_0 (F+c)^{\frac{1}{2}}, \tag{31}$$

where we have used c to represent the integration constant.

Eq. (31) is applicable to the flow of heat through a spring or lead to which a filament is attached. In such a case the heat flowing into the hot end may be such that there is no value of θ which makes $d\theta/d\varphi = 0$. A similar case arises if a filament is attached to two leads, one of which is at a temperature above T_M, while the other is below T_M, where T_M is the temperature to which the current A would heat the central part of the filament if it were infinitely long. The value of Q is then not zero even when $\theta = \theta_M$. In such cases the integration constant c is to be determined by the boundary conditions.

With a filament having two leads at the temperature T_0, c becomes $-F_1$, and the heat that flows into each lead is given by

$$Q_0 = A_0 h_0 (-F_1)^{\frac{1}{2}} \tag{32}$$

since, by Eq. (18), $F = 0$ when $\theta = 0$.

Eqs. (19), (22), and (31) represent the general solutions of the problems of the temperature distribution, the resistance and the heat flow in filaments. There are, however, certain special cases in which the equations can be so simplified as to facilitate the calculations. We shall consider some of these.

Case 1: Low Values of θ_1. When β differs only little from β_0, the temperature of the whole filament is not far above T_0 so that we may take λ as constant and then put $k = 0$. Furthermore, in Eq. (16) we may expand the terms involving powers of $1+\theta$. If we omit terms involving powers of θ higher than the first, the equation becomes linear and can be integrated. Choosing the integration constants so that $d\theta/d\varphi = 0$ when $\varphi = 0$, and at the leads where $\varphi = \varphi_0$, $\theta = 0$, we thus find that the temperature distribution along the filaments is given by

$$\theta = \frac{2(\beta - \beta_0)}{C^2}\left[1 - \frac{\cosh C\varphi}{\cosh C\varphi_0}\right], \tag{33}$$

where $$C^2 = 2[\omega - \epsilon + \beta_0(\epsilon - \rho)]. \tag{34}$$

The temperature at the center of the filament is found by putting $\varphi = 0$:

$$\theta_1 = [2(\beta - \beta_0)/C^2](1 - \operatorname{sech} C\varphi_0). \tag{35}$$

By expanding the factor $(1+\theta)^\rho$ in Eq. (20), combining with Eq. (21) and inserting the value of θ as given by Eq. (33) we find

$$\Delta\Omega/\Omega_0 = \frac{2\rho(\beta - \beta_0)}{C^2}\left[1 - \frac{\tanh C\varphi_0}{C\varphi_0}\right]. \tag{36}$$

Short Filament: When φ_0 is sufficiently small, we can expand the cosh factors in Eq. (33) and so reduce the equation to

$$\theta = (\beta - \beta_0)(\varphi_0^2 - \varphi^2)[1 - (C^2/12)(5\varphi_0^2 - \varphi^2)]. \tag{37}$$

Thus when φ_0^2 is small compared to unity the

temperature distribution is parabolic, and the heat transfer by radiation is small compared to that conducted.

A similar expansion applied to Eq. (36) gives

$$\Delta\Omega/\Omega_0=(2/3)(\beta-\beta_0)\rho\varphi_0^2(1-2C^2\varphi_0^2/5). \quad (38)$$

Long Filament: When the filament is so long that $C^2\varphi_0^2>6$, then the relationship of Eq. (33) may be sufficiently accurately expressed (within 1 percent) by

$$\theta=\theta_M[1-e^{C(\varphi-\varphi_0)}], \quad (39)$$

where

$$\theta_M=2(\beta-\beta_0)/C^2. \quad (40)$$

In this case the temperature is practically uniform at θ_M over the central part of the filament.

When $C^2\varphi_0^2\gg 6$ the hyperbolic tangent in Eq. (36) becomes unity so that

$$\Delta\Omega/\Omega_0=\frac{2\rho(\beta-\beta_0)}{C^2}-B_\infty/\varphi_0, \quad (41)$$

where

$$B_\infty=2\rho(\beta-\beta_0)/C^3. \quad (42)$$

Thus when the filament is long, $\Delta\Omega/\Omega_0$ varies linearly with $1/\varphi_0$.

Case 2: Large values of β (*or* $\epsilon=\rho$). If a filament is very long, the cooling effect of the leads becomes inappreciable in the central part of the filament and for this region we may put in Eq. (16) $d\theta/d\varphi$ and $d^2\theta/d\varphi^2$ both equal to zero and thus obtain

$$(1-\beta_0)+\beta(1+\theta_M)^{\rho-\epsilon}=(1+\theta_M)^{\omega-\epsilon}, \quad (43)$$

where θ_M is the value of θ over the central part of a very long filament corresponding to a temperature T_M.

Let us now introduce into Eq. (18) a new variable defined by

$$\sigma=(1+\theta)/(1+\theta_M)=T/T_M. \quad (44)$$

If we then eliminate β by Eq. (43), we find for the value of $F-F_1$, which is needed for Eq. (19),

$$F-F_1=(1+\theta_M)^{\omega+k+1}(H_1-H), \quad (45)$$

where

$$H=\frac{\sigma^{\rho+k+1}}{\rho+k+1}-\frac{\sigma^{\omega+k+1}}{\omega+k+1}+\left(\frac{\sigma^{\epsilon+k+1}}{\epsilon+k+1}-\frac{\sigma^{\rho+k+1}}{\rho+k+1}\right)\Big/\left(1+\frac{(1+\theta_M)^{\rho-\epsilon}\beta}{1-\beta_0}\right) \quad (46)$$

and H_1 is obtained from this equation by putting $\sigma=\sigma_1=(1+\theta_1)/(1+\theta_M)$.

The last term in Eq. (46) becomes negligible when $\epsilon=\rho$; $\sigma\ll 1$; or when $\beta/(1-\beta_0)$ is very large. This occurs acccording to Eq. (11) if T_B is small compared to T_0 or if β is very large compared to unity. The data previously published[1] have given $\omega=5.332$; $\rho=1.23$; and $\epsilon=0.87$ for the temperature range from 250° to 600°K. Because of this small difference of 0.36 between ρ and ϵ the errors made by replacing ϵ by ρ in Eq. (46) are small even when β is comparable with unity.

The greatest errors in φ_0 with small values of β occur with filaments so long that σ_1 is nearly unity and may approach a limiting fractional error of $(\rho-\epsilon)/2(\omega-\rho)$ or about 4.5 percent. With shorter filaments for which σ_1 is considerably less than unity, the errors are much smaller.

Replacing ϵ by ρ in Eq. (46), substituting in Eqs. (45) and (19), we are led to the following equations:

$$\varphi=\sigma_0^{(\omega-k-1)/2}(Y_1-Y), \quad (47)$$

where

$$\sigma_0=1/(1+\theta_M), \quad (48)$$

$$Y=(1/2)\int_0^\sigma \sigma^k d\sigma(G_1-G)^{-\frac{1}{2}}, \quad (49)$$

and

$$G=\frac{\sigma^{\rho+k+1}}{\rho+k+1}-\frac{\sigma^{\omega+k+1}}{\omega+k+1}. \quad (50)$$

Similarly from Eqs. (20) and (21) we obtain

$$\Omega/\Omega_0=\sigma_0^{-\rho}(Z_1-Z_0)/(Y_1-Y_0), \quad (51)$$

where

$$Z=(1/2)\int_0^\sigma \sigma^{\rho+k}d\sigma(G_1-G)^{-\frac{1}{2}}. \quad (52)$$

The temperature distribution and the resistance of filaments is thus given by Eqs. (47) and (51) in terms of the functions Y and Z. These calculations are most readily made by series expansions in terms of powers of σ or of $(1-\sigma)$. Although general expansions can be obtained for the coefficients of the terms of these series, they are too complicated to justify their presentation here. In the third part of this paper we shall give such series for the particular values of ω and ρ which have been adopted.

Case 3: A general method[9] *for calculating* φ_0 *and* Ω *by power series in* θ. It is seen from Eqs. (19) and (22) that the expressions for φ_0 and Ω/Ω_0 can be brought into the general form

$$2\psi(\theta_1)=\int_0^{\theta_1} N(\theta)[F(\theta)-F(\theta_1)]^{-\frac{1}{2}}d\theta, \quad (53)$$

where N and F represent any arbitrary functions which for $0<\theta<\theta_1$ can be expanded by Taylor's theorem into a series in powers of $\theta-\theta_1$ with coefficients that are functions of θ_1. The coefficients themselves can be expanded in powers of θ_1. In this way by carrying out the integration we obtain

$$(-F_1)^{\frac{1}{2}}\psi=A_1S+A_3S^3+A_5S^5+A_7S^7+\cdots, \quad (54)$$

where

$$S=(\theta_1)^{\frac{1}{2}},$$
$$A_1=N_0,$$
$$A_3=(2/3)N_1-(5/12)N_0F_2/F_1,$$
$$A_5=(4/15)N_2-(3/10)N_1F_2/F_1-(11/60)N_0F_3/F_1+(43/160)N_0(F_2/F_1)^2,$$
$$A_7=(8/105)N_3-(13/105)N_2F_2/F_1-(29/210)N_1F_3/F_1+(23/112)N_1(F_2/F_1)^2-(31/560)N_0(F_4/F_1)+(27/112)N_0(F_2/F_1)(F_3/F_1)-(177/896)N_0(F_2/F_1)^3.$$

Here N_n and F_n are the nth derivatives of $N(\theta)$, $F(\theta)$ with respect to θ at the point $\theta=0$.

Thus in calculating φ_0 and Ω/Ω_0 we may take $F(\theta)$ as given by Eq. (18) so that

$$F_1=\beta_0-\beta,$$
$$F_2=\omega-\epsilon+(\beta_0-\beta)(\rho+k)-\beta_0(\rho-\epsilon) \text{ etc.}$$

In calculating φ_0 by Eq. (19) we place

$$N(\theta)=(1+\theta)^k,$$
$$N_0=1;\ N_1=k;\ N_2=k(k-1) \text{ etc.},$$

while for $\Delta\Omega/\Omega_0$ by Eq. (22) we split the second member into two integrals placing $N(\theta)=(1+\theta)^{\rho+k}$ for the first and $N(\theta)=(1+\theta)^k$ for the second.

III. General Equations for Tungsten Filaments Up to 600°K

We have shown[1] that the radiation and resistance of tungsten filaments between 220° and 600°K are accurately represented by Eqs. (1) and (13) if we place

$$\omega=5.332;\ \rho=1.23;\ \text{and}\ \epsilon=0.87. \quad (55)$$

In order to determine λ from our experimental data we at first assumed $k=0$, and were thus able to calculate φ_0 and $\Delta\Omega/\Omega_0$ in terms of β and θ_1 by the methods we shall outline. Experiments with low values of θ_1 (which justify the assumption $k=0$) and with various values of T_0 soon showed that

$$k=-0.30 \quad (56)$$

gave the variation of λ with temperature to a satisfactory approximation.

Values of Y and Z.

When the bulb temperature T_B is low compared to T_0 or when β is either large or very small, the temperature distribution is given accurately by Eq. (47), but even for intermediate values of β this equation gives a rather good approximation. Let us therefore derive methods for calculating Y.

Introducing the numerical values of ω, ρ, and k in Eqs. (49) and (50), expanding and integrating, we obtain

$$Y=+1.2033\sigma^{0.70}+0.2355\sigma^{2.630}J+0.1498\sigma^{4.560}J^2+0.129\sigma^{6.490}J^3-0.02944\sigma^{6.732}J+0.1279\sigma^{8.420}J^4-0.05046\sigma^{8.662}J^2+0.1380\sigma^{10.35}J^5-0.0724\sigma^{10.59}J^3, \text{ etc.}, \quad (57)$$

where $$J=(1.4705\sigma_1^{1.93}-0.4705\sigma_1^{6.032})^{-1}. \quad (58)$$

A similar method applied to Eq. (52) gives

$$Z=+0.4364\sigma^{1.93}+0.1604\sigma^{3.86}J+0.1180\sigma^{5.79}J^2+0.1084\sigma^{7.72}J^3-0.0249\sigma^{7.962}J+0.1115\sigma^{9.65}J^4-0.0412\sigma^{9.892}J^2, \text{ etc.} \quad (59)$$

For values of σ approaching σ_1, it was possible to develop other expansions giving Y_1-Y in terms of powers of $(\sigma_1-\sigma)/\sigma_1$. By adding the values of Y and Y_1-Y thus obtained in the range in which both series were accurate, the values of Y_1 were obtained and were found for $\sigma_1>0.6$ to be accurately given by

[9] We wish to thank Dr. H. Poritsky for obtaining the expressions involved in this method and for helpful discussions of other sections of this paper.

$$Y_1 = 1.0312 - 0.8039 \log_{10} y_1 + 0.390 y_1 + 1.573 y_1^2 - 1.31 y_1^3 + 0.050 y_1^4 + 1.5 y_1^5, \quad (60)$$

where $y_1 = 1 - \sigma_1$.

Similar calculations for Z_1, satisfactorily accurate for $\sigma_1 > 0.1$, give

$$Z_1 = 0.08782 - 0.8039 \log_{10} y_1 + 0.3029 y_1 - 0.448 y_1^2 + 0.06 y_1^3. \quad (61)$$

Infinitely long filament

For the special case that $\sigma_1 = 1$, which corresponds to $T_1 = T_M$, the value of Y, which we may denote by Y_M, is given accurately by the following equation over the range from $\sigma = 0.3$ to 1.0.

$$Y_M = 0.7892 - 0.8039 \log_{10} y - 0.3935 y - 0.1475 y^2 - 0.0641 y^3 - 0.0330 y^4 - 0.021 y^5 \cdots, \quad (62)$$

where $y = 1 - \sigma$. An analogous expression for Z_M, very accurate for $\sigma > 0.2$, is

$$Z_M = -0.1542 - 0.8039 \log_{10} y + 0.0360 y + 0.0698 y^2 + 0.0340 y^3 + 0.0108 y^4 + 0.00227 y^5. \quad (63)$$

By means of the foregoing methods, using 15 terms in Eqs. (57) and (59), tables were prepared giving Y and Z as functions of σ and σ_1 to an accuracy of about 1 in 3000. The family of curves in Fig. 1 represents the values of σ as functions of $Y_1 - Y$ for various values of σ_1. These curves give the temperature distributions, since the ordinates, according to Eq. (44), are proportional to the temperatures, while the abscissas $Y_1 - Y$ by Eq. (47) are proportional to distances measured along the filament from its center. These distances may also be expressed in terms of φ by Eq. (47) which takes the form

$$\varphi = \sigma_0^{2.316}(Y_1 - Y). \quad (64)$$

To calculate σ_0, the value of σ at the leads, we can use the following equation derived from Eqs. (43) and (48):

$$\beta = \sigma_0^{-4.102} - (1 - \beta_0)\sigma_0^{0.36}. \quad (65)$$

For the case that $\beta_0 = 0$ (that is, $T_B = T_0$), the values of β as a function of σ_0 are given in the first two columns of Table I (see Part V). Values of β for the case $\beta_0 = 1$, or $T_B = 0$, are given in the 6th column.

The temperature distribution near the central part of a long filament for which $\sigma_1 > 0.95$ is given by

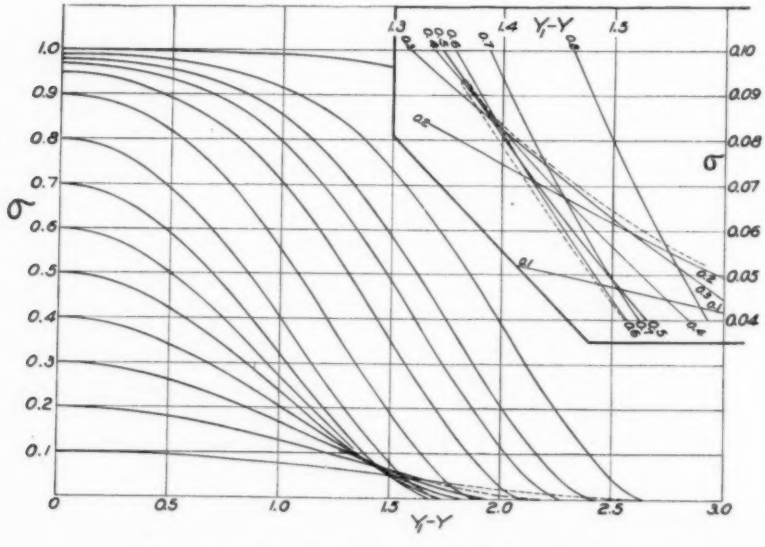

FIG. 1. σ as a function of $Y_1 - Y$ for various values of σ_1.

$$Y_1 - Y = 0.3491 \cosh^{-1}[(1-\sigma)/(1-\sigma_1)]. \quad (66)$$

Calculation of θ_1 as a function of φ_0 and β (Tables II to IV)

In most cases where it is desired to take into account the cooling effect of the leads upon the filament, it is not necessary to know the temperature distribution over the whole length of the filament, but a knowledge of the temperature at the center of the filament and the resistance of the filament suffices. Tables II to IV contain data on the values of θ_1 for selected integral values of β and a set of evenly spaced values of φ_0.

For low values of φ_0 the most convenient method of calculating θ_1 is by use of the series expansion furnished by Eqs. (53) and (54). Taking $\omega = 5.332$; $\rho = 1.23$; $\epsilon = 0.87$; $k = -0.30$, and $\beta_0 = 0$, we obtained in this way a series giving φ_0 in terms of θ_1/β. However, since we desired to tabulate θ_1 for specified values of φ_0 and β, this series, by reversion, was converted into the following:

$$\theta_1/\beta = \varphi_0^2 + (1.175\beta - 3.718)\varphi_0^4 + (1.552\beta^2 - 17.56\beta + 13.49)\varphi_0^6 + (2.206\beta^3 - 57.30\beta^2 + 144.3\beta - 48.84)\varphi_0^8 + \cdots. \quad (67)$$

Beyond the range of usefulness of this series we employed the Y function for which we had previously constructed tables giving Y as a function of σ for a set of 10 values of σ_1. For each of these σ_1 values we then interpolated by Newton's rule to find $Y_1 - Y_0$ for each of the values of σ_0 in Table I which correspond to integral values of β.

For each value of β we thus had a set of values of σ_1 for a number of definite values of $Y_1 - Y_0$. Taking then the selected values of φ_0 used in Tables II to IV and the values of σ_0 corresponding to β in Table I we calculated $Y_1 - Y_0$ by Eq. (64), and used these to obtain by interpolation the corresponding values of σ_1 from which θ_1 could be obtained by Eq. (44) and Eq. (48). This interpolation was carried out graphically. We found it was often advantageous for each value of β to plot $Y_1 - Y_0$ against colog $(1-\sigma_1)$, since for larger values of σ_1 a nearly straight line was obtained, which by Eq. (60) approached a limiting slope of 0.8039.

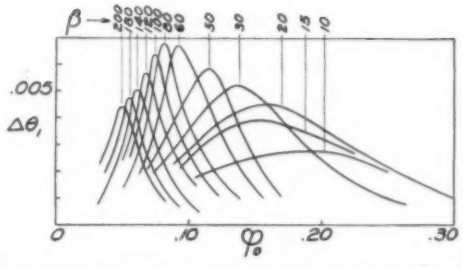

FIG. 2. Corrections $\Delta\theta_1$ applied in the calculation of θ_1 for the tables.

Since the tables are to be used mainly for the case that $T_B = T_0$, $(\beta_0 = 0)$, there is a slight error involved in the calculations of θ_1 by the foregoing method due to the replacement of ϵ by ρ in deriving Eq. (47). By using the series expansion of Eq. (54) again using $\epsilon = 1.23$ instead of 0.87 and comparing this with Eq. (67), it was possible to calculate the small correction, $\Delta\theta_1$, to apply to θ_1. As can be seen from Fig. 2, the correction was negligible for very large and very small values of both β and θ, and only rarely exceeded one percent. Many checks were made of the accuracy of these corrections by direct calculations of φ by Eq. (19), using numerical integration by Simpson's rule.

It is believed that with these corrections that were applied in calculating the data for Tables II to IV that the values of θ are accurate to within a couple of units in the last figure.

Calculations of $\Delta\Omega/\Omega_0$ in Tables V to VII

For sufficiently low values of θ_1 we obtain from Eq. (54) the following expansion:

$$\Delta\Omega/\Omega_0 = 0.8200\theta_1 + (0.01720 + 0.1220/\beta)\theta_1^2 + (0.0088 + 0.2510/\beta + 0.4148/\beta^2)\theta_1^3. \quad (68)$$

The lower values of θ_1 from Tables II to IV were used in this way to calculate $\Delta\Omega/\Omega_0$ for given values of φ_0 and β. For values of θ_1 too large for rapid convergence of this series, $\Delta\Omega/\Omega_0$ was calculated from Y and Z by Eq. (51). The necessary interpolations were facilitated by using the following relationships.

When θ_1 is small a very good approximation is given by

$$\Delta\Omega/\Omega_0=(1+\theta_1)^{\rho}[1-(\rho/3)\theta_1/(1+\theta_1)]. \quad (69)$$

By using the tables of Y and Z, values of $\Delta\Omega/\Omega_0$ were calculated and compared with those given by Eq. (69) placing $\rho=1.23$; the differences thus obtained were then plotted as a family of curves for various values of β and θ_1. These curves together with tables of the function involved in Eq. (69) were used for interpolation. This method was useful for values of θ_1 much larger than those for which Eq. (68) could be applied.

For still larger values of θ_1 we may calculate $\Delta\Omega/\Omega_0$ by

$$\Delta\Omega/\Omega_0=\sigma_0^{-\rho}-1-B/\varphi_0. \quad (70)$$

This equation, which is a generalization of Eq. (41), may be looked upon merely as a definition of B. It follows then from Eqs. (51) and (47) that

$$B=\sigma_0^{1.086}[(Y_1-Y_0)-(Z_1-Z_0)]. \quad (71)$$

As θ_1 approaches θ_M, so that $\sigma_1\to 1$, B approaches a limiting value B_∞ which may be obtained by combining Eqs. (71), (60), (61), (62), and (63):

$$B_\infty=\sigma_0^{1.086}(0.4294y_0+0.2173y_0^2+0.09815y_0^3 +0.04375y_0^4+0.02327y_0^5+\cdots). \quad (72)$$

This is sufficiently accurate for $\sigma_0>0.5$.

By calculating B by Eq. (71) for various values of β and σ_1 a family of curves was obtained giving $B-B_\infty$ as a function of σ_1 which was very convenient for accurate interpolation. Empirically it was found for large values of σ_1 and for values of β from 1 to 200 that

$$B-B_\infty=0.145\beta^{-0.21}(1-\sigma_1)^{1.17}. \quad (73)$$

By these various methods the values of $\Delta\Omega/\Omega_0$ were obtained which are given in Tables V, VI, and VII.

Let V be the voltage drop across the half filament. Then

$$V=\beta^{\frac{1}{2}}V_0(\Omega/\Omega_0).$$

If the leads did not cool the ends of the filament, the current A would heat the whole filament to T_M. Let V_M be the voltage drop that would then be required for the half-filament. We find readily that

$$V_M=\beta^{\frac{1}{2}}V_0\sigma_0^{-\beta}. \quad (74)$$

The effect of each lead in cooling the filament is thus to lower the voltage by an amount $\Delta V=V_M-V$. By Eqs. (70) and (26) we get

$$\Delta V=\beta^{\frac{1}{2}}h_0B, \quad (75)$$

where B is given by Eq. (73).

Effects due to the heating of the leads or springs

The tables in this paper are adapted primarily for calculations involving filaments whose ends are at the bulb temperature or some other definitely known temperature. The heat that is conducted from the filament into the leads must heat the junction, but if the diameter of the leads is 10 times that of the filament, the temperature drop in the leads is about that in a length of filament only one-hundredth of the lead length and so produces negligible effects.

In experimental work with tungsten filaments it is often desired to mount a filament in a definite position in a tube, such as at the axis of a cylindrical anode. To maintain the filament in this position even when it elongates upon heating, it is necessary to use a spring to hold the filament taut. The proper design[10] of springs for this purpose often requires that the spring shall contain a considerable length of wire of diameter ranging from 3 to 6 times the filament diameter. The heat conducted into the spring may then heat the spring to a degree that cannot be neglected in calculations of the temperature distribution and resistance of the filament.

Let T_2 be the temperature at the junction between the filament and spring. It is evident that with a given current A passing through the wire the temperature distribution over the whole filament will remain unchanged if we replace the spring by an additional section of filament whose length Δx is so chosen that the temperature drop in it is the same as that which occurs in the spring (T_2-T_0).

Thus, if we can calculate Δx for each lead and add these increments to the length of the filament before calculating φ_0 by Eq. (15), we can proceed

[10] K. B. Blodgett and I. Langmuir, Rev. Sci. Inst. **5**, 321 (1934).

to determine θ_1 by the equations and tables already given on the assumption that the lead temperature is T_0. Let us then find methods of calculating Δx.

The temperature distribution along a filament near a lead whose temperature is T_0 may be calculated by Eq. (19). The value of F can be obtained by expanding Eq. (18) in a power series in θ. Placing $\beta_0=0$ and using the data of Eq. (55) we get

$$F=-\beta\theta+(2.231-0.465\beta)\theta^2 +(3.42+0.011\beta)\theta^3. \quad (76)$$

Numerical calculations for springs of practical sizes have shown that θ_2 is so small that only the first term of this expansion is needed. By Eq. (19), by integrating between 0 and θ_2, we obtain

$$\beta\Delta\varphi=(-F_1)^{\frac{1}{2}}-(-F_1-\beta\theta_2)^{\frac{1}{2}}. \quad (77)$$

Introducing the value of F into Eq. (17) and letting b denote the value of $d\theta/d\varphi$ at the point θ_2 we have

$$b=(d\theta/d\varphi)_{\theta=\theta_2}=2(-F_1-\beta\theta_2)^{\frac{1}{2}}. \quad (78)$$

By eliminating F_1 between Eqs. (77) and (78), we find

$$\Delta\varphi=(\theta_2/b)(1-\beta\theta_2/b^2+\cdots). \quad (79)$$

In Fig. 2 let the curve ABC represent the temperature distribution along a filament. Eq. (79) enables us to calculate $\Delta\varphi$ (the distance AD) from θ_2 (the distance BD) and the temperature gradient at B. The heat flow Q at B, by Eqs. (29), (30) and (78), is found to be

$$Q=2A_0h_0(1+\theta_2)^kb. \quad (80)$$

Now if we replace the section AB of the filament by a spring along which the temperature distribution is EFB, the curve BC is unchanged. If the spring is of very great length, it will be heated, except near its ends, to a uniform temperature T_S by the current A that flows through it. We may calculate this temperature from the data of Table II. Let A_S be the current that would be needed to maintain the spring at T_0 if its ends are at T_0 while the bulb is at 0°K. Since the current to heat a long filament to any temperature varies with $d^{\frac{3}{2}}$ where d is the diameter, we have

$$A_S=s^{\frac{3}{2}}A_0, \quad (81)$$

where s is the ratio of the diameter of spring wire to that of the filament. The value of β for the spring wire, by Eq. (6), is

$$\beta_S=(A/A_S)^2=(A/A_0)^2/s^3=\beta/s^3. \quad (82)$$

Since s^3 is large, β_S is small, and therefore in Table II we take $\beta=0$, $\varphi_0=\infty$, and so find

$$\theta_S=0.224\beta/s^3. \quad (83)$$

In general, the temperature distribution along a spring of finite length will be of the type illustrated by the curve EFB in Fig. 3. We may assume that one end is welded to a lead of such large diameter that $\theta=0$, while the other end, which joins the filament, is heated to θ_2 which is greater than θ_S. Thus to calculate the temperature distribution, we cannot use Eq. (17) for this was based on the assumption that $d\theta/d\varphi=0$ at θ_1, but must go back to Eq. (16). By a method like that used in the derivation of Eq. (33) we thus find that the temperature distribution along the spring is given by

$$C\varphi_S=\sinh^{-1}(C\theta_S/a)+\sinh^{-1}[C(\theta_2-\theta_S)/a], \quad (84)$$

where C is defined by Eq. (34) and a is an integration constant which is equal to the value of $d\theta/d\varphi$ at θ_S.

By analogy with Eq. (78), we let b_S be the value of $d\theta/d\varphi_S$, for the spring at its junction with the filament (θ_2).

Applying Eq. (80) to both the spring and filament and considering Eq. (81) we find

$$b_S=b/s^{\frac{1}{2}}. \quad (85)$$

By obtaining $d\theta/d\varphi$ at θ_S and at θ_2 from Eq. (84) and equating these derivatives to a and b_S, we obtain the relation

$$a^2=b_S^2-C^2(\theta_2-\theta_S)^2. \quad (86)$$

In Eqs. (78), (79), (83), (84), (85), and (86) we have six equations involving six unknowns, θ_2, θ_S, a, b, b_S, and $\Delta\varphi$ and so may solve for $\Delta\varphi$ in terms of the known parameters s, φ_S, β, and F_1 (or θ_1). A few numerical calculations involving springs of practicable design have shown that θ_S is negligible in its effect and that F_1, according to Eq. (76), can be replaced without appreciable loss of accuracy by $-\beta\theta_1$. The problem is thus greatly simplified so that the calculation of $\Delta\varphi$ can be reduced to the following procedure.

Calculate a quantity P (which is equal to θ_2/b) by the equation

$$P=(1/Cs^{\frac{1}{2}})\tanh C\varphi_S. \tag{87}$$

If $C\varphi_S\gg 1$ this reduces to

$$P=(1/Cs^{\frac{1}{2}})(1-2e^{-2C\varphi_S}\cdots). \tag{88}$$

If $C\varphi_S\ll 1$ it becomes

$$P=(\varphi_S/s^{\frac{1}{2}})[1-(2/3)C^2\varphi_S^2]. \tag{89}$$

Then $\Delta\varphi$ is given by

$$\Delta\varphi=P-P^2\beta/b, \tag{90}$$

where

$$b/\beta=2(\theta_1/\beta)^{\frac{1}{2}}-2P. \tag{91}$$

This may be used to calculate Q by Eq. (80).

The value of θ_2, when desired, may be found from

$$\theta_2=2P\beta[(\theta_1/\beta)^{\frac{1}{2}}-P]. \tag{92}$$

According to Eqs. (34) and (55), the numerical value of C is 2.99. The value of φ_S used in these calculations can be obtained from the length x_S of the spring wire by Eq. (15) using a value of II_S which by Eq. (8) is sII where II is the value for the filament.

From Eqs. (90) and (15)

$$\Delta x=(2II)^{\frac{1}{2}}P(1-P\beta/b), \tag{93}$$

while for short spring wires or leads this becomes,

$$\Delta x=x_S/s^2. \tag{94}$$

If for short leads a material is used which has a heat conductivity λ_S, the value of Δx given by the above equation should be multiplied by (λ_0/λ_S).

The heating of the leads has also an effect on the change in resistance. As seen in Fig. 3 the observed resistance when a spring is attached is the sum of the resistance Ω_S of the spring and the resistance Ω_F of the filament, so that

$$\begin{aligned}\Omega&=\Omega_S+\Omega_F=\Omega_S+\Omega_2+\Omega_0\\&=\Omega_S-\Omega_{AD}+2\Omega_0\end{aligned} \tag{95}$$

since $\Omega_2=\Omega_0-\Omega_{AD}$.

On passing a current, the resulting changes in resistance are given by

$$\Delta\Omega_S=(b\rho\Omega_S/C^2s^{\frac{1}{2}}\varphi_S)(1-1/\cosh C\varphi_S), \tag{96}$$

(neglecting θ_S compared to θ_2) and

$$\Delta\Omega_{AD}=\tfrac{1}{2}\rho\theta_2\Omega_{AD}, \tag{97}$$

where Ω_S and Ω_{AD} are the cold resistances. The increase in Ω_0, *viz.*, $\Delta\Omega_0$ may be calculated from β and φ_0 by the tables.

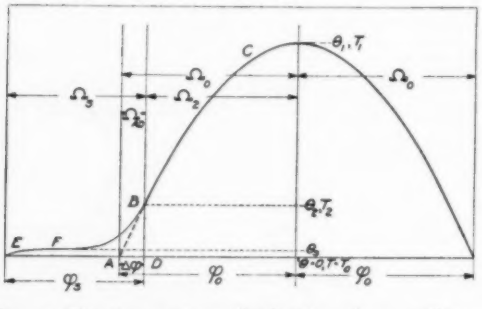

FIG. 3. The temperature distribution along a filament supported at one end by a spring.

IV. EXPERIMENTAL DETERMINATION OF THE HEAT CONDUCTIVITY λ

The relations given in Part II show that the heat conductivity λ may be calculated from a determination of the value of T or of Ω resulting from passage of a current through the filament. For filaments below 600°K it is more convenient to use the resistance Ω. The experimental procedure was as follows.

Three tubes were used. One (Tube No. 1) was the tube described in Paper I which by use of hollow copper leads allowed control of T_0 independently of T_B. Two other tubes (Nos. 2 and 3) had heavy leads of 120-mil molybdenum, arc-welded in hydrogen to the filament to insure good thermal contact. The filaments were of thoriated tungsten 0.00499 cm in diameter, and had total lengths in Tubes 1, 2, and 3 of 25.82 cm, 12.86 cm and 5.87 cm, respectively. The use of three filament lengths provided a check on the method of calculation and increased the range of values of β, for which Ω could be accurately measured. For the shortest filament, low values of β gave changes in resistance too low to be measured accurately, while for long filaments the higher values of β gave filament temperatures outside the range for which radiating properties had been determined.

The tubes were baked at 450°C and pumped during the experiments through liquid-air traps. The filaments were heated initially at 2000°K

to produce a fine grained structure and then at 2400° and 2800°, as described in Paper I, to a condition where further aging caused no change in resistance or emissivity.[11]

In most of the experiments T_0 was made equal to T_B by immersing the tube and its leads in a constant temperature bath. The filament current A and resistance Ω were found from voltage measurements with a precision potentiometer.

An example is given below of the steps and quantities involved in the calculation of the heat conductivity from experimental data.

Tube No.	l (cm)	$T_0=T_B$ (°K)	A (amp.)	β	$A_0\times10^3$	$V_0\times10^3$	$R_0\times10^4$	Ω_0
2	12.86	244.1	0.01949	20	4.358	6.3871	4.4567	1.4665
3	5.87	244.1	0.01949	20	4.358	2.9154	4.4567	0.6675

Tube No.	$\Omega-\Omega_0$ $=\Delta\Omega$	$\frac{\Delta\Omega}{\Omega_0}$	φ_0	h_0	λ_0	λ (Eq. 104)	θ_1	T_1-T_0	T_1 (°K)
2	0.3335	0.2274	0.1050	0.06083	1.701	1.720	0.2765	67.5	311.6
3	0.02545	0.03813	0.0473	0.06177	1.745	1.720	0.0473	11.6	255.7

Ω_0, the resistance of the filament when entirely at the temperature T_0, was first determined as in Paper I, and then the change in resistance, $\Omega-\Omega_0=\Delta\Omega$, caused by passage of the current A. This current A was chosen by calculation from (Eq. (6) Part II)

$$\beta=(A/A_0)^2 \tag{98}$$

to correspond exactly to integral values of β. In the examples shown, β is 20. A_0, and the quantities V_0 and R_0 were obtained from Paper I, Table II, using the equations

$$V_0=V''x_0/d^{\frac{1}{2}}, \tag{99}$$

$$A_0=A'd^{\frac{1}{2}}, \tag{100}$$

$$R_0=R'\pi/4. \tag{101}$$

From the value of β and $\Delta\Omega/\Omega_0$, given by the experiments, the corresponding value of φ_0 was found from Tables V, VI, or VII of Part V.

Now from Eq. (26) of Part II,

$$h_0=V_0/\varphi_0, \tag{102}$$

and so the heat conductivity, λ_0, at the temperature, T_0, of the leads could be calculated from Eq. (27).

$$\lambda_0=h_0^2/2R_0T_0. \tag{103}$$

The values of θ_1, $=(T_1-T_0)/T_0$, and of T_1 were found as described later in Part V.

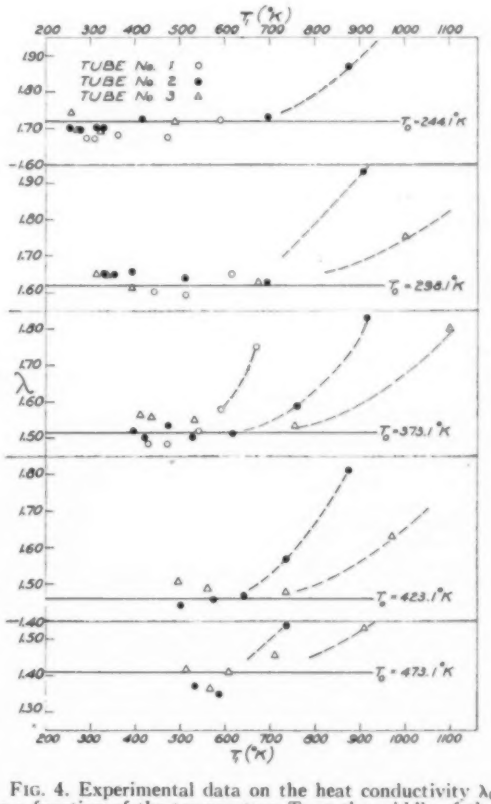

FIG. 4. Experimental data on the heat conductivity λ_0 as a function of the temperature T_1 at the middle of the filament as determined for five values of lead temperature T_0.

[11] It should be noted that brief aging (few minutes) at temperatures even as high as 2600°K will not produce a tungsten filament which is unchanged by further heating. For example, in the case of filaments used in these experiments, after the initial aging at 2000° for about 2 minutes, aging at 2400°K caused a decrease in cold (264°K) resistance of 2 percent after 1 minute, 5 percent after 40 minutes, and after 4 hours at 2400° and 30 seconds at 2800° the total decrease was about 7 percent. At the same time, in spite of this decrease in cold resistance, the voltage for a constant current giving a maximum filament temperature of about 600°K increased. Thus the emissivity had decreased, which indicates either a cleaning or a smoothing of the filament surface. (See also reference 6.) It is possible that filaments when only slightly aged are clean, but unless special tests are made, it is clear that the filament temperature is uncertain. Experiments, involving adsorbed films on tungsten for example, can be interpreted most easily when the tungsten by proper aging has been brought into a condition where its surface and temperature are reproducible.

By experiments at values of $T_0(=T_B)$ from 244° to 473°K, the dependence of λ_0 on T_0 was determined. For each value of T_0 a series of values of β (i.e. of A) was used giving temperatures, T_1, at the middle of the filament up to 1100°K. However, in each case, the calculation as described above gave λ_0, i.e., λ at $T=T_0$.

Preliminary experiments (described below) under simplifying conditions had indicated that the variation of λ with T was given by

$$\log \lambda = 0.9518 + k \log T, \qquad (104)$$

where $k=-0.30$. This value of k was used in the construction (see Part III) of the tables in Part V. That the present much more extensive experiments confirm this choice of k is shown by examination of the collected data in Fig. 4.

λ_0 is plotted as a function of T_1, for the five values of T_0 from 244 to 473°K. Considering only values of T_1 below 600°K,[12] it is seen that λ_0, at each T_0, is independent of T_1 and shows no significant change in the three different tubes, i.e., no change with filament length. This fact that λ_0 is independent of T_1 indicates that the value of k equal to -0.30 used in Eq. (104) is correct. Otherwise there would have been a progressive change in λ_0 as T_1 was varied.

The values of λ at the five values of $T=T_0$, calculated from Eq. (104) are given as solid horizontal lines in Fig. 4. The evident agreement (below $T_1=600$°K) of the experimentally determined points with these calculated values of λ is an independent confirmation of the correctness of k.

Since we at first had no knowledge of k, i.e., of the variation of λ with T, the preliminary experiments mentioned above were carried out. Using Tube No. 1, the bulb was immersed in liquid nitrogen and the leads were held at temperatures, T_0, between 240 and 450°K. At each value of T_0 the resistance, Ω, was measured for several values of current, A, chosen to cause only small deviations of the filament temperature from T_0. Since for each value of T_0 the maximum temperature rise was small ($\sim 10°$), λ could be taken as independent of temperature ($k=0$), and Eq. (36) of Part II, Case I (low values of θ_1), could be applied. With the bulb in liquid nitrogen T_B is effectively equal to zero and this equation takes the form,

$$\Delta\Omega/\Omega_0 = 0.300(\beta-1)\left[1-\frac{\tanh 2.864\varphi_0}{2.864\varphi_0}\right], \qquad (105)$$

where β and Ω_0 are found as already described.

Since the resistance changes, $\Delta\Omega$, are small, the measurements tend to be less accurate than in the experiments where T_1-T_0 was large. However, it is seen from Eq. (105) that for the small resistance changes involved $\Delta\Omega$ is a linear function of β (or of A^2). So by plotting $\Delta\Omega$ *vs.* A^2, the slope of a line through the individual points allowed a satisfactorily accurate calculation of φ_0. From Eqs. (102) and (103), λ_0 was then calculated.

Thus at several temperatures $T(=T_0)$, $\lambda(=\lambda_0)$ was determined and found to depend on temperature as given by Eq. (104).

The values of λ determined in the present work may be extrapolated to join the data of Forsythe and Worthing,[2] giving a curve of λ *vs.* T which has a minimum at about 1300°K and joins $F-W$ at 1500°K. Values of λ from this curve are as follows.

T (°K)	λ	T (°K)	λ
600	1.313	1200	1.00
800	1.18	1300	0.98
1000	1.08	1500	0.99

These values justify the corrections to the $F-W$ equation found necessary by Langmuir, Mac-

[12] In experiments where T_1 exceeded 600°K, λ_0 increased with T_1. This behavior, observed in all tubes, was not caused by changes in emissivity due to an attack of the filament surface by residual gases, since on returning to temperatures below 600° the normal values of λ_0 were obtained. Also the effect was independent of bulb temperature. It was most marked in Tube No. 1, which had the longest filament and least in Tube No. 3 with the shortest filament. It is believed that the explanation lies in the fact that the relations of Paper I between energy radiated and filament temperature are not applicable much above the maximum filament temperature (580°K) for which they were determined. Between 225 and 580°K, the energy radiated is given by $W_R=KT^{5.332}$. However, as pointed out on p. 325 of Paper I, the exponent of T must increase above 600°K in order to reach the values of Jones and Langmuir and Forsythe and Watson which are accepted as accurate above 1000°K. Calculations show that this can account for both the magnitude and direction of the observed deviations of λ_0. The effect should be greatest for the longest filament, since a greater proportion of its length is at temperatures near T_1.

Incidentally, it was observed that very slight traces of water vapor from bulbs insufficiently baked cause appreciable changes in emissivity which increase with bulb temperature, and are immediately recognized by the lag effects produced when the filament temperature is raised or lowered.

Lane and Blodgett[3] for temperatures below 1500°K (see Introduction).

Since the variation of λ with T is established by the experiments, an equation for h as a function of T can be derived. From Eqs. (27a), (101), and Eq. (6) of Paper I,

$$\log h = 96.4826 - 100 + 0.965 \log T. \quad (106)$$

Likewise $(2H)^{\frac{1}{2}}$ for use in Eq. (93) can be expressed as a function of T. Since H depends not only on T but also on the filament radius r, it is convenient to use the quantity $(r/2H)^{\frac{1}{2}}$. From Eqs. (15) and (104) and Eqs. (6) and (7) of Paper I,

$$\log (r/2H)^{\frac{1}{2}} = 91.3793 - 100 + 2.316 \log T. \quad (107)$$

Table VIII in Part V gives h, λ, and $(r/2H)^{\frac{1}{2}}$ for a series of values of T, as calculated from the above equations.

V. Calculation of Filament Temperature and Resistance from the Tables

Tables I to VIII, prepared as described in Part III, are given to facilitate calculations of filament temperature or resistance from a knowledge of the filament dimensions, the filament current, and the lead and bulb temperature. Directions and examples are given for the several usual cases. The theory and equations in Parts II and III need not be referred to.

In general there will be known:

r = radius of filament (cm),
x_0 = half length of filament (cm),
T_0 = lead temperature (°K),
T_B = bulb temperature (°K),
A = filament current (amp.).

Case 1. ($T_B = T_0$)

This is the experimental condition existing, for example, when the bulb and the filament leads are immersed in a bath at constant temperature. The filament leads are to be chosen of such a diameter (at least 10 times filament diameter) and as short as possible so that they are not appreciably heated by the filament currents to be used, or by conduction of heat from the filament.

It is ordinarily convenient to construct a table or curve giving filament temperature as a function of current, from which temperatures can be found for any value of current used in experiments. This is done in the following way.

From Table VIII or Eq. (107) find the value of $(r/2H)^{\frac{1}{2}}$ corresponding to T_0. Then using the known value of r, calculate φ_0 from

$$\varphi_0 = x_0/(2H)^{\frac{1}{2}}. \quad (108)$$

Now for integral values of β as given in the Tables (II, III, IV) find the values of θ_1 corresponding to this value of φ_0. T_1, the temperature at the middle of the filament, is given by

$$T_1 = (1 + \theta_1) T_0. \quad (109)$$

The currents, A, required to produce each temperature T_1, are found from the values of β using the equation

$$\beta = (A/A_0)^2, \quad (110)$$

where A_0 for the filament in question is calculated from

$$A_0 = A' d^{\frac{1}{2}}, \quad (111)$$

where d is the filament diameter and A' is taken from Table II in Paper I, or calculated from the equation

$$\log A' = 96.1952 - 100 + 2.051 \log T_0. \quad (112)$$

$\Delta\Omega/\Omega_0$ is found in a similar way by using φ_0,

Table I. *Limiting values of various functions.*

1 β $(\beta_0 = 0)$	2 φ_0	3 θ_M	4 B_∞	5 $(\Delta\Omega/\Omega_0)_\infty$	6 β $(\beta_0 = 1)$ $(\varphi_0^{-4.102})$	7 $\varphi_0^{0.36}$
0	1.0000	0.0000	0.00000	0.0000	1.000	1.000
1	0.8504	.1759	.0577	.2205	1.943	0.943
2	.7708	.2974	.0839	.3775	2.910	.910
3	.7182	.3923	.0983	.5024	3.888	.888
4	.6798	.4709	.1075	.6074	4.87	.870
6	.6257	.5981	.1186	.7801	6.84	.845
8	.5881	.7004	.1248	.9212	8.83	.826
10	.5594	.7877	.1287	1.043	10.81	.811
15	.5104	.9594	.1336	1.287	15.79	.785
20	.4774	1.095	.1355	1.483	20.77	.766
25	.4529	1.208	.1361	1.649	25.75	.752
30	.4338	1.305	.1361	1.793	30.74	.740
40	.4051	1.468	.1354	2.038	40.72	.722
50	.3840	1.604	.1343	2.245	50.71	.709
60	.3676	1.720	.1330	2.425	60.70	.697
80	.3429	1.916	.1305	2.730	80.68	.680
100	.3249	2.078	.1281	2.986	100.7	.667
120	.3109	2.217	.1260	3.209	120.7	.657
140	.2994	2.340	.1241	3.407	140.6	.648
160	.2899	2.450	.1223	3.586	160.6	.640
180	.2817	2.550	.1207	3.750	180.6	.634
200	.2746	2.641	.1192	3.902	200.6	.628

β, and Tables V, VI, and VII.[13] This value of $\Delta\Omega/\Omega_0$ is usually not required, but if compared with a measured value of $\Delta\Omega/\Omega_0$ serves as a check on the calculation of T_1. Also if the filament length and hence φ_0 are unknown, then a determination of Ω_0 and of $\Delta\Omega$ caused by the current A enables one to find φ_0 and then θ_1 (and T_1) from the tables.

Case 2. ($T_B < T_0$)

In some types of experiments the bulb may be at a lower temperature than the leads. The tables have been prepared primarily for use when $T_B = T_0$. However, when $T_B < T_0$, a current temperature scale may be obtained by the following procedure:

Calculate φ_0 for the lead temperature T_0 which is to be used and find θ_1 and T_1 for the various values of β in the tables exactly as in Case 1. These values of β, however, must not be used to calculate the currents A. Instead, a new value of β must be calculated using Eq. (65) of Part III,

$$\beta = \sigma_0^{-4.102} - (1-\beta_0)\sigma_0^{0.36}, \tag{113}$$

where from Eq. (11), Part II,

$$\beta_0 = 1 - (T_B/T_0)^{4.462}, \tag{114}$$

and σ_0 is assigned the values given in the tables (just below the values of β which are applicable only to Case 1). σ_0, $\sigma_0^{0.36}$, and $\sigma_0^{-4.102}$ are given in Table I.

[13] It should be noted that for convenience in tabulation, θ_1/β and $\Delta\Omega/\beta\Omega_0$ are given in Tables II and V instead of θ_1 and $\Delta\Omega/\Omega_0$ as in the remainder of the tables.

TABLE II. θ_1/β *as function of* φ_0 *and* β.

φ_0	$\beta=0$ $\sigma_0=$ 1.0000	$\beta=1$ $\sigma_0=$ 0.8504	$\beta=2$ $\sigma_0=$ 0.7708	$\beta=3$ $\sigma_0=$ 0.7182	$\beta=4$ $\sigma_0=$ 0.6798	$\beta=6$ $\sigma_0=$ 0.6257	$\beta=8$ $\sigma_0=$ 0.5881	$\beta=10$ $\sigma_0=$ 0.5594
0.00	0.00000	0.00000	0.00000	0.00000	0.00000	0.00000	0.00000	0.00000
.02	.00040	.00040	.00040	.00040	.00040	.00040	.00040	.00040
.04	.00159	.00159	.00160	.00160	.00160	.00161	.00162	.00162
.06	.00355	.00357	.00358	.00359	.00361	.00364	.00367	.00370
.08	.00625	.00630	.00634	.00638	.00643	.00653	.00662	.00672
.10	.00964	.00974	.00984	.00993	.01006	.01029	.01053	.01078
.12	.01367	.01385	.01405	.01424	.01450	.01495	.01543	.01595
.14	.01827	.01857	.01891	.01922	.01970	.02072	.02162	.02234
.16	.02337	.02382	.02434	.02488	.02560	.02660	.02800	.0294
.18	.02891	.02951	.03024	.03105	.03208	.03318	.03514	.0369
.20	.03481	.03554	.03646	.03754	.03890	.04078	.0429	.0442
.22	.04099	.04179	.04285	.04412	.04575	.04850	.0505	.0507
.24	.04740	.04857	.0499	.0514	.0530	.0554	.0566	.0563
.26	.05396	.05506	.0565	.0585	.0604	.0616	.0619	.0611
.28	.06061	.0618	.0633	.0656	.0674	.0674	.0668	.0647
.30	.06730	.0686	.0700	.0720	.0733	.0727	.0706	.0676
.32	.07398	.0753	.0765	.0781	.0788	.0772	.0737	.0698
.34	.08061	.0820	.0829	.0838	.0836	.0810	.0763	.0717
.36	.08714	.0881	.0885	.0889	.0879	.0838	.0784	.0731
.38	.09355	.0941	.0940	.0937	.0919	.0863	.0801	.0743
.40	.09981	.0996	.0988	.0978	.0952	.0885	.0814	.0751
.42	.10591	.1049	.1035	.1017	.0982	.0902	.0826	.0759
.44	.11181	.1102	.1080	.1051	.1008	.0918	.0835	.0765
.46	.11751	.1149	.1120	.1083	.1031	.0931	.0842	.0769
.48	.12301	.1197	.1157	.1110	.1050	.0942	.0848	.0773
.50	.12829	.1239	.1190	.1134	.1067	.0950	.0852	.0776
.55	.14052	.1336	.1260	.1181	.1100	.0966	.0862	.0781
.60	.15146	.1413	.1313	.1214	.1124	.0977	.0867	.0784
.65	.16110	.1476	.1354	.1240	.1139	.0984	.0870	.0785
.70	.16956	.1530	.1384	.1258	.1150	.0988	.0872	.0786
.75	.1771	.1573	.1408	.1272	.1158	.0991	.0873	.0787
.80	.1834	.1608	.1426	.1280	.1163	.0993	.0874	
.85	.1890	.1637	.1440	.1288	.1167	.0995	.0875	
.90	.1938	.1660	.1451	.1293	.1170	.0995		
1.00	.2016	.1687	.1466	.1300	.1174	.0996		
1.10	.2074	.1712	.1474	.1303	.1175	.0996		
1.20	.2116	.1728	.1479	.1305	.1176			
1.30	.2148	.1738	.1482	.1306	.1177			
1.40	.2172	.1746	.1484	.1307				
∞	.2241	.1759	.1487	.1308	.1177	.0997	.0876	.0788

TABLE III. θ_1 *as function of* φ_0 *and* β.

φ_0	$\beta=15$ $\sigma_0=$ 0.5104	$\beta=20$ $\sigma_0=$ 0.4774	$\beta=25$ $\sigma_0=$ 0.4529	$\beta=30$ $\sigma_0=$ 0.4338	$\beta=40$ $\sigma_0=$ 0.4051	$\beta=50$ $\sigma_0=$ 0.3840	$\beta=60$ $\sigma_0=$ 0.3676	$\beta=80$ $\sigma_0=$ 0.3429
0.00	0.0000	0.0000	0.0000	0.0000	0.0000	0.0000	0.0000	0.0000
.01	.0015	.0020	.0025	.0030	.0040	.0050	.0060	.0081
.02	.0060	.0081	.0101	.0121	.0163	.0204	.0247	.0332
.03	.0136	.0183	.0229	.0278	.0375	.0473	.0575	.0784
.04	.0245	.0330	.0417	.0505	.0687	.0877	.1075	.1497
.05	.0388	.0526	.0666	.0813	.1120	.1448	.1800	.2582
.06	.0568	.0774	.0991	.1216	.1705	.2239	.2886	.429
.07	.0786	.1081	.1401	.1730	.2473	.3328	.429	.684
.08	.1048	.1456	.1909	.2384	.3494	.4839	.641	1.027
.09	.1358	.1908	.2527	.3206	.4800	.674	.895	1.321
.10	.1718	.2447	.3259	.4170	.6330	.879	1.121	1.521
.11	.2135	.310	.414	.532	.794	1.065	1.296	1.650
.12	.2605	.377	.509	.651	.945	1.209	1.418	1.734
.13	.3137	.452	.608	.770	1.068	1.312	1.502	1.788
.14	.3703	.533	.704	.873	1.164	1.387	1.561	1.827
.15	.428	.609	.789	.961	1.233	1.440	1.604	1.854
.16	.486	.681	.864	1.031	1.286	1.478	1.634	1.871
.17	.543	.745	.926	1.084	1.326	1.509	1.656	1.884
.18	.597	.803	.977	1.126	1.357	1.531	1.672	1.894
.19	.643	.850	1.019	1.161	1.380	1.548	1.685	1.900
.20	.684	.889	1.053	1.188	1.399	1.561	1.694	1.905
.21	.721	.921	1.081	1.210	1.414	1.571	1.701	1.908
.22	.754	.948	1.1027	1.227	1.425	1.579	1.706	1.911
.24	.806	.990	1.1354	1.253	1.441	1.589	1.712	1.914
.26	.844	1.020	1.1580	1.271	1.451	1.595	1.716	1.915
.28	.873	1.0409	1.1733	1.282	1.458	1.599	1.718	1.916
.30	.8945	1.0557	1.1837	1.289	1.462	1.601	1.719	
.35	.9271	1.0772	1.1980	1.299	1.466	1.603	1.720	
.40	.9430	1.0868	1.2038	1.303	1.468	1.604		
∞	.9594	1.0946	1.2078	1.305	1.468	1.604	1.7205	1.916

When T_B is so low, e.g. when the bulb is immersed in liquid air, that back-radiation is negligible; then T_B may be taken as effectively equal to zero. For this condition, then from Eq. (114),

$$\beta_0=1, \quad \text{and} \quad \beta=\sigma_0^{-4.102}.$$

In Table I, column 6, there are tabulated the values of β for this special case ($\beta_0=1$), corresponding to the values in column 1 of β for Case 1 ($T_B=T_0$), for which, from Eq. (114), $\beta_0=0$. In column 2 are the values of σ_0. Columns 1 and 2 list the same β's and σ_0's as head the Tables II to VII.

Case 3. Filament joined to a spring

As discussed in Part III it is often necessary to hold a filament taut by means of a spring between one end of the filament and its lead. The spring, heated by conduction of heat from the filament, may increase the maximum temperature T_1 of the filament. It was shown in III that the effect is as if the filament length were increased by an amount Δx.

TABLE IV. θ_1 *as function of* φ_0 *and* β.

φ_0	$\beta=100$ $\sigma_0=$ 0.3249	$\beta=120$ $\sigma_0=$ 0.3109	$\beta=140$ $\sigma_0=$ 0.2994	$\beta=160$ $\sigma_0=$ 0.2899	$\beta=180$ $\sigma_0=$ 0.2817	$\beta=200$ $\sigma_0=$ 0.2746
0.000	0.0000	0.0000	0.0000	0.0000	0.0000	0.0000
.005	.0025	.0030	.0035	.0040	.0045	.0050
.010	.0101	.0122	.0142	.0163	.0184	.0205
.015	.0231	.0279	.0327	.0376	.0425	.0475
.020	.0419	.0508	.0599	.0691	.0786	.0882
.025	.0673	.0821	.0974	.1132	.1295	.1465
.030	.1003	.1230	.1476	.1732	.2002	.2288
.035	.1425	.1766	.2145	.2544	.2987	.3465
.040	.196	.2458	.3040	.3673	.4390	.5203
.045	.264	.3386	.4258	.526	.646	.789
.050	.350	.461	.594	.762	.957	1.197
.055	.463	.630	.829	1.081	1.371	1.642
.060	.612	.846	1.141	1.446	1.719	1.956
.065	.794	1.112	1.440	1.723	1.963	2.161
.070	1.013	1.364	1.669	1.920	2.128	2.297
.075	1.228	1.578	1.838	2.058	2.239	2.391
.080	1.407	1.713	1.960	2.157	2.320	2.458
.085	1.544	1.828	2.050	2.226	2.377	2.506
.090	1.656	1.917	2.114	2.279	2.419	2.541
.095	1.742	1.977	2.164	2.319	2.451	2.566
.100	1.809	2.027	2.202	2.349	2.475	2.585
.105	1.863	2.066	2.232	2.373	2.493	2.600
.110	1.902	2.096	2.256	2.390	2.506	2.610
.115	1.934	2.121	2.274	2.403	2.516	2.617
.120	1.960	2.139	2.288	2.414	2.524	2.623
.130	1.999	2.166	2.307	2.428	2.535	2.631
.140	2.024	2.184	2.319	2.436	2.541	2.636
.150	2.041	2.196	2.327	2.442	2.544	2.638
∞	2.078	2.217	2.339	2.449	2.549	2.641

Δx is found from either Eq. (93),

$$\Delta x = (2H)^{\frac{1}{2}} P(1 - P\beta/b)$$

or from Eq. (94),

$$\Delta x = x_S/s^2.$$

In Eq. (93), $2H$ is obtained from the value of $(r/2H)^{\frac{1}{2}}$ for the filament just as in Case 1; P has the values given by Eqs. (88) or (89); and β/b is given by Eq. (91).

In Eq. (94), x_S is the total length of the spring in cm, and s is the ratio of the diameter of the spring to that of the filament.

For springs of practical design,[10] the simpler Eq. (94) is usually sufficiently accurate. If for some reason the spring must be longer than required by usual design, it may become necessary to use Eq. (93).

Having obtained Δx, φ_0 is calculated from Eq. (108), in which x_0 is now not the actual half-length of the filament as before, but the half-length plus $\Delta x/2$. θ_1, T_1, and A are then found as in Cases 1 or 2.

The above method must be used, of course, even in the absence of a spring, when the filament leads are of such small diameter or so long as to be heated by conduction from the filament. As can be seen from Eq. (94), this is avoided if the leads are only a few cm long and have a diameter at least 10 times that of the filament.

TABLE V. $\Delta\Omega/\beta\Omega_0$ *as function of* φ_0 *and* β.

φ_0	$\beta=0$ $\sigma_0=$ 1.0000	$\beta=1$ $\sigma_0=$ 0.8504	$\beta=2$ $\sigma_0=$ 0.7708	$\beta=3$ $\sigma_0=$ 0.7182	$\beta=4$ $\sigma_0=$ 0.6798	$\beta=6$ $\sigma_0=$ 0.6257	$\beta=8$ $\sigma_0=$ 0.5881	$\beta=10$ $\sigma_0=$ 0.5594
0.00	0.00000	0.00000	0.00000	0.00000	0.00000	0.00000	0.00000	0.00000
.02	.00033	.00033	.00033	.00033	.00033	.00033	.00033	.00033
.04	.00130	.00131	.00131	.00131	.00131	.00132	.00132	.00134
.06	.00291	.00293	.00294	.00295	.00296	.00299	.00302	.00307
.08	.00513	.00517	.00520	.00524	.00528	.00536	.00544	.00553
.10	.00792	.00799	.00808	.00818	.00827	.00846	.00866	.00888
.12	.01123	.01139	.01156	.01174	.01194	.01232	.01273	.01318
.14	.01502	.01528	.01557	.01588	.01624	.01711	.01788	.01851
.16	.01924	.01962	.02007	.02060	.02114	.02201	.02326	.02446
.18	.02382	.02434	.02497	.02577	.02655	.02754	.02933	.0309
.20	.02871	.02934	.03015	.03120	.03228	.03394	.03604	.0371
.22	.03385	.03443	.0353	.0366	.03806	.04056	.0428	.0433
.24	.0392	.04022	.0414	.0429	.0444	.0466	.0483	.0484
.26	.0447	.04579	.0472	.0491	.0509	.0522	.0534	.0534
.28	.0503	.0515	.0531	.0553	.0571	.0577	.0580	.0573
.30	.0559	.0573	.0589	.0609	.0624	.0629	.0620	.0605
.32	.0616	.0629	.0644	.0661	.0675	.0673	.0654	.0634
.34	.0672	.0687	.0700	.0712	.0719	.0707	.0684	.0660
.36	.0728	.0740	.0750	.0758	.0760	.0741	.0712	.0682
.38	.0783	.0792	.0798	.0802	.0800	.0771	.0736	.0702
.40	.0837	.0841	.0842	.0842	.0835	.0798	.0757	.0719
.42	.0890	.0889	.0885	.0878	.0867	.0823	.0777	.0735
.44	.0942	.0936	.0927	.0914	.0897	.0846	.0794	.0750
.46	.0992	.0979	.0963	.0946	.0925	.0866	.0810	.0763
.48	.1041	.1023	.1002	.0978	.0951	.0885	.0825	.0774
.50	.1088	.1063	.1036	.1006	.0974	.0902	.0838	.0785
.55	.1200	.1157	.1114	.1070	.1026	.0939	.0867	.0809
.60	.1302	.1236	.1179	.1123	.1068	.0970	.0891	.0829
.65	.1394	.1306	.1235	.1167	.1103	.0995	.0911	.0845
.70	.1478	.1368	.1283	.1204	.1133	.1017	.0928	.0859
.75	.1554	.1426	.1324	.1236	.1159	.1037	.0944	.0872
.80	.1622	.1476	.1360	.1264	.1182	.1053	.0956	.0882
.85	.1684	.1520	.1392	.1288	.1202	.1068	.0968	.0892
.90	.1741	.1559	.1420	.1310	.1220	.1081	.0978	.0900
1.00	.1838	.1625	.1467	.1347	.1250	.1102	.0996	.0915
1.10	.1920	.1679	.1506	.1377	.1274	.1120	.1010	.0926
1.20	.1989	.1723	.1538	.1402	.1294	.1135	.1022	.0936
1.30	.2047	.1761	.1565	.1423	.1312	.1148	.1032	.0944
0.140	.2098	.1793	.1588	.1441	.1326	.1159	.1040	.0951
∞	.27566	.2205	.18875	.16746	.15185	.13002	.11515	.10433

TABLE VI. $\Delta\Omega/\Omega_0$ *as function of* φ_0 *and* β.

φ_0	$\beta=15$ $\sigma_0=$ 0.5104	$\beta=20$ $\sigma_0=$ 0.4774	$\beta=25$ $\sigma_0=$ 0.4529	$\beta=30$ $\sigma_0=$ 0.4338	$\beta=40$ $\sigma_0=$ 0.4051	$\beta=50$ $\sigma_0=$ 0.3840	$\beta=60$ $\sigma_0=$ 0.3676	$\beta=80$ $\sigma_0=$ 0.3429
0.00	0.0000	0.0000	0.0000	0.0000	0.0000	0.0000	0.0000	0.0000
.01	.0012	.0016	.0020	.0025	.0033	.0041	.0050	.0066
.02	.0049	.0066	.0083	.0100	.0134	.0168	.0202	.0273
.03	.0112	.0150	.0188	.0228	.0308	.0389	.0472	.0644
.04	.0201	.0271	.0342	.0414	.0564	.0721	.0884	.1231
.05	.0318	.0432	.0547	.0669	.0921	.1192	.1483	.2129
.06	.0466	.0636	.0815	.1000	.1405	.1848	.2386	.356
.07	.0646	.0889	.1186	.1426	.2043	.2759	.3563	.574
.08	.0862	.1200	.1575	.1969	.2900	.4046	.539	.879
.09	.1118	.1575	.1804	.2657	.4005	.569	.763	1.152
.10	.1418	.2010	.2200	.3480	.5343	.748	.970	1.363
.11	.1766	.257	.318	.446	.677	.916	1.142	1.511
.12	.2161	.314	.429	.550	.812	1.061	1.278	1.624
.13	.2610	.378	.517	.655	.929	1.174	1.378	1.715
.14	.3091	.448	.597	.749	1.030	1.262	1.459	1.791
.15	.359	.515	.676	.835	1.109	1.333	1.527	1.856
.16	.409	.578	.749	.909	1.174	1.394	1.586	1.912
.17	.458	.637	.812	.968	1.230	1.447	1.638	1.961
.18	.506	.694	.867	1.019	1.277	1.494	1.682	2.004
.19	.550	.742	.913	1.063	1.319	1.534	1.722	2.044
.20	.591	.784	.953	1.102	1.357	1.571	1.758	2.078
.21	.629	.821	.989	1.137	1.390	1.604	1.790	2.109
.22	.664	.854	1.021	1.168	1.420	1.633	1.819	2.137
.24	.720	.910	1.076	1.222	1.472	1.685	1.870	2.187
.26	.764	.956	1.122	1.267	1.517	1.728	1.913	2.228
.28	.803	.995	1.161	1.306	1.554	1.765	1.950	2.264
.30	.837	1.029	1.194	1.338	1.586	1.797	1.981	2.295
.35	.906	1.096	1.260	1.404	1.652	1.861	2.045	2.358
.40	.952	1.144	1.309	1.453	1.700	1.909	2.092	2.404
∞	1.2872	1.4830	1.6489	1.7930	2.0385	2.2449	2.4247	2.7304

TABLE VII. $\Delta\Omega/\Omega_0$ *as function of* φ_0 *and* β.

φ_0	$\beta=100$ $\sigma_0=$ 0.3249	$\beta=120$ $\sigma_0=$ 0.3109	$\beta=140$ $\sigma_0=$ 0.2994	$\beta=160$ $\sigma_0=$ 0.2899	$\beta=180$ $\sigma_0=$ 0.2817	$\beta=200$ $\sigma_0=$ 0.2746
0.000	0.0000	0.0000	0.0000	0.0000	0.0000	0.0000
.005	.0021	.0025	.0029	.0033	.0037	.0041
.010	.0083	.0100	.0117	.0134	.0151	.0168
.015	.0190	.0229	.0268	.0308	.0349	.0390
.020	.0344	.0417	.0492	.0568	.0646	.0725
.025	.0553	.0675	.0800	.0930	.1066	.1205
.030	.0824	.1013	.1215	.1426	.1650	.1887
.035	.1172	.1457	.1768	.2100	.2469	.2867
.040	.162	.2037	.2512	.3042	.3646	.4329
.045	.218	.2801	.3534	.438	.540	.663
.050	.290	.383	.496	.640	.810	1.023
.055	.385	.527	.699	.921	1.182	1.435
.060	.511	.714	.977	1.247	1.512	1.746
.065	.670	.951	1.252	1.522	1.764	1.980
.070	.864	1.184	1.473	1.734	1.956	2.150
.075	1.061	1.389	1.647	1.892	2.098	2.283
.080	1.228	1.549	1.796	2.018	2.215	2.393
.085	1.364	1.665	1.904	2.120	2.312	2.487
.090	1.486	1.768	2.002	2.209	2.397	2.569
.095	1.588	1.854	2.082	2.286	2.472	2.641
.100	1.670	1.928	2.153	2.354	2.537	2.706
.105	1.741	1.994	2.216	2.415	2.597	2.764
.110	1.803	2.052	2.272	2.470	2.650	2.815
.115	1.858	2.105	2.323	2.519	2.698	2.863
.120	1.908	2.153	2.369	2.564	2.743	2.908
.130	1.994	2.236	2.450	2.644	2.821	2.985
.140	2.067	2.307	2.519	2.712	2.888	3.050
.150	2.132	2.368	2.579	2.770	2.945	3.107
∞	2.9861	3.2087	3.4069	3.5860	3.7501	3.9020

TABLE VIII. *Values of* h, λ *and* $(r/2H)^{\frac{1}{2}}$.

T_0(°K)	h	λ	$(r/2H)^{\frac{1}{2}}\times10^3$
240	0.0602	1.729	0.780
250	.0626	1.708	0.857
260	.0650	1.688	0.938
270	.0674	1.669	1.024
273	.0682	1.663	1.051
280	.0698	1.651	1.114
290	.0722	1.633	1.209
298	.0742	1.620	1.287
300	.0746	1.617	1.307
310	.0770	1.601	1.410
350	.0866	1.544	1.868
400	.0985	1.483	2.545
450	.1104	1.432	3.343
500	.1222	1.387	4.267
550	.1340	1.348	5.321
600	.1457	1.313	6.510

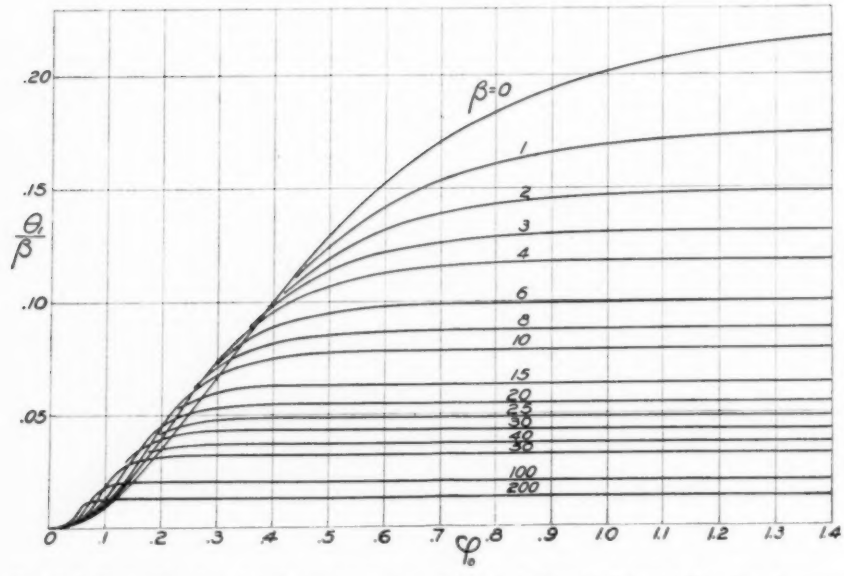

FIG. 5. θ_1/β as a function of φ_0 for various values of β as in Tables II, III, and IV. For clearness some of the curves are not completed to the origin.

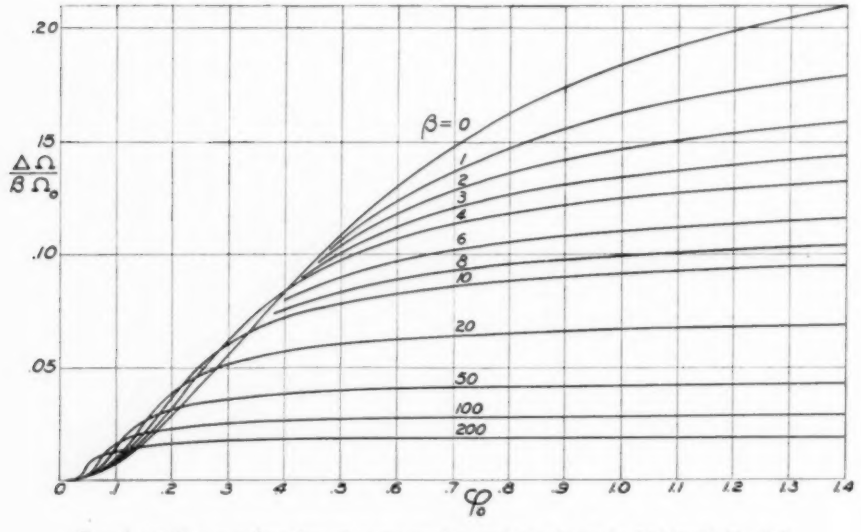

FIG. 6. $\Delta\Omega/\beta\Omega_0$ as a function of φ_0 for various values of β as in Tables V, VI, VII.

Examples of the calculation

Consider the filament in tube No. 2, used in the experiments on heat conductivity, which had a length of 12.86 cm and a diameter of 0.00499 cm ($\sim$2 mil).

	T_0 (°K)	T_B (°K)	β_0	Δx (cm)	x_0 (cm)	$(r/2H)^{\frac{1}{2}}$ $\times 10^3$	φ_0
(1)	300	300	0	0	6.43	1.3071	0.1683
(2)	300	0	1	0	6.43	1.3071	0.1683
(3)	300	300	0	0.40	6.63	1.3071	0.1735

	θ_1	T_1 (°K)	β	A' amp. $cm^{-3/2}$	$A_0\times 10^3$ (amp.)	A (amp.)
(1)	0.740	522.0	20	18.869	6.651	0.02974
(2)	0.740	522.0	20.77	18.869	6.651	0.03031
(3)	0.768	530.4	20	18.869	6.651	0.02974

(1) Given $T_B=T_0=300°K$, the filament mounted directly on heavy leads. Calculate T_1 and the corresponding current A, for $\beta=20$. This is an example of Case 1. As shown in the accompanying table x_0, the half-length, is $12.86/2=6.43$ cm. $(r/2H)^{\frac{1}{2}}$ at 300° from Table VIII is 1.3071×10^{-3}. From x_0, $(r/2H)^{\frac{1}{2}}$, the known value of the filament radius r, and Eq. (108), φ_0 is then calculated to be 0.1683. From Table III for $\beta=20$ and this value of φ_0, θ_1 is found to be 0.740. From Eq. (109) T_1 is 522°K. From Table II, Paper I, A' at 300° is 18.869, so that by Eq. (111) A_0 is 6.651×10^{-3} amp. Finally, using Eq. (110) with $\beta=20$ and this value of A_0, we find A to be 0.02974 amp.

(2) Given $T_0=300°K$ as in Example (1), but the bulb is now immersed in liquid air so that $T_B=0$. Calculate T_1 and A for $\beta=20$. This is an example of Case 2, $\beta_0=1$.

One proceeds exactly as in Example (1) up to the calculation of A. Here instead of using $\beta=20$, the corresponding value of β in column 6 of Table I, equal to 20.77, is used with Eq. (110) to calculate A. As to be expected, this value is slightly larger than the current required in Example (1).

(3) $T_0=T_B=300°K$ as in Example (1), but one end of the filament is joined to a *spring*. Calculate T_1 and A. This is an example of Case 3.

Making use of the relations given in reference 10 on spring design, one finds that a spring suitable for a filament of the present length and diameter can have the following dimensions: a 10-cm length of 10-mil spring wire wound into a spring of 12-mm diameter ($\sim$3 turns).

Δx equal to 0.40 cm is found from Eq. (94), in which x_S is the spring length (10 cm) and s is the ratio $(10/2=5)$ of the diameters of spring and filament. φ_0, equal to 0.1735, is calculated as before from Eq. (108) in which x_0 is now 6.43 $+(\Delta x/2)$ or 6.63 cm. The remaining steps in the calculation of T_1 and A are unchanged. One notes that although the current is the same as in Example (1), the presence of the spring has increased T_1 about 8°.

Table I

Table I gives limiting values of various functions, and has in part been referred to under case 2. In addition, column 3 lists values of θ_M. $(1+\theta_M)T_0=T_M$, the temperature at the middle of the filament when it is infinitely long, or so long that the central part is not cooled by the leads. For a filament of given diameter, θ_1 approaches θ_M as a limit as the filament is made longer and as β is increased. $(\Delta\Omega/\Omega_0)_\infty$ in column 5 is the corresponding limiting value of $\Delta\Omega/\Omega_0$. This behavior is shown in Figs. 5 and 6 which are plots of Tables II to VII. It will be noted in Tables II, III, and IV that θ_1 as a function of φ_0 extends practically to the value of θ_M. However, in Tables V, VI, and VII for the same values of φ_0, $\Delta\Omega/\Omega_0$ has not closely approached its limiting value. These tabulated values of $\Delta\Omega/\Omega_0$ may be extended to $(\Delta\Omega/\Omega_0)_\infty$ by calculation from the equation

$$\Delta\Omega/\Omega_0=(\Delta\Omega/\Omega_0)_\infty-B_\infty/\varphi_0,$$

where B_∞ has the values given in column 4 of Table I.

Column 7 gives values of $\sigma_0^{0.36}$ for use with Eq. (113). In this same equation $\sigma_0^{-4.102}$ is given by the values of β in column 6.

Statistical Analysis of Counter Data

L. I. SCHIFF, *Massachusetts Institute of Technology*

(Received February 24, 1936)

A general relation is derived for the number of counts registered by a Geiger-Müller tube counter or similar electrical counting device exposed to a radioactive source whose strength varies arbitrarily with the time when the counter has a finite, constant resolving time. This is applied specifically to the case of an exponentially decaying source superposed on a uniform background, the solution of the resulting formula being represented nomographically. The number of spurious coincidences observed in a set of P counters used coincidentally is calculated when the resolving times of the individual counters are neglected in comparison with the resolving time of the combining electrical circuit for coincidences. This general expression is applied to the cosmic-ray "telescope" and the double coincidence magnetic spectrometer such as that of Henderson and Alichanow. The constancy of the resolving time of a single counter and the justification for neglecting individual resolving times in comparison with the coincidence resolving time are discussed.

1. INTRODUCTION

IT is well known that Geiger-Müller tube counters and similar electrical counting devices fail, because of their finite resolving time, to register a certain fraction of the ionizing particles that pass through them. Moreover, when several such counters are arranged to respond only to particles that traverse all of them, a certain number of spurious coincidences will be recorded due to the finite resolving time of the combining electrical circuit. The purpose of the following investigation is to show how these effects can be corrected for in some cases of interest.

2. THE DISTRIBUTION LAW

To begin with we require a knowledge of the distribution in time of the arriving particles. Because of the finite solid angle subtended by the counter at the source, not all of the particles emitted by the source pass through the counter. Now it is convenient in the present discussion to consider only those atoms of the source which when they disintegrate will each give off a particle that goes through the counter. The number of these atoms is always proportional to the total number of atoms in the source and will be used throughout as the definition of number of atoms present at a particular time. In this paper we shall exclude chain disintegrations from consideration, since the time and space relations between successively emitted particles of a chain will complicate the following theory; however, we believe that the theory can be modified to deal with this case.

For any one of the M atoms present at $t=0$, let the chance that it disintegrate between times t and $t+s$ be $f(t, s)$. Then the chance that N' of the original M disintegrate between t and $t+s$ and that $M-N'$ do not is given by the binomial law:

$$[M!/N'!(M-N')!]f^{N'}(1-f)^{M-N'}.$$

This expression reduces exactly to Fry's formula[1] when we give $f(t, s)$ the form corresponding to exponential decay. Now we can never know the number of atoms present at the beginning of any particular trial, but only (under ideal conditions) the average number for several trials. Suppose that the source is an artificially radioactive material, prepared by exposure to a substance of very long mean life or to an artificially accelerated beam of particles. In either case the number of bombarding particles appearing in any interval is governed by Poisson's law.[2,3] Hence the numbers of new radioactive atoms produced during the time of bombardment in different trials under identical conditions are distributed according to Poisson's law. This argument is readily extended to the case in which the bombarding material has a relatively short mean life (for if we trace back far enough, we will eventually find an original or parent source of effectively infinite mean life, and starting

[1] T. C. Fry, *Probability and Its Engineering Uses* (1928), p. 237, Eq. (114). See also A. E. Ruark and L. Devol, Phys. Rev. **48**, 772 (1935).

[2] See D. J. Struik, M. I. T. Jour. Math. and Phys. **9**, 151 (1930) for an excellent discussion of Poisson's distribution law.

[3] Reference 1, Fry, p. 214 *et seq.*

from this we can use Eq. (1) repeatedly to obtain the desired result). Then the chance that the initial number of atoms is M when the average number present initially is N is: $(N^M/M!)e^{-N}$. Thus the chance that N' atoms disintegrate between times t and $t+s$ when N atoms are present on the average at $t=0$ is:

$$\sum_{M=N'}^{\infty}\left\{\frac{N^M e^{-N}}{M!}\cdot\frac{M!}{N'!(M-N')!}f^{N'}(1-f)^{M-N'}\right\}=\frac{(Nf)^{N'}e^{-Nf}}{N'!}. \quad (1)$$

Eq. (1) is simply what Poisson's law gives for the chance that N' events occur in the interval t, $t+s$ when $Nf(t, s)$ occur on the average. It should be noted that the number of atoms $Nf(t, s)$ that disintegrate on the average between t and $t+s$ may be taken as the average number of particles that arrive at the counter in this interval, regardless of origin, and includes the counter background as well as particles from the source without affecting the mathematical argument. We shall denote this number in the future by $F(t, s)$.

By defining only such quantities as possess experimental significance and therefore assuming in the above derivation that the number of atoms present initially is not a definitely known or determinable quantity, we have obtained in Eq. (1) a distribution law that is much simpler to work with than the binomial form[1, 4] used by Fry for the β-emission problem.

3. The Resolving Time

In order for a counter to register a particle, that particle must be preceded by a certain small interval during which no particle arrives at the counter. The length of this blank interval is called the resolving time of the counter. Before proceeding further, we must consider the constancy of this resolving time for a particular counter. Danforth[5] has found experimentally that the time of recovery from a pulse for the counters on which he worked depended on the magnitude of the change in voltage across the counter in that pulse, which in turn depended on the time that had elapsed since the previous pulse. This means that the resolving time of the counter depends somewhat on its past history. Ramsey and Lipman,[6] on the other hand, found that in the counters which they examined the voltage peak in a pulse had always the same magnitude, and was such that the extinction voltage (the voltage across the counter at peak) was equal to the threshold voltage (the minimum voltage across the counter necessary for the production of counts). Under these conditions, the resolving time is constant. According to Ramsey,[7] these characteristics vary from counter to counter, and while the extinction voltage is always less (sometimes by two to three hundred volts) than the threshold voltage, the difference may be very small for many counters operating over certain voltage ranges. Skinner[8] has considered a statistical distribution of resolving times for a source of constant strength, basing his assumptions on Danforth's observations. However, it is readily seen that a single statement concerning the resolving time that will apply to all counters cannot be made; when there are amplifying and recording circuits associated with the counter the assumption of a constant value is probably just as valid as that of a statistical distribution.[9] This is true especially when the value used for the constant resolving time can be measured under the conditions of the experiment by a method to be described in section 5 (this procedure automatically gives the right sort of averaging in case the resolving time is not

[4] Recently A. Ruark and L. Devol, Phys. Rev. **49**, 355 (1936) have written a theory of fluctuations in radioactive disintegration based on the binomial type of distribution function. It should be noted that their Eqs. (12) and (16) can be written down immediately (they are of the binomial form) by using the argument at the beginning of section 2 of the present paper. Thus, putting $t=T_1$, $s=T_2$, $M=N$, $N'=n$, and $f(t, s)=gA[e^{-\lambda t}-e^{-\lambda(t+s)}]$, the expression at the beginning of our section 2 becomes the right-hand side of their Eq. (16). Their Eq. (12) can be obtained similarly with even less algebra, using $f(t, s)=e^{-\lambda t}-e^{-\lambda(t+s)}$.

[5] W. E. Danforth, Phys. Rev. **46**, 1026 (1934).

[6] W. E. Ramsey and M. R. Lipman, Rev. Sci. Inst. **6**, 121 (1935).

[7] A private communication, for which the writer is indebted to Mr. Ramsey.

[8] S. M. Skinner, Phys. Rev. **48**, 438 (1935).

[9] For a counter whose threshold and extinction voltages are equal, Skinner's tube parameter d is equal to unity, and his theory predicts one hundred percent counting efficiency for all counting rates. This disagrees with the well-known phenomena of decreasing counting efficiency and eventual paralysis because the effect of the amplifying and recording circuits has not been taken into account. This effect should be considered even at small counting rates.

constant). In addition, the hypothesis of constant resolving time has the considerable advantage of being amenable to mathematical analysis in the case of decaying sources, while the statistical distribution of resolving times leads to quite complicated results even in the relatively simple case of a source of constant strength.[8] In view of all these considerations, we shall assume throughout that the resolving time of a particular counter is constant and has the value that would be determined experimentally by the method of section 5.

4. General Theory for a Single Counter

From the definition of resolving time given at the beginning of section 3 we see that a particle arriving at the counter between times t and $t+dt$ is recorded only if it is preceded by an interval τ in which no particle arrives at the counter. Suppose that the expectation that a particle arrive at the counter between t and $t+dt$ is $\Lambda(t)dt$, where $\Lambda(t)$ depends on the nature of the source and on the counter background. The number of particles expected on the average between times $t-\tau$ and t is then

$$F(t-\tau,\ \tau)=\int_{t-\tau}\Lambda(t)dt,$$

and from Eq. (1) the chance that no particles appear in this interval is $e^{-F(t-\tau,\ \tau)}$. Then of the particles arriving between t and $t+dt$, we expect to count the fraction $e^{-F(t-\tau,\ \tau)}$. Hence in an observation period T_1, T_2, where τ is very small compared to the time of observation $T=T_2-T_1$ (this must hold if we are to get useful data), we expect to *count*

$$n=\int_{T_1}^{T_2}\Lambda(t)e^{-F(t-\tau,\ \tau)}dt, \tag{2}$$

where $$F(t-\tau,\ \tau)=\int_{t-\tau}^{t}\Lambda(t)dt.$$

This is to be compared with the expected number of *particles* that passed through the counter

$$n_0=\int_{T_1}^{T_2}\Lambda(t)dt. \tag{3}$$

5. Constant Source; Determination of the Resolving Time

For a source of constant strength, giving off n_0 particles that go through the counter in time T (this includes the counter background), we obtain immediately from Eq. (2) (setting $\Lambda(t)\equiv n_0/T$):

$$n=n_0e^{-n_0\tau/T} \tag{4}$$

for the number n of counts registered in the time T. This result was obtained by Volz[10] in a somewhat less general way. He went on to show how the resolving time of any particular counter could be determined with the aid of Eq. (4).

We shall now give what is essentially Volz' second method for the evaluation of τ. If we solve Eq. (4) for n in terms of n_0/n (the ratio of number of particles to number of counts) we obtain:

$$n\tau/T=[\ln(n_0/n)]/(n_0/n), \tag{5}$$

which is plotted in Fig. 1. This has a maximum at $n\tau/T=1/e$, $n_0/n=e$. Thus to determine τ, we bring a source up to the counter until it reads at its maximum rate $n_{\max}$, whence:

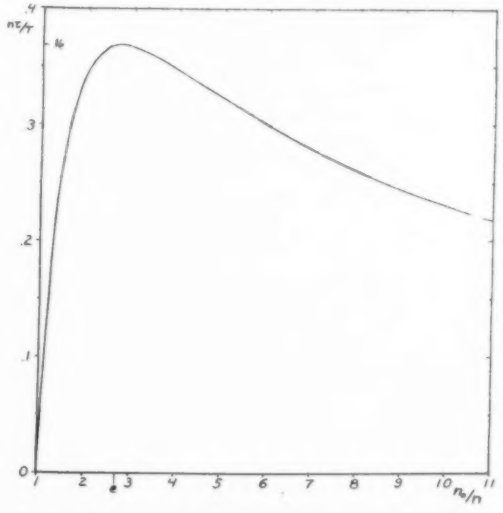

Fig. 1. Counting rate expressed as average number of counts per resolving time of the counter plotted against the ratio of number of particles to number of counts; this is for a source of constant strength.

[10] H. Volz, Zeits. f. Physik **93**, 539 (1935).

$\tau = T/e \cdot n_{\max}$. Fig. 1 permits us to find immediately the true number of particles from the observed number of counts; however, it must be remembered that this includes the counter background.

For an example, suppose that the maximum counting rate of a given counter is $n_{\max}/T = 630$ counts per minute $= 10.5$ per second; then $\tau = 1/10.5e = 0.035$ second. Now with the same counter, we count an average of 480 counts per minute from a particular source, and an average of 50 counts per minute with the source removed (background). The first figure gives a value of $480 \times 0.035/60 = 0.28$ for $n\tau/T$ (average number of counts in a resolving time), and the second a value of $50 \times 0.035/60 = 0.03$. Referring to Fig. 1, we see that the source reading is to be multiplied by 1.5, giving 720 for the number of particles per minute, while the background reading is so small that the correction is negligible. Thus the actual number of particles per minute due to the source alone is 670. It will be observed that the ordinate $n\tau/T = 0.28$ gives a value for n_0/n of 7.1 as well as 1.5. The former figure corresponds to a particle frequency of 3400 per minute. The larger figure indicates that the counter is almost completely paralyzed. To distinguish between the two in case of doubt, we simply remove the source slightly. If the counter is nearly paralyzed this will result in an increased counting rate, while if it is operating normally the counting rate will fall off. For ordinary counter usage the lower figure for the particle frequency is the correct one. This method is applicable to sources of constant or slowly varying strength.

6. Determination of Decay Constant; Peierls' Method

Peierls[11] has shown how the decay constant λ of a radioactive element can be determined with the least possible error, using a counter exposed to the source and influenced by its natural background. His method requires that the observation period be divided into intervals of equal lengths d less than $0.3/\lambda$, and that the number of particles arriving in each of these intervals be measured. When the intervals d are of length equal to or less than $0.2/\lambda$, we can find the number of particles from the number of counts by using Fig. 1 (and subtracting the background counts), with an error of less than one percent. If it happens that the intervals d must be taken much larger than $0.2/\lambda$ the method of section 5 should not be used; rather the results of section 7 are to be applied. However, the application of these results requires a knowledge of the decay constant, which is just what we are trying to determine. Therefore an approximate value for λ must be assumed; from this the number of particles in each interval is calculated by the method of the next section. These particle numbers are then used to get a closer approximation to λ. Usually, however, it will be feasible (and it is always preferable) to take $d \leq 0.2/\lambda$, in which case section 5 may be applied directly.

[11] R. Peierls, Proc. Roy. Soc. **A149**, 467 (1935). See particularly p. 475.

7. Exponentially Decaying Source with Constant Background

Consider a counter exposed to a source of decay constant λ, on which is superposed a constant background or natural effect of strength β particles per unit time. Let N be the average number of atoms of the decaying material present at $t=0$ (using number of atoms in the sense defined at the beginning of section 2), and N_1 and N_2 be the numbers present on the average at times T_1 and T_2, respectively, where these are the limits of the observation time. Then in Eq. (2) we put

$$\Lambda(t) \equiv \beta + N\lambda e^{-\lambda t} \tag{6}$$

and obtain, on performing the integrations,[12]

$$n = (e^{-\beta\tau}/e^{\lambda\tau} - 1)\{\exp[-N_2(e^{\lambda\tau} - 1)] - \exp[-N_1(e^{\lambda\tau} - 1)]\} + (\beta/\lambda)e^{-\beta\tau} \times \{Ei[-N_1(e^{\lambda\tau} - 1)] - Ei[-N_2(e^{\lambda\tau} - 1)]\}, \tag{7}$$

where $n_0 = N_1 - N_2$ is the expected number of particles due to the source alone that passed through the counter in the time of observation

[12] $\exp(-z) = e^{-z}$; $Ei(-z) = -\int_z^\infty e^{-v}/v\,dv$. For tables of the exponential integral and related functions with argument going from zero to one by intervals of 0.001, see W. L. Miller and T. R. Rosebrugh, Trans. Roy. Soc. Canada **9**, 73 (1903); reprinted as University of Toronto Studies, Papers from the Chemical Laboratories, no. 43.

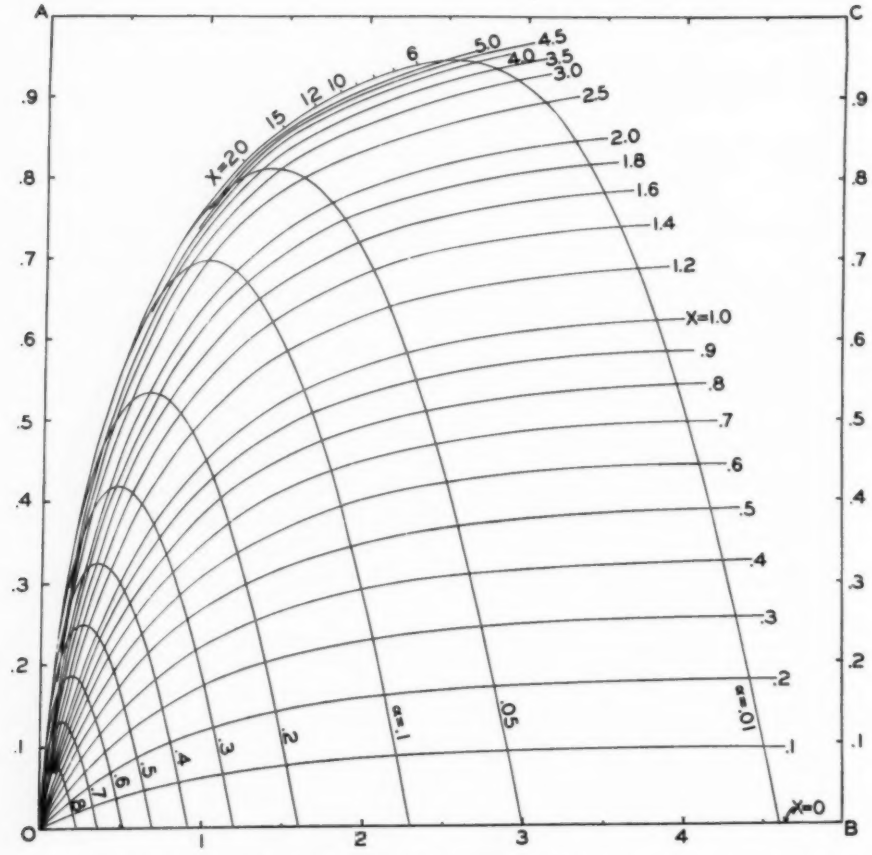

FIG. 2. Nomogram for the solution of Eq. (8). $a=n\lambda\tau e^{\beta\tau}$ is plotted along the OA scale, and $b=a-5\beta\tau$ is plotted along the BC scale; a straight line joining points a and b intersects the curve for a particular value of α at values of x which are solutions of Eq. (8).

$T=T_2-T_1$. Making use of the relations $N_1=n_0/(1-\alpha)$, $N_2=\alpha n_0/(1-\alpha)$, where $\alpha=e^{-\lambda T}$, and remembering that τ must be very small compared to $1/\lambda$ to obtain data of any value at all, we may write Eq. (7) to good approximation:

$$n=(e^{-\beta\tau}/\lambda\tau)[e^{-\alpha x}-e^{-x}]+(\beta/\lambda)e^{-\beta\tau}\times[Ei(-x)-Ei(-\alpha x)], \quad (8)$$

where $x=n_0\lambda\tau/(1-\alpha)$. It is impossible to solve Eq. (8) analytically for x (or n_0) in terms of n and the other parameters, and any approximation good enough to cover the whole field of experimental application is of little value. However, as there are just four independent parameters (x, α, and two others which may be regarded as the coefficients of the bracket terms divided by n), a fairly simple nomographic representation is possible (see Fig. 2).

The nomogram consists of a set of curves of constant α and a set of curves of constant x. The studs on the curve for $\alpha=0.01$ above $x=5$ give the points of intersection with the curves (not drawn) for eight values of x from 6 to 20. The values of λT corresponding to each α are given by the intersection of that α-curve with the OB scale and are also found in Table I.

TABLE I. *Values of* $\lambda T=-\ln\alpha$ *for the ten* α*-curves of Fig. 2.*

α	0.01	0.05	0.1	0.2	0.3	0.4	0.5	0.6	0.7	0.8
λT	4.605	2.996	2.302	1.609	1.204	0.916	0.693	0.511	0.357	0.223

The α-curves are drawn for ten values of α ranging from 0.01 ($\lambda T = 4.605$) to 0.8 ($\lambda T = 0.223$). An observation time greater than $4.6/\lambda$ would hardly ever be used in practice because of the low intensity of the source towards the end of the run and the consequent increase in importance of the background. On the other hand, for $T < 0.2/\lambda$ the variation of the source strength during the time of observation is so small that Fig. 1 of section 5 may be used directly with an error of less than one percent, and the procedure of this section is unnecessary. It is obvious that a choice of simple values of α rather than of λT simplifies enormously the computation of the nomogram while it does not materially affect its convenience in use, since the time of observation will depend on λ as well as λT and will not in general be a simple number.

To use the nomogram we first find the resolving time of the counter by the method of section 5, the decay constant λ of the source by Peierls' method corrected as in section 6, and the background strength β corrected as in section 5. These will be constant throughout a particular experiment. By using the observed number of counts n we then calculate two numbers a and b defined as

$$a = n\lambda\tau e^{\beta\tau} \tag{9}$$

$$b = a - 5\beta\tau. \tag{10}$$

(Since the background strength is generally rather small, it will facilitate computation to note that $e^{\beta\tau}$ may be replaced by $1+\beta\tau$ with an error of less than one percent when $\beta\tau < 0.14$.) We then mark off the point a on the OA scale and the point b on the BC scale of the nomogram. From the length of observation time T we find the number $\alpha = e^{-\lambda T}$, and select the corresponding curve from the set for constant α. (It is advisable to use a value of α for which a curve is drawn; otherwise it is necessary to interpolate.) We then draw a straight line through the points a and b on the OA and BC scales, respectively; this in general intersects the curve of constant α that we have chosen at two values of x which we shall call x_1 and x_2, where x_1 is the smaller. From these values of x we find two values of n_0 from the relation:

$$n_0 = x(1-\alpha)/\lambda\tau. \tag{11}$$

The smaller value of n_0 thus obtained corresponds to normal operation of the counter and the larger to operation close to paralysis. In general it is safe to say that x_1 should be used to determine n_0.

An example will perhaps clarify the use of the nomogram of Fig. 2. Suppose that we have found by the methods of sections 5 and 6 that $\tau = 0.023$ second, $\beta = 1.83$ seconds^{-1}, $\lambda = 0.0126$ second^{-1} (half-value time = 55.0 seconds) for a particular counter and source. Now suppose that it happens that it is most convenient in this experiment for us to take readings over a period of about five minutes. This being the case, we choose $\alpha = 0.01$, which gives $\lambda T = 4.60$, or $T = 6.09$ minutes. Our reading at the end of this time is $n = 3070$ counts. We then calculate a and b from Eqs. (9) and (10) and obtain: $a = 0.929$, $b = 0.719$. Laying off these values on the OA and BC scales, respectively, we see that the straight line through these points intersects the curve for $\alpha = 0.01$ at $x_1 = 1.60$, $x_2 = 14.2$. We find that the counter is operating normally by removing the source slightly and noting that the counting rate decreases (if the counter were nearly paralyzed a removal of the source would at first increase the counting rate). Therefore, we use x_1 and obtain $n_0 = 5460$, which is the number of particles from the source (exclusive of background) during the 6.09 minutes of observation.

8. General Theory for Multiple Coincidence Counters

A true P-fold coincidence is produced in a set of P coincidence counters when a particle traverses all the counters, or when the individual members of a burst traverse all simultaneously. A certain number of spurious coincidences will also be produced by particles (other than those that cause true coincidences) arriving at each of the P counters so that their arrival times are grouped within a small interval of time. The length τ' of this interval is called the resolving time of the combining electrical circuit for coincidences and is assumed to be constant. The spurious counts may be produced by distinct particles in each counter, by single particles in some of the counters and true partial coincidences in the rest, or by any combination of

single particles and true partial coincidences. A true partial coincidence is defined here as a true coincidence produced by one particle traversing more than one but not all of the counters. In the following analysis we shall assume that the resolving times of the individual counters may be neglected in comparison with that of the combining circuit for coincidences. While this is not strictly true, as long as the counters are operated well below their maximum counting rate (as is usually the case in coincidence work) the principal effect of the finite resolving times of the separate counters is to increase somewhat the effective coincidence resolving time; this is automatically allowed for when τ' is measured as indicated at the end of section 9.

Let the expectation that a particle pass through only the ith of P coincidence counters between times t and $t+dt$ be $\Lambda_i(t)dt$; likewise let the expectation of a true partial coincidence in only counters $i, j, \cdots l$ between times t and $t+dt$ be $\Lambda_{i,j,\cdots l}(t)dt$. We shall make the simplifying assumptions throughout that $\Lambda_i(t) \gg \Lambda_{ij}(t) \gg \cdots \gg \Lambda_{i,j,\cdots l}(t)$, etc., in order of increasing number of subscripts, and that ${}_P\Lambda(t) \ll 1/\tau'$, where ${}_P\Lambda(t)$ is the expectation function for true P-fold coincidences. These conditions generally hold; however, the theory can be developed without them, although it would have an even more complicated form than that given below. It is also assumed that the various Λ's are independent; this is quite valid since a particle which causes a true partial coincidence in any group of counters at a particular time can have no effect on any of the counters at any other time. In general, these Λ's will depend only on the geometrical arrangement of sources and counters. Then according to Eq. (1) the chance that at least one particle appear in only the ith counter between t and $t+\tau'$ is $1-e^{-F_i(t,\,\tau')}$, where

$$F_i(t,\,\tau') = \int_t^{t+\tau'} \Lambda i(t)dt;$$

also, the chance that at least one true partial coincidence appear only in counters $i, j, \cdots l$ between t and $t+\tau'$ is $1-e^{-F_{i,\,j\,\cdots\,l}(t,\,\tau')}$, where

$$F_{i,\,j,\,\cdots l}(t,\,\tau') = \int_t^{t+\tau'} \Lambda_{i,\,j,\,\cdots l}(t)dt.$$

Now a spurious coincidence is caused by an initiating particle (or true partial coincidence) in one (or more) of the counters being followed by particles (either single or members of a true partial coincidence) through each of the other counters within the time τ'. This is provided that at least one of the counters other than that (or those) which initiated the spurious coincidence had no particle through it for a time τ' in the past; this assures that the combining circuit was clear when the initiating particle arrived. For example, with a group of six counters, it is seen that the expectation that a true double coincidence occur in counters 2 and 4 between times t and $t+dt$, followed by a single particle through counter 6 and a true triple coincidence in counters 1, 3, and 5 within a time τ' is:

$$\{1-\prod_{i=1,\,3,\,5,\,6}(1-e^{-F_i(t-\tau',\,\tau')})\}\Lambda_{24}(t) \times(1-e^{-F_6(t,\,\tau')})(1-e^{-F_{135}(t,\,\tau')})dt, \quad (12)$$

when at least one of counters 1, 3, 5, and 6 was not discharging for a time τ' before t. In order to find the expected number m of spurious coincidences observed between times T_1 and T_2, we must add together all possible combinations of the Λ's and the F's of the form of Eq. (12) that involve all of our P counters, and then integrate over the time from T_1 to T_2. It is evident that with more than three counters the result is very complicated indeed. Making the assumptions above that the Λ's decrease rapidly as the number of subscripts increases and that ${}_P\Lambda \ll 1/\tau'$, we obtain for two counters used coincidentally:

$$m_2 = \int_{T_1}^{T_2} \{e^{-F_2(t-\tau',\,\tau')}\Lambda_1(t)(1-e^{-F_2(t,\,\tau')}) + e^{-F_1(t-\tau',\,\tau')}\Lambda_2(t)(1-e^{-F_1(t,\,\tau')})\}dt. \quad (13)$$

The similar expressions for three and four counters would contain nine and thirty-six terms, respectively, instead of two as in Eq. (13). No matter how complicated, however, the general expression for any number of counters can always be written down by using the above method, and it will be shown in the next section that the results simplify considerably in an important special case.

9. Multiple Coincidences; Constant Sources

In the case where the average number of particles per unit time at any counter is independent of the time (as in the cosmic-ray "telescope"), we may put: $\Lambda_i(t) \equiv \nu_i$, $\Lambda_{i,\,j,\,\ldots\,l} \equiv \nu_{i,\,j,\,\ldots\,l}$. When the various ν's are small compared to $1/\tau'$, the expected spurious counting rates for two, three, and four counter coincidence units, respectively, become to good approximation:

$$
\begin{aligned}
&m_2/T = 2\tau'\nu_1\nu_2\,;\\
&m_3/T = 3\tau'^2\nu_1\nu_2\nu_3 + 2\tau'(\nu_1\nu_{23} + \nu_2\nu_{13} + \nu_3\nu_{12})\,;\\
&m_4/T = 4\tau'^3\nu_1\nu_2\nu_3\nu_4 + 3\tau'^2(\nu_1\nu_2\nu_{34} + \nu_1\nu_3\nu_{24}\\
&\quad + \nu_2\nu_3\nu_{14} + \nu_1\nu_4\nu_{23} + \nu_2\nu_4\nu_{13} + \nu_3\nu_4\nu_{12})\\
&\quad + 2\tau'(\nu_{12}\nu_{34} + \nu_{13}\nu_{24} + \nu_{14}\nu_{23})\\
&\qquad + 2\tau'(\nu_1\nu_{234} + \nu_2\nu_{134} + \nu_3\nu_{124} + \nu_4\nu_{123}).
\end{aligned}
\tag{14}
$$

Similar expressions are readily written down for any number of counters. It must be remembered in using Eq. (14) that the various ν's represented there are the average numbers of particles per unit time that belong *only* to the classifications indicated by the subscripts. In practise it is impossible to measure these quantities directly. For example, the quantity ν_{234} in a four counter coincidence unit is given by:

$$\nu_{234} = \mu_{234} - 3\tau'^2_{234}\nu_2\nu_3\nu_4 - 2\tau'_{234}(\nu_2\nu_{34} + \nu_2\nu_{24} + \nu_4\nu_{23}),$$

where μ_{234} is the observed number of coincidences per unit time between counters 2, 3, and 4 only, τ'_{234} is the coincidence resolving time for these counters, and the ν's appearing on the right-hand side above must themselves be obtained from similar expressions. Thus the ν's can be found accurately only as the solution of a set of simultaneous nonlinear equations. This would be a very laborious process at best; however, a good approximation is generally obtained by using the observed μ's for the ν's, and neglecting the correction terms.

The experimental measurement of the coincidence resolving time τ' may be effected by arranging the P counters in space so that true coincidences are very unlikely between any combination of two or more counters. In this case all of the ν's that possess more than one subscript vanish, and it is readily seen that the spurious counting rate is given by:

$$m_P/T = P(\tau')^{P-1}\nu_1\nu_2\cdots\nu_P. \tag{15}$$

Since the counters are arranged so that all of the observed P-fold coincidences are spurious, m_P/T, $\nu_1, \nu_2, \cdots \nu_P$ can be measured directly, and τ' is readily calculated. This method for the determination of τ' tends to compensate for neglecting the individual counter resolving times.

10. The Double Coincidence Magnetic Spectrometer

Henderson,[13] Alichanow,[14] and others have employed a magnetic spectrometer in the measurement of beta-ray and positron energy distribution spectra. The apparatus is designed to respond to coincidences produced by electrons that are deflected around a semicircular path by a magnetic field and traverse two counters placed in their path. On the other hand, gamma-rays from the source can set off either one of the counters but never both. Because of the finite coincidence resolving time, the gamma-rays from the source, and the natural backgrounds of the two counters, a certain number of spurious coincidences will be produced. To calculate this number for an exponentially decaying source we put into Eq. (13):

$$\Lambda_1(t) \equiv \Lambda_2(t) \equiv \beta_0 + N\lambda e^{-\lambda t}, \tag{16}$$

where β_0 is the constant counter background, N the average number of atoms for each counter at zero time (defined as at the beginning of section 2), and λ the decay constant of the source. Since the counters are generally similar in construction and placed symmetrically with respect to the source, β_0 and N will be the same for both.[15] Putting Eq. (16) into Eq. (13) and carrying out the integrations, we find that the result is most easily expressed in the notation of section 7:

$$m_2 = 2(n_1 - \tfrac{1}{2}n_2). \tag{17}$$

In Eq. (17), m_2 is the expected number of spurious coincidences observed in the double

[13] W. J. Henderson, Proc. Roy. Soc. **A147**, 572 (1934).
[14] A. I. Alichanow et al., Zeits. f. Physik **90**, 249 (1934); **93**, 350 (1935).
[15] Eq. (17) is readily modified if this is not the case, although the result is somewhat more complicated.

coincidence unit in the time T; if n^0 is the number of counts due to the source alone observed in this time in each counter separately (these should be about the same for the two counters), then n_1 is given by Eq. (8) when we set $\tau=\tau'$, $\beta=\beta_0$, and $n_0=n^0$, and n_2 is given by Eq. (8) with $\beta=2\beta_0$ and $n_0=2n^0$. n^0, T, and β_0 are directly observable. To calculate n_1 and n_2 rapidly from Eq. (8) without having to look up exponentials and exponential integrals, the nomogram of Fig. 2 may be used as follows. We select the curve of constant α corresponding to our value of λT (again it is advisable to choose T so that the resulting value of α is one for which a curve is drawn in Fig. 2; this removes the necessity for interpolation). We find the value of x corresponding to $n_0(=n^0)$ from the second of Eq. (8) (with $\tau=\tau'$), and mark this point on the correct α-curve. Then the ordinate of this point is the value of $[e^{-\alpha x}-e^{-x}]$, the first bracket expression in Eq. (8), and the abscissa is the value of $[Ei(-x)-Ei(-\alpha x)]$, the second bracket expression in Eq. (8). This facilitates the calculation of n_1. The bracket expressions for n_2 are found in exactly the same manner, except that $2n^0$ is used for n_0.

To illustrate, suppose that we are examining a source of decay constant $\lambda=2.87\times10^{-4}$ seconds^{-1} (half-value time$=40.2$ minutes) with a double coincidence arrangement of resolving time $\tau'=0.078$ second, and that a convenient length of observation time is about an hour. We then choose $\alpha=0.4$, which gives $\lambda T=0.916$, or $T=53.1$ minutes. The constant background for each counter is found to be $\beta_0=0.37$ count per second. We observe for 53.1 minutes, and find an average total $(=n^0+\beta_0 T)$ of 3430 single counts in each of the counters; subtracting the number of background counts gives $n^0=2250$. We now proceed to find n_1. From the second of Eq. (8) (with $\tau=\tau'=0.078$) we obtain $x=0.084$; this point on the curve of Fig. 2 for $\alpha=0.4$ has an ordinate of 0.045 and an abscissa of 0.87. Substituting these values for the bracket expressions into Eq. (8) we obtain $n_1=3040$. Similarly for n_2, we have $n_0=2n^0=4500$, $x=0.168$ with an ordinate of 0.085 and an abscissa of 0.80, giving $n_2=5510$ when we use $\beta=2\beta_0=0.74$ second^{-1}. Substitution into Eq. (17) gives immediately $m_2=570$ for the number of spurious coincidences expected under these conditions.

11. Concluding Remarks

The aim of the writer in this treatment of the statistics of electrical counting devices has been to develop the theory necessary for the correction of single and multiple coincidence counter readings for finite resolving time in as general a way as possible; and then to apply the general theory to specific cases of interest, the results being represented in such a manner as to be readily available for experimental application. Two main assumptions have been made: (1) The resolving time of a single counter is constant; (2) the resolving times of the individual counters in a multiple coincidence arrangement can be neglected in comparison with the resolving time of the combining electrical circuit for coincidences. There is no doubt that neither of these assumptions is always strictly true. On the other hand, it seems very probable that the results obtained with the aid of these assumptions when the procedures outlined are followed differ from the truth only by an amount that is of smaller order than the corrections to the actual readings introduced by the above theory. Also, assumption (1) in particular seems to be as accurate over a wide range of operating conditions as any moderately simple one that can be made. In any case, the simplifications in the mathematical theory and the resulting ease of application to any given experimental situation more than compensate for the second order errors that appear as a consequence.

The writer wishes to express his sincere appreciation to Professor Robley D. Evans for suggesting this problem and for continued interest in the progress of its solution; to Professor D. J. Struik of the mathematics department for helpful discussion of probability theory in general; and to Professor L. H. Thomas of the Ohio State University for illuminating conversations on certain points of the theory, particularly section 2.

LETTERS TO THE EDITOR

Prompt publication of brief reports of important discoveries in physics may be secured by addressing them to this department. Closing dates for this department are, for the first issue of the month, the twentieth of the preceding month, for the second issue, the fifth of the month. The Board of Editors does not hold itself responsible for the opinions expressed by the correspondents.

Communications should not in general exceed 600 words in length.

New and Unexplained Effects in Laue X-Ray Reflection in Calcite

In the course of an effort[1] to ascertain the validity of x-ray crystal methods for determining the electronic charge, e, the following unexplained effects in Laue x-ray reflection through thin cleaved plates of calcite were observed.

Fig. 1 shows schematically the arrangement of the photographic spectrometer. The molybdenum target of the

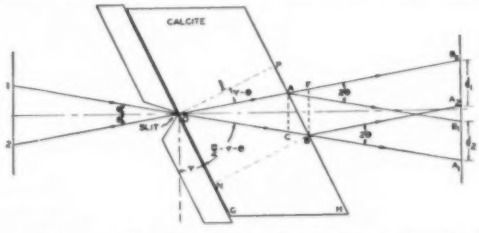

x-ray tube was situated either in the line $O1$ or $O2$ with its long axis nearly vertical (normal to the plane of the figure) so that the rays left the target surface at a small angle of 2° to 3°. The round focal spot had thus sufficient horizontal extension to subtend from the slit with careful setting about the angular range required for the complete Mo K spectrum. Most of the observations, however, were made on the α-lines only. The crystal plates used were a millimeter or less in thickness, OP, and ran about 2×1.5 cm in height and breadth. The crystals had narrow rocking curves and were of excellent quality. The design of crystal support was the result of careful study with the two crystal spectrometer to avoid strain in the crystal. All appropriate alignments and orientations were carefully made by optical means. The photographic plate could be situated at about 60 cm from the crystal but closer distances were also used. The slit is purposely put on the tube side of the crystal. With the slit on the plate side of the crystal very fine uniform and perfect spectral lines had been obtained with the same identical crystals. The plate was shielded with lead from the direct beam transmitted through the crystal. We list below our observations:

(1) The regions on the plate A_1B_1 and A_2B_2 were not filled out with exposed emulsion the blackening being only in the vicinity of A_1 or B_1, A_2 or B_2 as though reflection by internal planes parallel to GH occurred only near entrance and exit surfaces in the regions near O, A or B. This would have been expected with disturbed surfaces but is a little surprising with excellent cleavage surfaces. No intermediate lines such as those reported[2] in quartz were observed.

(2) By moving the plate closer to the crystal it was found that the beams A_1 and B_1 were not propagated to the plate along exactly parallel lines but that they converged very slightly. This was also the case with beams A_2 and B_2. By measuring separations d_1 and d_2 at two slit-plate distances and extrapolating back to the crystal itself the separations BF and AC were found to be in good agreement with the values computed from crystal thickness and geometry assuming that the reflections occur very close to entrance and exit surfaces.

(3) *Along the lengths of the paired spectral lines* (normal to the plane of the figure) marked fluctuations of intensity were observed, the line being completely extinguished in the case of some samples at more or less uniformly spaced intervals and apparently more or less at the same heights on both components such as A_1B_1. A study of these fluctuations at different plate-crystal distances and also with the tube at varying heights seemed to indicate that the extinguishing effect came from definite regions of the crystal independent of the vertical angle between the beam and the plane of the figure.

(4) We inserted auxiliary slit jaws moved by micrometer screws so as to cover either or both of the emerging reflected beams in the region near A or B. With either component shielded the remainder of the pattern including the fluctuations along the length of the lines remained unchanged thus apparently ruling out interference at the plate as an explanation. With both components covered leaving only a fine slit through which radiation could pass only if it had been reflected in the central interior of the crystal some fifteen times the exposure was necessary to obtain lines and these were very diffuse and quite unlike the above-mentioned sharp lines obtained with the slit on the plate side of the same crystal. We have shown that these effects cannot be caused by any structure in the focal spot.

We believe these strange effects would warrant further investigation.

It is a pleasure to acknowledge our indebtedness to Dr. Leon L. Watters of New York whose generous financial support through the Frances Hayes Watters Memorial Fund has made this, as well as a number of other recent investigations, possible at this Institute.

JESSE W. M. DUMOND
V. L. BOLLMAN

California Institute of Technology,
June 3, 1936.

[1] See Letter to the Editor in this issue entitled "Tests of the Validity of X-Ray Crystal Methods of Determining e."
[2] Carleton Murdock, Phys. Rev. **45**, 117 (1934).

A Mass-Spectrographic Determination of the Mass Difference $N^{14}+H^1-N^{15}$ and the Nitrogen Disintegration Reactions

The rare isotopic ion of nitrogen, N^{15+}, has been matched in intensity with the molecular ion $(N^{14}H^1)^+$ and photographed by means of a high resolving power, high dispersion linear scale mass spectrograph.[1] The doublets were photographed in several different plate positions and a line density sufficiently great for accurate measurement was obtained with exposure times of four to six minutes. Measurements of the doublet separations were made on a comparator and checked by means of calibrated microphotometer curves. The agreement was within 0.005 mm in every case.

With these measured doublet separations in conjunction with the known dispersion curve for the plate, the following mass difference was obtained.

$$N^{14}H^1-N^{15}=0.01074\pm0.0002 \text{ mass unit.}$$

This value, in combination with the mass difference previously reported[2] for the $[{}_1H^2-D^2]$ doublet allows us to compute a value for the energy release in the deuteron nitrogen disintegration in which long range protons are emitted. This reaction

$$N^{14}+D^2\rightarrow N^{15}+H^1+Q_1$$

can be expressed in the following form

$$Q_1=[N^{14}H^1-N^{15}]-[{}_1H^2-D^2]$$

in which the terms included within the brackets are the mass differences of the doublets which have been measured on the mass spectrograph and reported above. Thus from mass considerations alone, the magnitude of the energy release is $Q_1=8.57\pm0.2$ MEV, which agrees within the limits of error with the value 8.53 MEV obtained from disintegration experiments.[3, 4]

The reactions involving the production of radio-oxygen[5]

$$N^{14}+D^2\rightarrow O^{15}+{}_0n^1+Q_2$$
$$O^{15}\rightarrow N^{15}+e^++\mu+Q_3,$$

can be written in an analogous manner. The mass of the neutrino is considered less than the probable error in the nitrogen doublet mass determination. Thus

$$Q_2+Q_3=[N^{14}H^1-N^{15}]-\text{Binding Energy of Deuteron}-[e^++(e^-)].$$

$Q_2+Q_3=6.82$ MEV.

A direct measurement of Q_3 has been made,[6] thus the expected value of the neutron energy can be calculated for any given deuteron energy. An absolute check on this equation awaits the direct determination of Q_2.

The nitrogen deuteron reaction in which alpha-particles are released

$$N^{14}+D^2\rightarrow C^{12}+He^4+Q_4$$

can be combined with the oxygen deuteron reaction $O^{16}+D^2\rightarrow N^{14}+He^4+Q_5$ and be written in the following form

$$Q_4-Q_5=[C^{12}H_4-O^{16}]-2[C^{12}H_2-N^{14}].$$

The mass differences of the doublets which appear in the brackets on the right-hand side have been reported[7] and give us the value $Q_4-Q_5=10.14\pm0.3$ MEV. Here again the agreement with the disintegration value[3, 4] for this difference is quite good. It must be noticed, however, that this is not a check on either Q_5 or Q_4 individually, since both may be in error in such a way that (Q_4-Q_5) remains unchanged. A check on the individual reactions can only be obtained by measuring all the mass differences involved.

Harvard University,
June 15, 1936.

EDWARD B. JORDAN*
KENNETH T. BAINBRIDGE

* National Research Fellow.

[1] K. T. Bainbridge and E. B. Jordan, Phys. Rev. **49**, 421 (1936). Abstract No. 68.
[2] K. T. Bainbridge and E. B. Jordan, Phys. Rev. **49**, 883A (1936).
[3] J. D. Cockcroft and W. B. Lewis, Proc. Roy. Soc. **A154**, 261 (1936).
[4] E. O. Lawrence, E. McMillan and M. C. Henderson, Phys. Rev. **47**, 273 (1935).
[5] M. S. Livingston and E. McMillan, Phys. Rev. **46**, 437 (1934).
[6] W. A. Fowler, L. A. Delsasso and C. C. Lauritsen, Phys. Rev. **49**, 561 (1936).
[7] E. B. Jordan and K. T. Bainbridge, Phys. Rev. **49**, 883A (1936).

The Isotopic Constitution of Iron and Nickel

Using a discharge in iron carbonyl, J. de Gier and P. Zeeman have recently observed four isotopes in iron[1] with atomic masses 54, 56, 57, and 58. The observations of Dr. Aston[2] had given only the first three. With a spark between pure electrolytic iron electrodes (Hilger spectroscopic brand) the four masses mentioned all appeared with great intensity the heaviest at 58 being the weakest. No line at 60 was observable. A very faint line at 59 could be ascribed to cobalt as the report of the spectroscopic investigation of this iron recorded a trace of cobalt.

The isotopic constitution of nickel is still uncertain. Dr. Aston considered masses at 56 and 64 as possibly due to some element or component other than nickel.[3] J. de Gier and P. Zeeman[1] were unable to find the isotope at 61 reported by Aston. This is possibly due to insufficient resolving power in their parabola method. With nickel the question of the purity of the metal is of very great importance as the impurities are very likely to be the neighboring elements and to give lines at 54, 56, 57 (Fe), 59 (Co), 63 (Cu), and 64 (Zn). In the nickel of exceptional purity made by fractionating nickel carbonyl, as supplied by Hilger & Company, zinc, cobalt, and copper are eliminated although a trace of iron is still present. A photograph made with electrodes of this iron is shown in Fig. 1. There can be no doubt that the masses at 58, 60, 61, 62, and 64 are all isotopes of nickel. The lines at 61 and 64 were of approximately equal intensity in all the photographs. The trace of iron still present in the nickel gave a mass at 56 and a very faint mass at 54. The relative intensity of these with respect to the other lines differed on different photographs, and was different with other samples of nickel, so that there is every reason to suppose that these masses are due to iron.

Ryerson Physical Laboratory,
University of Chicago,
June 12, 1936.

A. J. DEMPSTER

[1] J. de Gier and P. Zeeman, Proc. Amst. Acad. Sci. **38**, 810, 959 (1935).
[2] F. W. Aston, Proc. Roy. Soc. **A149**, 402 (1935).
[3] F. W. Aston, Proc. Roy. Soc. **A149**, 401 (1935); Nature **137**, 613 (1936).

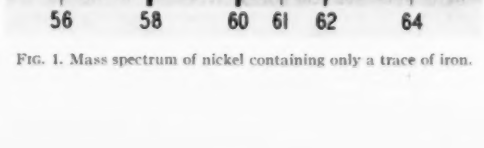

FIG. 1. Mass spectrum of nickel containing only a trace of iron.

Disintegration Constant of Thorium and Branching Ratio of Thorium C

Up to the present there has been an uncertainty in the value of the disintegration constant of thorium, a discrepancy of thirty percent existing between the Geiger-Rutherford value and the Kirsch value.

Using a mechanical counter to determine the rate of emission of α-particles from a thin specimen of thorium (ThO_2) and its products covered by a film of celluloid to impound the thorium emanation, we find for the disintegration constant of thorium, $\lambda = 5.17\ (10)^{-11}$ yr.$^{-1}$, the corresponding half-value period being $T = 1.34\ (10)^{10}$ yr. This is a preliminary value given by about a million "counts" from four specimens derived from the same source, a thorite, as that used by Geiger and Rutherford originally. Correction for the small amount of ionium in the mineral has been made. Counting on specimens derived from other sources is still in progress.

During the course of the work a certain number of counts were taken with aluminum foils of sufficient thickness placed over the specimens to absorb all α-particles except those due to thorium C′. This allows a determination of the branching ratio of thorium C to be made. The value obtained is 0.660, which checks closely the accepted value given by Meitner and Freitag.

ALOIS F. KOVARIK
NORMAN I. ADAMS, JR.

Sloane Laboratory,
Yale University,
June 16, 1936.

The Spectra Be III and Be IV

Wave-lengths of the $1s^2\ {}^1S_0 - 1s \cdot np\ {}^1P_1$ series of Be III which have been reported in these columns from two different laboratories[1, 2] show considerable disagreement among the higher series members in spite of the fact that both authors measured them partially in the second order against known standards. It has been possible to supplement these measurements on a new 5 meter 4° grazing incidence vacuum spectrograph designed by Professor Siegbahn and built in the workshops of this institute. The measurements of the first two lines have been supplemented by higher order determinations on a 1 meter 5.4° grazing incidence spectrograph. The results are listed in Table I.

The line at 100A checks exactly with the previous measurements; the line at 88A has been measured in three orders on five different plates. The line at 84A has been measured in two orders on three plates and the others in the first order only on three plates. Each plate has been measured twice against known oxygen standards where possible or against the lower Be series members and strong

TABLE I. *The $1s^2\ {}^1S_0 - 1s \cdot np\ {}^1P_1$ series of Be III* ($^1S_0 = 1{,}241{,}225$ cm^{-1}).

n	λ(A)	ν(cm^{-1})	$1s \cdot np\ {}^1P_1$	n^*
2	100.254	997,466	243,759	2.0128
3	88.314	1,132,323	108,902	3.0114
4	84.758	1,179,830	61,395	4.0107
5	83.202	1,201,894	39,331	5.0109
6	82.377	1,213,931	27,294	6.0107
7	81.891	1,221,135	20,090	7.0113

TABLE II. *$1s\ {}^2S - np\ {}^2P$ series of Be IV.*

n		n	
2	75.9251	5	59.3179
3	64.0629	6	58.5723
4	60.7414	7	58.1316

phosphorus lines measured in from two to ten orders during the present investigation.

Table II lists the lines of Be IV which have been observed. The listed wave-lengths have been calculated from the Penney[3] formula. These lines have also been used as standards in this region.

The Be III series herein listed together with new determinations of the He I-like series from Li II to N VI show surprisingly good agreement with values calculated by means of the Hylleraas[4] formula when the mass and relativity corrections are applied. The subject is being discussed in detail elsewhere.

HOWARD A. ROBINSON

Irving Langmuir Fellow,
American Scandinavian Foundation,
Physical Institute, University of Uppsala, Sweden,
May 10, 1936.

[1] P. G. Kruger and F. S. Cooper, Phys. Rev. **44**, 418 (1933).
[2] B. Edlén, Phys. Rev. **44**, 778 (1933).
[3] W. G. Penney, Phil. Mag. **9**, 661 (1930).
[4] For a complete account see H. Bethe, *Handbuch der Physik*, Vol. 24/1 (1933), pp. 324 *et seq.* Several of Bethe's numerical calculations are incorrect.

Some Lattice Sums Involved in the Calculation of Elastic Constants

In recent calculations the theoretical values for the elastic constants of crystals of the CsCl type were needed. The electrostatic part of the elastic constant C_{11}, usually called $A^{(e)}$,[1] could not be found in the literature. We calculated it with the method of Ewald as used by Heckmann[2] for the elastic constants of ZnS and CaF_2. Most of the Fourier and D'Alembert series needed for the calculation were already tabulated by Heckmann. A check on the accuracy is obtained in the usual manner by making the calculation for two different values of the arbitrary separation constant E. Here $E = \pi$ and $E = 2$ were chosen. The results were

$$A^{(e)} = (e^2/\delta^4) \times 2 \cdot 1253$$

and $$A^{(e)} = (e^2/\delta^4) \times 2 \cdot 1252 \text{ respectively,}$$

where e is the charge of the ions, δ the side of the cubic cell (δ^3 = volume per molecule).

The electrostatic part of the elastic constant C_{12}, called $B^{(e)}$ by Born, can then be found from the equation connecting it with $A^{(e)}$ and the Madelung constant

$$B^{(e)} = -(e^2/\delta^4) \times 1 \cdot 5715.$$

The signs of these constants are opposite to those for the NaCl type lattices.

M. GOEPPERT-MAYER
ALBERT MAY

The Johns Hopkins University,
Catholic University,
May 26, 1936.

[1] M. Born, *Atom theorie des festen Zustandeo* (Berlin, 1923), p. 571.
[2] G. Heckmann, Zeits. f. Physik **23**, 47 (1924); Zeits f. Kristallographie **61**, 287 (1924).